

**UNIVERSIDADE FEDERAL DE JUIZ DE FORA
INSTITUTO DE CIÊNCIAS EXATAS
PÓS GRADUAÇÃO EM QUÍMICA**

Carla Vieira Soares

**Computational evaluation of MOFs for their adsorption and catalytic degradation
performances with respect to chemical warfare agents**

Juiz de Fora

2020

Carla Vieira Soares

Computational evaluation of MOFs for their adsorption and catalytic degradation performances with respect to chemical warfare agents

Tese apresentada ao Programa de Pós-graduação em Química da Universidade Federal de Juiz de Fora como requisito parcial à obtenção do título de Doutora em Química

Orientador: Dr. Alexandre Amaral Leitão

Coorientador: Dr. Guillaume Maurin

Juiz de Fora

2020

Ficha catalográfica elaborada através do programa de geração automática da Biblioteca Universitária da UFJF, com os dados fornecidos pelo(a) autor(a)

Soares, Carla Vieira.

Computational evaluation of MOFs for their adsorption and catalytic degradation performances with respect to chemical warfare agents / Carla Vieira Soares. -- 2020.

233 f. : il.

Orientador: Alexandre Amaral Leitão

Coorientador: Guillaume Maurin

Tese (doutorado) - Universidade Federal de Juiz de Fora, Instituto de Ciências Exatas. Programa de Pós-Graduação em Química, 2020.

1. Materiais Híbridos porosos. 2. MOFs. 3. Agentes de guerra química. 4. Monte Carlo. 5. Teoria do Funcional da Densidade. I. Leitão, Alexandre Amaral, orient. II. Maurin, Guillaume, coorient. III. Título.

Carla Vieira Soares

Computational evaluation of MOFs for their adsorption and catalytic degradation performances with respect to chemical warfare agents

Tese apresentada ao Programa de Pós-Graduação em Química da Universidade Federal de Juiz de Fora como requisito parcial à obtenção do título de Doutora em Química.

Aprovada em 29 de maio de 2020.

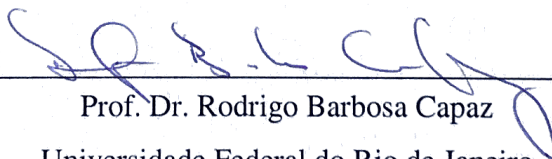
BANCA EXAMINADORA



Prof. Dr. Alexandre Amaral Leitão - Orientador
Universidade Federal de Juiz de Fora



Prof. Dr. Guillaume Maurin - Coorientador
Université de Montpellier 2



Prof. Dr. Rodrigo Barbosa Capaz
Universidade Federal do Rio de Janeiro



Prof. Dr. Heitor Avelino de Abreu
Universidade Federal de Minas Gerais



Prof. Dr. Luiz Ant nio Sodr  da Costa
Universidade Federal de Juiz de Fora



Profa. Dra. Sabine Devautour-Vinot
Université de Montpellier 2

To my parents Glécia e José Carlos (in memoriam), my dear grandfather Nilo (in memoriam), my siblings Kélvia e Kéven and my love Matheus.

ACKNOWLEDGEMENTS

I would first like to thank God for being so generous throughout my life. My faith gives me the strength to keep going in the direction of my dreams.

There are so many people that have helped me reach this point that I have to thank them all for their efforts. Starting with the important role that my supervisors Dr. Alexandre Amaral Leitão and Dr. Guillaume Maurin have played in providing support, guidance, and encouragement. Alexandre gave me the opportunity as undergraduate student, when I was just nineteen years old, and since then he had motivated me and taught me so much. He always gave me good advice and ideas. I am immensely thankful for all the opportunities he has provided me throughout all of these years. Guillaume Maurin has provided me an incredible support; without him this international joint PhD would not have been possible. I greatly appreciate his enthusiasm for research and his mentorship in guiding me to become a researcher.

I would also like to thank past and present GFQSI group members, who have been invaluable with scientific discussions, nice talks and useful parallel connections all these years. Especially, my dearest friend Carla for her endless fondness and incentive. And, of course, my colleagues working at the DAMP group for being very supportive, kind and for enriching my career significantly through helpful discussions at the lab and also during our coffee-breaks. Special thanks to Rocio and Sabine to be so nice to me and helping me during my internship in Montpellier. Also, to Anusha and Paulo, they became more than my colleagues, each one knows how much they did for me. Thank you for the friendship and helping hand in the many moments I needed.

I would also thank all members of the jury for having agreed to serve as rapporteurs and examiners. Specially acknowledging the rapporteurs for taking time out to read my work. The Capes and the program Capes/Cofecub, for the grant, which has supported me during my thesis and also my internship in Montpellier for one year.

To my friends, Marcela, Aline, Carla, Mathieu, Patrícia and Márcia, thank you for always being there for me, listening and offering me advice. The well-wishes, prayers, good laughs, phone calls, lunches, rides, nice talks at happy hours after a long work day, afternoons at the beach, texts, and visits were very important throughout this entire process.

Finally, I would not have made it this far without the support of my family. My deepest appreciation goes to my mother, who has done many sacrifices to make sure that me, my brother and sister could have the best education. I am extremely grateful to my father (i.m.). Eventhough, he is not been around these many years, I am constantly inspired by his

determination, persistence and optimism. And also, to my grandfather (i.m.) who acted as a father by taking care of us, and teaching us many values. To my sister and brother for their endless love. They have given me extra strength and motivation to get things done. I am so grateful to have been blessed with them. And my love, Matheus, my best friend, he is truly everything I could have asked for and more as a partner. Thank you for always being there for me.

RESUMO

Esta tese de doutorado tem como objetivo realizar a avaliação computacional de uma vasta série de Redes Metalorgânicas (MOF) contendo Zr ou Ti como centros metálicos a fim de prever suas performances com relação a adsorção e degradação dos agentes de guerra química: agentes neurotóxicos (Sarin e Soman), agentes vesicantes (Gás Mostarda) e seus simulantes Metilfosfonato de dimetilo, Isofluorofato, Pinacolyl metilfosfonato e Cloreto de 2-etiltioetilo. Cálculos baseados na Teoria do Funcional da Densidade (DFT) e simulações de Monte Carlo foram combinados para avaliar a capacidade adsorptiva, a energia e os sítios de adsorção preferenciais para cada par MOF/CWA. A racionalização do banco de dados gerado foi posteriormente realizada, a fim de estabelecer relações estrutura-propriedade de adsorção levando em consideração descritores geométricos e eletrônicos que caracterizam as MOF, os CWA e também as interações CWA/MOF. Posteriormente, foram realizados cálculos de DFT para elucidar os mecanismos de degradação de CWA e seus simulantes utilizando MOF formadas por titânio ou zircônio, e analisar os principais estados da reação de degradação e as energias de ativação resultantes. E por fim, o mecanismo de hidrólise de uma série de Zr e Ti-MOF foi explorado por meio de cálculos de DFT com o objetivo de identificar os principais parâmetros que governam a estabilidade das MOF sob umidade. Espera-se que este estudo computacional revele MOF com elevado desempenho de captura/degradação a serem potencialmente aplicadas como filtros de CWA.

Palavras-chave: Materiais Híbridos porosos. MOF. Agentes de guerra química. Adsorção. Catálise. Degradação. Monte Carlo. Teoria do Funcional da Densidade.

ABSTRACT

The present PhD thesis aims to perform a computational evaluation of a large series of Metal Organic Frameworks (MOFs) containing Zr or Ti as the metal centers for their adsorption and degradation performances with respect to chemical warfare agents: nerve agents (Sarin and Soman), vesicant agents (Sulfur Mustard) as well as their simulants, Dimethyl methylphosphonate, Diisopropyl phosphorofluoridate, Pinacolyl methylphosphonate and 2-Chloroethyl ethyl sulfide. This was achieved by combining Density Functional Theory (DFT) calculation and Monte Carlo simulations to assess the adsorption uptake, the energetics and the preferential adsorption sites for each considered MOF/CWA pair. The rationalization of the so-generated database was further achieved in order to establish structure-adsorption property relationships with the consideration of geometric and electronic descriptors characterizing MOFs, CWAs as well as CWA/MOF interactions. As a further step, DFT calculations were performed to elucidate the degradation mechanisms for CWAs and their simulants on the Ti or Zr-MOFs analyzing the main states of the degradation reaction and the resulting activation energies. Finally, the hydrolysis mechanism of a series of Zr and Ti-MOFs was explored by means of DFT calculations with the objective to identify the key parameters that control their stability under humidity. This computational work is expected to pave the way towards refined MOFs with improved capture/degradation performances to be potentially applied as CWA filters.

Keywords: Hybrid Porous materials. MOFs. Chemical Warfare Agents. Adsorption. Catalysis. Degradation. Monte Carlo simulations. Density Functional Theory calculations.

RÉSUMÉ

Cette thèse vise à effectuer un criblage computationnel d'une grande série de structures métal-organiques (MOFs) contenant du Zr ou du Ti afin de prédire leurs performances vis-à-vis l'adsorption et dégradation des agents chimiques de guerre (ACGs). Cette étude inclut des agents neurotoxiques (Sarin et soman), agents vésicants (gaz moutarde) ainsi que leurs simulants, à savoir, le diméthyl méthylphosphonate, le diisopropyl phosphorofluoridate, le pinacolyl méthylphosphonate et le 2-chloroéthyl éthyl sulfure. Des calculs basés sur la Théorie de la Fonctionnelle de la Densité (DFT) ont été couplés à des simulations de Monte Carlo pour évaluer la capacité adsorptive, l'énergie et les sites d'adsorption préférentiels pour chaque paire MOF/ACG considérée. Ensuite, ces données ont été rationalisées afin d'établir des relations structure-propriété d'adsorption en prenant en compte des paramètres géométriques et électroniques caractéristiques des MOF, des ACGs ainsi que de leurs interactions croisées. Postérieurement, des calculs DFT ont été effectués afin d'élucider les mécanismes de dégradation des ACG et de leurs simulants sur les MOFs en analysant les principaux états intermédiaires de leurs réactions de dégradation et les énergies d'activation résultantes. Finalement, les mécanismes d'hydrolyse d'une série de MOFs à base de Ti et Zr ont été explorés par la voie des calculs DFT dans le but d'identifier les paramètres clés qui contrôlent leur stabilité sous humidité. Ces études computationnelles doivent ouvrir la voie à des nouvelles MOF avec des performances de capture/dégradation améliorées qui pourraient être appliquées comme filtres de ACGs.

Mots clefs: Matériaux Hybrides poreux. MOFs. Agents Chimiques de guerre. Adsorption. Catalyse. Dégradation. Monte Carlo. Théorie de la Fonctionnelle de la Densité.

LIST OF ILLUSTRATIONS

Figure 2.1	-	Categories of Chemical Warfare Agents.....	29
Figure 2.2	-	a) Basic chemical structure of nerve agents. b) Tabun, c) Sarin, d) Soman and e) VX.....	30
Figure 2.3	-	Chemical structure of blister agents.....	32
Figure 2.4	-	a) Acetylcholinesterase activity and b) Inhibition of enzymatic activity.....	34
Figure 2.5	-	A scheme depicting the mechanism for the alkylation of a guanine unit by a nitrogen mustard (HN2) molecule. This reaction mechanism is the stereotypical route of reaction of all mustards.....	36
Figure 2.6	-	Molecular structures of nerve agent simulants.....	37
Figure 2.7	-	Molecular structures of HD simulants.....	38
Figure 2.8	-	Nerve agents hydrolysis reaction.....	39
Figure 2.9	-	Detoxifying reactions of sulfur mustard.....	39
Figure 2.10	-	Sulfur mustard hydrolysis.....	40
Figure 2.11	-	Versatile chemistry & topology/connectivity of MOFs.....	44
Figure 2.12	-	Henry's constants for water as a function of the largest cavity diameter (LCD) in MOF structures at 298 K. Purple and blue dashed lines depict water KH in ZIF-8 and HKUST-1, respectively. Color code represents isosteric heat of adsorption (Qst) for water.....	49
Figure 2.13	-	MOF rankings of 1544 MOFs for: DMMP (blue) and Sarin (green) (on the left) and DMNP (blue) and Soman (green) (on the right) when ordered by the heat of adsorption of (a) Sarin and (b) Soman, respectively.....	50
Figure 2.14	-	(a) Connectivity of the octahedral pore in UiO-66. $X_1=X_2=H$ for UiO-66, $X_1=NO_2$ and $X_2=H$ for UiO-66- NO_2 , $X_1=X_2=OH$ for UiO-66-(OH) $_2$, and $X_1=NH_2$ and $X_2=H$ for UiO-66-NH $_2$. (b) Connectivity of the octahedral pore in UiO-67(Zr). $X=H$ for UiO-67, $X=NH_2$ for UiO-67-NH $_2$, and $X=N(CH_3)_2$ for UiO-67-NMe $_2$. (c) Hydrolysis rate of UiO-66 (blue), UiO-66- NO_2 (red), UiO-66-(OH) $_2$ (green), and UiO-66-NH $_2$ (pink). (d) Hydrolysis rate of UiO-67 (blue), UiO-67-NH $_2$ (red) and UiO-67-NMe $_2$ (green)..	53
Figure 2.15	-	(a) Essential Steps in the Reaction Mechanism for Degradation of GB on Dry Zr-Based MOFs. (b) Potential energy diagram for the central steps of the reaction mechanism of GB hydrolysis with the SBUs of dry UiO-66(Zr)	

	(black trace) and MOF-808 (red). Atom colors are Zr: teal, O: red, C: brown, H: white, F: green and P: yellow.....	55
Figure 2.16 -	M06-2X/Def2-TZVP//M06-L/Def2-SVP 298 K free energies and enthalpies for hydrolysis of sarin along different cluster-model benzoate-capped reaction coordinates relative to separated reactants.....	56
Figure 2.17 -	(a) Dual-reaction setup to transform toxic CWA simulants CEES and DMNP to nontoxic oxidative and hydrolytic products, respectively. (b) Kinetic profiles for hydrolysis of DMNP and oxidation of CEES. (c) Kinetic profiles for the destruction of a second injection of DMNP and CEES into the “MOF-catalyzed dual-reaction”.....	57
Figure 2.18 -	Illustrations of the inorganic Zr and Ti building blocks present in a few representative 3D-MOFs.....	58
Figure 3.1 -	(a) The crystal solid with the unit cell of the lattice in black. (b) The atoms that must be included in the simulation are colorful, where the primitive cell is highlighted in blue. (c) The reciprocal lattice of the crystal with the origin (gamma point) highlighted in red. Both the reciprocal unit cell (black) and the first Brillouin zone (BZ) (red) are highlighted. (d) First BZ divided by a uniform mesh of k -points. Because of the point group symmetry, only those within the gray triangle need to be explicitly considered in the calculation.....	69
Figure 3.2 -	Illustration of the pseudo-wave function and the potential (red solid line) compared to the all-electron wave function and electronic potential (blue dashed line) plotted against the distance from the nucleus. The cut-off radius denotes the radius at which the electron and pseudo-electron values are identical.....	72
Figure 3.3 -	Plot of the Lennard–Jones potential function.....	84
Figure 3.4 -	Partial charges used for the united-atom models considered for the CWAs molecules: (a) Soman, (b) Sarin, (c) DMMP, (d) DIFP and (e) PMP.....	86
Figure 4.1 -	Illustration of the CWAs molecules: (a) Soman, (b) Sarin, (c) DMMP, (d) DIFP and (e) PMP considered in this work.	91
Figure 4.2 -	GCMC simulated saturation uptakes at 298 K for all MOFs with respect to sarin, soman, DMMP and DIFP calculated using a pressure of 5000 kPa...	92
Figure 4.3 -	GCMC simulated uptakes for all CWAs in MOFs as a function of the N ₂ -accessible surface area of the MOFs (reported in Table 4.1).....	93

Figure 4.4	-	GCMC simulated uptakes for all CWAs in MOFs as a function of the free volume of the MOFs (reported in Table 4.1).	94
Figure 4.5	-	Structure-adsorption uptake relationship for CWAs in MOF (a) for all studied MOFs and (b) where the materials MIL-125(Ti)NH ₂ , MOF-808-OH-H ₂ O and UiO-66(Zr)NH ₂ were removed.	95
Figure 4.6	-	Structure-adsorption uptake relationship for CWAs in MOF (a) for all studied MOFs and (b) for MIL-125-Ti, MIL-140G, MIP-177-OH-H ₂ O, MIP-200-OH-H ₂ O, NU-1000, MOF-808-OH-H ₂ O, UiO66-NH ₂ -defects6, UiO66-Zr-defects3, UiO-67, UiO-68 and Zr-AzoBDC.	96
Figure 4.7	-	GCMC simulated adsorption enthalpy as a function of α (a) for all studied MOFs and (b) for MIL-125-Ti, MIL-125-Ti(NH ₂), MIP-177-OH-H ₂ O, MIP-200, MIP-200-OH-H ₂ O, MOF-808-F, MOF-808-OH-H ₂ O, UiO66-Cl, UiO66-NH ₂ -defects6, UiO66-Zr, UiO66-Zr(OH) ₂ , UiO66-Zr(CO ₂ H), UiO66-Zr-defects3, UiO-67, UiO-68 and Zr-AzoBDC.....	97
Figure 4.8	-	GCMC simulated adsorption enthalpy at 298 K for all MOFs with respect to sarin, soman, DMMP and DIFP calculated at low coverage.	98
Figure 4.9	-	A typical illustration of the preferential sittings for (a) Sarin, (b) Soman, (c) DIFP and (d) DMMP in the pores of the defective UiO-66(Zr)-NH ₂ and the corresponding CWA/MOF radial distribution functions averaged over all the MC configurations.	100
Figure 4.10	-	GCMC simulations at low loading. A typical illustration with the preferential sittings for a) Soman and b) DIFP in the pores of MOF-808-OH-H ₂ O and the radial distribution functions between all the hydrogen atom of the active sites and the oxygen of guest molecules.	103
Figure 5.1	-	a) Adjacent SBUs with bridging formates connected by 3,3',5,5'-tetracarboxydiphenylmethane (H4mdip) linkers. b) Unit cell and c) Illustration of the crystal structure of MIP-177(Ti). The creation of the Ti open site through dehydration leads to a hydroxyl group coordinated in a bidentate manner to the Ti1 and Ti2.	108
Figure 5.2	-	Simulated Minimum Energy Path corresponding to the degradation mechanism of Sarin on the Ti activated site. b) Evolution of the main characteristic distances involving the atoms of Sarin (F, P and O(sp ²)) and of Ti-MOF (Ti, H(OH)) along the reaction coordinate.	109

- Figure 5.3 - Illustration of the degradation mechanism of Sarin on the Ti activated site of MIP-177(Ti). a) Reactant (Ti-MOF + Sarin), b) Transition state (TS) and c) Product (Ti-MOF-IMPA-HF). The main distances involved in the degradation process, P-F (pink), F-H(OH) (blue) and O(sp²)-Ti (red) are represented and expressed in Å..... 110
- Figure 5.4 - a) Simulated Minimum Energy Path corresponding to the degradation mechanism where the Ti active site binds to the fluorine atom of Sarin. b) Evolution of the main characteristic distances involving the atoms of Sarin (F, P) and of Ti-MOF (Ti, O(OH)) along the reaction coordinate..... 111
- Figure 5.5 - Illustration of the degradation mechanism of Sarin on the Ti activated site of MIP-177(Ti) where the Ti active site binds to the fluorine atom of Sarin. a) Reactant (Ti-MOF + Sarin), b) Transition state (TS) and c) Product (Ti-MOF-F-IMPA). The main distances involved in the degradation process, P-F (pink), F-Ti (blue) and O(OH)-P (red) are represented and expressed in Å..... 113
- Figure 5.6 - Simulated Minimum Energy Paths corresponding to the degradation mechanism of (a) DIFP and (b) DMMP on the Ti activated site..... 114
- Figure 5.7 - Illustration of the degradation mechanism of DIFP on the Ti activated site of MIP-177(Ti). a) Reactant (Ti-MOF + DIFP), b) Transition state (TS) and c) Product (Ti-MOF-DIHP-HF). The main distances involved in the degradation process, P-F (pink), F-H(OH) (blue) and O(sp²)-Ti (red) are represented and expressed in Å. 115
- Figure 5.8 - Illustration of the degradation mechanism of DMMP on the Ti activated site of MIP-177(Ti). a) Reactant (Ti-MOF + DMMP), b) Transition state (TS) and c) Product (Ti-MOF-DMHP-MeOH). The main distances involved in the degradation process, P-O(CH₃) (pink), O(CH₃)-H(OH) (blue) and O(sp²)-Ti (red) are represented and expressed in Å. 117
- Figure 5.9 - Illustration of the degradation mechanism of sarin on the activated Ti site of MIP-177(Ti) in the presence of water where sarin interacts predominantly with the MOF framework. (a) Reactant (Ti- MOF + sarin + H₂O), (b) transition state (TS), and (c) product (Ti- MOF-IMPA-HF). The main distances involved in the degradation process, P-F (pink), F-H(H₂O) (blue), and O(H₂O)-P (red) are represented and expressed in Å. The black dashed lines indicate the interaction between the molecules (water and IMPA) and the framework. 119

Figure 5.10 -	Illustration of the degradation mechanism of Sarin on the Ti activated site of MIP-177(Ti) in the presence of water. a) Reactant (Ti-MOF + Sarin + H ₂ O), b) Transition state (TS) and c) Product (Ti-MOF-IMPA-HF). The main distances involved in the degradation process, P-F (pink), F-H(H ₂ O) (blue) and O(H ₂ O)-P (red) are represented and expressed in Å. The black dashed lines indicate the interaction between the molecules (water and IMPA) and the framework.	120
Figure 5.11 -	Simulated Minimum Energy Paths corresponding to the degradation mechanism of Sarin on the Ti activated site in the presence of water. (a) Related to the configurations reported on Figure 5.9 and (b) Related to the configurations reported on Figure 5.10.	121
Figure 5.12 -	a) Illustration of the crystal structure of MIP-200(Zr), b) Unit cell and c) A single 8-connected SBU and a 4-coordinated H4mdip linker.	123
Figure 5.13 -	a) Illustration of the crystal structure of UiO-66(Zr)-defects6, b) Unit cell. c) A single 10-connected SBU.	124
Figure 5.14 -	Simulated Minimum Energy Path corresponding to the degradation mechanism of Sarin on the MIP-200(Zr).	125
Figure 5.15 -	Illustration of the degradation mechanism of Sarin on the Zr activated site of MIP-200(Zr). a) Reactant (Zr-MOF + Sarin), b) Transition state (TS) and c) Product (Zr-MOF-IMPA-HF). The main distances involved in the degradation process, P-F (pink), F-H(OH) (blue) and O(sp ²)-Ti (red) are represented and expressed in Å.	126
Figure 5.16 -	Illustration of the degradation mechanism of Sarin on the Zr activated site of UiO-66(Zr). a) Reactant (Zr-MOF + Sarin), b) Transition state (TS) and c) Product (Zr-MOF-IMPA-HF). The main distances involved in the degradation process, P-F (pink), F-H(OH) (blue) and O(sp ²)-Ti (red) are represented and expressed in Å.	128
Figure 5.17 -	Simulated Minimum Energy Path corresponding to the degradation mechanism of Sarin on the UiO66-defects6(Zr).	129
Figure 5.18 -	Illustration of the degradation mechanism of Sarin in UiO66-defects6(Zr)-NH ₂ . a) Reactant (Zr-MOF + Sarin), b) Transition state (TS) and c) Product (Zr-MOF-IMPA-HF). The main distances involved in the degradation process, P-F (pink), F-H(OH) (blue) and O(sp ²)-Zr (red) are represented and expressed in Å.	131

Figure 5.19 -	a) Simulated Minimum Energy Path corresponding to the degradation mechanism of Sarin on the UiO66-defects6(Zr)-NH ₂	132
Figure 5.20 -	Illustration of the adsorption configurations (Reactants) involved in the Sarin degradation process. a) UiO-66(Zr) and b) UiO-66(Zr)-NH ₂ . The main distances between Sarin and the SBU (black) and Sarin and the linker (red) are expressed in Å.	133
Figure 5.21 -	Illustration of the degradation mechanism of Soman in UiO66-defects6(Zr)-NH ₂ . a) Reactant (Zr-MOF + Soman), b) Transition state (TS) and c) Product (Zr-MOF-PMP-HF). The main distances involved in the degradation process, P-F (pink), F-H(OH) (blue) and O(sp ²)-Zr (red) are represented and expressed in Å.	134
Figure 5.22 -	Simulated Minimum Energy Path corresponding to the degradation mechanism of Soman in UiO66-defects6(Zr)-NH ₂	135
Figure 5.23 -	Simulated Minimum Energy Path corresponding to the degradation mechanism of Soman in UiO66-defects6(Zr).	136
Figure 5.24 -	Illustration of the degradation mechanism of Soman in UiO66-defects6(Zr). a) Reactant (Zr-MOF + Soman), b) Transition state (TS) and c) Product (Zr-MOF-PMP-HF). The main distances involved in the degradation process, P-F (pink), F-H(OH).	137
Figure 5.25 -	Illustration of the adsorption configurations (Reactants) involved in the Soman degradation process. a) Non-functionalized UiO-66(Zr) and b) Functionalized UiO-66(Zr). The main distances between Soman and the SBU (black) and Sarin and the linker (red) are expressed in Å.	138
Figure 5.26 -	Illustration of the degradation mechanism of HD on the UiO66-defects6(Zr)-NH ₂ . a) Reactant (Zr-MOF + HD), b) Transition state (TS) and c) Product (Zr-MOF-half_HD-Cl). The main distances involved in the degradation process, Cl-C (gray), C-OH (red), H(H ₂ O)-Cl (green) and H(OH)-Cl (blue) are represented and expressed in Å.	140
Figure 5.27 -	Simulated Minimum Energy Path corresponding to the degradation mechanism of HD on the UiO66-defects6(Zr)-NH ₂	141
Figure 5.28 -	Illustration of the degradation mechanism of HD on the UiO66-defects6(Zr). a) Reactant (Zr-MOF + HD), b) Transition state (TS) and c) Product (Zr-MOF-half_HD-Cl). The main distances involved in the degradation process,	

	Cl-C (gray), C-OH (red), H(H ₂ O)-Cl (green) and H(OH)-Cl (blue) are represented and expressed in Å.....	142
Figure 5.29	- Simulated Minimum Energy Path corresponding to the degradation mechanism of HD on the UiO66-defects6(Zr).....	143
Figure 5.30	- Illustration of the degradation mechanism of CEES on the UiO66-defects6(Zr)-NH ₂ . a) Reactant (Zr-MOF + CEES), b) Transition state (TS) and c) Product (Zr-MOF-ETE-Cl). The main distances involved in the degradation process, Cl-C (gray), C-OH (red), H(H ₂ O)-Cl (green) and H(OH)-Cl (blue) are represented and expressed in Å.....	144
Figure 5.31	- Simulated Minimum Energy Path corresponding to the degradation mechanism of CEES in UiO66-defects6(Zr)-NH ₂	145
Figure 6.1	- Illustration of the hydrolysis mechanism of UiO-66(Zr). a) Reactant (UiO-66(Zr) + H ₂ O), b) First transition state (TS1), c) Intermediate 1, d) Second transition state (TS2) and e) Intermediate 2 (UiO-66(Zr):[OH ⁻][H ⁺]). The main distances involved in the dissociative chemisorption of water are represented and expressed in Å. Color scheme: MOF (Zr: blue, C: gray, O: red and H: white) and water (O: dark blue and H: white).....	150
Figure 6.2	- Simulated Minimum Energy Path corresponding to the dissociative chemisorption of 1 water molecule per unit cell of UiO-66(Zr).....	151
Figure 6.3	- a) Illustration of the crystal structure of UiO-67(Zr), b) Unit cell. c) A single 12-connected SBU and a 4,4'-biphenyldicarboxylate linker to clarify the bond between them.	152
Figure 6.4	- DFT optimized water loaded UiO-67(Zr). The most stable arrangements of water in the pores of UiO-67(Zr). Structures for the 3 corresponding configurations (b, c and d) compared to the DFT optimized structure for the empty UiO-67(Zr). Color scheme: MOF (Zr: blue, C: gray, O: red and H: white) and water (O: dark blue and H: white).....	153
Figure 6.5	- a) Illustration of the crystal structure of NU-800(Zr), b) Unit cell. c) A single 12-connected SBU and a TPT linker to clarify the bond between them....	154
Figure 6.6	- Simulated Minimum Energy Path corresponding to the dissociative chemisorption of 1 water molecule per unit cell of NU-800(Zr).....	155
Figure 6.7	- Illustration of the hydrolysis mechanism of NU-800(Zr). a) Reactant (NU-800(Zr) + H ₂ O), b) First transition state (TS) and c) Intermediate (NU-800(Zr):[OH ⁻][H ⁺]). The main distances involved in the dissociative	

	chemisorption of water are represented and expressed in Å. Color scheme: MOF (Zr: blue, C: gray, O: red and H: white) and water (O: dark blue and H: white).....	156
Figure 6.8	- Illustration of the hydrolysis mechanism of MIP-200(Zr). a) Reactant (MIP-200(Zr) + H ₂ O), b) First transition state (TS1), c) Intermediate 1, d) Second transition state (TS2) and e) Intermediate 2 (MIP-200(Zr):[OH ⁻][H ⁺]). The main distances involved in the dissociative chemisorption of water are represented and expressed in Å. Color scheme: MOF (Zr: blue, C: gray, O: red and H: white) and water (O: dark blue and H: white).....	157
Figure 6.9	- Simulated Minimum Energy Path corresponding to the dissociative chemisorption of 1 water molecule per unit cell of MIP-200(Zr).....	158
Figure 6.10	- Simulated Minimum Energy Path corresponding to the dissociative chemisorption of 1 water molecule per unit cell of MIP-177(Ti).....	161
Figure 6.11	- Illustration of the hydrolysis mechanism of MIP-177(Zr). a) Reactant (MIP-177(Zr) + H ₂ O), b) First transition state (TS1), c) Intermediate 1, d) Second transition state (TS2) and e) Intermediate 2 (MIP-177(Zr):[OH ⁻][H ⁺]). The main distances involved in the dissociative chemisorption of water are represented and expressed in Å. Color scheme: MOF (Ti: light gray, C: gray, O: red and H: white) and water (O: dark blue and H: white).....	162

LIST OF TABLES

Table 2.1	-	Physical Properties of nerve agents.....	31
Table 4.1	-	Calculated parameters for the MOFs used in this work.....	90
Table 4.2	-	Bader charge analysis for the isolated and adsorbed CWAs in the defective UiO-66(Zr)-NH ₂	101
Table 4.3	-	Simulated adsorption uptakes and enthalpies for sarin, soman, DMMP, DIFP and PMP in two representative MOF materials investigated in this study.	102
Table 6.1	-	The average of the measurements of the angles for the linkers in the presence of the water molecule compared with the MOF without water in the pore cavity.....	160

LIST OF ABBREVIATIONS

ACh	Acetylcholine
AChE	Acetylcholinesterase
ASZM-TEDA	Activated Carbon, impregnated with Copper, Silver, Zinc, Molybdenum, and Triethylenediamine
BDC	1,4 benzenedicarboxylate
CEES	2-Chloroethyl ethyl sulfide or Half-mustard
CEMS	2-Chloroethyl methyl sulfide
CEPS	Chloroethyl phenyl sulfide
CH-TG	Hemi mustard thiodiglycol aggregate
CWAs	Chemical Warfare Agents
CWC	Chemical Weapons Convention
DCNP	Diethyl cyanophosphonate
DCP	Diethyl chlorophosphate
DES	Diethyl sulfide
DIFP	Diisopropylphosphorofluoridate
DIMP	Diisopropyl methylphosphonate
DMHP	dimethyl hydrogen phosphate
DMMP	Dimethyl methylphosphonate
DMNP	Methyl paraoxon
DMPT	O,S-dimethyl methylphosphonothioate
DNP	Polarization functions
DPMP	Diphenyl methylphosphonate
DFT	Density Functional Theory
ETE	2-(Ethylthio)ethanol
GA	Tabun
GB	Sarin or Isopropyl methylphosphonofluoridate

GCMC	Grand canonical Monte Carlo
GD	Soman or 1,2,2-trimethylpropyl methylphosphonofluoridate
GGA	Generalized Gradient Approximation
Half_HD	Half mustard
HD	Sulfur mustard
H ₄ mdip	tetracarboxylate ligand
HN2	Methylbis(2-chloroethyl)amine
ICP-AES	Inductively Coupled Plasma - Atomic Emission Spectrometry
KS	Kohn and Sham
LDA	Local Density Approximation
IMPA	Isopropyl methyl phosphonic acid
mdip	tetracarboxydiphenyl-methane
MIP	Materials of the Institute of Porous Materials of Paris
MEP	Minimum Energy Path
MOFs	Metal-Organic Frameworks
MPA	Methylphosphonic acid
NEB	Nudged Elastic Band
OPCW	Organization for the Prohibition of Chemical Weapons
PMP	Pinacolyl methylphosphonate or Pinacolyl methylphosphonic acid
PW	Perdew and Wang
PZ	Perdew and Zunger
Q_{st}	Isosteric heat of adsorption
RDFs	Radial Distribution Functions
SBU	Secondary Building Units
TDG	Thiodiglycol
TICs	Toxic Industrial Compounds
TPT	1,4-benzenedipropynoic acid

TraPPE	Transferable Potentials for Phase Equilibria
UiO	University of Oslo
VWN	Vosko-Wilk-Nusair
VX	Ethyl ({2-[bis(propan-2-yl)amino]ethyl}sulfanyl)(methyl)phosphinate

TABLE OF CONTENTS

1	INTRODUCTION.....	24
2	OVERVIEW ON THE ADSORPTION AND DEGRADATION OF CWAs.....	27
2.1	DEFINITION AND CLASSIFICATION OF CHEMICAL WARFARE AGENTS.....	27
2.1.1	Intoxification by nerve agents and mustards.....	33
2.1.2	Appropriate simulants.....	36
2.1.3	Hydrolysis degradation of CWAs.....	38
2.2	PROTECTIVE MATERIALS AGAINST CWAs.....	40
2.2.1	Materials for the degradation of CWAs.....	42
2.2.2	MOFs for the capture and degradation of CWAs.....	43
2.2.2.1	<i>MOFs for the capture of CWAs – experimental approach.....</i>	<i>45</i>
2.2.2.2	<i>MOFs for the capture of CWAs – computational approach.....</i>	<i>47</i>
2.2.2.3	<i>MOFs for the degradation of CWAs – experimental approach.....</i>	<i>50</i>
2.2.3.4	<i>MOFs for the degradation of CWAs – computational approach.....</i>	<i>54</i>
2.3	CONCLUSION.....	59
3	QUANTUM AND FORCE-FIELD BASED MOLECULAR SIMULATIONS.....	60
3.1	THE MANY-BODY PROBLEM AND BORN-OPPENHEIMER APPROXIMATION.....	60
3.1.1	Density functional theory.....	61
3.1.2	The Kohn-Sham equations.....	63
3.1.3	The exchange-correlation functional.....	65
3.1.3.1	<i>Dispersion forces in DFT.....</i>	<i>67</i>
3.1.4	Periodic systems.....	68
3.1.5	Pseudopotential approximation.....	71
3.1.6	Nudged elastic band.....	73
3.2	STATISTICAL MECHANICS-ENSEMBLES.....	75
3.2.1	Monte Carlo simulations.....	78
3.2.2	Interatomic potentials.....	82
3.2.3	Microscopic description of the host Metal-Organic Frameworks....	85

3.2.4	Microscopic description of the adsorbate.....	85
4	COMPUTATIONAL EVALUATION OF THE CWAS CAPTURE PERFORMANCES OF ROBUST MOFs.....	87
4.1	CWA UPTAKE AND ENERGETIC PERFORMANCES IN MOFs.....	89
4.2	UNDERSTANDING OF THE CWA/MOFS INTERACTIONS.....	99
4.3	COMPARISON BETWEEN THE ADSORPTION BEHAVIORS OF CWAs AND THEIR SIMULANTS.....	101
4.4	CONCLUSION.....	103
5	COMPUTATIONAL EXPLORATION OF THE CATALYTIC DEGRADATION OF CWAs BY Ti- AND Zr- MOFs.....	105
5.1	DEGRADATION OF SARIN ON THE ACTIVATED Ti SITE OF MIP-177(Ti).....	107
5.1.1	Degradation of the simulants of sarin on the activated Ti site of MIP-177(Ti).....	114
5.2	DEGRADATION OF SARIN IN THE PRESENCE OF WATER ON THE ACTIVATED Ti SITE OF MIP-177(Ti).....	118
5.3	DEGRADATION OF SARIN ON THE ACTIVATED Zr SITE OF Zr-MOFs.....	122
5.4	EFFECT OF THE MOF LINKER FUNCTIONALIZATION ON THE DEGRADATION OF SARIN AND SOMAN: CASE OF UiO-66(Zr) AND UiO-66(Zr)-NH ₂	130
5.5	DEGRADATION OF HD ON THE ACTIVATED Zr SITE OF UiO-66(Zr) AND UiO-66(Zr)-NH ₂	139
5.5.1	Degradation of the simulant of HD on the activated Zr site of UiO-66(Zr) and UiO-66(Zr)-NH₂.....	143
5.6	CONCLUSION.....	145
6	COMPUTATIONAL EXPLORATION OF THE STABILITY OF MOFs UNDER HUMIDITY.....	147
6.1	STABILITY OF Zr-MOFs.....	149
6.1.1	UiO-66(Zr).....	149
6.1.2	UiO-67(Zr).....	151
6.1.3	NU-800(Zr).....	154
6.1.4	MIP-200(Zr).....	156

6.2	RATIONALIZATION OF THE STABILITY OF Zr-MOFs.....	159
6.3	STABILITY OF THE Ti-MOFs.....	161
6.4	CONCLUSION.....	162
7	CONCLUSION AND PERPECTIVES.....	164
	REFERENCES.....	167
	ANNEX A – Atomic partial charges of MOFs.....	188
	ANNEX B – Articles.....	213

1 INTRODUCTION

The Chemical Weapons Convention targets to eliminate an entire category of weapons of mass destruction by prohibiting the development, production, acquisition, stockpiling, retention, transfer or use of Chemical Warfare Agents (CWAs) by States Parties under any circumstances (OPCW, 2005; SZINICZ, 2005). Unfortunately, even though their strictly prohibited, the world has not been able to be safe from terrorist groups and ill-intentioned governments. The number of incidents involving CWAs has significantly increased and some of them, such as the poisoning of Sergei Skripal, who acted as a double agent for the UK's intelligence services, and his daughter with a Novichok nerve agent by the Russian and the assassination of Kim Jong-un's half-brother, who died less than 20 minutes later that two women had attacked him with a VX nerve agent, have also demonstrated that civilian populations may also be exposed to these toxic agents. This sadly emphasizes that threat of exposure to CWAs is still considered as a major military issue.

Currently, filters for masks and protective overgarments are made of activated carbons. However, some issues are related to the use of this material, such as: a complete suit typically weighs about 2 kg; in warm weather, periods of heavy exertion cause heat stress and it must be safely discard due to the absence of degradation process by these materials (OUDEJANS, 2014). Therefore, it is becoming essential to develop technological methods and search for news materials for the sustainable neutralization of chemical warfare agents.

In this context, the hybrid porous materials, namely, the metal organic frameworks (MOFs) (FÉREY, 2008; HOSKINS; ROBSON, 1989; KONDO et al., 1997; MAURIN et al., 2017; YAGHI; LI, 1995), have been recently envisaged as an alternative solution to the standard activated carbons for practical better-performing protective equipment owing to their unique degree of variability in terms of chemical features (FÉREY, 2008; KUPPLER et al., 2009). This offers an unprecedented opportunity to identify porous adsorbents with the ability to capture a broad range of hazardous molecules to respond to diverse menaces and store high CWA.

The key objective of the PhD is to identify efficient MOFs to neutralize and destroy CWAs. In this context, molecular simulations were performed to study the adsorption performances of a large series of MOFs as well as their potentiality to catalytically degrade these toxic molecules.

There are clear advantages in performing simulations instead of real experiments. Besides the cost of the experiments, the CWAs cannot be manipulated at the academic level (NATIONAL RESEARCH COUNCIL, 1999). Indeed, the legislation on the

acquisition/holding/use of CWA is very restrictive due to security issues and toxicity of these substances. Thus, the handling of CWA requires equipment only available in military premises or being a laboratory accredited by the Organization for the Prohibition of Chemical Weapons. Therefore, for obvious reasons, the experiments must be carried out using simulants and in this case, molecular simulations are highly required to make the connection between these simulants and the real target CWA (KENAR; KARAYILANOĞLU; KOSE, 2002; NATIONAL RESEARCH COUNCIL, 1999; OPCW, 2019).

Molecular simulations integrate a wide panel of theoretical techniques: (i) the classical simulations based on the use of forcefield are useful to explore the adsorption and the dynamics properties of confined molecules in porous materials (FRENKEL; SMIT; RATNER, 1997; ROUQUEROL et al., 2014), (ii) quantum mechanical methods are for instance needed to explore systems at the electronic level when chemical reactions are in play (FIOLHAIS, CARLOS, FERNANDO NOGUEIRA, 2003; SHOLL, DAVID; STECKEL, 2011).

Therefore, in this thesis, DFT calculations and Monte Carlo simulations have been combined to elucidate the adsorption and degradation of CWAs by MOFs as well as to explore the water stability of the most promising MOFs materials. The manuscript is thus constructed as follows:

The second chapter describes CWAs and their potential simulants in terms of classification and properties. This is followed by the state of the art regarding the current protection devices and the recent envisaged materials for the capture and degradation of CWAs with a special emphasis on the studies related to the family of MOFs for such application.

The third chapter provides an overview of the molecular simulation techniques used in this thesis. The main pillars of Density Functional Theory applied to the solid-state as well as the basic principles of Monte Carlo techniques, including the microscopic models and forcefields used to represent the MOF frameworks and the CWAs molecules are described.

The fourth chapter reports a systematic computational evaluation of the CWA capture performances of a series of Zr- and Ti- MOFs, concerning Sarin and Soman as well as their most common simulants used in experiments, the Dimethyl methylphosphonate, the Diisopropyl phosphorofluoridate and Pinacolyl methylphosphonate. Grand Canonical Monte Carlo simulations have been combined with DFT calculations to assess the adsorption uptakes and the energetics for each MOF/CWA pair and to evidence the preferential adsorption sites and the resulting CWA/MOF interactions. As a further step, this computational database has been used to build model structure-adsorption performances in order to identify the key parameters of the MOFs that drive the CWA capture. Finally, the comparison of the simulated

adsorption behaviors of CWA and their simulants allowed us to define the most reliable simulant that mimics as fairly as possible the real molecules.

The fifth chapter explores three possible hydrolysis mechanisms for Sarin and its simulants on the activated Ti site of MIP-177(Ti) in presence/absence of water. This is followed by the study of the degradation of Sarin and Soman on pristine and functionalized Zr-MOFs. The whole set of data (the main states of the degradation reaction and the resulting activation energies) were further compared with the corresponding data reported in the literature in order to assess the promises of the investigated MOFs. Finally, the hydrolysis reaction of Sulfur mustard and its simulant 2-Chloroethyl ethyl sulfide, also known as half-mustard was computationally investigated in tandem with the experimental work performed in collaboration with Prof. J.S. Chang (KRICT, Korea).

The sixth chapter depicts a systematic exploration of the hydrolysis mechanism of a series of Zr and Ti-MOFs. The reactants, transition states and intermediates as well as the activation energy barriers were carefully analyzed aiming to identify the key parameters that control their stability under humidity and to establish a structure-property relationship for the most promising materials investigated in Chapter 4.

Finally, the last section delivers the main conclusions of this work and the perspectives it may offer.

2 OVERVIEW ON THE ADSORPTION AND DEGRADATION OF CWAs

The objective of this chapter is to introduce the readers to the main concepts and the state-of-the art related to the adsorption and degradation of chemical warfare agents.

The first section provides a theme contextualization of chemical warfare agents. A brief historical introduction is followed by a discussion about the classification of these hazardous substances according to their actions to humans. Their chemical and physico-chemical features are further detailed. The toxic effects to exposed humans and the mechanism of action of the nerve and blistering intoxicants on the human body are outlined. The structure of the non-toxic molecules namely as surrogates, analogs or simulants and the importance related to the choice of them to mimic the hazardous substances were discussed. Finally, the deactivation reactions of sulfur mustard and G-series were illustrated, with some discussion of intermediate and final degradation products and their toxicity.

The second part of the chapter is dedicated to the description of protective materials against chemical warfare agents. The current protection devices for the capture of CWA from air streams including gas masks and filters involve carbon materials (the so-called ASZM-TEDA). Recent developments have been also devoted to the detection of CWAs using notably pure or functionalized silica, zeolites, alumina or titania. Although these existing adsorbents exhibit many desirable characteristics for the capture and the destruction of CWAs, they show relatively low adsorption capacities, rapid deactivation of their active sites and/or lack of tailorability. This leaves significant room to identify other porous materials with improved performances for such application. In this context, the studies related to application of Metal-Organic Frameworks for the identification, adsorption and/or catalytic degradation of these hazardous molecules were discussed.

2.1 DEFINITION AND CLASSIFICATION OF CHEMICAL WARFARE AGENTS

The expression “chemical warfare”, first mentioned in 1917, refers to all tactical war assets which use incendiary mixtures, smokes and irritating, vesicant, poisonous or asphyxiating gases (SIDELL, F. R.; TAKAFUJI, E. T.; FRANZ, 1997). The use of poisonous chemicals from plant extracts to poison individuals is widely documented throughout the Middle Ages and Renaissance, but it was not until the expansion of industrial chemistry in the nineteenth century that mass production and deployment of Chemical Warfare Agents (CWAs) appeared (HAYES; GILBERT, 2009; SZINICZ, 2005). It is considered that modern chemical

war started during the First World War, when the German Army employed large quantities of chlorine gas against the Allied Forces in Ypres, Belgium. A series of first-generation CWAs were developed, some of which, like phosgene, diphosgene, hydrogen cyanide, cyanogen chloride and mustard gas, were even more toxic than chlorine.

The development, production, stockpiling and use of CWAs have been prohibited since 1993 thanks to the signature of the Chemical Weapons Convention (CWC) (NORADOUN et al., 2005). According to this convention, CWA are generally defined as toxic chemicals and their precursors, munitions and devices, and any equipment specifically designed for use in connection with such weapons. Among the Weapons of Mass Destruction, chemical warfare is probably the most brutal one created by mankind. CWAs are extremely toxic synthetic chemicals that can be dispersed as a gas, liquid or aerosol or as agents adsorbed to particles to become a powder. These CWAs have either lethal or incapacitating effects on humans (AAS, 2003). They differ from explosive chemicals in which the destructive effects are caused by shear force and are localized. Thousands of toxic substances are known, but only some of them are considered as CWAs based on their characteristics, e.g. high toxicity, imperceptibility to senses and rapidity of action after dissemination and persistency. They are listed as scheduled chemicals according to the Organization for the Prohibition of Chemical Weapons (OPCW) that was created in order to establish a world free of chemical weapons and of the threat of their uses [Available from: <http://www.opcw.org>]. Even though their strictly prohibited, CWAs are still be used throughout the world by terrorist groups and unprincipled governments with the most recent occurrence in Syria, where the United Nations believes sarin was handled.

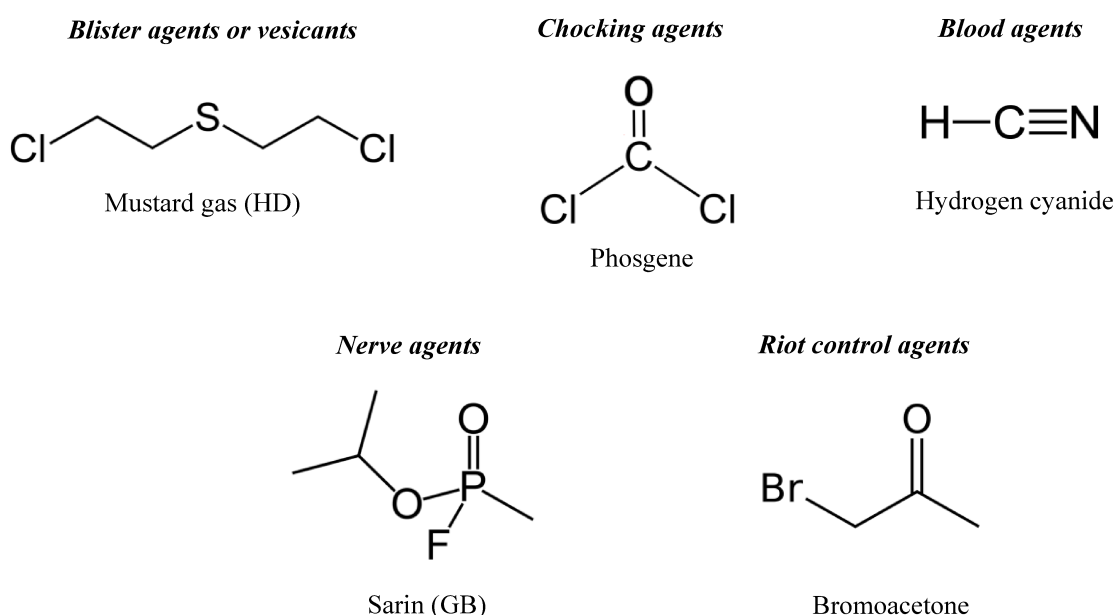
The CWAs are classified in several categories (Figure 2.1), according to their mechanisms of action to humans (DICHTWALD; WEINBROUM, 2008; VALDEZ et al., 2018):

- (i) **Blister agents or vesicants**, which cause irritation and vesication of the skin and mucous membranes mainly the lungs. The mustard gas ($\text{ClCH}_2\text{CH}_2\text{SCH}_2\text{CH}_2\text{Cl}$) represents the most representative CWAs of this family. Although vesicants can lead to death, they usually have only an incapacitating effect, where, for instance, the victims of mustard gas require one to four months of hospitalization.
- (ii) **Chocking agents** attack the respiratory tract, damage the peripheral portions of the lung, terminal bronchioles and alveoli causing choking. The main substances of the group are phosgene (COCl_2), chlorine gas (Cl_2) and diphosgene (Cl_3COCOCl).
- (iii) **Blood agents**, which are compounds that release cyanide ions in the body, being cyanogen chloride (ClCN) and hydrogen cyanide (HCN) the most common. The major

mechanism of toxicity of cyanides occurs by inhibition of the ability of blood cells to use and transfer oxygen, effectively causing the body to suffocate. Blood agents are distributed via the blood and generally enter the body through inhalation.

- (iv) **Riot control agents** are substances that produce temporary physiological or mental effects, rendering their victims inactive. The most remarkable among them are: the tear gases – chloroacetophenone (C_8H_7ClO), o-chlorobenzylidenemalononitrile ($C_{10}H_5ClN_2$), bromoacetone (C_3H_5BrO) -, the vomiting gases – chloropicrin (Cl_3CNO_2) - and psychoactive agents - 3-quinoclidinyl benzilate ($C_{21}H_{23}NO_3$).
- (v) **Nerve agents** affect the functioning of the nervous system, causing several deleterious effects which can lead to death. They act primarily by absorption through the lungs and skin, being fatal due to their ability to cause paralysis of the respiratory muscles (SMITH, 2008). The most important ones are tabun ($C_5H_{11}N_2O_2P$), sarin ($C_4H_{10}FO_2P$), soman ($C_7H_{16}FO_2P$) and VX ($C_{11}H_{26}NO_2PS$).

Figure 2.1 - Categories of Chemical Warfare Agents.



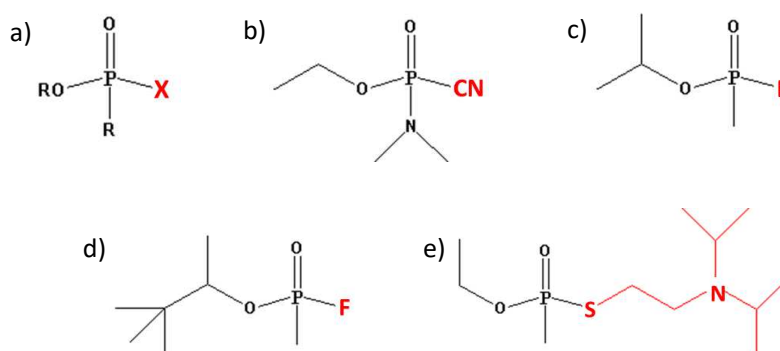
Source: Elaborated by the author (2019).

In addition to this classification defined above, CWAs can also be classified based on their volatility or chemical structure. Related to the volatility, CWAs are categorized as persistent or non-persistent agents. Thus, the more volatile an agent, the quicker it evaporates and disperses, i.e., the more volatile agents like chlorine, phosgene and hydrogen cyanide are non-persistent agents whereas the less volatile agents like sulfur mustard (HD) and Ethyl (2-

[bis(propan-2-yl)amino]ethyl}sulfanyl)(methyl)phosphinate (VX) are persistent agents. On the other hand, based on their chemical structure, they can be categorized as organophosphorus, organosulfur and organofluorine compounds, and arsenicals (BARTELT-HUNT; KNAPPE; BARLAZ, 2008; MUNRO; AMBROSE; WATSON, 1994).

Nerve agents which were mostly explored in my thesis, belong to the group of phosphororganic cholinesterase inhibitors. The high toxicity of these agents had not been recognized until the 1930s when German scientists described effects, which they noticed during synthesis of some OP with the P-F bond (SMITH, 2008; SZINICZ, 2005). The first developed was Tabun (GA) followed by Sarin (GB) and Soman (GD), leading to a series of nerve agents known as the G-agents. Indeed, a variety of nerve agents were developed till 1960 for military use and much importance was given to increase their potency and environmental persistence. Thus, the V-agents, as more stable versions of the G-agents were developed (SINGH, BEER; PRASAD, GANGAVARAPU KRISHNA; PANDEY, K S; DANIKHEL, R K; VIJAYARAGHAVAN, 2010). Their basic chemical structure all have in common a central phosphorus atom bound to an oxygen atom, a leaving group, an alkyl radical and a OR group (Figure 2.2). The structural diversity of OP is due to different substituents attached to the phosphorus atom. sarin and soman have as R1 a methyl and as R2 an alcohol group which are isopropanoxy and pinacoloxy groups, respectively. The other group, X, is a fluorine atom.

Figure 2.2 - a) Basic chemical structure of nerve agents. b) Tabun, c) Sarin, d) Soman and e) VX.



Source: Elaborated by the author (2019).

Table 2.1 summarized some physical, chemical and toxicological properties of these nerve agents. These compounds are clear, colorless liquids without well described odors, so these odors should not be used for detection or warning. Their boiling points vary from 158°C (Sarin) to 298°C (VX), where, the most volatile is sarin, followed by soman, tabun, and VX.

G-series compounds are relatively volatile and offer more risk when inhaled while VX is very little volatile, and it may be necessary weeks before its complete dissipation. In this way, VX presents an elevated risk of being absorbed through the skin. The most common means of exposure to these agents is by vapor. After vapor exposure, the effects start almost immediately, reach maximal intensity within minutes. One can notice, in Table 2.1, that a few milligrams of these molecules are enough to kill an adult of about 70 kg (DELFINO; RIBEIRO; FIGUEROA-VILLAR, 2009).

Table 2.1 - Physical Properties of nerve agents.

Property / Nerve Agent	Tabun	Sarin	Soman	VX
Boiling point (°C)	230	158	198	298
Volatility at 25 °C (mg m ⁻³)	610	22000	3900	10.5
LC ₅₀ by inhalation (mg min m ⁻³)	400	100	50	10
LD ₅₀ by contact (mg 70kg ⁻¹)	1000	1700	350	6-10

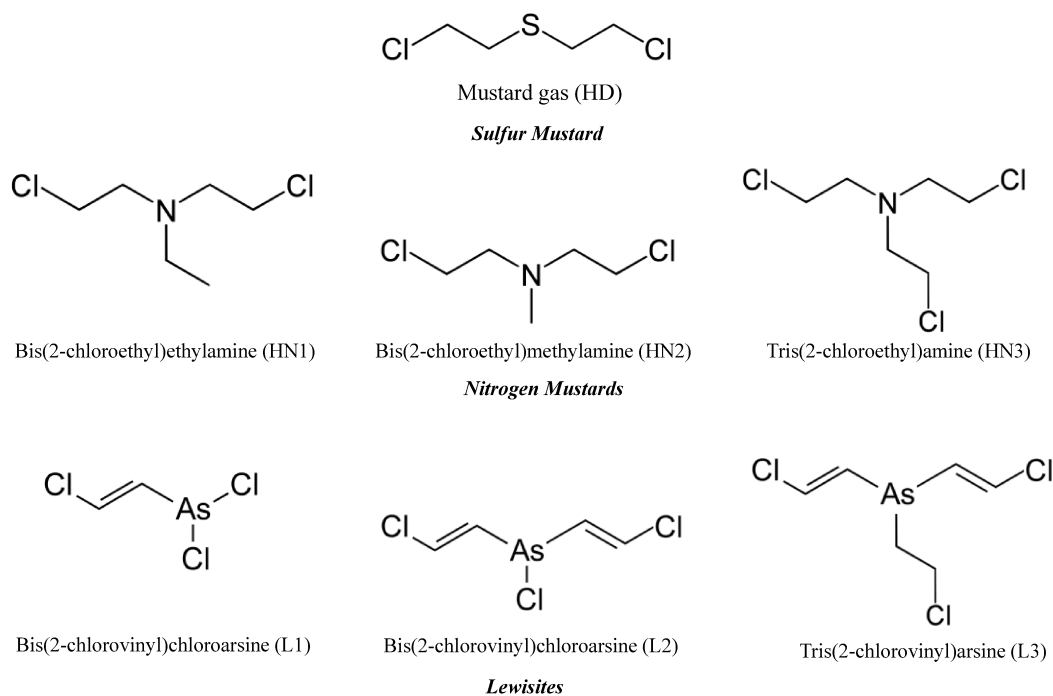
Source: Adapted from (DELFINO; RIBEIRO; FIGUEROA-VILLAR, 2009).

Note: Standard measure of the toxicity that will kill half of the sample population in a specified period.

According to the toxicity (Table 2.1), nerve agents are considered as the most hazardous families of all chemical weapons, and along with vesicants, constitute the majority of the modern chemical arsenals (MUNRO; AMBROSE; WATSON, 1994).

Regarding **blister agents** that were also explored in my PhD, the associated acute mortality is low, however, they can incapacitate the enemy and overload the already burdened health care services during wartime (GHABILI et al., 2011). One example is the widely used gas mustard during the Iran–Iraq war (1980–1988), resulting in over 100,000 chemical casualties (KHATERI et al., 2003). There are two forms of blister agents: mustards (sulfur or nitrogen mustards) and arsenicals (Lewisites) as illustrated in Figure 2.3.

Figure 2.3 - Chemical structure of blister agents.



Source: Elaborated by the author (2019).

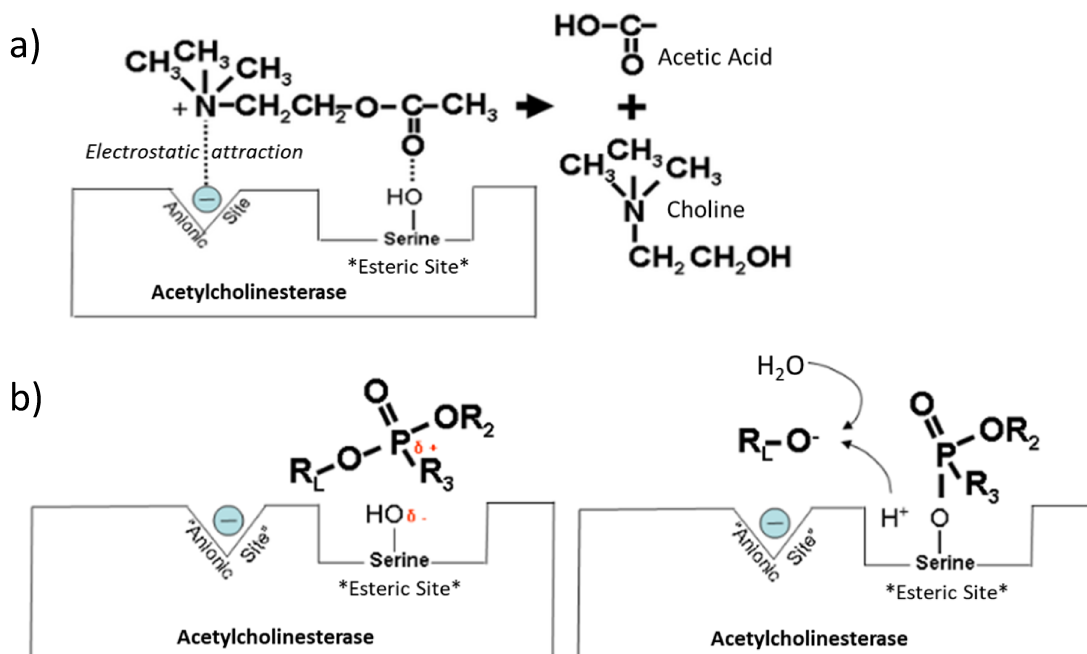
Mustards are compounds with the general structure $R-CH_2CH_2X$, where R is a leaving group and X is a Lewis base. Many are bifunctional: $(R-CH_2CH_2)_2X$ (SINGH, BEER; PRASAD, GANGAVARAPU KRISHNA; PANDEY, K S; DANIKHEL, R K; VIJAYARAGHAVAN, 2010). The most important substance in this class of CWAs is sulfur mustard. It is a light yellow to brown thick liquid, very persistent in cold and temperate climates (melting point of 14°C and boiling point of 218°C at 1 atmosphere pressure, it decomposes before boiling) and has a characteristic smell similar to mustard or garlic. Its volatility is low (610 mg m^{-3} at 20°C), but in warm weather or when present in large amount, its vapor can pass readily through clothing and skin. So, the risk of human contact is not only with droplets of liquid but also with vapor (GHABILI et al., 2011). Other compounds such as nitrogen mustard were developed during World War II, but found to be unsuitable as a munition due to their stability. Soon after discovering methylbis(2-chloroethyl)amine (HN2) became the first non-hormonal agent used in cancer chemotherapy. A number of HN2 derivatives including cyclophosphamide, ifosfamide, mechlorethamine, melphalan and chlorambucil are valuable cytotoxic and radiomimetic agents for the treatment of cancer (MUNRO et al., 1999).

2.1.1 Intoxification by nerve agents and mustards

The **nerve agents** are amongst the most potent of all CWAs and they are highly toxic in both liquid and vapor form. In vapor form, they can be inhaled or absorbed through the skin or the conjunctiva of the eye and as a liquid absorbed through the skin, conjunctiva, and upper gastrointestinal tract (PANAHI; ABDOLGHAFFARI; SAHEBKAR, 2018; ZILKER, 2005). Since they are essentially colorless, odorless, tasteless, and nonirritating to the skin, their entry into the body may not be perceived by the individual until grave signs and symptoms appear. Within seconds after exposure to low levels of nerve agent vapor, local effects may be observed in the eyes and the respiratory system of humans. The time of onset of moderate systemic effects depends in part on the route of exposure; it is within seconds to a minute after inhalation, within 45 minutes after ingestion, and within 2-18 hours after application on the skin (MUNRO; AMBROSE; WATSON, 1994; SIDELL, F. R.; TAKAFUJI, E. T.; FRANZ, 1997). Exposure to lethal doses, however, can lead to collapse within seconds and death within 10 minutes after a single deep inhalation. After short-term exposure, mild systemic effects may last for several hours to days, whereas moderately severe symptoms can last for 1-6 days (PANAHI; ABDOLGHAFFARI; SAHEBKAR, 2018).

The toxicity of these substances is associated with two factors. On the one hand, the amphiphilic nature of these compounds facilitates tissue penetration and on the other hand the labile nature of the P—X bond gives rise to irreversible binding to the active site of acetylcholinesterase (AChE). AChE belongs to the class of enzymes called esterases which catalyze the hydrolysis of esters like acetylcholine (ACh). AChE has the physiological function to continuously break down the ACh in acetate and choline (Figure 2.4). Then, the choline is taken up by the presynaptic terminal membrane and further reutilized for the synthesis of new Ach (DICHTWALD; WEINBROUM, 2008).

Figure 2.4 - a) Acetylcholinesterase activity and b) Inhibition of enzymatic activity.



Source: Adapted from (<https://www.atsdr.cdc.gov/csem/cholinesterase/docs/cholinesterase.pdf>).

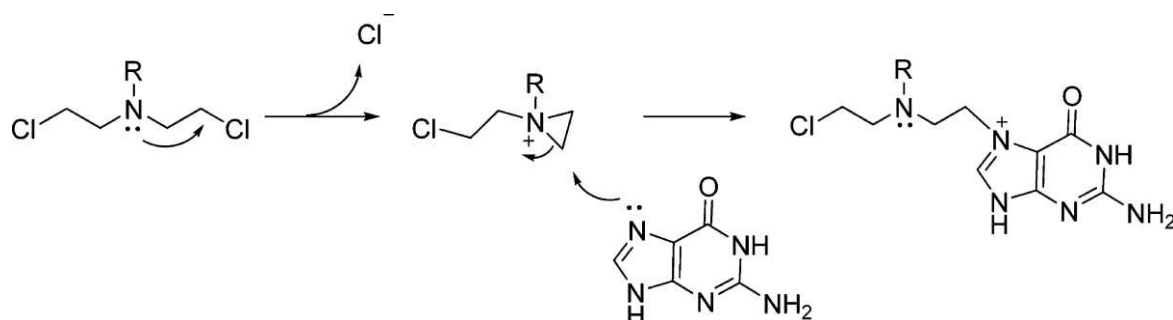
Inhibition of acetylcholinesterase leads to an accumulation of acetylcholine resulting in a variety of effects such as salivation, hypotension, bradycardia, muscle tremors, convulsions and respiratory failure. When nerve agents bind covalently to AchE (Figure 2.4b) this leads to an irreversible inhibition caused by phosphorylation of the serine residue in the active site of the enzyme. Consequently, unlimited accumulation of ACh at the neuroeffector junctions disrupts normal synaptic transmission and leads to oxygen deprivation and ultimately to the death by asphyxiation (DICHTWALD; WEINBROUM, 2008).

Sulfur mustard is known to be absorbed through the skin or respiratory tract. It is a lipophilic and very reactive chemical and when delivered as liquid or vapor, skin is the main route of exposure (GERACI, 2008). In the form of gas or aerosol, mustard attacks the skin, eyes and the respiratory tract. Applied to the skin, about 80% is evaporated, 20% penetrates the skin and around 10% of the penetrated HD is estimated to remain locally bound to skin and the rest transported with the circulation (KORKMAZ; TAN; REITER, 2008). Adipose tissue and particularly the subcutaneous fat most probably form a depot from which sulfur mustard can be further delivered to circulation (PAROMOV et al., 2007). The analyses of tissues from an Iranian soldier who died seven days after exposure to sulfur mustard showed main accumulation in subcutaneous fat, brain, kidney, liver, spleen, and lungs (DRASCH et al., 1987). There is

also strong evidence that occupational exposure to sulfur mustard can cause cancer principally in the respiratory tract and larynx area (EASTON; PETO; DOLL, 1988).

The clinical hallmark of mustard exposure is the relative lack of symptoms following exposure. The length of this latent period and rapidity and intensity of symptom development depend on the mode of exposure, concentration of the agent and environmental conditions. Chemical damage starts in 1 minute after contact, but onset of pain is delayed for 4–6 hours. Sulfur mustard acts as an alkylating agent with long-term toxic effects on several body organs, where the extent of tissue injury depends on the duration and intensity of exposure (KEHE; SZINICZ, 2005). Many studies provide evidence that acute toxicity of sulfur mustard is related to its alkylating capacity, and ability to induce oxidative stress and inflammation in affected tissues. These events in turn cause detrimental changes in metabolic, genetic, and other cellular functions leading to cell death by apoptosis or necrosis (PAPIRMEISTER et al., 1985; PAROMOV et al., 2007). The strong reactivity of mustards is due to ionization of its chlorine atoms that can lead to the formation of an ethylene sulfonium ion intermediate and carbonium ion. These are strong alkylating agents, which react with cellular nucleophilic centers (-SH, -NH₂- groups) in DNA, RNA, proteins, and lipids (DACRE; GOLDMAN, 1996). Several studies have shown that sulfur mustard can modify DNA through the formation of DNA mono-adducts and DNA cross-links and thus inhibit cell division (FIDDER et al., 1994; LUDLUM et al., 1994; STEINRITZ; THIERMANN, 2016). Figure 2.5 illustrates the mustard mechanism of action. The mustards eliminate a terminal chlorine to form a highly reactive sulfonium or nitrogen cation which goes on to react with the guanine. Although the exact mechanisms underlying chronic toxicity of sulfur mustard are not clear, it is apparent that the events in acute toxicity are related to long-term toxicity. Some studies suggest autoimmune basis for the cause of chronic toxicity. Sulfur mustard alters proteins resulting in protein-sulfur mustard products that may stimulate autoimmune reactions in exposed tissues (JAVADI et al., 2005; SOLBERG; ALCALAY; BELKIN, 1997).

Figure 2.5 - A scheme depicting the mechanism for the alkylation of a guanine unit by a nitrogen mustard (HN2) molecule. This reaction mechanism is the stereotypical route of reaction of all mustards.



Source: Adapted from (STEINRITZ; THIERMANN, 2016).

2.1.2 Appropriate Simulants

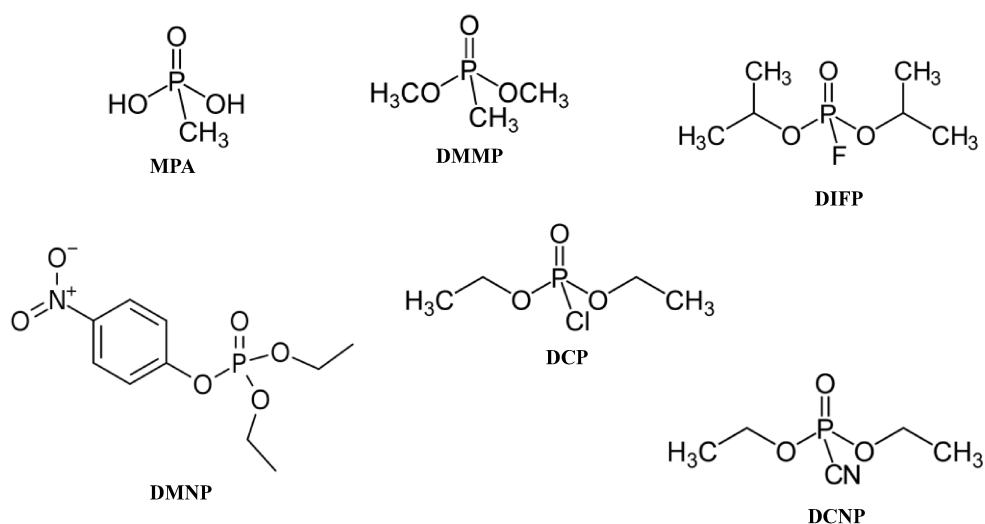
The extreme toxicity of CWAs and their restricted use in academic laboratories have urged the researchers to consider simulant compounds. An ideal simulant would mimic all relevant chemical and physical properties of the CWA, while remaining non-toxic at the dose employed. Although many molecules have been used as simulants, each of them can only mimic certain aspects of the specific agent. Therefore, prior selecting a simulant, it is important to determine which property of the CWA is to be addressed. One must be aware of the differences scrutinized between the CWAs and their simulants, for each property, there are many simulant choices (SINGER et al., 2005; WAGNER; MACIVER, 1998; YANG; BAKER; WARD, 1992).

The selection of an appropriate simulant must be made in consideration of the targeted property, i.e., physisorption or degradation (reactivity). A first criterion is that the simulants should have a molecular size similar to that of the correlated CWA because adsorption/desorption rates are governed by diffusion of adsorbates through the porous structure of the adsorbent. Simulants that are larger than the CWAs, especially those containing aromatic functional groups, may diffuse more slowly, while simulants that are smaller than the CWAs may diffuse more rapidly (BARTELT-HUNT; KNAPPE; BARLAZ, 2008; WITKIEWICZ et al., 2018). Furthermore, since the hydrolysis degradation of CWAs is governed primarily by the reactivity of a given site, the most important criterion in this case is to consider a simulant presenting similar chemical composition in particular the presence of the bonds at which the hydrolysis reaction occurs. Indeed, the best simulant will closely match the structure of the

original agent and can potentially form the same or similar hydrolysis products (BARTELT-HUNT; KNAPPE; BARLAZ, 2008).

There is a long list of potential simulants that have similar molecular structures than the nerve agents, including MPA (methylphosphonic acid), DMMP (dimethyl methylphosphonate), DIFP (diisopropylphosphorofluoridate), DMNP (methyl paraoxon), DCP (diethyl chlorophosphate) and DCNP (diethyl cyanophosphonate). Considering that the hydrolysis reactions of nerve agents occur at the P-F bond, DIFP might be the best choice to mimic Sarin and Soman since it contains this neurotoxic bond (see Figure 2.6). However, another important characteristic to be evaluated is that the presence of the P-F bond confers a higher toxicity to the simulants (MANGUN et al., 2001; RABER; MCGUIRE, 2002; SINGER et al., 2005; TAN et al., 2018; YUE et al., 2001).

Figure 2.6 - Molecular structures of nerve agent simulants.

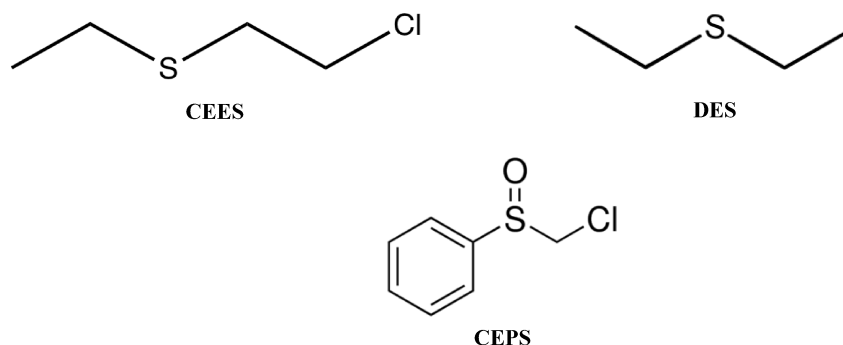


Source: Elaborated by the author (2019).

The hydrolysis of gas mustard occurs via a complex pathway, but the ultimate product is thiodiglycol, which is formed via a dechlorination reaction. The monofunctional derivatives of mustard, RSCH₂CH₂Cl (R = methyl, ethyl, or phenyl) and RSCH₂CH₂X (X = tosylate, brosylate, Br⁻, I⁻, or other leaving group), react via the same mechanisms as those of HD, but their reaction products and kinetic rate expressions are much simpler. Therefore, for HD, the best simulant choices based on structural similarities are CEES (2-Chloroethyl ethyl sulfide, half-mustard) and CEMS (2-chloroethyl methyl sulfide) (see Figure 2.7), as these compounds

still retain one ethyl chloride functional group (BARTELT-HUNT; KNAPPE; BARLAZ, 2008).

Figure 2.7 - Molecular structures of HD simulants.



Source: Elaborated by the author (2019).

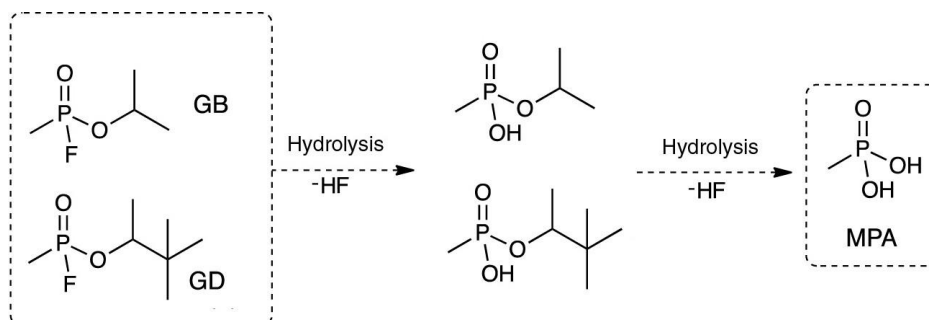
2.1.3 Hydrolysis degradation of CWAs

CWAs can be decomposed through different processes such as hydrolysis, thermal decomposition, combustion, catalytic decomposition, photolysis, microbial degradation and so forth. Hydrolysis is the primary mechanism for many CWAs in aqueous systems, with reported half-lives on the order of minutes to days. And, the toxicities of most of the degradation products of these agents are currently considered quite low (KINGERY; ALLEN, 1995).

The decontamination of G-agents is often considered to be less of a technical challenge than decontamination of the less volatile, less soluble, and less labile agents because G-agents have relatively high vapor pressures, are moderately soluble in water and hydrolyze in water with half-lives on the order of a day (SMITH, 2008).

Indeed, the degradation of nerve agents is generally obtained by hydrolysis to the corresponding alkyl methylphosphonate, followed in some cases by a second hydrolysis to methylphosphonic acid, as illustrates Figure 2.8. Hydrolysis proceeds by phosphorus SN₂ nucleophilic attack, this reaction gives the nontoxic products isopropyl methylphosphonic acid in the case of sarin and pinacolyl methylphosphonic acid in the case of soman. Hydrolysis rates of nerve agents are slower than those of HD, with half-lives of 39 hours at pH 7.5 and 25 °C, and 60 hours at pH 6 and 25 °C for GB, and GD, respectively (MORRILL, L.G., REED, L.W., AND CHINN, 1985; MUNRO et al., 1999).

Figure 2.8 - Nerve agents hydrolysis reaction.

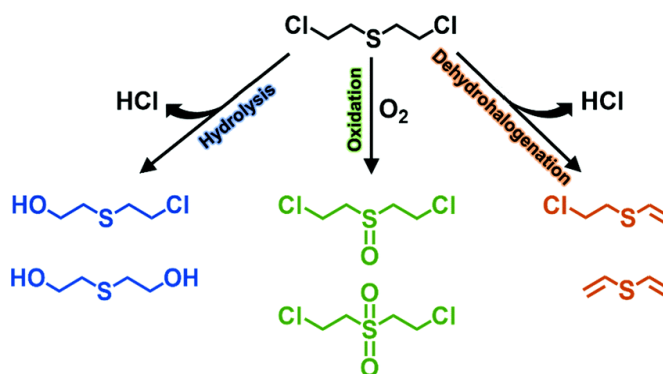


Source: Adapted from (VALDEZ et al., 2018).

The rate of CWA hydrolysis depends on different factors such as temperature and pH. Hydrolysis rates increase with increasing temperature. For example, the rate of HD hydrolysis at 70 °C was 28 times that at 30 °C (HARVEY, S.P., SZAFRANIEC, L.L., BEAUDRY, W.T., EARLEY, J.T., AND IRVINE, 1997). For GB at pH 7, hydrolysis half-lives of 2650 hours and 39–41 hours were reported at 0 °C and 25 °C, respectively. The effect of pH on CWA hydrolysis varies; e.g., GD hydrolysis is acid catalyzed with half-lives of 3, 50, and 60 hours at pH 2, 7.6, and 9, respectively. The hydrolysis rate of HD does not vary between pH = 5 and 10 however, high chloride ion concentrations can inhibit HD hydrolysis (BARTELT-HUNT; KNAPPE; BARLAZ, 2008).

Sulfur mustard, can be detoxified by dehydrohalogenation to form the chloroethyl vinyl sulfide, by nucleophilic attack to displace an activated aliphatic halogen, or by oxidation, as reported in Figure 2.9.

Figure 2.9 - Detoxifying reactions of sulfur mustard.

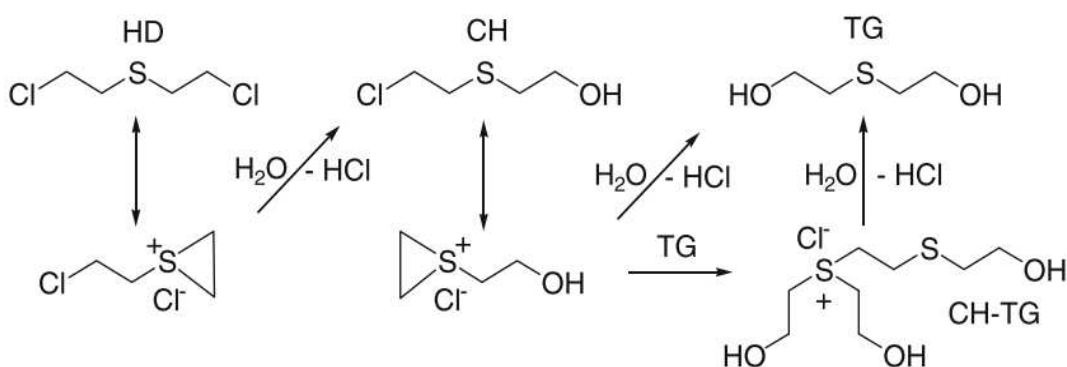


Source: Adapted from (BOBBITT et al., 2017).

HD may be detoxified by partial oxidation to the sulfoxide, but further oxidation to the sulfone is not welcome since the sulfone also causes blisters. While hydrolysis of HD to produce thiodiglycol (TG) occurs in water with a half-life estimated to be on the order of 5 minutes, HD has very low solubility in water and drops of the agent dispersed in water tend to form a form a set of ionic products, limiting the effectiveness of hydrolytic catalysis (MUNRO et al., 1999). The closest approach to promoting hydrolysis of sulfur mustard has probably been the formation of microemulsions that bring the agent and the water nucleophile into close proximity (SMITH, 2008).

As both sarin and soman are miscible in water, their reactivities can be enhanced in the presence of a small amount of water or hydrophilic substances (MA et al., 2011a). In contrast, due to the oily nature of HD, its hydrolysis must occur through several steps including the formation of a fleeting intermediate in water (chlorohydrin - CH) via the hydrolysis of Cl atoms and the formation of thiodiglycol, stable hydrolysis product, through the hydrolysis of the second Cl group (Figure 2.10) (PETERSON; WAGNER, 2014). It is worth mentioning that the rate of chlorohydrin compound formation is faster than that of TG. Nonetheless, the overall slower kinetics induces the formation of a transition complex, namely hemi mustard thiodiglycol aggregate (CH-TG), which is slowly hydrolyzed to TG (Figure 2.10) (MUNRO et al., 1999).

Figure 2.10 - Sulfur mustard hydrolysis.



Source: Adapted from (PETERSON; WAGNER, 2014).

2.2 PROTECTIVE MATERIALS AGAINST CWAs

Understanding of the interfacial chemistry and reaction pathways of CWAs on various heterogeneous materials have been of great interest from many years. Since World War I

military respirators with a cartridge filled with carbonaceous adsorbents, such as activated charcoals, activated carbons (KOWALCZYK et al., 2013), single-wall carbon nanotubes (BERMUDEZ, 2005), and activated carbon fibers have been used for capturing highly volatile CWAs. These porous materials are a family of carbon-based solid sorbents typically prepared by heat treating wood (BASHKOVA; BANDOSZ, 2009), coal (NOWICKI; PIETRZAK, 2011), coconut shells (AHMADPOUR; OKHOVAT; DARABI MAHBOUB, 2013), polymers (SEREDYCH; DELIYANNI; BANDOSZ, 2010), and even sewage waste (YUAN; BANDOSZ, 2007) and other carbonaceous substances.

The first solid adsorbent material used for adsorption and detoxification was introduced in 1989 and is called the M291 decontamination kit. This kit contains fiber pads that are filled with a high surface area carbonaceous material which physically removes the agent from skin by adsorption. An ion-exchange resin then neutralizes the chemical agent (MICHAEL A. WARTELL, MICHAEL T. KLEINMAN, BEVERLY M. HUEY, 1999).

Today's protection devices for the capture of CWA from air streams including gas masks and filters involve carbon materials with a mixture of nanoparticles of metal or metal oxides, the so-called ASZM-TEDA Activated Carbon, impregnated with Copper, Silver, Zinc, Molybdenum, and Triethylenediamine, that act as specific adsorption sites for the targeted highly toxic molecules (DECOSTE; PETERSON, 2014).

Activated carbon is a versatile material that shows several attractive properties such as large surface area, fire-resistant, robustness and availability of aplenty. While highly effective in capturing a variety of dangerous species, microporous carbon-based materials suffer from limited selectivity to CWAs due to their ill-defined pore sizes, shapes, and pore chemistry (BOBBITT et al., 2017). Thus, the amount of chemical that can be removed by the filter is limited by the space available for physical adsorption in the pore structure of the adsorbent and the amount of reactive impregnant contained on the adsorbent. Besides other disadvantages include heavy weight, low breathability, high cost and poor stability in the presence of liquid water (JACOBY, 2014). In addition, activated carbon merely adsorbs the agents and once it becomes saturated, it turns out a hazardous material, due to the potential remission of CWAs, necessitating safe disposal. Thus, the used suits must be sent back to the supplier of manufacturer where it would be essentially decontaminated by bleaching and then disposed by incineration or landfill. Therefore, if an adsorbent can ensure breathability with light weight and high capacity to decontaminate the adsorbed CWA in situ, it would be the ideal scenario for use in the protective clothing (OUDEJANS, 2014).

2.2.1 Materials for the degradation of CWAs

Considering the shortcomings described above for the activated carbon, which is the current state-of-the-art, significant research efforts have been focused on the development of solid adsorbent materials that not only adsorb, but also quickly and efficiently hydrolyze and detoxify CWAs. Some of the heterogeneous materials investigated are: Brucite (VAISS; BORGES; LEITÃO, 2011), MgO(001) (ALVIM et al., 2013; WAGNER et al., 1999), CaO (WAGNER et al., 2000), TiO₂ (MOSS et al., 2005; PANAYOTOV; MORRIS, 2008, 2009; RUSU; YATES, 2000; TRUBITSYN; VORONTSOV, 2005; WAGNER; CHEN; WU, 2008; WAGNER; PETERSON; MAHLE, 2012; YANG et al., 2011a, 2013), Zr(OH)₄ (BANDOSZ et al., 2012), pure or functionalized silica (BERMUDEZ, 2007a; KANAN; TRIPP, 2001; SAXENA et al., 2012), Rh(100) (HEGDE; GREENLIEF; WHITE, 1985), Mo(111) (SMENTKOWSKI; HAGANS; YATES, 1988), Pt(111) (HENDERSON; WHITE, 1988), Ni(111) (GUO; YOSHINOBU; YATES, 1990), Pd(111) (GUO; YOSHINOBU; YATES, 1990), Al₂O₃ (BERMUDEZ, 2007b, 2009; TEMPLETON; WEINBERG, 1985; VERMA et al., 2013; WAGNER et al., 2001), Fe₂O₃ (HENDERSON; JIN; WHITE, 1986), La₂O₃ and Y₂O₃ (GORDON; TISSUE; MORRIS, 2007). Henderson *et al.* (HENDERSON; WHITE, 1988) studied the adsorption as well as the decomposition of DMMP on Pt(111) surface using various spectroscopic techniques. The catalyzed hydrolysis of soman was studied by Ward *et al.* (WARD et al., 1988), where the nucleophilic substitution of F⁻ by OH⁻ reveals the way of deactivation of this acetylcholinesterase inhibitor. Vaiss *et al.* (VAISS; BORGES; LEITÃO, 2011) investigated the hydrolysis of sarin on the layered hydroxide brucite (Mg(OH)₂) through dissociative chemisorptions using density functional theory (DFT). Templeton *et al.* (BERMUDEZ, 2009) examined the adsorption and decomposition of DMMP, diisopropyl methylphosphonate (DIMP) and diphenyl methylphosphonate (DPMP) on an aluminum oxide surface via tunneling spectroscopy. Šečkutė *et al.* (ŠEČKUTE et al., 2005) studied the potential energy diagram for the alkaline hydrolysis of sarin and O,S-dimethyl methylphosphonothioate (DMPT) using ab initio and DFT methods.

Following the initial studies into the chemistry of CWAs on the surfaces, extensive research has been dedicated toward developing an understanding of the CWAs and their simulants on various heterogeneous materials such as zeolites (KNAGGE et al., 2006), metalloporphyrin dimers (TOTTEN et al., 2012, 2013a), porous organic polymers (TOTTEN et al., 2013b), surfactants/metallosurfactants (HAFIZ, 2005; HAFIZ et al., 2005) and others.

A handful of metal oxides such as MgO, CaO and Al₂O₃ show reactivity towards nerve agents however they suffer from stability issues under humidity as well as poisoning due to the hydrolysis product inhibition, which reduces their activity over time (WAGNER et al., 2001, 1999, 2000). Various nanomaterials based on TiO₂ have also been studied and these materials are effective for hydrolysis due to their high surface areas and abundance of surface hydroxyl groups (WAGNER; CHEN; WU, 2008; WAGNER; PETERSON; MAHLE, 2012). Owing to their high surface areas and abundance of surface hydroxyls, nanotubular titania and nanocrystalline titania were found to be particularly effective, with the latter exhibiting extremely short half-lives for adsorbed VX (WAGNER; PETERSON; MAHLE, 2012). Related to the TiO₂-based systems, zirconium hydroxide and polymorphic zirconia have also been investigated. For example, an amorphous Zr(OH)₄ presented unprecedented hydrolysis rates toward VX and besides proved effective for degradation of GD (BANDOSZ et al., 2012).

Although these existing adsorbents exhibit many desirable characteristics for the capture and the destruction of CWAs, they show relatively low adsorption capacities, rapid deactivation of their active sites and/or lack of tailorability. This leaves significant room to identify other porous materials with improved performances for such application.

The current trend is to develop new protection materials with a smaller volume to reduce the burden to the user, highly efficient adsorbents targeting one CWA class or adsorbents possessing the ability to remove a broad range of chemical threats, since the chemical threat is typically unknown before an event occurs (DECOSTE; PETERSON, 2014). In this concern, many efforts have been deployed to discover and implement novel materials and methods for identification, adsorption and/or degradation of CWAs.

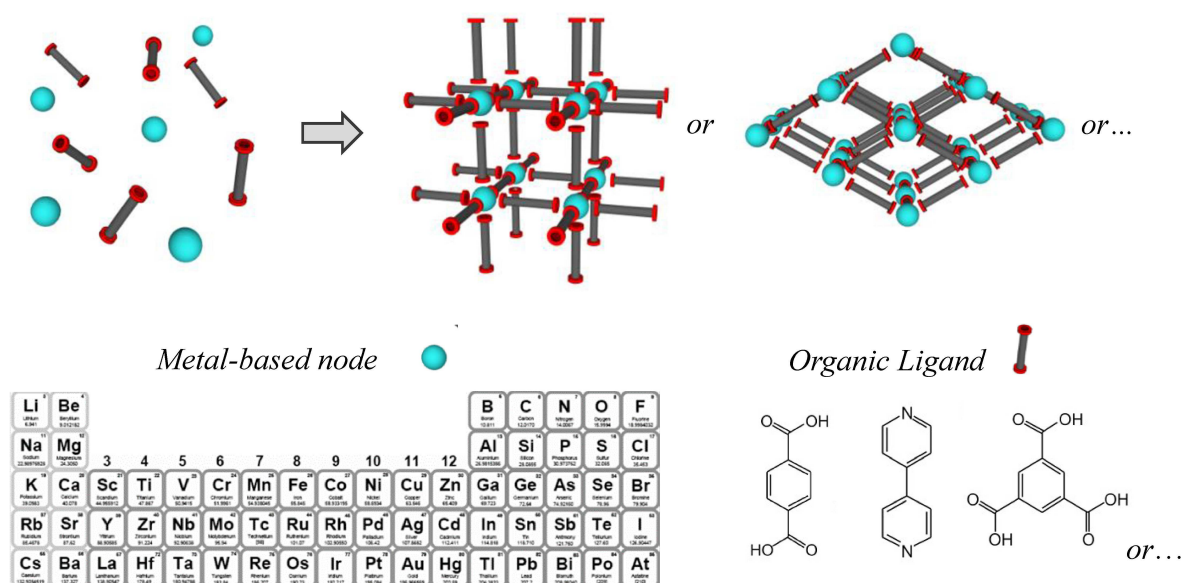
2.2.2 MOFs for the capture and degradation of CWAs

In this context, Metal-Organic Frameworks (MOFs) have been envisaged as promising candidates for the identification, adsorption and/or catalytic degradation of CWAs (BOBBITT et al., 2017). This family of materials is especially of interest due to the wide range of frameworks that can be prepared and their attractive properties in societally relevant domains such as gas storage, molecular separation, biomedicine, energy conversion and storage including the capture and/or decomposition of harmful volatile chemicals (BOBBITT et al., 2017; CHEN; WU, 2018; EVANS; LUEBKE; PETIT, 2018; FÉREY et al., 2011; PETIT, 2018; SILVA et al., 2015; WANG; LUSTIG; LI, 2018).

MOFs are crystalline porous materials consisting of a highly ordered extended network of metal ions coordinated to organic complexing linkers. The inorganic parts, usually termed as Secondary Building Units (SBU) can be simple polyhedra, clusters, chains layers or even inorganic 3D arrangements, while the organic linkers are mainly anionic O (polycarboxylates, polyphosphonates) and N (imidazolates, polypyrazolates, polytetrazolates) donors. Consequently, MOFs offer several attractive features that make them unique, such as: high porosity, high internal surface area, crystallinity, strong organic metal-ligand interaction, potentially valuable active sites, polynuclear sites, flexibility, ability to incorporate various molecules, specific interaction between active site and substrate, and adjustable hydrophobicity (FÉREY, 2008; FÉREY et al., 2011; KUPPLER et al., 2009).

The potential of these hybrid porous solids lies in the huge spectrum that can be wisely and finely tuned, in terms of the chemical nature (metal cations and the length and/or the functionalization of the organic linker), pore size (microporous or mesoporous) and the shape/type of cavities (cages or channels), where almost all of the elements of the periodic table have been used to date as summarized in Figure 2.11 (FÉREY, 2008; HOSKINS; ROBSON, 1989; KONDO et al., 1997; MAURIN et al., 2017; YAGHI; LI, 1995; ZHOU; KITAGAWA, 2014).

Figure 2.11 - Versatile chemistry & topology/connectivity of MOFs.



Source: Elaborated by the author (2019).

In the targeted field, the attractiveness of MOFs prevails in the possibility to identify porous solids able to capture high quantities of CWA per volume for a broad range of highly toxic molecules. This would lead to a decrease in size and weight of any personal protective device. The high tunability of MOFs allows an oriented control and design of structural features such as pore size and geometry, high surface areas and the ability to tailor the chemical functionality in a controlled manner within the MOF. This combination of properties cannot be achieved for other porous sorbents, such as zeolites or activated carbons (BOBBITT et al., 2017; DECOSTE; PETERSON, 2014).

Another distinctive opportunity compared to the benchmark active carbons is to select MOFs containing well-dispersed diverse adsorption sites and/or bimodal pores, that will potentially be able to respond to a range of CWA molecules with different properties, for example acidity or basicity. This tailoring of the MOF chemistry will help to avoid the competition of molecules for one given adsorption site. Besides, the possible use of a mixture of MOFs allows a single efficient cartridge to be used even if the menace is unknown. However, in some previous studies of these materials, two drawbacks have been mentioned. The first is the cost, the second drawback is related to their stability to humidity (LÓPEZ-MAYA et al., 2015; ROY et al., 2013). Indeed, in any gas mask type application, there will be expected to be humidity in the air and more importantly in the breath.

2.2.2.1 MOFs for the capture of CWAs – experimental approach

Among several methods to capture toxic chemicals, the adsorption process is the most attractive. In this regard, the selective and effective capture of CWAs into the porous of MOFs is of clear interest to establish the potential of this class of materials for sensing, capturing, or decomposing these agents. Besides, the adsorption process of CWAs was identified to be rate limiting (MOMENI; CRAMER, 2018a, 2018b), and therefore it remains a critical first step for the degradation of these chemicals.

Only a few studies have been reported so far on the MOF/CWA capture topic, all of them being reported in the last 3 years. We can cite the experimental work on the adsorption of blister agent chlorine in IRMOF-3(Zn), IRMOF-62(Zn), MOF-177(Zn) and Cu-BTC (BRITT; TRANCHEMONTAGNE; YAGHI, 2008), UiO-66(Zr), UiO-66-OH(Zr), UiO-66-NH₂(Zr), MIL-53(Al), MIL-53-NH₂(Al), Cu-BTC and ZIF-8(Zn) (DECOSTE et al., 2015), blood agent arsine in Cu-BTC (PETERSON et al., 2015), cyanogen chloride in MOF-74(M) analogues (M = Zn, Co, Ni and Mg) (GRANT GLOVER et al., 2011), tabun and *O*-ethyl-*S*-

2[2(diethylamino)ethyl]methylphosphonothiate in several IRMOFs, MIL-53p(Cr), and Cu-BTC (LEE et al., 2010) and dimethyl methylphosphonate in MOF-5(Zn) (NI et al., 2007) and NENU-11(Cu) (MA et al., 2011b), methylphosphonic acid in $[\text{Zn}_2\text{Ca}(\text{BTC})_2(\text{H}_2\text{O})_2](\text{DMF})_2$ (ZOU et al., 2010), as well as diisopropyl fluorophosphate in lithium alkoxide doped UiO-66(Zr) (LÓPEZ-MAYA et al., 2015) and diethyl sulfide in $[\text{Zn}_4\text{O}(3,5\text{-dimethyl-4-carboxy-pyrazolato})_3]$ (MA et al., 2011a).

The removal of DMMP, a simulant of sarin, was reported by Ni *et al.* (NI et al., 2007) using the MOF-5(Zn) as an adsorbent. Indeed, this MOF was shown to outperform other materials such as pitch-based P7 Activated Carbon Fiber and the commercialized Norit activated carbons (KOWALCZYK et al., 2013) with 7.3 mmol g^{-1} , $0.806 \text{ mmol g}^{-1}$ and $0.161 \text{ mmol g}^{-1}$ of DMMP, respectively. However, it should be noted that the practical application of MOF-5(Zn) is limited due to its poor water/air stability. $[\text{Zn}_2\text{Ca}(\text{BTC})_2(\text{H}_2\text{O})_2](\text{DMF})_2$ was the first MOF shown to be effective for the capture of a nerve agent simulant, methylphosphonic acid (ZOU et al., 2010). This material demonstrated a high capacity to capture MPA, 3.42 mmol/g , while other studies on goethite particles reported a very low loading of 0.08 mmol g^{-1} . In complement to this experimental study, periodic DFT calculations suggested that the interaction between the guest and host takes places through the coordinatively unsaturated Zn centers (ZOU et al., 2010). Shortly after, a MOF-5 analogue named Zn-DMCP $[\text{Zn}_4\text{O}(3,5\text{-dimethyl-4-carboxy-pyrazolato})_3]$ was shown to adsorb DIFP and DES (Diethyl sulfide) (MONTORO et al., 2011). However, the performance of Zn-DMCP approached that of the activated carbon material Carboxen®, suggesting a similar adsorption process addressed by the small size and hydrophobic nature of the pores.

Padial *et al.* designed an isorecticular series of MOFs, $[\text{Ni}_8(\text{OH})_4(\text{H}_2\text{O})_2(\text{L})_6]_n$ (shortened as $[\text{Ni}_8(\text{L})_6]$), to performed DES capture study. The pore size and polarity of these materials were controlled by connecting bi-pyrazolate and mixed pyrazolate–carboxylate linkers of different lengths to 12-connected Ni^{II} hydroxo clusters. In a dry environment, the kinetics of DES uptake proved to be relatively independent of the MOFs, where the best performing system was $[\text{Ni}_8(\text{L4})_6]$. For the case of an 80% relative-humidity atmosphere, however, only $[\text{Ni}_8(\text{L5-CF}_3)_6]$ was found to efficiently capture DES, indicating an insensitivity to humidity upon fluorine functionalization (PADIAL et al., 2013). The comparison with the species employed in Saratoga® filtering systems (activated carbon Blücher-101408, provided by Blücher GmbH) shows that both materials ($[\text{Ni}_8(\text{L5-CF}_3)_6]$ and $[\text{Ni}_8(\text{L5-CH}_3)_6]$) are able to efficiently capture DES under extreme humidity conditions and that the maximum amount of adsorbed water is in line with the pore size and cell volume. This

work brings to light that the rational design of MOFs may be useful in the development of advance protection systems.

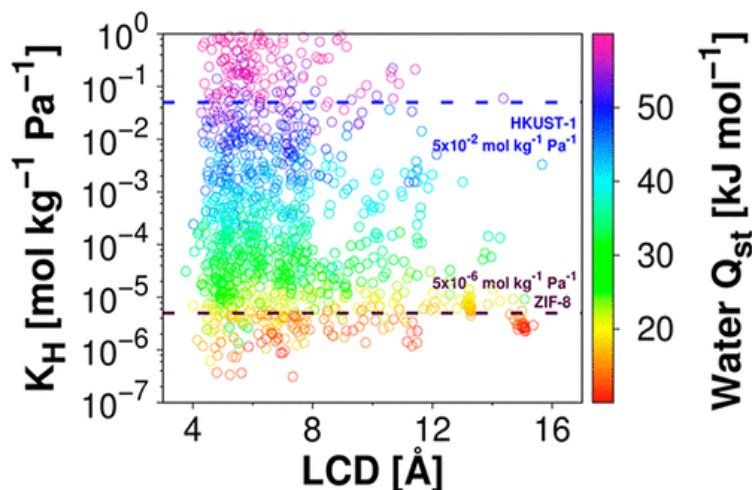
We can also find studies which investigate further insights into the adsorption of CWAs. Mandal *et al.* (ASHA; SINHA; MANDAL, 2017) choose NU-1000(Zr) and UiO-67(Zr) to studied the adsorption kinetics of an analog of sulfur mustard (CEES) and DMMP using Inductively Coupled Plasma - Atomic Emission Spectrometry (ICP-AES) data. They showed that it processes follow the pseudo-order model and the interactions adsorbates/adsorbents are chemical due to the presence of hydrogen bonds between Zr-OH moiety and the thioether and chloro groups of CEES and with the phosphate in DMMP. NU-100 exhibited outstanding performances with adsorptive capacities of 4.19 and 1.70 mmol g⁻¹ for CEES and DMMP, respectively; while UiO-67(Zr) adsorbed 4.0 and 0.90 mmol g⁻¹. Stassen and colleagues (STASSEN *et al.*, 2016) achieved a highly sensitive gas detection approach by monitoring the work function shift of UiO-66-NH₂(Zr), which has a missing linker defect site, coated electrodes upon exposure to ppb-level concentrations of DMMP. Lastly, Harvey *et al.* (HARVEY *et al.*, 2019) combining modelling and experimental spectroscopic techniques to identify binding sites of sarin in UiO-66(Zr) using P=O stretch frequency as a probe. As previously hypothesized, the undercoordinated Lewis acid metal site is the most favorable binding site. Although multiple sites contribute to the adsorption process, e.g. sarin form hydrogen bonds with the Zr-chelated hydroxyl groups and weakly interacts with fully coordinated metals.

2.2.2.2 MOFs for the capture of CWAs – computational approach

Molecular simulations have been also considered to explore the adsorption performances of MOFs providing interesting data that might minimize cost and laboratory hours besides maximize the security. In this respect, Grand canonical Monte Carlo (GCMC) simulations were performed by Greathouse *et al.* (GREATHOUSE *et al.*, 2010) in order to identify trends in low-pressure adsorption of tabun and O-ethyl-S-[2-(diethylamino) ethyl] methylphosphonothioate by Zn-IRMOFs (IRMOFs 1, 2, 3, 7 and 8), MIL-53lp(Cr), and Cu-BTC(Cu). These calculations suggested that with the exception of tabun in IRMOF-2, both toxic agents did not interact significantly with any of the MOFs studied. Inanc and Yazaydin (INANC; YAZAYDIN, 2015) calculated the Henry's coefficients of sarin, sulfur mustard, phosgene and water in ten selected zeolitic imidazolate frameworks (ZIFs). All the predicted Henry's coefficients of sarin were lower than water, which means that none of the selected

matrices will adsorb sarin preferentially under humid conditions. In contrast, the predicted Henry's coefficients of phosgene were many orders of magnitude higher than water in all selected ZIFs and for sulfur mustard were higher in ZIF-68 and ZIF-70. Most recently studies reported the use of molecular simulations as a predictive tool to anticipate the capture performance of a series of MOFs for diverse CWAs (AGRAWAL *et al.*, 2018; MATITO-MARTOS *et al.*, 2018). Matito-Martos *et al.* (MATITO-MARTOS *et al.*, 2018) designed a high-throughput screening strategy to identify MOFs able to capture sarin, soman and sulfur mustard and their non-toxic simulants in humid environments. They collected 2932 MOFs from the CoRE database with point charges assigned (NAZARIAN; CAMP; SHOLL, 2016) to account for CWA-MOF electrostatic interactions during the simulations. Firstly, 1275 MOFs were discarded because the pore limiting diameters were too narrow to accommodate CWA molecules, lower than 3.72 Å. Secondly, they simulated adsorption of the CWAs and their simulants at dilute conditions, computing their Henry coefficients and isosteric heats of adsorption via Widom insertions. The heats of adsorption of the real CWAs and its simulants were reasonably correlated for sulfur mustard/diethylsulfide, but less so for sarin and soman/dimethyl methylphosphonate and diisopropylfluorophosphate. The highest Henry coefficients of CWAs are referred to the MOFs with cavities of around 5 Å. In order to account for competitive adsorption of water from the environment they computed the Henry coefficients of water in each MOF, then 156 hydrophobic structures were selected by comparison with well-known hydrophobic ZIF-8, and the hydrophilic Cu-BTC, as illustrated in Figure 2.12 (KÜSGENS *et al.*, 2009). Then the authors ran GCMC simulations of blister agent (sulfur mustard) and nerve agents (sarin and soman) at 13.8 and 0.6 Pa, respectively, an estimate of the lethal concentrations. Of eight MOFs predicted to exhibit the largest sarin, soman, and sulfur mustard gas uptakes, where the three were strongly correlated. Then, they selected Ni₁₃₃(BTP)₂₂ for experimental synthesis and column breakthrough experiments on the basis of its reported thermal and chemical stability (COLOMBO *et al.*, 2011). The authors showed that Ni₁₃₃(BTP)₂₂ readily captured DES for more than 7 hours, at which point the MOF became saturated. Finally, the thermogravimetric analysis and temperature programmed desorption indicated water was desorbed at a lower temperature than for DES, proving that the framework is selective for this molecule over water.

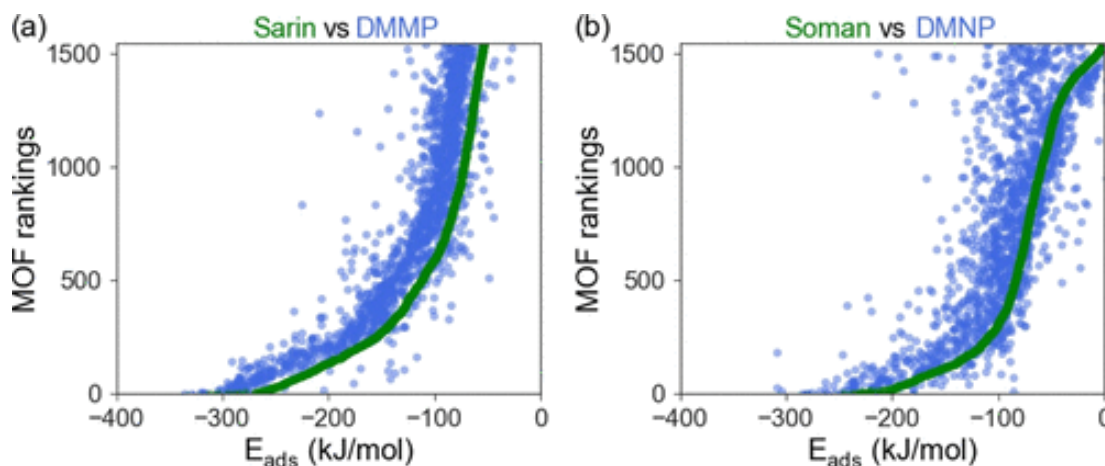
Figure 2.12 - Henry's constants for water as a function of the largest cavity diameter (LCD) in MOF structures at 298 K. Purple and blue dashed lines depict water KH in ZIF-8 and HKUST-1, respectively. Color code represents isosteric heat of adsorption (Q_{st}) for water.



Source: Adapted from (MATITO-MARTOS *et al.*, 2018).

Agrawal *et al.* (AGRAWAL *et al.*, 2018) also perform molecular simulation at dilute conditions in the CoRE MOFs aiming ascertain how effectively CWA simulants mimic the adsorption properties of Sarin and Soman. A set of 2969 MOFs were examined with two independent force fields. Judging from the correlation between the simulated heats of adsorption for the real nerve agents and the simulants, DCP and DMMP were found to mimic reasonably sarin while soman is better described by DMNP Figure 2.13 illustrates the predictive quality of these simulants, showing the connection between rankings of MOFs using their heat of adsorption and the numerical value of the heat of adsorption. However, there is still effort to be deployed to search for an alternative simulant that can mimic more accurately this series of nerve agents. Consistent with the conclusions drawn by Matito-Martos *et al.* (MATITO-MARTOS *et al.*, 2018) MOFs with the highest affinity for Sarin were found to show pore diameters in the range of 6-8 Å. This observation was shown not to be depend on the force field. However, one can notice that a range of additional physical properties may be relevant to analyze the performance of MOFs in applications involving CWAs.

Figure 2.13 - MOF rankings of 1544 MOFs for: DMMP (blue) and Sarin (green) (on the left) and DMNP (blue) and Soman (green) (on the right) when ordered by the heat of adsorption of (a) Sarin and (b) Soman, respectively.



Source: Adapted from (AGRAWAL et al., 2018).

Ruffley *et al.* (RUFFLEY et al., 2019) proposed that different functional groups incorporated into MOF linkers can be used to tune the adsorption strength of CWAs. At the outset, they assumed that in relatively defect-free MOFs the adsorbent/adsorbate interactions can be tuned by introducing functional groups on the linker. These results demonstrated that functionalized MOF domains with a differential affinity for CWAs can be fabricated, providing a foundation on which stratified MOFs for CWA capture may be based. A joint of experimental and computational methods predicted that a stratified MOF consisting of UiO-67-NH₂ (strongest) < UiO-67-CH₃ (intermediate) < UiO-67 (weakest) will show an equilibrium concentration gradient of DMMP induced by the differential binding energies of this simulant.

Summarizing, the variability in terms of chemical features, nature of metal-active sites and organic linkers, as well as shape/size of porosity of MOFs is expected to allow an effective adsorption of CWAs, which makes this class of materials attractive for protection and sensing.

2.2.2.3 MOFs for the degradation of CWAs – experimental approach

Developments based on the catalytic degradation of CWAs into nontoxic products need to be considered as the next step after the capture of these molecules. Very recent studies revealed progress toward developing MOFs capable of destroying CWAs. The first material investigated was NENU-11(Cu) by Su, Liu, and colleagues (MA et al., 2011b). This material exhibits a good storage capacity of 15.5 molecules/formula unit, and the incorporation of acid

polyoxometalates in its pore structure improved the catalytic activity, so the DMMP simulant was easily decomposed by a hydrolysis reaction. Roy and co-workers (ROY et al., 2012) reported the hydrolysis for sarin and sulfur mustard simulants CEPS (chloroethyl phenyl sulfide), CEES, DCP and DCNP. They found that the moisture increase content enhanced the hydrolysis rates, leading to a more efficient conversion for nerve agent CEPS simulants on Cu-BTC. However, the high moisture in MOF worked as a barrier for the adsorption of lipophilic blister agents causing their slower degradation. The same material was investigated by Peterson and Wagner (PETERSON; WAGNER, 2014) for the removal of soman, sulfur mustard and VX. The reactions were monitored *in situ* via gas chromatography and nuclear magnetic resonance. The Lewis acid nature of the Cu open metal sites seemed to favor the hydrolysis of these molecules, although a slow degradation was observed with a reaction half-life of 13 hours for sulfur mustard, 29 hours for VX and 2 days for soman. Although Cu-BTC showed good performances for CWA degradation one can notice that the practical application of Cu-BTC based materials is limited due to its poor water stability.

The materials MIL-101(Al)-NH₂ and MIL-53(Al)-NH₂ were reported as components of self-detoxifying surfaces. The pristine structures did not react with DIFP, then the incorporation 4-methylaminopyridine into the pores of both materials dramatically increased the reactivity. Combining the MOFs with the film resulted in even longer half-lives, but still proved to be quite reactive over time (55% conversion after 24 hours). Nevertheless, this study showed the ability of MOFs to break the neurotoxic bond, and it also exhibited the possibility to engineer reactive adhesives, which themselves can be deposited onto a variety of surfaces (BROMBERG et al., 2012). However, the catalytic activity of Al-MOFs is low when compared with Cu-BTC. It can be assigned to the poor substitutional lability of oxygen-bound ligands of Al³⁺. Shortly after, Wang *et al.* (WANG et al., 2013) showed that a nerve agent simulant methyl paraoxon hydrolysis is not catalyzed by the chromium ions of MIL-101(Cr), but instead by the tethered Brønsted-basic amine. Thus, we might expect metal-oxy/hydroxy species based on trivalent cations to be similarly poorly catalytic, despite their appreciable Lewis acidities.

Recently, researchers have explored Zr-MOFs, which are characterized by exceptional thermal and chemical stability, as active catalysts for the rapid hydrolysis of CWAs. They showed that the hexa-zirconium (IV) building block results in an even higher density of accessible strong Lewis acidic sites in this type of MOF compared to others. Besides some of the most thermal and chemically stable MOFs are constructed from Zr₆-based nodes linked to carboxylates ligands. These features make Zr-MOFs very promising catalysts in CWAs

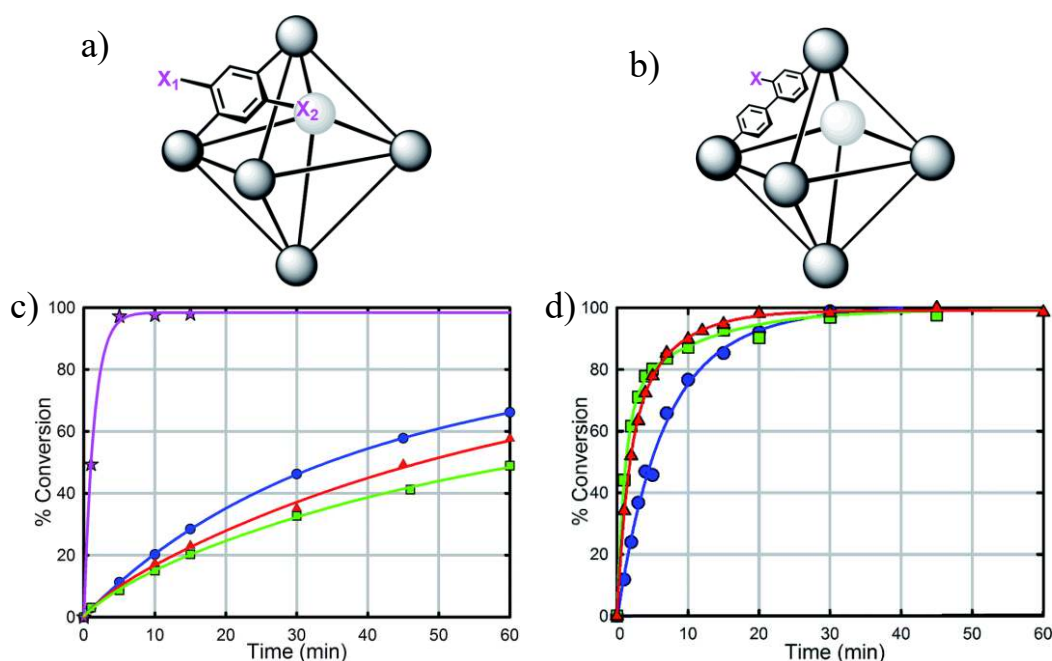
adsorption and catalytic detoxification (KATZ et al., 2014, 2015b; MONDLOCH et al., 2013, 2015).

With the aim of further exploring this field, Farha and collaborators (KATZ et al., 2014) reported that a UiO-66(Zr) adequately hydrolyzed DMNP, benefiting from the strong Lewis acidic Zr (IV) and bridging hydroxide anions on its pore surface. However, it still had a slow half-life (45 minutes) at room temperature. In order to explore the degree of connectivity as well as the ligand length of Zr-MOFs, Hupp, Farha, and colleagues (KATZ et al., 2015b) studied the degradation of DMNP by UiO-67(Zr), an analogue of UiO-66(Zr) constructed by longer spacers (Figure 2.14). A faster catalytic degradation of DMNP (4.5 minutes) by UiO-67(Zr) was attributed to the longer distance between nodes that prevents steric crowding around neighboring nodes, allowing for a faster accessibility of the molecule to the reactive sites. Furthermore, they showed that the amine functionalized UiO-66(Zr) and 67 derivatives exhibit significantly enhanced hydrolysis activity, where UiO-66-NH₂(Zr) presented a 20-fold increase in hydrolysis rate ($t_{1/2}$ of 1 min) over the pristine UiO-66(Zr). However, under the same conditions, UiO-66-NO₂ and UiO-66-(OH)₂ presented no significant difference in hydrolysis rate when compared with UiO-66(Zr), while UiO-67-NH₂ and UiO-67-NMe₂ show faster degradation than UiO-67(Zr) (Figure 2.14), suggesting that amino group acts as a Bronsted acid during the reaction (KATZ et al., 2015b).

Considering the aforementioned UiO-66(Zr) and UiO-67(Zr) series had been active for the catalytic hydrolysis of phosphoester bond, researchers (LI et al., 2015; MONDLOCH et al., 2015; MOON et al., 2015) investigated MOFs with more easily accessible Zr active sites. Mondloch *et al.* (MONDLOCH et al., 2015) were among the first to demonstrate the efficiency of an 8-connected Zr₆-MOF NU-1000 for the degradation of soman and the simulant DMNP. The structure shows four non-bridging Zr-OH and four Zr-H₂O sites per node and large mesopores of 31 Å. The NU-1000 is shown to be 3 to 30 times faster than UiO-66(Zr) (KATZ et al., 2014) in hydrolyzing the phosphoester bonds. Soman and its simulant DMNP were hydrolyzed by NU-1000 at a rate 200 and 1500 times faster than by using Cr based MOF MIL-101 (WANG et al., 2013) and HKUST-1(Cu) (PETERSON; WAGNER, 2014) respectively. The dehydrated form of NU-1000 reduces the half-life for DMNP hydrolysis to 1.5 minutes, compared to 15 minutes for the fully hydrated MOF. However, the dehydrated NU-1000 and UiO-66-NH₂ (MONDLOCH et al., 2013) both demonstrate comparable $t_{1/2}$ even when the latter exhibited only surface catalysis. The computational and experimental analysis suggests that the extraordinary activity of the NU-1000 is attributed to unique eight cornered Zr₆ node, weak intermolecular interaction that direct orientations between molecule and catalyst linker

components, favorable energetics and mesoporous channels that allow bulky phosphate ester molecules to permeate the entire framework and access to highly acidic metal sites.

Figure 2.14 - (a) Connectivity of the octahedral pore in UiO-66. $X_1=X_2=H$ for UiO-66, $X_1=NO_2$ and $X_2=H$ for UiO-66- NO_2 , $X_1=X_2=OH$ for UiO-66-(OH) $_2$, and $X_1=NH_2$ and $X_2=H$ for UiO-66- NH_2 . (b) Connectivity of the octahedral pore in UiO-67(Zr). $X=H$ for UiO-67, $X=NH_2$ for UiO-67- NH_2 , and $X=N(CH_3)_2$ for UiO-67- NMe_2 . (c) Hydrolysis rate of UiO-66 (blue), UiO-66- NO_2 (red), UiO-66-(OH) $_2$ (green), and UiO-66- NH_2 (pink). (d) Hydrolysis rate of UiO-67 (blue), UiO-67- NH_2 (red) and UiO-67- NMe_2 (green).



Source: Adapted from (STASSEN et al., 2016).

Subsequently, Moon *et al.* (MOON et al., 2015) introduced MOF-808, another Zr-MOF with even lower node connectivity, as the catalyst for the hydrolysis reaction of DMNP. The six connected MOF-808 comprised of tritopic carboxylate linkers has six aqua and hydroxo groups per node. They have noted an extraordinary activity for this hydrolysis ($t_{1/2}$ of < 30s) when compared with previous studies involving the materials, UiO-66(Zr) (KATZ et al., 2014), UiO-66- NH_2 (KATZ et al., 2015b), NU-1000 and its dehydrated form (LI et al., 2015; MONDLOCH et al., 2015). The elevated activity of MOF-808 can be attributed to its architectural construction where the low node connectivity and sizeable apertures give accessibility of Zr-based active sites and facilitate diffusion. Thus, one can notice that important factors contribute to the observed differences in modulating the catalytic rate, such as: the

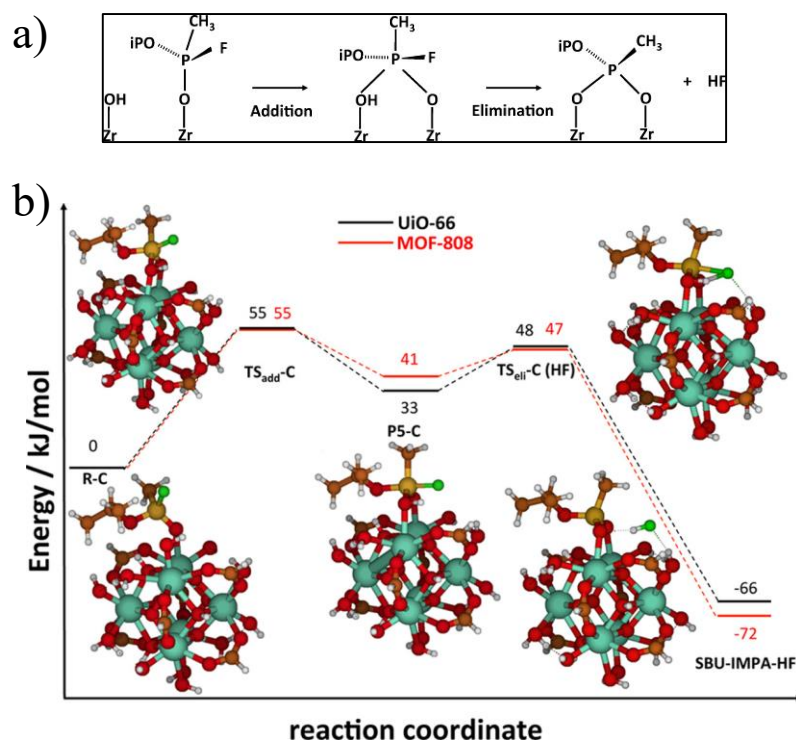
number of water molecules ligated to the zirconium, the relative accessibility of nodes to reactant molecules, ligand acidity and rates of aqua ligand exchange with the solvent.

Later, Plonka *et al.* (PLONKA *et al.*, 2017) and Wang *et al.* (WANG *et al.*, 2017) revealed that the catalytic conversion of DMMP is inhibited due to the strong bonds formed between the degraded products and the MOF frameworks. This observation motivated further investigations with the consideration of refined MOFs containing either functionalized linkers (ISLAMOGLU *et al.*, 2018; KALAJ *et al.*, 2019; PLONKA *et al.*, 2017; RUFFLEY *et al.*, 2019) or based on different metal centers (rare earth, Ce) (ISLAMOGLU *et al.*, 2017; MOMENI; CRAMER, 2019; SAVA GALLIS *et al.*, 2018) for the degradation of various nerve agents including soman, sarin and the analogues methyl paraxon, diisopropyl fluorophosphate, and diethyl chlorophosphate.

2.2.2.4 MOFs for the degradation of CWAs – computational approach

The literature is much less exhaustive in terms of computational studies related to the catalytic degradation of CWAs and their simulants using MOFs. Typically, Troya *et al.* (TROYA, 2016) carried out DFT calculations at the cluster level using localized basis sets to explore three hydrolysis degradation mechanism of sarin by UiO-66(Zr) and MOF-808(Zr) in a dry and hydrated conditions. Figure 2.15 summarized the central steps of the most stable reaction energy profile for MOF-808(Zr) in comparison with those on UiO-66(Zr). Thus, from an electronic structure perspective, the reactivity of UiO-66(Zr) and MOF-808(Zr) should be similar, and therefore, the changes to the rate measured probably are dominated by the accessibility of the nerve agent to the SBUs. One can notice that the decomposition products formed during the elimination step are bound to the catalyst and require desorption for a fully catalytic process.

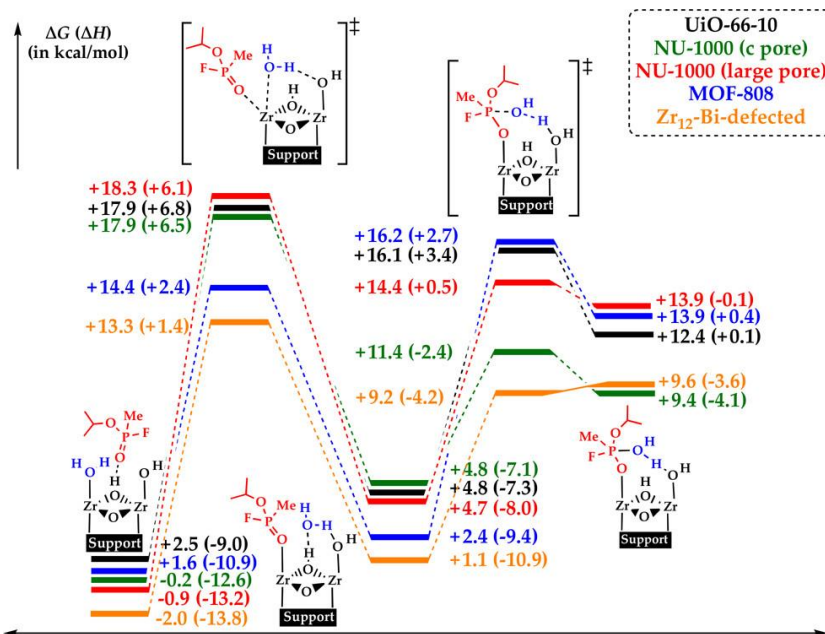
Figure 2.15 - (a) Essential Steps in the Reaction Mechanism for Degradation of GB on Dry Zr-Based MOFs. (b) Potential energy diagram for the central steps of the reaction mechanism of GB hydrolysis with the SBUs of dry UiO-66(Zr) (black trace) and MOF-808 (red). Atom colors are Zr: teal, O: red, C: brown, H: white, F: green and P: yellow.



Source: Adapted from (TROYA, 2016).

Wang *et al.* (WANG *et al.*, 2017) and Chen *et al.* (CHEN *et al.*, 2018) followed the same computational strategy to investigate the decomposition of DMMP and DMNP by UiO-67(Zr) and NU-1000, respectively. Extended clusters were considered by Momeni *et al.* (MOMENI; CRAMER, 2018a) to model the hydrolysis of sarin by Zr-based MOFs, MOF-808, NU-1000, and defective UiO-66(Zr). Extended and truncated cluster models to represent the Zr-defective structure of $[\text{Zr}_{12}(\mu_3\text{-O})_8(\mu_3\text{-OH})_8(\mu_2\text{-OH})_6(\text{TPDC})_{18}]$ were further used by Momeni *et al.* (MOMENI; CRAMER, 2018a) to model the hydrolysis of sarin in aqueous solution. They showed that the double-node MOF had superior reactivity than various Zr_6 single-node analogs tested for this reaction to date (Figure 2.16) (ISLAMOGLU *et al.*, 2017; KATZ *et al.*, 2014, 2015a, 2015b; LÓPEZ-MAYA *et al.*, 2015; MONDAL; HOLDT, 2016; MONDLOCH *et al.*, 2015; MOON *et al.*, 2015; PETERSON *et al.*, 2015; PLONKA *et al.*, 2017).

Figure 2.16 - M06-2X/Def2-TZVP//M06-L/Def2-SVP 298 K free energies and enthalpies for hydrolysis of sarin along different cluster-model benzoate-capped reaction coordinates relative to separated reactants.



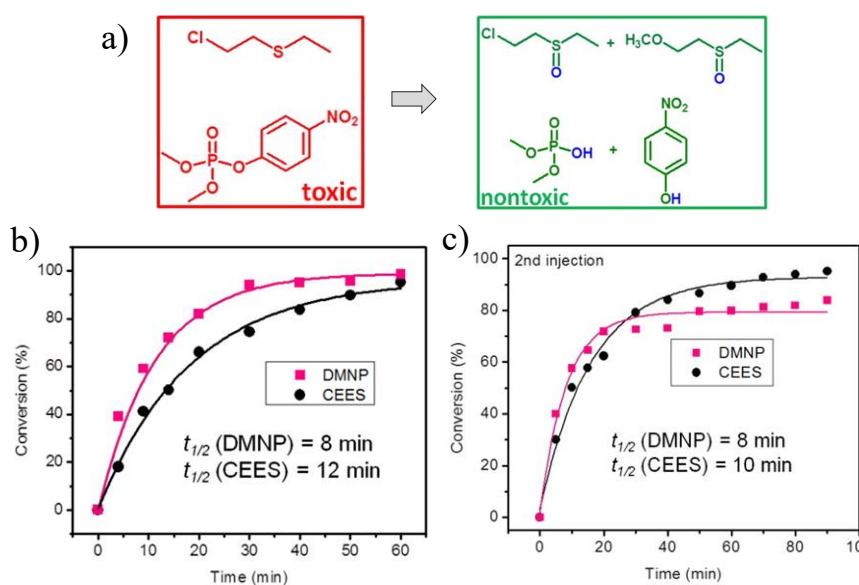
Source: Adapted from (TROYA, 2016).

More recently, Harvey *et al.* (HARVEY; GREATHOUSE; SAVA GALLIS, 2018) emphasized the importance of using periodic DFT calculations to more accurately capture the reactivity of organophosphorus compounds confined in the pores of MOFs. Typically, these authors mentioned that the consideration of a Zr formate cluster leads to an overestimation of the binding energy for DIFP and sarin compared to the scenario encountered with the use of a periodic system. This trend was explained by the lowering of the strength of interactions between the bulky isopropyl groups of the CWA and the active sites at the periodic level due to the steric hindrance induced by the MOF framework.

For the degradation of sulfur mustard agents and their simulants using MOFs its necessary taken into account that the dehydrohalogenation pathway is too slow to be effective for decontamination application (SMITH, 2008; WAGNER *et al.*, 2001, 1999, 2000; WAGNER; CHEN; WU, 2008) and hydrolysis is hindered by the immiscibility of sulfur mustard in water as well as the formation of intermediate products that slow down the reaction (MUNRO *et al.*, 1999b). Another detoxification method is partial oxidation to its sulfoxide product. However, this reaction requires the use of a selective oxidant to control product formation because over-oxidation can lead to its sulfone product that is nearly as toxic as HD itself. In this context, López-Maya *et al.* (LÓPEZ-MAYA *et al.*, 2015) reported that the

introduction of lithium alkoxide into the UiO-66(Zr) framework not only is able to hydrolyze P—F bond in DIPF and P—O bond in DMMP but also the degradation of CEES, an analogue of the vesicant mustard gas. They concluded that the insertion of lithium alkoxides in the zirconium oxide clusters gives rise to a boosting of the phosphotriesterase catalytic activity for the hydrolysis of toxic bonds. Hupp, Farha, and colleagues (LIU et al., 2015) investigated an endowed MOF (PCN-222/MOF-545) in order to generate dual detoxification material. The porphyrin linkers when irradiated can sensitize the photochemical conversion of triplet dioxygen to its much more reactive singlet, which selectively oxidizes CEES to an innocuous sulfoxide, and 8-connected Zr_6 nodes, which could hydrolyze the phosphonic acids. This material simultaneously degraded methyl paraoxon and CEES with half-lives of 8 and 12 min see Figure 2.17, respectively and it is the only reported example to date capable of simultaneously detoxifying blistering CWAs.

Figure 2.17 - (a) Dual-reaction setup to transform toxic CWA simulants CEES and DMNP to nontoxic oxidative and hydrolytic products, respectively. (b) Kinetic profiles for hydrolysis of DMNP and oxidation of CEES. (c) Kinetic profiles for the destruction of a second injection of DMNP and CEES into the “MOF-catalyzed dual-reaction”.



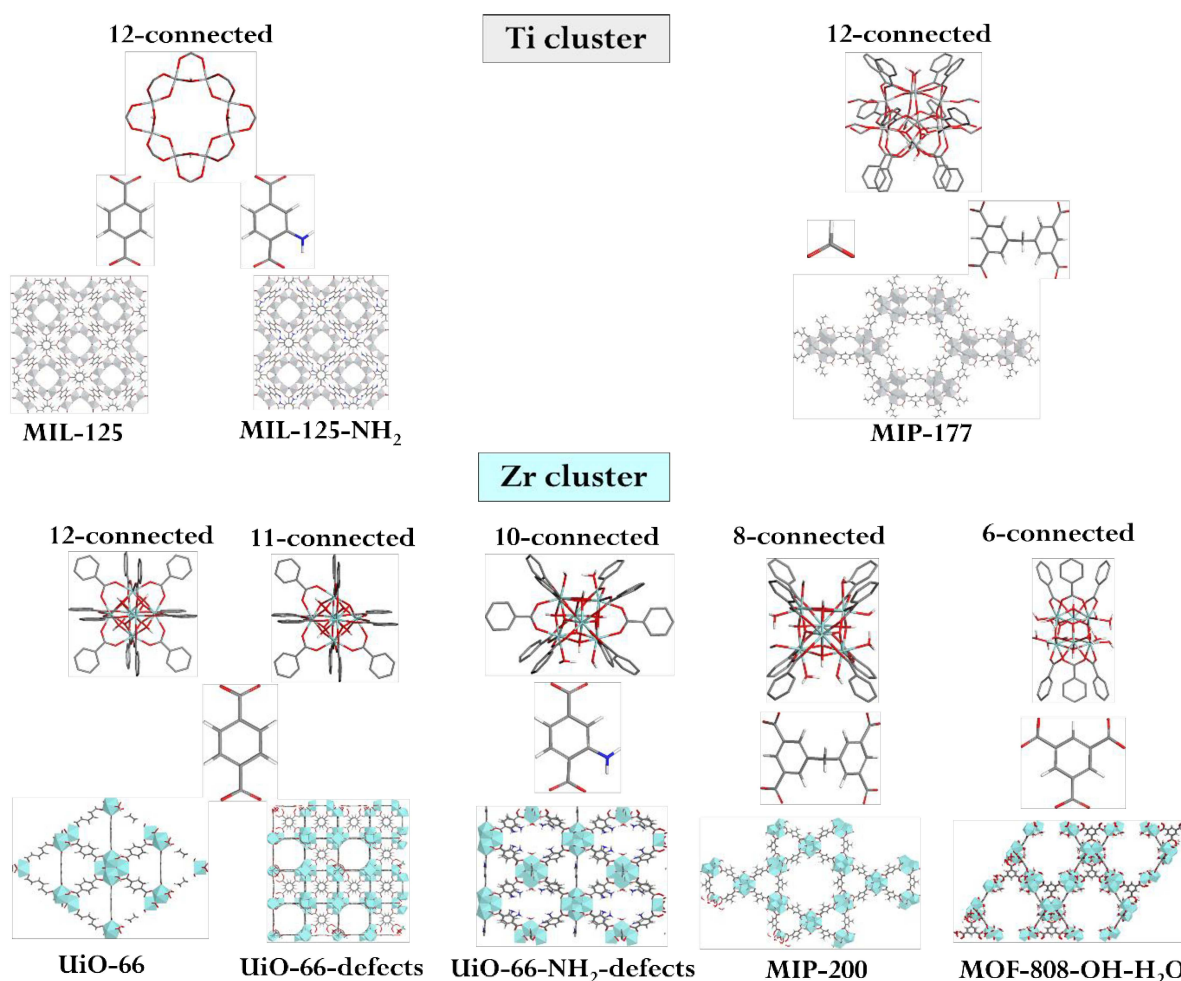
Source: Adapted from (LIU et al., 2015).

The number of MOFs studied so far with CWAs is a minute percentage with respect to the large collection of hybrid porous solids discovered to date. Moreover, some of the tested MOFs were revealed to be unstable in the presence of humidity which hampers their use for

CWA capture since humidity in the air and in the breath is usually present in operating conditions.

In this context, priority has to be given to explore CWA capture in chemical stable MOF containing high-valent cations, e.g. Zr^{4+} and Ti^{4+} , as metal centres, to ensure that the performances can be maintained under operating conditions over prolonged periods. Another requirement is to favor MOFs incorporating relatively cheap commercially available organic linkers, easily scaled-up, and prepared via green synthesis routes in order to be cost-competitive with respect to the ASZM-TEDA active carbons currently used as filters. In this context, Figure 2.18 illustrates the inorganic Zr and Ti building blocks of some MOFs explored in this study. All structures are connected by aromatic carboxylate ligands to form porous frameworks with different pore sizes, topology and adsorption sites.

Figure 2.18 - Illustrations of the inorganic Zr and Ti building blocks present in a few representative 3D-MOFs.



Source: Elaborated by the author (2019).

2.3 CONCLUSION

Unfortunately, the world has not been able to be safe from terrorist attacks such as that previously reported in the Middle East. This scenario emphasizes the global requirement for efficient systems to neutralize and destroy CWAs, provide protection devices and eliminate chemical stockpiles. Consequently, the applicability of novel porous materials such as Metal-Organic Frameworks should be advantageous.

Thus, we can conclude that the use of MOFs with adequate pore size/shape is not enough, thus other factors including adsorption kinetics and specific interactions between the toxic adsorbates and the adsorbents should be taken into account. For example, the presence of open metal sites or certain functionalizations on the pore surface may enhance the adsorption selectivity/efficiency of MOFs toward specific toxic compounds via coordination bonds, acid–base electrostatic interactions, Π -complex, H-bonding formation, and so on. On the other hand, the node connectivity, sizeable apertures, the number of water molecules coordinated to the metal, ligand acidity and rates of aqua ligand exchange with the solvent are extremely important factors to the degradation of CWAs into nontoxic products. In this context, computational and experimental works have mainly focused on Zr-MOFs, which are characterized by exceptional thermal and chemical stability. However, although MOFs containing high-valent cations, e.g. Ti^{4+} , might be also of interest for the catalytic degradation of CWAs. Besides, a special attention needs to be paid when one selects reasonably substitute for the target agent in the specific reaction pathway or reaction conditions under investigation. Finally, computational simulations are valuable tool to the investigate the adsorption and degradation process anticipating the performances of the related materials, which might minimize cost, laboratory hours and maximize the security.

3 QUANTUM AND FORCE-FIELD BASED MOLECULAR SIMULATIONS

This chapter presents the molecular simulation techniques that have been employed throughout my PhD to model the adsorption and degradation of chemical warfare agents by MOFs as well as the water stability of these hybrid porous materials. The main aspects of the quantum calculations applied to periodic systems using the Density Functional Theory are first detailed. The second section dedicated to force-field based approaches, presents the basic principles of Monte Carlo techniques and further presents the microscopic models and forcefields (also called interatomic potentials along the manuscript) used to represent the MOF frameworks and the CWAs molecules as well as to describe their interactions.

3.1 THE MANY-BODY PROBLEM AND THE BORN-OPPENHEIMER APPROXIMATION

In quantum mechanics the microscopic properties of a system formed by interacting particles, as atoms, molecules and solids, can be determine through the resolution of the time-independent Schrödinger equation (SHOLL, DAVID; STECKEL, 2011).

$$\hat{H}|\psi(\vec{R}_\mu, \vec{r}_i)\rangle = E|\psi(\vec{R}_\mu, \vec{r}_i)\rangle \quad (\text{equation 3.1})$$

where, \hat{H} is the Hamiltonian operator, E is the eigenvalue and $|\psi(\vec{R}_\mu, \vec{r}_i)\rangle$ is the state function of the system. μ and i are the indexes of the nucleus and electrons, while \vec{R} and \vec{r} are the coordinate vectors of electrons and nucleus, respectively.

The Hamiltonian of this system can be written as follows:

$$\hat{H} = \hat{T}_n + \hat{T}_e + \hat{V}_{n-n} + \hat{V}_{n-e} + \hat{V}_{e-e} \quad (\text{equation 3.2})$$

This equation can be developed and rewritten as follows:

$$\hat{H} = -\sum_{\mu=1}^M \frac{\hbar^2}{2M_\mu} \nabla_{\vec{R}_\mu}^2 - \sum_{i=1}^N \frac{\hbar^2}{2m_i} \nabla_{\vec{r}_i}^2 + \frac{1}{4\pi\epsilon_0} \sum_{\mu=1}^M \sum_{j=\mu+1}^M \frac{e^2 Z_\mu Z_j}{|\vec{R}_\mu - \vec{R}_j|} \quad (\text{equation 3.3})$$

$$-\frac{1}{4\pi\epsilon_0} \sum_{\mu=1}^M \sum_{i=1}^N \frac{e^2 Z_{\mu}}{|\vec{R}_{\mu} - \vec{R}_i|} + \frac{1}{4\pi\epsilon_0} \sum_{i=1}^N \sum_{j=i+1}^N \frac{e^2}{|\vec{R}_i - \vec{R}_j|}$$

where, \hbar is the Plank constant h divided by 2π , m_i and e are the mass and the charge of electron, M_{μ} and Z are the mass and the atomic number of the nuclei.

The Schrödinger equation for systems with more than one electron cannot be solved exactly because (i) the motion of electrons is coupled with the motion of the nuclei and (ii) there are repulsion interactions between electrons.

The Born-Oppenheimer approximation (BORN, M., & OPPENHEIMER, 1927) is used to simplify the many body Schrödinger equation. Considering the large difference in mass and mobility between the nuclei and electrons, it is assumed the atom cores are stationary whilst the electrons are mobile. This eliminates the kinetic energy term for nuclei and reduces the potential energy due to the nucleus-nucleus repulsion to a constant which can simply be added to the electronic energy determined by the Schrödinger equation. Therefore, the terms of \hat{H} that need to be computed for the exact description of the electronic structure are the following:

$$\hat{H} = \hat{T}_e + \hat{V}_{n-n} + \hat{V}_{n-e} + \hat{V}_{e-e} \quad (\text{equation 3.4})$$

where \hat{T}_n is zero and \hat{V}_{n-n} is a constant.

The term in the Hamiltonian defining electron–electron interactions is the most critical one from the point of view of solving the Schrödinger equation. The form of this contribution means that the individual electron wave cannot be found without simultaneously considering the individual electron wave functions associated with all the other electrons. In other words, in an N -electron system there are N wavefunctions, one for each electron, so the Hamiltonian contains N equations (CAPELLE, 2006). Therefore reasonable approximations must be employed to treat the electronic interactions (FIOLHAIS, CARLOS, FERNANDO NOGUEIRA, 2003).

3.1.1 Density functional theory

DFT provides a way to systematically map the many-body problem, onto a single-body problem. This is achieved by describing the total energy and all other observables as a functional of the electron density $\rho(\vec{r})$. Note that the electron density is a function only of one vectorial variable (\vec{r}).

$$\rho(\vec{r}) = N \int d^3\vec{r}_2 \int d^3\vec{r}_3 \dots \int d^3\vec{r}_N |\psi(\vec{r}, \vec{r}_2, \dots, \vec{r}_N)|^2 \quad (\text{equation 3.5})$$

where $\rho(\vec{r})$ determines the probability of finding any of the N electrons within the volume element $d^3\vec{r}_1$ but with arbitrary spin while the other N-1 electrons have arbitrary positions and spins in the state represented by ψ . It is to be noted that the multiple integral as such represents the probability that one particular electron is within the volume element $d^3\vec{r}_1$. However, since electrons are indistinguishable the probability of finding any electron at this position is just N times the probability for one particular electron. Clearly, $\rho(\vec{r})$ is a non-negative function of only the three spatial variables which vanishes at infinity and integrates to the total number of electrons:

$$\int \rho(\vec{r}) d^3\vec{r}_1 = N \quad (\text{equation 3.6})$$

The theorems put forward and proven by Hohenberg and Kohn in 1964 are the main principles in DFT (RAJAGOPAL; CALLAWAY, 1973). The first theorem states that: “*The ground-state energy from Schrödinger equation is a unique functional of the electron density.*” This can be reformulated by stating that the ground-state electron density is a fundamental function from which the other observables of a system may be derived. Consequently, this uniquely determines all properties, including the energy and wave function, of the ground state. The main consequence from this theorem is that this reduces the problem from requiring many wave functions, each based on the motion of individual electrons, to one wave function based on the electron density, and hence on three spatial variables, $r = x, y, z$.

The second Hohenberg–Kohn theorem defines an important property of the functional: “*The electron density that minimizes the energy of the overall functional is the true electron density corresponding to the full solution of the Schrödinger equation.*” Therefore, if the “true” functional form would be known, the electron density could be varied until the energy from the functional is minimized. Thus, for the energy to be minimized, it must satisfy the following variational equation:

$$\frac{\delta E(\rho(\vec{r}))}{\delta \rho(\vec{r})} = 0 \quad (\text{equation 3.7})$$

Then one may write the energy as a functional of the density:

$$E[\rho(\vec{r})] = T_e[\rho(\vec{r})] + V_{e-e}[\rho(\vec{r})] + \int \rho(\vec{r})V_{ext}(\vec{r})d^3\vec{r} \quad (\text{equation 3.8})$$

where the first and the second terms are universal in the sense that the treatment of the kinetic and internal potential energies are the same for all systems and the last term is the external potential due to the nuclei.

3.1.2 The Kohn-Sham equations

One can note that finding explicit expressions for the functional represents the major challenge in DFT. In this context, Kohn and Sham (KS) (KOHN et al., 1965) introduced the concept of a non-interacting reference system built from a set of orbitals such that the major part of the kinetic energy can be computed to good accuracy. By this method, as much information as possible is computed exactly, leaving only a small part of the total energy to be determined by an approximate functional.

In the Kohn-Sham approach, the kinetic term $T[\rho(\vec{r})]$ is divided into non-interacting $T_s[\rho(\vec{r})]$ and correlation $T_c[\rho(\vec{r})]$ terms while the internal electrostatic potential $V_{e-e}[\rho(\vec{r})]$ can be separated in three terms, a Hartree interaction term $V_H[\rho(\vec{r})]$, an exchange term $V_x[\rho(\vec{r})]$ and a correlation term $V_c[\rho(\vec{r})]$. Thus, Equation 3.7 can be rewritten as:

$$E[\rho(\vec{r})] = T_s[\rho(\vec{r})] + T_c[\rho(\vec{r})] + V_H[\rho(\vec{r})] + V_x[\rho(\vec{r})] + V_c[\rho(\vec{r})] + \int \rho(\vec{r})V_{ext}(\vec{r})d^3\vec{r} \quad (\text{equation 3.9})$$

The terms $T_c[\rho(\vec{r})]$, $V_x[\rho(\vec{r})]$ and $V_c[\rho(\vec{r})]$, which include all the quantum mechanical effects, can be grouped in a single term called exchange-correlation potential $V_{xc}[\rho(\vec{r})]$.

$$E[\rho(\vec{r})] = T_s[\rho(\vec{r})] + V_H[\rho(\vec{r})] + V_{xc}[\rho(\vec{r})] + \int \rho(\vec{r})V_{ext}(\vec{r})d^3\vec{r} \quad (\text{equation 3.10})$$

It is important to note that the non-interacting kinetic energy ($T_s[\rho(\vec{r})]$) can be calculated in terms of single-particle orbitals, the Kohn-Sham orbitals $[\phi_i^{KS}(\vec{r})]$, as demonstrated in Equation 3.11.

$$T_s[\rho(\vec{r})] = -\frac{\hbar^2}{2m} \sum_{i=1}^N \int \phi_i^{*KS}(\vec{r}) \nabla^2 \phi_i^{KS}(\vec{r}) d^3\vec{r} \quad (\text{equation 3.11})$$

Since, the $T_s[\rho(\vec{r})]$ is explicitly a functional of the Kohn-Sham orbitals and implicitly a functional of the electronic density, the electronic density must itself be defined by the summation of these orbitals, as stated below:

$$\rho(\vec{r}) = \sum_{i=1}^N f_i |\phi_i^{KS}| \quad (\text{equation 3.12})$$

where f_i is the occupation of the i band state according to the Fermi-Dirac distribution.

The minimization of the energy leads to the following expression:

$$\begin{aligned} 0 &= \frac{\delta E[\rho(\vec{r})]}{\delta \rho(\vec{r})} = \frac{\delta T_s[\rho(\vec{r})]}{\delta \rho(\vec{r})} + \frac{\delta V_H[\rho(\vec{r})]}{\delta \rho(\vec{r})} + \frac{\delta V_{XC}[\rho(\vec{r})]}{\delta \rho(\vec{r})} + \frac{\delta V_{ext}[\rho(\vec{r})]}{\delta \rho(\vec{r})} \quad (\text{equation 3.13}) \\ &= \frac{\delta T_s[\rho(\vec{r})]}{\delta \rho(\vec{r})} + v_H(\vec{r}) + v_{XC}(\vec{r}) + v_{ext}(\vec{r}) = 0 \end{aligned}$$

Considering the fictitious system of N non-interacting electrons moving in the effective potential (V_{ef}) the Equation 3.13 can be rewritten as:

$$\frac{\delta T_s[\rho(\vec{r})]}{\delta \rho(\vec{r})} + v_{ef}^{KS}[\rho(\vec{r})] = 0 \quad (\text{equation 3.14})$$

Thus, the form of the Schrödinger equation for the ground state energy, called the Kohn-Sham equations, can be represented as:

$$\left[-\frac{\hbar^2 \nabla^2}{2m} + v_{ef}^{KS}[\rho(\vec{r})] \right] \phi_i^{KS}(\vec{r}) = \varepsilon_i \phi_i^{KS}(\vec{r}) \quad (\text{equation 3.15})$$

The basic idea is to replace the Schrödinger equation for the interacting electronic system with a set of single-particle equations with the same density as the original system. Provided that the explicit forms of all these potentials are known, we can determine v_{ef}^{KS} and by solving the Kohn-Sham equations, which is initially defined using the trial electron density, we

can define the single-particle wave functions. Then a new electronic density is calculated and this process continues until a given convergence criteria is attained.

Since we do not know the potential ($V_{xc}[\rho(\vec{r})]$) due to the exchange-correlation energy it is necessary to introduce an approximation for this potential. Thus, the Kohn-Sham approach is in principle exact, where the approximation only enters when we have to decide on an explicit form of the unknown functional for the exchange-correlation energy and the corresponding potential. In this concern, approaches such as the Local Density Approximation (LDA) (PERDEW; ZUNGER, 1981; PERDEW; WANG, 1992) and the Generalized Gradient Approximation (GGA) (PERDEW; BURKE; ERNZERHOF, 1996) have been applied in this field.

3.1.3 The exchange-correlation functional

The exchange-correlation energy term in the LDA approach depends on the electron density of a homogeneous electron gas (MAHAN, 2000). It is supposed that the electronic density is constant at all points around (\vec{r}). The analytical expression for the LDA to the exchange-correlation energy is the following:

$$E_{xc}^{LDA}[\rho(\vec{r})] = \int \rho(\vec{r}) \epsilon_{xc}^{LDA}[\rho(\vec{r})] d^3\vec{r} \quad (\text{equation 3.16})$$

where, ϵ_{xc}^{LDA} is the exchange-correlation energy per electron as a function of a homogeneous electron gas density.

The exchange term used is explicit:

$$\epsilon_x^{LDA}[\rho(\vec{r})] = -\frac{e^2}{4\pi\epsilon_0} \frac{3}{4} \left(\frac{3}{\pi}\right)^{1/3} \rho(\vec{r})^{1/3} \quad (\text{equation 3.17})$$

There is no explicit expression for determining ϵ_c , but it is usually derived through empirical fitting or derived analytically. The most commonly used representations for ϵ_c are those developed by Perdew and Zunger (PZ) (PERDEW; ZUNGER, 1981), Perdew and Wang (PW) (PERDEW; WANG, 1992) and Vosko-Wilk-Nusair (VWN) (VOSKO; WILK; NUSAIR, 1980).

The LDA assumes that the electron density is constant, and the interactions are local, while in reality this is not the case. This approach provides bond lengths and thus the geometries

of molecules and solids usually with an astonishing accuracy of 1%. However, it gives ionization energies of atoms, dissociation energies of molecules and cohesive energies with fair accuracy of typically 10–20% (KOHN, 1999).

The generalized gradient approximation (GGA) (PERDEW; WANG, 1992), which includes the information about the gradient of the charge density $\nabla\rho(\vec{r})$, has been successfully applied to solid state chemistry. Thus, the gradient expansion to the LDA to the exchange-correlation energy is as follows:

$$E_{xc}^{GGA}[\rho(\vec{r})] = \int \rho(\vec{r}) \epsilon_{xc}(\rho(\vec{r})) F_{xc}[\rho(\vec{r}), |\nabla\rho(\vec{r})|] d^3\vec{r} \quad (\text{equation 3.18})$$

where, $F_{xc}[\rho(\vec{r}), |\nabla\rho(\vec{r})|]$ modifies the LDA expression according to the density variation in the vicinity of a given point (\vec{r}).

The different ways of including the density gradient through the GGA approximation generates the different exchange and correlation functions. Several suggestions for the functional F exist, including semiempirical functionals which contain parameters that are calibrated against reference values rather than being derived from first principles. Currently, Perdew and Wang (PW91) and Perdew Burke Ernzerhof (PBE) functionals are the most popular and most reliable GGAs employed in the literature (PERDEW; BURKE; ERNZERHOF, 1996; PERDEW; WANG, 1992).

In 1996, Perdew, Burke and Ernzerhof (TAVERNELLI; LIN; ROTH LISBERGER, 2009; VON LILIENFELD et al., 2004) showed how to construct a much simpler form of the PW91 GGA and with a much easier derivation way. A GGA exchange energy typically is written in terms of an enhancement factor, F_x , with respect to local exchange as follows:

$$E_x[\rho(\vec{r})] = \int \rho(\vec{r}) \epsilon_x^{LDA}[\rho(\vec{r})] F_x(s) d^3\vec{r} \quad (\text{equation 3.19})$$

where the dimensionless gradient s is given by the equation:

$$s(\vec{r}) = \frac{|\nabla[\rho(\vec{r})]|}{2\kappa_F[\rho(\vec{r})]} \quad (\text{equation 3.20})$$

As mentioned above, PBE was introduced with the intention of simplifying the complicated PW91 form while keeping its predictive capabilities. The much simpler PBE enhancement factor is expressed as follows:

$$F_x^{PBE}(s) = 1 + \kappa - \frac{\kappa}{1 + \frac{\mu s^2}{\kappa}}, \quad \mu = \frac{\beta \pi^2}{3} \quad (\text{equation 3.21})$$

where, μ and κ are non-empirical parameters.

The PBE correlation energy is given by the following equation:

$$E_c^{PBE}[\rho(\vec{r})] = \int \rho(\vec{r}) \epsilon_c[\rho(\vec{r})] H^{PBE}(r_s, t) d^3\vec{r} \quad (\text{equation 3.22})$$

where t is a dimensionless density gradient and r_s is the dimensionless Seitz radius.

3.1.3.1 Dispersion forces in DFT

The accurate description of weak nonbonding interactions is one of the challenges for DFT. Indeed, it is well-established that popular GGA functional is inadequate for the description of the long-range electron correlations. The fundamental reason for this failure of standard DFT functionals is their inability to account for a nonlocal electron correlation effect.

Several approaches have been developed that allow dispersion to be accounted for. This includes the DFT-D2 and DFT-D3 methods of Grimme and co-workers (GRIMME, 2004, 2006; GRIMME et al., 2010), van der Waals density functionals (vdW-DF) of Lundqvist, Langreth, and co-workers (ANDERSSON; LANGRETH; LUNDQVIST, 1996; DION et al., 2004; LEE et al., 2010), the dispersion-corrected atom-centered pseudopotential method of Roethlisberger and co-workers (TAVERNELLI; LIN; ROTH LISBERGER, 2009; VON LILIENFELD et al., 2004), and the vdW-TS method of Tkatchenko and Scheffler (TKATCHENKO; SCHEFFLER, 2009).

One conceptually simple correction for the shortcomings of DFT regarding dispersion forces is to simply add a dispersion-like contribution to the total energy between each pair of atoms in a material. This idea was developed by Grimme, so in DFT-D calculations, the total energy is augmented as follows:

$$E_{DFT-D} = E_{DFT-GGA} + E_{dispersion} \quad (\text{equation 3.23})$$

The dispersion correction is given by an attractive semi-empirical pair potential defined below:

$$E_{dispersion} = -s_6 \sum_{i=1}^{N_{at}-1} \sum_{j=i+1}^{N_{at}} \frac{C_6^{ij}}{R_{ij}^6} f_{dmp}(R_{ij}) \quad (\text{equation 3.24})$$

In this equation, N_{at} is a number of atoms in the system, R_{ij} is the distance between atoms i and j , C_6^{ij} is a dispersion coefficient for atoms i and j . The only empirical parameter in this expression is s_6 , a scaling factor that is applied uniformly to all pairs of atoms, which is specific for each exchange-correlation functional (e.g. $s_{6-PBE} = 0.75$ and $s_{6-PW91} = 0.7$).

To avoid near-singularities for small R , a damping function f_{dmp} must be used which is given by:

$$f_{dmp}(R_{ij}) = \frac{1}{1 + e^{-\alpha(R/R_0-1)}} \quad (\text{equation 3.25})$$

where, R_0 is the sum of atomic van der Waals radii.

3.1.4 Periodic Systems

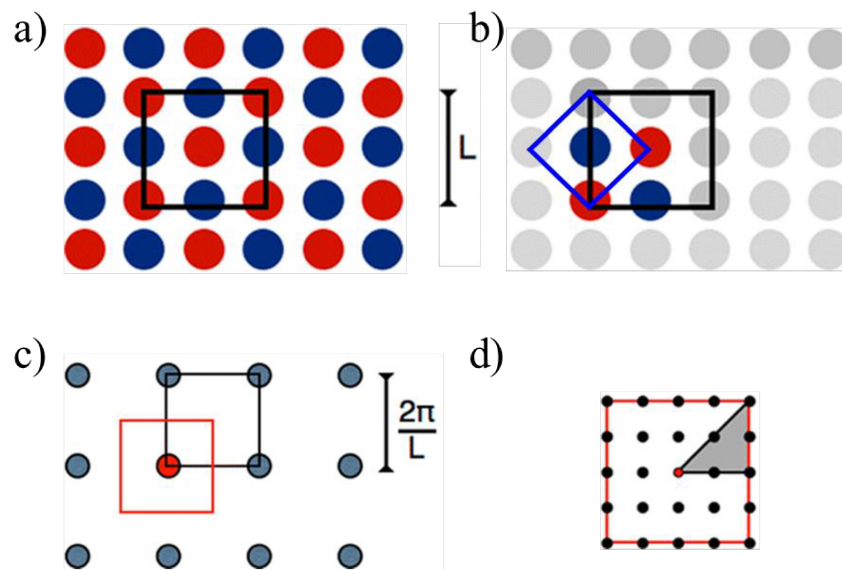
The coordinates of the atoms in a crystalline solid may be described by the Bravais lattice, which consists of all points with position vector \vec{R} of the form:

$$\vec{R} = n_1 \vec{a}_1 + n_2 \vec{a}_2 + n_3 \vec{a}_3 \quad (\text{equation 3.26})$$

where, \vec{a}_1 , \vec{a}_2 and \vec{a}_3 are any three vectors not all in the same plane, known as primitive vectors and responsible to generate the lattice, and n_1 , n_2 and n_3 range through all integral values.

Solid state materials generally contain large numbers of electrons, and a direct simulation of such systems would not be possible. Fortunately, many solids possess symmetries at the atomistic level and, therefore it is sufficient to consider only the unit cell of material subject to periodic boundary conditions, see Figure 3.1. This typically reduces the number of atoms and hence the number of electrons that must be considered in the simulations.

Figure 3.1 - (a) The crystal solid with the unit cell of the lattice in black. (b) The atoms that must be included in the simulation are colorful, where the primitive cell is highlighted in blue. (c) The reciprocal lattice of the crystal with the origin (gamma point) highlighted in red. Both the reciprocal unit cell (black) and the first Brillouin zone (BZ) (red) are highlighted. (d) First BZ divided by a uniform mesh of k -points. Because of the point group symmetry, only those within the gray triangle need to be explicitly considered in the calculation.



Source: Adapted from (BONHOMME et al., 2012).

A basis set is the set of one-electron wavefunctions that describe the motion of the electrons of a system. It can be typically expanded as a linear representation using a set of basis functions.

$$\psi_i(\vec{r}) = \sum_u C_{u,i} \lambda_u(\vec{r}) \quad (\text{equation 3.27})$$

Exact orbital representation requires an infinite set of basis functions, which are summed over an infinite number of expansion coefficients, $C_{u,i}$. In order to make the calculation tractable the summations need to be truncated. There are two general approaches applicable for the construction of basis sets. One is to consider atomic-like basis functions, which is generally done by the linear combination of functions used to represent each one of the atomic orbitals. These atom centered basis functions are also referred as basis sets and are mainly represented

by functions of Gaussian- and Slater-type. These basis sets may be composed by one basis function, minimal basis set or multiples basis functions (double-zeta, triple-zeta and etc.) per orbital. The other approach to describe the electronic wave function is to consider plane waves.

Plane-waves are chosen as basis sets in the solid state because Bloch's theorem (ASHCROFT, NEIL W., 1976) allows the electronic wavefunctions to be expanded in terms of a discrete set of plane-waves.

The eigenstates ψ of the one-electron Hamiltonian $H = -\hbar^2 \nabla^2 / 2m + V_{ef}(\vec{r})$, where $V_{ef}(\vec{r}) = V_{ef}(\vec{r} + \vec{R})$ is periodic with respect to the real lattice vector \vec{R} for all Bravais lattice translation vectors, can be chosen to be a plane wave times a function with the periodicity of the Bravais lattice.

$$\psi_{n\vec{k}}(\vec{r}) = e^{i\vec{k}\vec{r}} u_{n\vec{k}}(\vec{r}) \quad (\text{equation 3.28})$$

where, \vec{k} is a wave vector confined to the first Brillouin zone of the reciprocal lattice and the subscript n indicates a band index; \vec{r} is the position vector in the real space. $u_{n\vec{k}}$ is the cell-periodic part and can be written as follows:

$$u_{n\vec{k}}(\vec{r}) = u_{n\vec{k}}(\vec{r} + \vec{R}) \quad (\text{equation 3.29})$$

Note that the Equations 3.28 and 3.29 implies that:

$$\psi_{n\vec{k}}(\vec{r} + \vec{R}) = e^{i\vec{k}\vec{R}} \psi_{n\vec{k}}(\vec{r}) \quad (\text{equation 3.30})$$

This relation is known as in the Bloch's theorem.

The cell-periodic part can be represented as a Fourier series expansion of plane wave functions (PAYNE et al., 1992):

$$u_{n\vec{k}}(\vec{r}) = \sum_{\vec{G}} C_{n,G} e^{i\vec{G}\vec{r}} \quad (\text{equation 3.31})$$

where \vec{G} is a wave vector that represents the reciprocal lattice vectors of the crystal and $C_{n,G}$ are plane-wave coefficients.

Note that the wave vector k can always be confined to the first Brillouin zone, where any k' not in the first Brillouin zone can be written as: $\vec{k}' = \vec{k} + \vec{G}$. Thus, the set of one-electron

wave functions can then be expressed in terms of a linear combination of plane-waves (PAYNE et al., 1992):

$$\psi_{n\vec{k}}(\vec{r}) = \sum_{\vec{G}} C_{n,(k+G)} e^{i(\vec{k}+\vec{G})\vec{r}} \quad (\text{equation 3.32})$$

Therefore, when plane waves are used as a basis set, the Kohn-Sham equations assume a particularly simple form:

$$\sum_{\vec{G}} \left[\frac{\hbar^2}{2m} |\vec{k} + \vec{G}|^2 \delta_{\vec{G}\vec{G}'} + V_{ef}(\vec{G} - \vec{G}') \right] (C_{n,(k+G)}) = \varepsilon_i C_{n,(k+G)} \quad (\text{equation 3.33})$$

which is obtained by a substitution of Equation 3.31 into Equation 3.15.

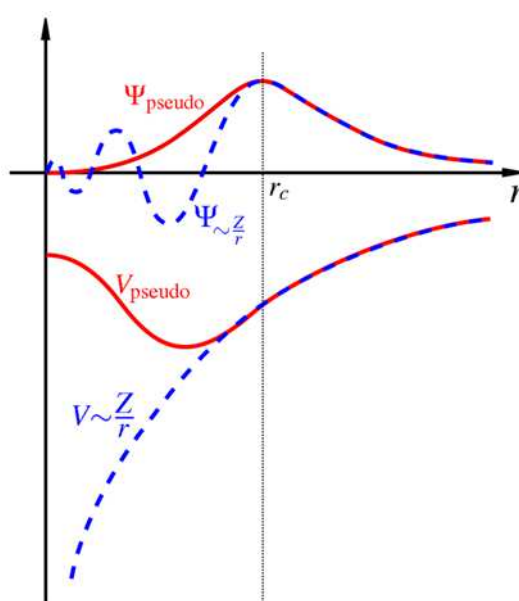
Since there are n wave functions for each \vec{k} -point in a periodic solid, the electronic band index n is introduced as an additional quantum number. Each \vec{k} represents a quantum number that indexes the wave vectors of a free electron that is always confined to the first Brillouin zone of the reciprocal lattice. Both n and \vec{k} can now identify the electronic state in a system completely. Note that n is discrete and \vec{k} is continuous, although we treat it point by point by sampling. Here, \vec{G} and \vec{G}' represent different vectors for plane waves and provide the indexes for the row and column elements in Hamiltonian matrix. In this form, the kinetic energy is diagonal, and the various potentials are described in terms of their Fourier transforms. The solution of Equation 3.33 proceeds by diagonalization of a Hamiltonian matrix, whose matrix elements are given by the terms in the brackets. The size of this matrix is determined by the choice of cutoff energy, given by: $[(\hbar^2/2m)|\vec{k} + \vec{G}|^2]$.

3.1.5 Pseudopotential approximation

It is well known that core electrons are not especially important in defining chemical bonding and other physical characteristics of solids since these properties depend on the valence electrons. Therefore, the key point is effectively freezing the nucleus and the core electrons, reducing the atom to an ionic core that interacts with the valence electrons. The use of an effective interaction, a pseudopotential, that approximates the potential felt by the valence electrons, leads to a significant reduction in the number of electrons in a system to be calculated

and to a much easier description and computation of the valence wave functions. Figure 3.2 illustrates that the pseudopotential and pseudo-wavefunction replace the all-electron counterparts of the core up to the certain cut-off radius (r_c) and mimic the valence region exactly.

Figure 3.2 - Illustration of the pseudo-wave function and the potential (red solid line) compared to the all-electron wave function and electronic potential (blue dashed line) plotted against the distance from the nucleus. The cut-off radius denotes the radius at which the electron and pseudo-electron values are identical.



Source: Adapted from (PAYNE et al., 1992).

One can notice that when the valence wave function passes by the region occupied by the core electrons it oscillates rapidly due to the strong ionic potential in this region. These oscillations maintain the orthogonality between the core wave functions and the valence wave functions. The orthogonal criterion guarantees each wave function to be unique and independent and thus to obey the Pauli exclusion principle.

Pseudopotentials are currently generated from all -electron atomic calculations and this pseudopotential can be then used reliably for calculations that place this atom in any chemical environment. Current DFT codes typically provide a library of pseudopotentials that includes an entry for all elements of the periodic table. The most widely used method of defining pseudopotentials is based on work by Vanderbilt, known as ultrasoft pseudopotentials (VANDERBILT, 1990).

3.1.6 Nudged Elastic Band Method

In a chemical reaction the rearrangement of the atoms follows a trajectory on the potential energy surface from the reactant to the product. A path connecting the initial and final states that typically corresponds to the highest statistical weight is the minimum energy path (MEP) (HENKELMAN; JÓHANNESSON; JÓNSSON, 2002).

The MEP is found by constructing a set of images of the system to connect the initial and final states passing from one minimum to another and overcoming the saddle point. Each point (\vec{R}) along the MEP correspond to a nuclear configuration of all the atoms in the system, where the relative distances between them define a reaction coordinate (HENKELMAN; JÓNSSON, 2000).

The nudged elastic band (NEB) is an efficient method to find the MEP between initial and final states of a reaction and to assess the resulting energy barrier (CASPERSEN; CARTER, 2005; HENKELMAN; JÓNSSON, 2000). In this approach, a sequence of images is created and each of them is connected to neighbors by a virtual spring associated with a constant k used to represent the path from reagent (R) to product (P). Initially, the images are generated along a straight line by linear interpolation as represented by Equation 3.34:

$$R_i = R_0 + \frac{i}{N}(R_N - R_0) \quad (\text{equation 3.34})$$

Thus, the MEP is found by constructing a set of images with $N+1$ images between R and P, typically on the order of 4–20. These images can be denoted by $(R_0, R_1, R_2, \dots, R_N)$, where R_i defines the coordinates of the images. An optimization algorithm is then applied to relax the images down towards the MEP.

The total forces acting on an image is the sum of the spring force (F_i^S) and the true force (F_i^T), those resulting from the potential energy.

$$F_i^S = \frac{-\partial E_i^S}{\partial R_i} \quad ; \quad F_i^T = \frac{-\partial E_i^T}{\partial R_i} = -\nabla E (R_i) \quad (\text{equation 3.35})$$

where, $\nabla E (R_i)$ is the gradient of the energy with respect to the atomic coordinates in the system at image i , and $E_i^S = \sum_i k_S (R_{(i+1)} - R_i)^2$ (k_S is the spring constant). The spring forces to ensure equal spacing along the reaction path.

Given an estimate of the unit tangent to the path at each image (described below), $\hat{\tau}_i$, the force on each image should only contain the parallel component of the spring force, and perpendicular component of the true force in order to avoid the corner-cutting and the sliding-down problems (CASPERSEN; CARTER, 2005).

$$F_i = F_i^{T\perp} + F_i^{S\parallel} = -\nabla E (R_i)^\perp + F_i^{S\parallel} \quad (\text{equation 3.36})$$

$$F_i = -[\nabla E (R_i)^t - \nabla E (R_i)^{t\parallel} \cdot \hat{\tau}_i] + k_S (|R_{(i+1)} - R_i| - |R_i - R_{(i-1)}|) \cdot \hat{\tau}_i$$

This is what is referred to as ‘nudging’ and ensures that the spring forces

The tangent of the path at an image i is defined by the vector between the image and the neighboring image with higher energy. That is:

$$\tau_i = \begin{cases} \tau_i^+ & \text{if } E_{i+1} > E_i > E_{i-1} \\ \tau_i^- & \text{if } E_{i+1} < E_i < E_{i-1} \end{cases} \quad (\text{equation 3.37})$$

where:

$$\tau_i^+ = \vec{R}_{i+1} - \vec{R}_i \quad \text{and} \quad \tau_i^- = \vec{R}_i - \vec{R}_{i-1} \quad (\text{equation 3.38})$$

If both adjacent images are either lower in energy, or both are higher in energy than image i , the tangent is taken to be a weighted average of the vectors to the two neighboring images. If image i is at a minimum ($E_{i+1} > E_i < E_{i-1}$) or at a maximum ($E_{i+1} < E_i > E_{i-1}$), the tangent estimate becomes:

$$\tau_i = \begin{cases} \tau_i^+ \Delta E_i^{max} + \tau_i^- \Delta E_i^{min} & \text{if } E_{i+1} > E_{i-1} \\ \tau_i^+ \Delta E_i^{min} + \tau_i^- \Delta E_i^{max} & \text{if } E_{i+1} < E_{i-1} \end{cases} \quad (\text{equation 3.39})$$

where:

$$\begin{aligned} \Delta E_i^{max} &= \max(|E_{i+1} - E_i|, |E_{i-1} - E_i|) \\ \Delta E_i^{min} &= \min(|E_{i+1} - E_i|, |E_{i-1} - E_i|) \end{aligned} \quad (\text{equation 3.40})$$

A modification of the NEB method, known as the Climbing Image NEB (CI-NEB) (HENKELMAN; UBERUAGA; JÓNSSON, 2000), provides a precise estimation of the saddle point when compared with NEB. In the CI-NEB, after a few relaxation steps, the highest energy image feels no spring forces and climbs to the saddle via a reflection in the force along the tangent.

$$F_i = -\nabla E (R_i)^t + 2 \nabla E (R_i)^{t\parallel} \cdot \hat{\tau}_i \hat{\tau}_i \quad (\text{equation 3.41})$$

Thus, as long as the CI-NEB converges, a crude representation of the MEP is obtained and one of the images is sitting at the saddle point. It is important to highlight that there is no extra cost of turning one of the images into a climbing image since all the images are being relaxed simultaneously (HENKELMAN; UBERUAGA; JÓNSSON, 2000).

3.2 STATISTICAL MECHANICS-ENSEMBLES

Statistical mechanics attempts to describe a macroscopic system from a molecular point of view. For this, it is assumed that the macroscopic quantities can be obtained as averages over a myriad of microstates (ensemble), in a way compatible with macroscopic constraints.

The ensemble is a conceptual collection of systems described by the same set of microscopic interactions and sharing a common set of macroscopic properties, e.g. the same total energy, volume, and number of moles. Once an ensemble is defined, macroscopic observables can be calculated by performing averages over the systems in the ensemble. The main characteristics of the three most common ensembles, the microcanonical, canonical and grand canonical ensembles are described as follow (MCQUARRIE, DONALD ALLAN AND SIMON, 1997).

The most fundamental ensemble, called as *microcanonical ensemble*, represents an ideally isolated system that cannot exchange particles or energy with its surrounding, and whose volume is constant.

Typically, we consider an ensemble of A isolated systems, each with energy E , volume V , and numbers of particles N . Although all the systems have the same energy, they may be in different states because of degeneracy. Let the degeneracy associate with the energy E be $\Omega(E)$ for each state j . Now, let a_j be the number of systems in the ensemble that are in the state j . Because the A systems of the ensemble are distinguishable, the number of ways of having a_1 systems in state 1, a_2 systems in state 2, etc. is given by:

$$W (a_1, a_2, a_3, \dots) = \frac{A!}{a_1! a_2! a_3! \dots} = \frac{A!}{\prod_i a_j!} \quad (\text{equation 3.42})$$

with: $\sum_j a_j = A$

If all A systems are in one particular state, then $a_1 = A, a_2 = a_3 = 0$ and $W = 1$, which is the smallest value W can adopt. On the other hand, when all the a_j are equal, W takes on its largest value. Therefore, W can be taken to be a quantitative measure of the disorder of a system and the entropy is proportional to $\ln W$ according to:

$$S = k_B \ln W \quad (\text{equation 3.43})$$

where k_B is the Boltzmann's constant. This relation also shows the role of the Boltzmann constant, which is to establish a connection between a macroscopic quantity and a quantity of microscopic origin.

Equation 3.43 can be used to derive an expression for the entropy in terms of the system partition function $Q(N, V, \beta)$. The energy and the pressure can be expressed in terms of Q :

$$U = k_B T^2 \left(\frac{\partial \ln Q}{\partial T} \right)_{N, V} = - \left(\frac{\partial \ln Q}{\partial \beta} \right)_{N, V} \quad (\text{equation 3.44})$$

and,

$$P = k_B T \left(\frac{\partial \ln Q}{\partial V} \right)_{N, T} \quad (\text{equation 3.45})$$

The substitution of Equation 3.42 into Equation 3.43 and the use of Stirling's approximation lead to the following equation:

$$S_{ensemble} = k_B A \ln A - k_B \sum_j a_j \ln a_j \quad (\text{equation 3.46})$$

Using the fact that the probability of finding system in the j th state is given by: $p_j = a_j/A$. The entropy of a typical system is given by:

$$S_{system} = \frac{S_{ensemble}}{A} = -k_B \sum_j p_j \ln p_j \quad (\text{equation 3.47})$$

Thus, to derive an expression for S in terms of $Q(N, V, T)$, Equation 3.48 should be substitute into Equation 3.47 resulting in the following equation:

$$p_j(N, V, \beta) = \frac{e^{-\beta E_j(N, V)}}{\sum_i e^{-\beta E_i(N, V)}} = \frac{e^{-\beta E_j(N, V)}}{Q(N, V, \beta)} \quad (2.48)$$

to further obtain:

$$S = \frac{U}{T} + k_B \ln Q \quad (2.49)$$

The main disadvantage of the microcanonical ensemble is that condition of constant total energy is not those under which experiments are performed. In this sense, the **canonical ensemble** reflects more common experimental setups. In this ensemble, the volume, temperature and number of particles are maintained fixed, which characterize a system in thermal contact with an infinite heat source (MCQUARRIE, DONALD ALLAN AND SIMON, 1997).

Coupling the Helmholtz free energy (F) definition ($F = U - TS$) with Equation 3.44 and Equation 3.49, makes possible to get Equation 3.50 for a system at constant temperature.

$$F = -k_B T \ln Q \quad (\text{equation 3.50})$$

The Helmholtz free energy is a characteristic state function of T , V and N . Therefore, the Helmholtz free energy and consequently the partition function is the starting point for the complete treatment of the system.

The **Grand Canonical ensemble** refers to an expanded canonical system where not only the energy but also the number and nature of particles are allowed to be exchanged. In this case, the temperature T , the volume V and the chemical potential μ are fixed.

By analogy with the canonical ensemble, which considers the Helmholtz free energy, the grand potential (Φ_G) is the characteristic state function for the grand canonical ensemble, and it is defined as:

$$\Phi_G(T, V, \mu) = -PV = F(T, V, N) - \mu N \quad (\text{equation 3.51})$$

In the grand canonical ensemble, we denote the partition function as $Z(\mu, V, T)$, and it is given by:

$$Z(\mu, T, V) = \sum_i e^{-\beta(N_i \mu - E_i)} \quad (\text{equation 3.52})$$

Thus, the fundamental relation of this grand canonical ensemble is given by:

$$\Phi_G = -k_B T \ln Z \quad (\text{equation 3.53})$$

Since each of the state functions (entropy, the Helmholtz free energy and the grand potential) are defined from a microscopic perspective by means of their respective partition functions, it is then possible to characterize the macroscopic properties of each system by averaging their microscopic properties (MCQUARRIE, DONALD ALLAN AND SIMON, 1997).

The thermodynamic observable $\langle A \rangle$ can be then calculated in terms of the partition function:

$$\langle A \rangle = \sum_j p_j A_i = \sum_j \frac{A_i e^{-\beta A_j}}{Q} \quad (\text{equation 3.54})$$

The partition function of any ensemble can be expressed as an integral of the appropriate Hamiltonian of the ensemble over the coordinates (\vec{r}^N) and momenta (\vec{p}^N) of all N particles.

$$Q = \frac{1}{h^{3N} N!} \int d\vec{p}^N d\vec{r}^N \exp \left[-\hat{H}(\vec{r}^N, \vec{p}^N) / k_b T \right] \quad (\text{equation 3.55})$$

Thus, Equation 3.54 can be rewritten as follows:

$$\langle A \rangle = \frac{\int d\vec{p}^N d\vec{r}^N A(\vec{r}^N, \vec{p}^N) \exp \left[\hat{H}(\vec{r}^N, \vec{p}^N) / k_b T \right]}{\int d\vec{p}^N d\vec{r}^N \exp \left[\hat{H}(\vec{r}^N, \vec{p}^N) / k_b T \right]} \quad (\text{equation 3.56})$$

The complexity relies on the computational calculation of the averages in the configurational space. Therefore, in the majority of cases, numeral techniques should be used.

3.2.1 Monte Carlo Simulations

One way around to compute an observable is to use a sampling scheme such as the Monte Carlo (MC) method. More specifically, the strategy adopted by Metropolis et al. (METROPOLIS et al., 1953) in 1953 selects a reasonable number of representative points to

ensure an optimal exploration of the system and thus allowing an accurate evaluation of the statistical average.

In this technique, the configurations generated by the Metropolis method are described by a Maxwell Boltzmann distribution. Starting with an initial configuration randomly generated, the MC simulations consist of several millions of random moves that allow an efficient sampling of the selected ensemble. Then, during the simulations, the considered moves include translational and rotational displacements of the molecules, while attempts to insert and to remove molecules ensure a variation in their number. The corresponding random moves are accepted or rejected with appropriate criteria, based on the Metropolis algorithm (FRENKEL; SMIT; RATNER, 1997).

Considering the initial configuration denoted by o (old) of the system \vec{r}^N with a Boltzmann density probability of $\eta(o)$ and $\pi(o \rightarrow n)$ the probability to switch from configuration o to the new one n (new), at equilibrium the average number of accepted moves from o to n must be exactly equal to the number of the reverse moves.

$$\eta(o) \times \pi(o \rightarrow n) = \eta(n) \times \pi(n \rightarrow o) \quad (\text{equation 3.57})$$

The probability $[\pi(o \rightarrow n)]$ can be expressed as the probability $[\alpha(o \rightarrow n)]$ of selecting the new configuration n , multiplied by the probability $[\text{acc}(o \rightarrow n)]$ of accepting this trial move.

$$\pi(o \rightarrow n) = \alpha(o \rightarrow n) \times \text{acc}(o \rightarrow n) \quad (\text{equation 3.58})$$

Considering a symmetric probability $[\alpha(o \rightarrow n) = \alpha(n \rightarrow o)]$, of selection from o to n and vice-versa, Equation 3.57 turns to:

$$\frac{\text{acc}(o \rightarrow n)}{\text{acc}(n \rightarrow o)} = \frac{\eta(n)}{\eta(o)} = \exp\{-\beta[U(n) - U(o)]\} \quad (\text{equation 3.59})$$

where $U(n)$ is the initial potential energy calculated, $U(o)$ is the new potential energy calculated and $\beta=1/kT$.

Thus, according to the Metropolis algorithm the trial move ($o \rightarrow n$) is accepted with a probability:

$$\text{acc}(o \rightarrow n) = \min\left(1, \frac{\eta(n)}{\eta(o)}\right) = \min(1, \exp[-\beta\Delta U]) \quad (\text{equation 3.60})$$

The attempt is thus accepted if the energy of the new configuration is lower than that of the old one. If this is not the case, the Boltzmann factor ($\exp(-\beta\Delta U)$) is calculated and compared with a random number (Ranf), which is generated in the interval $[0,1]$. If Ranf is higher than $\exp(-\beta\Delta U)$, the new configuration is accepted, otherwise it is rejected. This process continues for the defined number of steps in order to generate an ensemble of configurations that obey to the Boltzmann statistical rule. In order to approach the equilibrium in a most efficient way, the acceptance rate is usually fixed to be about 40-50%. For accurate statistical results, it is a good practice to equilibrate the system first and then the averages of interest calculated over several millions of configurations.

A typical Monte Carlo simulation consists of the following, randomly selected, trial moves. The most standard MC trials are thus the translation, rotation and insertion/deletion, partial/full regrow (FRENKEL; SMIT; RATNER, 1997; LEACH, 2001).

In the translation move, the position of the center of mass of a randomly selected molecule i in the system is displaced by a random vector:

$$\vec{r}(n) = \vec{r}(o) + \Delta r(\text{Ranf} - 0.5) \quad (\text{equation 3.61})$$

where Δr is the maximum displacement and Ranf a uniformly distributed random number between 0 and 1. This parameter has to be chosen to have a reasonable fraction of accepted moves. For small displacements, the movement is more likely to be accepted however a larger number of steps is required for an efficient sampling of the phase space. In contrast if Δr is very large, most of the trial moves will be rejected. Generally, the optimal value of Δr is selected in such a way that approximately the 50% of the trial moves is accepted (FRENKEL; SMIT; RATNER, 1997) (acceptance probability given by Equation 3.60).

The rotation move is considered for molecules with more than one interaction center (FRENKEL; SMIT; RATNER, 1997). It consists of assigning linear rotation transformations in the position vector where either the x, y or z axis of the coordinate system can be selected as a rotation axis. For example, a rotation along the x axis can be expressed as:

$$\vec{r}(n) = R_x \cdot \vec{r}(o) = \begin{bmatrix} 1 & 0 & 0 \\ 0 & \cos\Delta\theta & -\sin\Delta\theta \\ 0 & \sin\Delta\theta & \cos\Delta\theta \end{bmatrix} \cdot \vec{r}(o) \quad (\text{equation 3.62})$$

where $\vec{r}(o)$ and $\vec{r}(n)$ are the vectors that contain the coordinates of a molecule before and after the rotation, and $\Delta\theta$ the rotated angle. The maximum rotation angle is chosen such that on average a 50% of rotations are accepted (according to Equation 3.60).

In the grand-canonical ensemble, the number of guest molecules present in the system is not constant. Thus, the insertion of a molecule placed in a random position and orientation also follows a Metropolis scheme. The new configuration is accepted with the probability given by Equation 3.63:

$$acc(o \rightarrow n) = \min\left(1, \frac{\beta f V}{N + 1} \exp(-\beta \Delta U)\right) \quad (\text{equation 3.63})$$

where f is the fugacity of the molecule and V is the volume of the simulation box.

For complex adsorbates, which have a high degree of flexibility or large size, various statistical bias techniques have been developed to increase the acceptance rate of some trial moves that speeds up the Monte Carlo simulation by allowing a more efficient sampling of the configurational space. As a typical illustration, the configurational bias technique (CBMC) based on a scheme derived by Rosenbluth (FRENKEL; SMIT; RATNER, 1997) consists of segment the molecule in pre-defined beads. The first bead is then randomly inserted according to the Metropolis acceptance rule for an insertion move and then the rest of molecule is constructed by insertion trial moves obeying pre-defined intramolecular interactions. Typically, in this thesis, the CBMC was considered for the adsorption of CWAs.

Similarly, when a molecule is randomly removed, the new configuration is accepted with the probability given by Equation 3.64:

$$acc(o \rightarrow n) = \min\left(1, \frac{N}{\beta f V} \exp(-\beta \Delta U)\right) \quad (\text{equation 3.64})$$

The regrowth move trial is similar to the CBMC move. The molecules, which are discretized in bead, have their beads reorganized according to their intramolecular interactions. There are different possibilities for regrowing a molecule: removal of the molecule and their insertion back at a random position (full regrowth) or the partial removal of some of the beads followed by their regrowth (partial regrowth).

Another property of interest is the differential molar enthalpy of adsorption ΔH_{ads} which is commonly evaluated through the fluctuations over the number of molecules in the system N and the internal energy U .

$$\Delta H_{ads} = RT - \frac{\langle U \cdot N \rangle - \langle U \rangle \langle N \rangle}{\langle N^2 \rangle - \langle N \rangle^2} \quad (\text{equation 3.65})$$

This method assumes an ideal behavior of the gas phase, where considerably large number of steps are needed to get a reasonable statistic for the averages in this equation, principally when applied in the limit of low coverage. Alternatively, the use of a revised Widom's test particle approach employed in the canonical ensemble provides a more accurate strategy to obtain the heat of adsorption (VLUGT et al., 2008).

3.2.2 Interatomic potentials

The energy of the global system is calculated by an expression which has four general terms:

$$E_{tot} = E_{bond} + E_{angle} + E_{torsion} + E_{nb} \quad (\text{equation 3.66})$$

$$E_{tot} = \sum \frac{k_i}{2} (l_i - l_{i,0})^2 + \sum \frac{k_i}{2} (\theta_i - \theta_{i,0})^2 + \sum \frac{V_n}{2} (1 + \cos(n\omega))^2 + E_{nb}$$

where, the first term (E_{bond}) accounts for the interaction between pairs of bounded atoms, modelled by a harmonic potential, where l is the bond length and the k_i term is the force constant. The second term (E_{angle}) is a summation over all bond angles in the molecule. The third term ($E_{torsion}$) accounts for the energy changes as a bond rotates. The last term (E_{nb}) corresponds to the non-bonded interactions.

The non-bond terms are usually expressed in two terms, one comprising electrostatic interactions and the other van der Waals interactions. These interactions are modelled using a Coulomb potential term for electrostatic interactions and Lennard-Jones potential for van der Waals interactions (LEACH, 2001). The van der Waals interactions are composed by the attracting potential also called dispersive contribution and the repulsive contribution.

Appropriate forms and parameters of a mathematical function need to be selected with the aim to reproduce as fairly as possible the potential energy of the adsorbate/adsorbent

interactions. It is customary to assume that the pairwise interactions are additive and that they can be modelled by:

$$E = E_P + E_E + E_D + E_R \quad (2.67)$$

where, the polarization (E_P), the dispersion (E_D) and the repulsion (E_R) interactions are considered as non-specific interactions energy terms, while the electrostatic term (E_E) is classified as a specific interaction energy term since it is involved in only certain adsorbate/adsorbent system.

The polarization interactions arise as an effect of the proximity of the adsorbent electric field with the adsorbate. The resulting polarization energy is given by:

$$E_P = -\frac{1}{2} \sum_i \alpha_i E_i^2 \quad (\text{equation 3.68})$$

where E is the electric field created by the adsorbent and α is the dipole polarizability of the adsorbate.

The electrostatic interactions are often calculated using Coulomb's law:

$$E_E = \sum_{i,j} \frac{1}{4\pi\epsilon_0} \frac{q_i q_j}{r_{ij}} \quad (\text{equation 3.69})$$

where q_i and q_j are the charges carried by atoms of the adsorbate and the adsorbent, respectively, and ϵ_0 is the vacuum permeability (FRENKEL; SMIT; RATNER, 1997). The Ewald summation (EWALD, 1921) is the most used method to account the electrostatic interactions.

Considering that only minor contributions of non-bonded interactions to the overall potential are obtained for large interatomic distances, it is usual to either truncate or shift the potential to a zero value after a cutoff distance (r_{cutoff}). Different cutoff values should be tested and the shortest value from which no modification in the observables is noticed should be picked. However, the value of 12 Å is a default value normally employed in solid state.

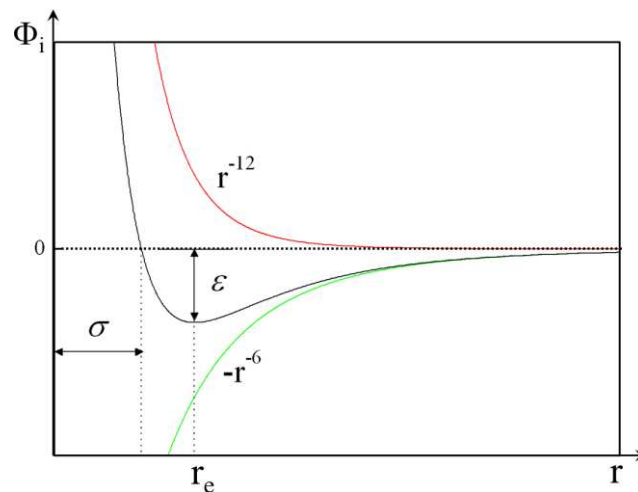
Another important point in MC simulation is the use of periodic conditions. Furthermore, in order to avoid the possibility of a particle to interact with their own mirror image, the shortest cell dimensions should be of at least double the size of the considered cutoff distance.

In most of the adsorbate/adsorbent interatomic potentials reported in the literature, the dispersion and repulsion terms are associated and converted to a Lennard–Jones (LJ) 12–6 potential energy type function.

$$E_R = \sum_i \sum_{j>i} 4\varepsilon_{ij} \left[\left(\frac{\sigma_{ij}}{r_{ij}} \right)^{12} - \left(\frac{\sigma_{ij}}{r_{ij}} \right)^6 \right] \quad (\text{equation 3.70})$$

The LJ 12–6 potential contains just two adjustable parameters: the collision diameter σ_{ij} (the separations for which the energy is zero) and the depth of the potential well (ε_{ij}), illustrated in Figure 3.3.

Figure 3.3 - Plot of the Lennard–Jones potential function.



Source: Adapted from (LEACH, 2001).

Note that in the LJ potentials the attractive part is modeled by functions (r^{-6}) and the repulsive part by r^{-12} .

The cross-term parameters for the pairs ij are usually obtained using mixing rules considering the individual ε_{ij} and σ_i parameters assigned to each atom, which are related to their polarizability and size respectively. In the case of the Lorentz-Berthelot mixing rule (LORENTZ, 1881) these parameters are obtained as follows:

$$\sigma_{ij} = \frac{\sigma_i + \sigma_j}{2} , \quad \varepsilon_{ij} = \sqrt{\varepsilon_i \varepsilon_j} \quad (\text{equation 3.71})$$

The LJ parameters for all atoms of the adsorbent are usually taken from generic force fields available in the literature, more particularly Universal Force Field (UFF) (RAPPÉ et al., 1992) and DREIDING (MAYO et al., 1990). Such popular force fields that contain LJ parameters for the majority of the atoms of the periodic table are revealed to be surprisingly well transferable for treating the adsorption in a wide class of porous solids. Regarding the atoms of the adsorbate, the corresponding LJ parameters are usually obtained from a fit of the experimental vapour liquid equilibrium data as, for instance, in the well-known transferable potentials for phase equilibria (TraPPE) force field (MARTIN; SIEPMANN, 1998). In such force fields, the adsorbates can be further modelled as either rigid or flexible molecules.

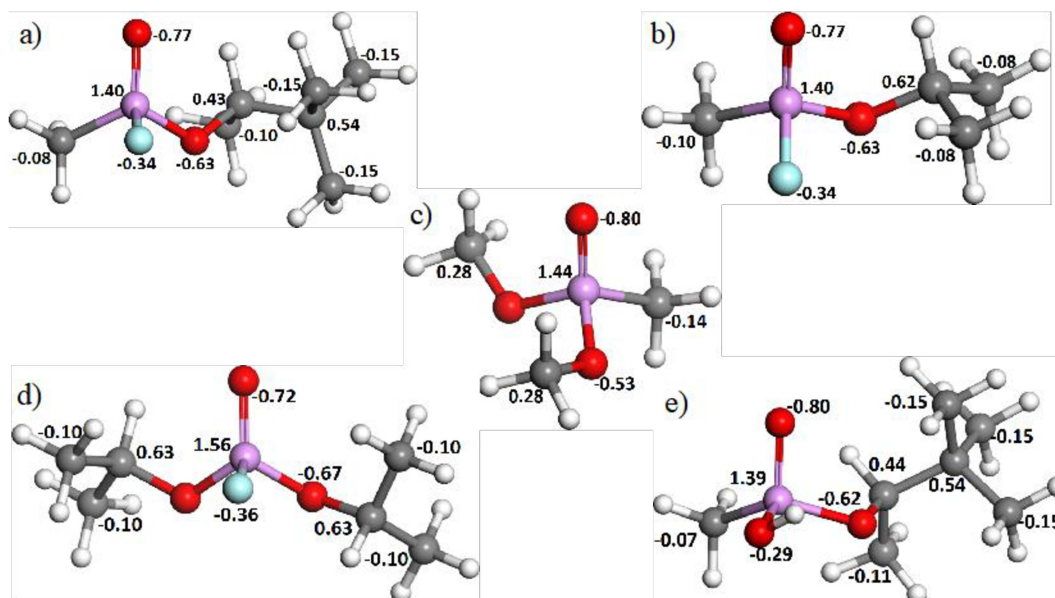
3.2.3 Microscopic description of the host Metal-Organic Frameworks

In this work, the atomic positions of all MOF frameworks were taken from the crystal structures previously solved experimentally. All these structures were further geometry optimized at the DFT level (DELLEY, 2000) (see Chapter 4). Each atom of these materials was treated by a single charged LJ center as it is usually operated in the field of porous materials and modelled as rigid frameworks. The LJ parameters for the atoms of MOFs are usually taken from generic forcefields available in the literature, in particular the Universal (UFF) (RAPPÉ et al., 1992) and DREIDING (MAYO et al., 1990) force fields for the description of the inorganic and organic nodes respectively. Finally, the Mulliken (MULLIKEN, 1955) partial charges for all atoms of the MOF frameworks were further obtained using single point energy calculations (see the annex in Chapter 4).

3.2.4 Microscopic description of the adsorbates

The CWAs, Sarin, Soman and DMMP molecules were described by a united atom representation including LJ point charges with parameters taken from the TraPPE force field, reported by Sokkalingam et al. (SOKKALINGAM et al., 2009). Same united atom representations were considered for the simulants DIFP and pinacolyl methylphosphonate (PMP) molecules with parameters taken from the previous work reported by Vishnyakov et al. (VISHNYAKOV et al., 2011) and Sokkalingam et al. (SOKKALINGAM et al., 2009), respectively. These molecules were considered as a rigid body. The charges assigned to all atoms of these molecules are illustrated in Figure 3.4.

Figure 3.4 - Partial charges used for the united-atom models considered for the CWAs molecules: (a) Soman, (b) Sarin, (c) DMMP, (d) DIFP and (e) PMP.



Source: Elaborated by the author (2019).

4 COMPUTATIONAL EVALUATION OF THE CWAS CAPTURE PERFORMANCES OF ROBUST MOFs

This chapter exposes the computational evaluation of the CWA capture performances of a series of MOFs. Priority was given to explore MOFs based on Zr- and Ti-metal ions, showing different pore size/topology and incorporating diverse adsorption sites, that have been proved to be water stable. Twenty-five chemical stable MOFs were selected to get insight into the adsorption properties of the nerve agents sarin and soman as well as their most common simulants used in experiments, i.e. DMMP, DIFP and Pinacolyl methylphosphonate (PMP) in terms of uptake, enthalpy and preferential adsorption sites. The computational methodology was defined as follows:

The structural models for all MOFs were taken from the literature and were further geometry optimized at the Density Functional Theory (DFT) level keeping the experimental unit cell parameters fixed. These calculations were performed using the PBE functional at generalized gradient approximation (PERDEW; BURKE; ERNZERHOF, 1996) combined with the Double Numeric basis set with Polarization functions (DNP) (HEHRE; DITCHFIELD; POPLE, 1972) on all atoms as implemented in DMol3 package (DELLEY, 2000). Using the same program, the Mulliken partial charges for all atoms of the MOF frameworks were further obtained using single point energy calculations (MULLIKEN, 1955).

Grand Canonical Monte Carlo (GCMC) simulations were performed at 298 K for all MOFs and CWAs selected in this work for a series of fugacity for the CWAs up to 5000 kPa in order to estimate the saturation capacity for each molecule. The simulation box considered for all MOFs was defined in such a way that all a, b and c dimensions were longer than 24 Å. The LJ cross parameters corresponding to the interactions between the CWAs and the MOFs framework were obtained using the Lorentz-Berthelot mixing rules. Short-range dispersion forces described by LJ potentials were truncated at a cutoff radius of 12 Å, whereas long-range electrostatic interactions were handled using the Ewald summation technique. For each state point, 2×10^8 Monte Carlo steps have been used for both equilibration and production runs. The adsorption enthalpy at low coverage for each molecule was calculated using the revised Widom's test particle insertion method (VLUGT et al., 2008). To gain insight into the arrangement of the CWAs in the pores of the MOFs, the CWA/CWA and CWA/MOF radial distribution functions (RDFs) were obtained by averaging over the whole configurations generated during the GCMC simulations.

Quantum calculations were performed using the codes available in the Quantum-Espresso package, (GIANNOZZI et al., 2009) which implements the DFT (KOHN; SHAM, 1965; RAJAGOPAL; CALLAWAY, 1973) at generalized gradient approximation (PERDEW; BURKE; ERNZERHOF, 1996) under periodic boundary conditions using plane wave functions as basis set (MAKOV; PAYNE, 1995). Vanderbilt (VANDERBILT, 1990) ultrasoft pseudopotentials were used to describe the ion cores of atoms. This methodology was applied to understand to in-depth characterize the nature of the CWA/MOF interactions. A Bader charge analysis was conducted on the MOF/CWA systems using a grid-based algorithm (HENKELMAN; ARNALDSSON; JÓNSSON, 2006) to analyze the potential charge transfer between the CWAs and the MOFs. The charge in all atoms of the system was defined as the difference between the valence charge and the Bader charge.

As a first stage, pore diameter, free pore volume and the N₂-accessible surface area were calculated from the crystal structure of all MOFs with the aim to use them to correlate with their CWA adsorption properties.

Secondly, GCMC simulated saturation uptakes at 298 K for all MOFs with respect to sarin, soman, DMMP and DIFP were calculated using a pressure of 5000 kPa. These performances are further correlated with the features of the MOFs. It was evidenced that the uptake of each CWA considered individually correlates rather well with the N₂- accessible surface area calculated for the MOFs, but the correlation is even better using the free pore volume as a descriptor of the MOFs. For this reason, a new term which is given by a relation between the free pore volume of the MOFs and the volume of the bulkier CWA, i.e. soman, and the other molecules was introduced. As a further step, this computational database has been used to build model structure-adsorption performances in order to identify the key parameters of the MOFs that drive the CWA capture.

Thirdly, the GCMC simulations were performed to evidence the preferential adsorption sites of CWAs and the nature of the CWA/MOF interactions by a careful analysis of the corresponding radial distribution functions averaged over all the MC configuration. This was completed by further DFT calculations to calculate the bader charges for the isolated and adsorbed CWAs in the structures.

Finally, the choice of reliable simulants to accurately mimic the adsorption behavior of real toxic molecules in MOFs has been further discussed and in particular it has been established that soman is better described considering the pinacolyl methylphosphonate rather than the standard dimethyl-methyl-phosphonate and diisopropyl fluorophosphate simulants.

In the following sections, the main results obtained in these different steps are summarized.

4.1 CWA UPTAKE AND ENERGETIC PERFORMANCES IN MOFs

The Zr-MOFs selected in this study can be categorized into five types of materials based on the connectivity of the Zr_6 nodes. The node connectivity ranges, which is the number of ligands coordinated to the secondary unit build, from nominally 12-connected [UiO-66-(Zr) (CAVKA et al., 2008), UiO-66-(Zr)-Cl, UiO-66-(Zr)-(OH)₂, UiO-66-(Zr)-CO₂H, UiO-66-(Zr)-NO₂, UiO-66-(Zr)-NH₂ (YANG et al., 2011b), UiO-67-(Zr), UiO-68-(Zr) (CAVKA et al., 2008), Zr₆-AZO-BDC (SCHAATE et al., 2012) and MIL-200 (WANG et al., 2018)] in which, ideally, all the Zr atoms are fully coordinated to organic linkers, 11-connected [UiO-66-(Zr)-defects₃ (ROGGE et al., 2016)], 10-connected [UiO-66-(Zr)-NH₂-defects₆ (ROGGE et al., 2016)], 8-connected [NU-1000 (MONDLOCH et al., 2013) and MIP-200-OH-H₂O (WANG et al., 2018b)] and 6-connected [MIL-140D (GUILLERM et al., 2012), MIL-140E and MIL-140G (SERRE, 2018; ZHANG et al., 2019), MOF-808-A, MOF-808-F, MOF-808-P and MOF-808-OH-H₂O (LIANG et al., 2014)]. The Ti-MOFs, MIL-125-(Ti) and MIL-125-(Ti)-NH₂ (DAN-HARDI et al., 2009), MIP-177 (WANG et al., 2018b) are 12-connected and the activated structure MIP-177-OH-H₂O (WANG et al., 2018b) 8-connected (see structures in the annex provided at the end of this chapter). The structures of MIP-177-OH-H₂O, MIP-200-OH-H₂O, MOF-808-OH-H₂O and defective UiO-66-(Zr) and UiO-66-(Zr)-NH₂ were preliminary saturated by hydroxyl and water groups. These atoms were added to the metal atoms of the inorganic nodes.

Table 4.1 reports calculated textural parameters for the MOFs mentioned above, as the pore diameter, free pore volume, the N₂-accessible surface area as well as ϕ corresponding to the ratio between the free pore volume and the bulk volume.

Table 4.1 - Calculated parameters for the MOFs used in this work.

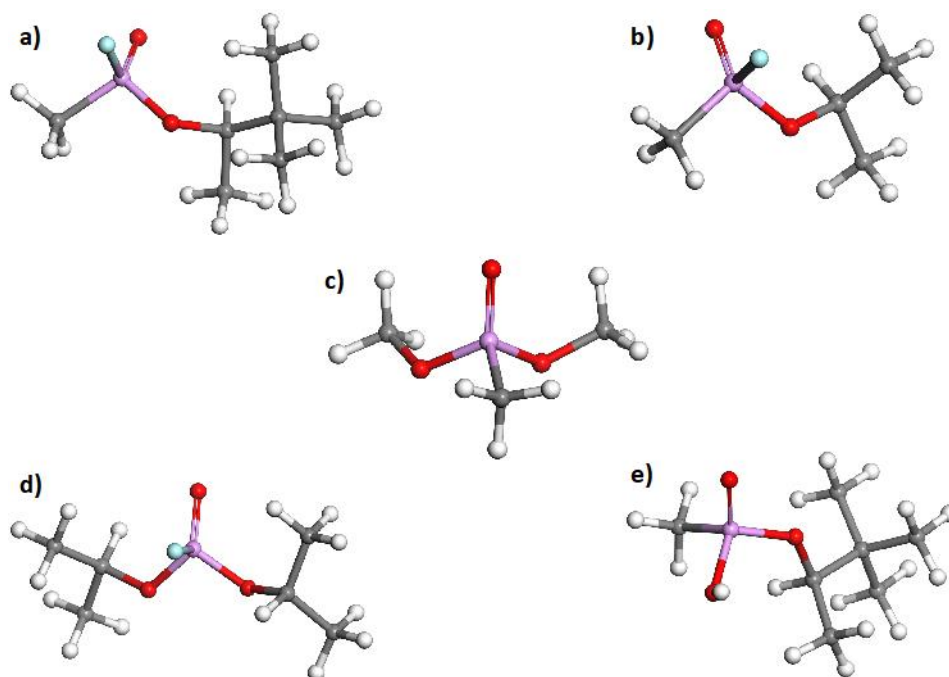
MOF^a	Pore Diameter (Å)	Free Volume (cm ³ g ⁻¹)	N ₂ -accessible Surface Area (m ² g ⁻¹)	φ (vol free / bulk vol)
MIL-125-Ti	11.825	0.832831	1177.726	0.6869
MIL-125-Ti-NH ₂	10.575	0.766283	856.7341	0.6672
MIL-140D	6.675	0.451392	842.6429	0.5563
MIL-140E	6.575	0.526423	1012.35	0.5678
MIL-140G	7.225	0.593178	1145.352	0.6016
MIP-177	12.075	0.424009	665.6882	0.5307
MIP-177-OH-H ₂ O	12.775	0.419972	609.0819	0.5354
MIP-200	13.125	0.58119	1271.794	0.6260
MIP-200-OH-H ₂ O	14.225	0.559583	1107.561	0.6349
MOF-808-A	16.425	0.835779	1716.062	0.7263
MOF-808-F	19.275	1.850036	3905.768	0.7586
MOF-808-OH-H ₂ O	18.425	0.996946	1639.882	0.7674
MOF-808-P	13.525	0.74394	1437.384	0.6873
NU-1000	28.375	1.660864	3063.163	0.8089
UiO-66(Zr)Cl	7.425	0.405001	279.3534	0.5604
UiO-66(Zr)NH ₂	6.825	0.231553	156.9568	0.5670
UiO-66(Zr)NO ₂	5.725	0.374718	422.4698	0.5346
UiO66(Zr)NH ₂ -defects6	7.175	0.464642	727.0506	0.5810
UiO-66(Zr)	7.875	0.465402	284.4096	0.5721
UiO-66(Zr)(OH) ₂	7.475	0.41349	293.0811	0.5666
UiO-66(Zr)CO ₂ H	6.175	0.367697	208.1366	0.5230
UiO-66(Zr)defects3	7.975	0.564295	790.9662	0.6307
UiO-67(Zr)	12.275	1.036771	2915.656	0.7342
UiO-68(Zr)	13.775	1.750584	4074.305	0.8093
Zr ₆ -AzoBDC	13.825	1.372035	3440.579	0.7833

Source: Elaborated by the author (2019).

^aSee Annex.

The saturation capacities for all the MOFs mentioned above were simulated for the molecules listed in Figure 4.1.

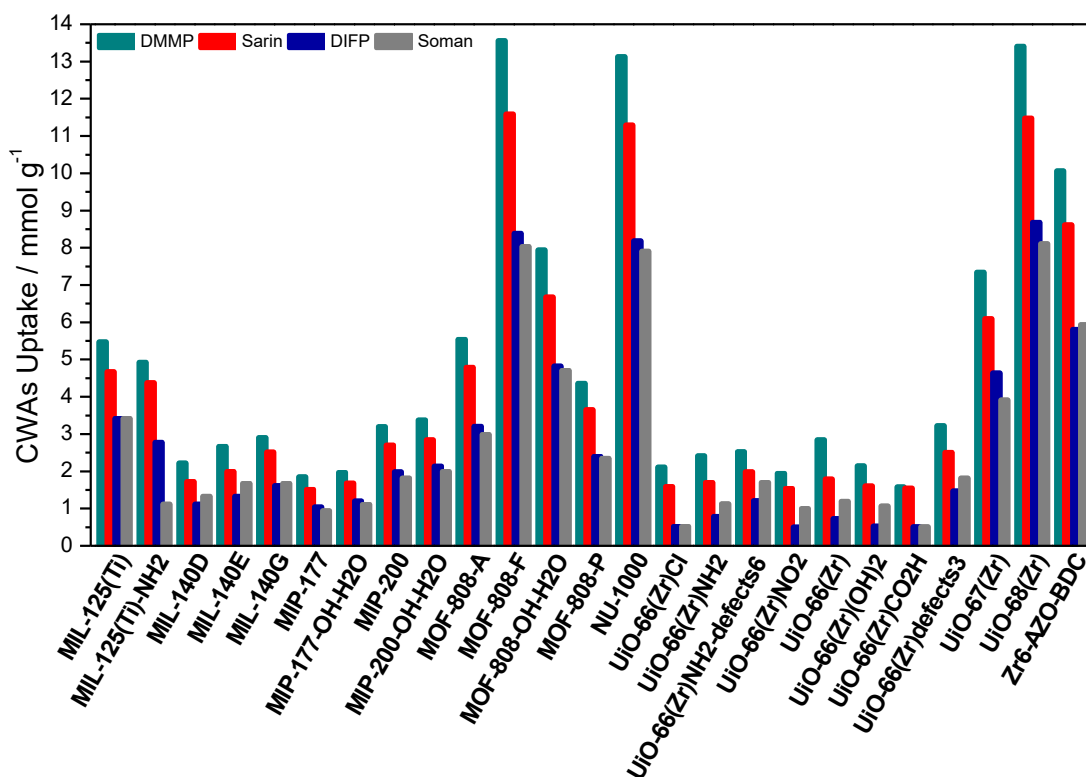
Figure 4.1 - Illustration of the CWAs molecules: (a) Soman, (b) Sarin, (c) DMMP, (d) DIFP and (e) PMP considered in this work.



Source: Elaborated by the author (2019).

One can observe that the best materials for CWA capture are MOF-808s, NU-1000, UiO-68(Zr) and Zr-Azo-BDC (see Figure 4.2). This conclusion remains valid for all real CWAs and their simulants with adsorption uptakes above 2 mmol g^{-1} . This level of performances significantly surpasses that of previously reported MOFs and other standard porous materials. Typically, the activated carbons adsorb much lower amounts of CWAs. As an illustration Kowalczyk *et al.* (KOWALCZYK *et al.*, 2013), demonstrated that pitch-based P7 Activated Carbon Fiber (ACF) and the commercialized Norit activated carbons adsorb only $0.806 \text{ mmol g}^{-1}$ and $0.161 \text{ mmol g}^{-1}$ of DMMP respectively. In addition, the current activated carbon ASZM-TEDA showed a sarin adsorption uptake of 0.04 mg m^{-3} (OUDEJANS, 2014). Regarding MOFs, as mentioned in the chapter 1, only a very few studies have been reported on their CWA adsorption performances. It is possible to cite the sodalite-type MOF, NENU-11(Cu) (MA *et al.*, 2011b), MOF-5(Zn) (NI *et al.*, 2007), NU-1000(Zr) (ASHA; SINHA; MANDAL, 2017) and UiO-67(Zr) (ASHA; SINHA; MANDAL, 2017) that were shown to adsorb 1.92 mmol g^{-1} , 7.3 mmol g^{-1} , 1.7 mmol g^{-1} and 0.90 mmol g^{-1} of DMMP respectively.

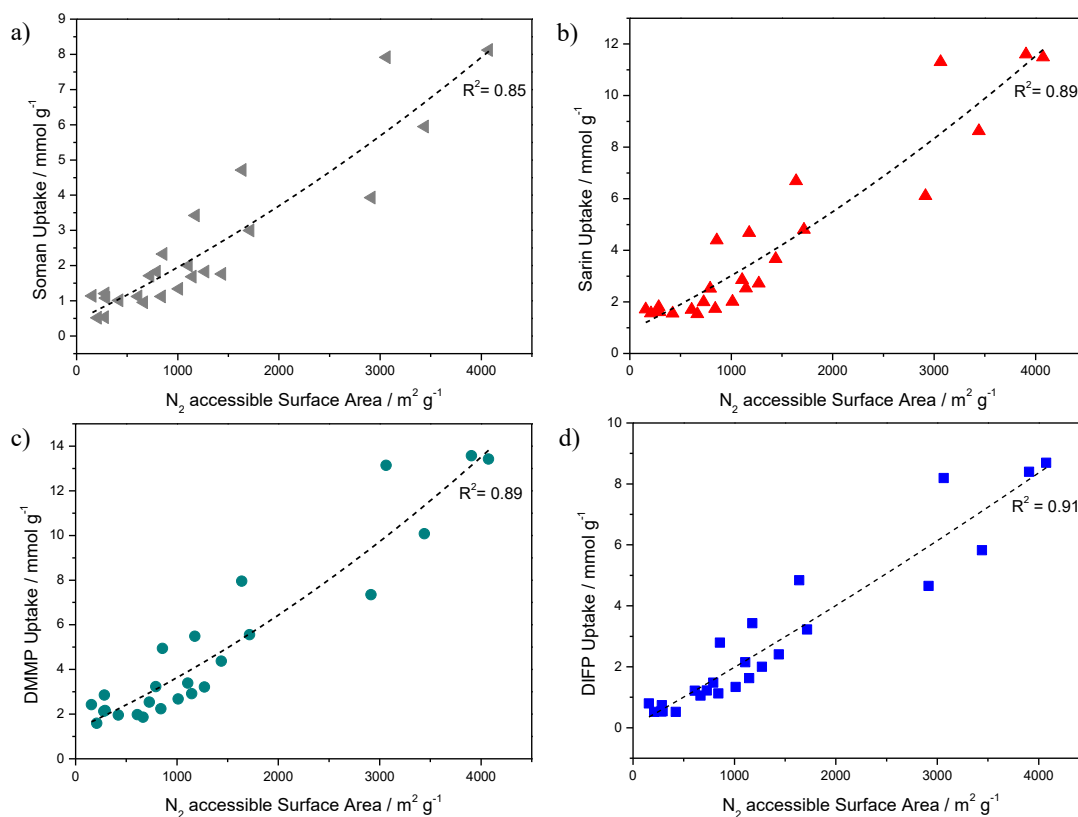
Figure 4.2 - GCMC simulated saturation uptakes at 298 K for all MOFs with respect to sarin, soman, DMMP and DIFP calculated using a pressure of 5000 kPa.



Source: Elaborated by the author (2019).

As a further step, I concentrated my effort to identify the features of the MOFs at the origin of these high CWA uptakes. The uptake of each CWA considered individually was shown to correlate rather well with the N_2 -accessible surface area calculated for the MOFs (c.f. Figure 4.2 and Table 4.1). Figure 4.3 illustrates the GCMC simulated uptakes for all CWAs in MOFs as a function of the N_2 -accessible surface area of the MOF, with the correlation coefficients R^2 varying from 0.84 to 0.90. These correlations showed the same tendency for all CWAs, where, as larger is the surface area higher is the capacity of adsorbed the molecule. However, the structures: Zr_6 -AZO-BDC, NU-1000 and UiO-67(Zr) did not fit very well on this correlation, since lower values were found for the correlation coefficient, indicating that the N_2 -accessible surface area is most probably not the best parameter to be correlated with the capacity of stockpiling CWA in MOFs.

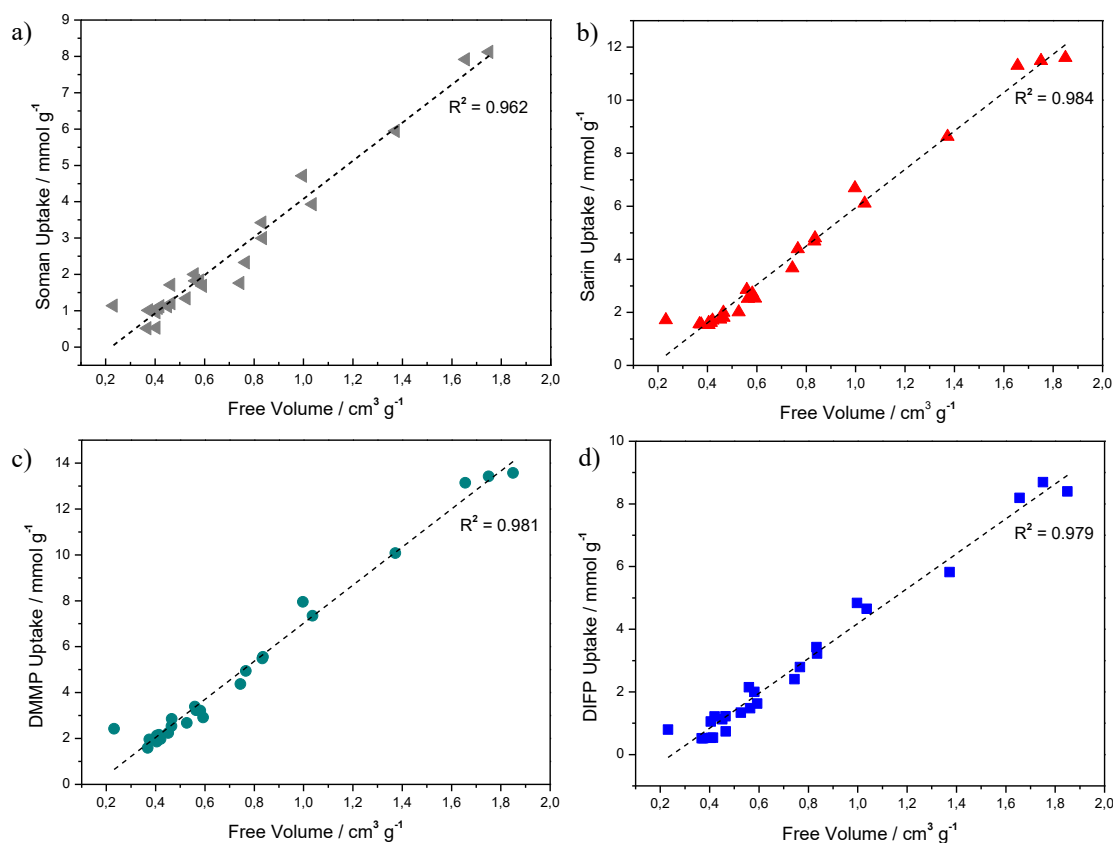
Figure 4.3 - GCMC simulated uptakes for all CWAs in MOFs as a function of the N₂-accessible surface area of the MOFs (reported in Table 4.1).



Source: Elaborated by the author (2019).

Then, the correlation of the uptake for all CWAs in MOFs as a function of the free pore volume of the MOFs was evaluated. Figure 4.4 shows that it is much better to use the free pore volume as a descriptor of the MOFs, with correlation coefficients higher than 0.96, indicating that the adsorption process of CWAs is accurately correlated to the space available in the pores of this materials.

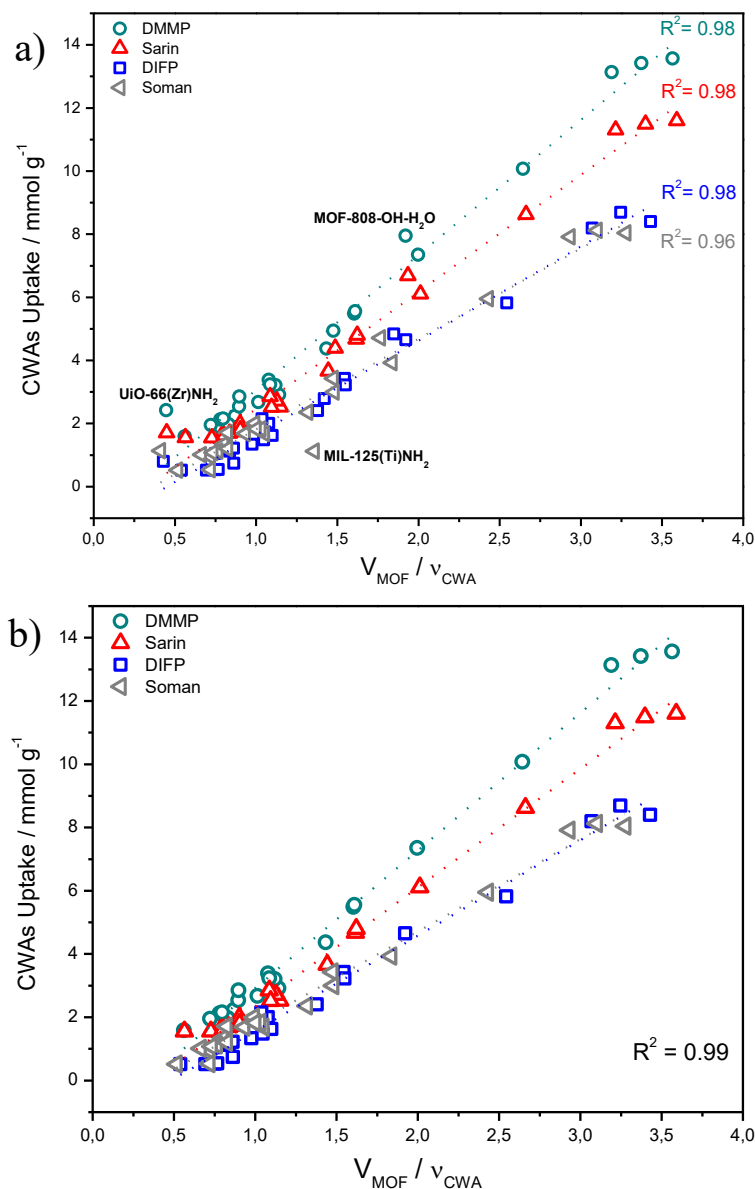
Figure 4.4 - GCMC simulated uptakes for all CWAs in MOFs as a function of the free volume of the MOFs (reported in Table 4.1).



Source: Elaborated by the author (2019).

Figure 4.5 further illustrates the correlation for all CWAs between the uptake capacity of the MOF with the fraction free pore volume of the MOF/volume of the adsorbed molecule ($V_{\text{MOF}}/V_{\text{CWA}}$). One can notice that excluding the materials MOF-808-OH-H₂O, MIL-125(Ti)NH₂ and UiO-66(Zr)NH₂ (Figure 4.5b) was obtained a very good coefficient of correlation of 0.99. Indeed, the adsorption uptakes also depend on the CWAs volume, where the highest loading is found for DMMP followed by sarin, DIFP and lastly soman.

Figure 4.5 - Structure-adsorption uptake relationship for CWAs in MOF (a) for all studied MOFs and (b) where the materials MIL-125(Ti)NH₂, MOF-808-OH-H₂O and UiO-66(Zr)NH₂ were removed.

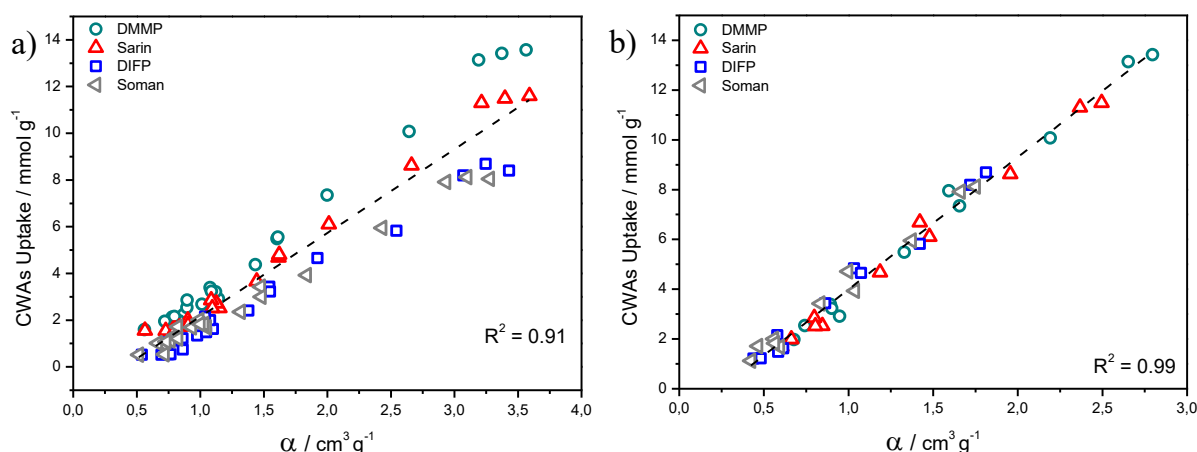


Source: Elaborated by the author (2019).

In order to obtain a more generic correlation, another geometric descriptor labelled as α was introduced. It is given by the following expression: $\alpha = \left(\frac{V_{MOF}}{v_{Soman}} \right)$, where V_{MOF} corresponds to the free pore volume of the MOF, v_{Soman} and v_{CWA} are the volume of the bulkier CWA, i.e. soman, and the other molecules respectively. Figure 4.6a shows the correlation for all studied MOFs, where the correlation coefficient of 0.91 can be explained by the fact that

some MOFs presents a loading capacity for DMMP slightly higher than for sarin and soman. Thus, Figure 4.6b evidences an excellent correlation between the uptakes and α for MIL-125-Ti, MIL-140G, MIP-177-OH-H₂O, MIP-200-OH-H₂O, NU-1000, MOF-808-OH-H₂O, UiO66-NH₂-defects6, UiO66-Zr-defects3, UiO-67, UiO-68 and Zr-AzoBDC (correlation coefficient R^2 of 0.99). This structure-adsorption uptake performance relationship emphasizes that the capacity of stockpiling CWA in MOFs is predominantly governed by a pore filling mechanism, the higher porosity leading to the higher CWA uptake. Typically, the best materials UiO-68(Zr) and MOF-808s show the highest free pore volumes of 1.75 and 1.85 cm³ g⁻¹ respectively (see Table 4.1).

Figure 4.6 - Structure-adsorption uptake relationship for CWAs in MOF (a) for all studied MOFs and (b) for MIL-125-Ti, MIL-140G, MIP-177-OH-H₂O, MIP-200-OH-H₂O, NU-1000, MOF-808-OH-H₂O, UiO66-NH₂-defects6, UiO66-Zr-defects3, UiO-67, UiO-68 and Zr-AzoBDC.

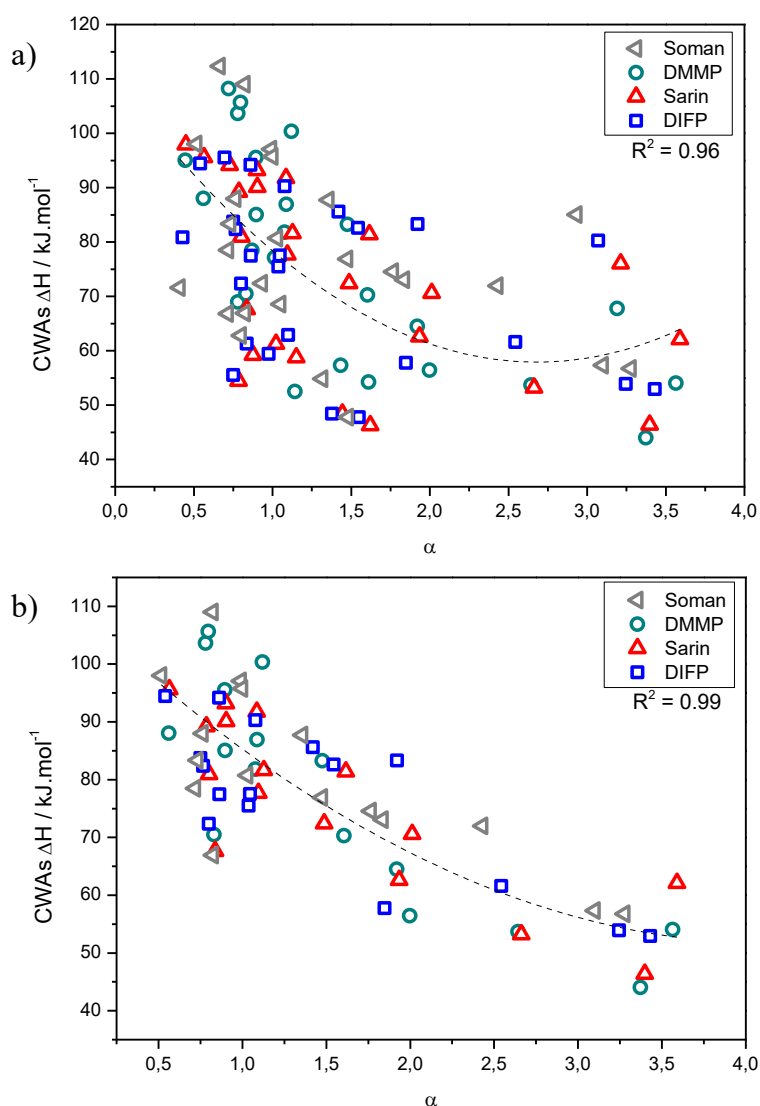


Source: Elaborated by the author (2019).

I further evidenced that the calculated adsorption enthalpy is higher for all CWAs in the case of the MOFs showing the lowest free pore volume, although a direct correlation was not found since the chemical features of the MOFs also impact the CWA/MOF interactions (Figure 4.7). This observation is consistent with the systematic computational study reported by Agrawal *et al.*, which demonstrated that the MOFs with the pore limiting diameters in the range of 6-8 Å show the highest affinity for Sarin (AGRAWAL *et al.*, 2018). Even though a certain degree of scatter exists, the trend shows that each adsorbate occupies about the same pore volume for a given relative pressure. One clearly sees that more confinement induces higher interaction energy, as it is usually observed for many guests adsorbed in porous materials. It is

to be noted that while a linear fitting was used to correlate the results described above, in this analysis (Figure 4.7) was performed a polynomial fitting of order 2 with a fix intercept at 110.

Figure 4.7 - GCMC simulated adsorption enthalpy as a function of α (a) for all studied MOFs and (b) for MIL-125-Ti, MIL-125-Ti(NH₂), MIP-177-OH-H₂O, MIP-200, MIP-200-OH-H₂O, MOF-808-F, MOF-808-OH-H₂O, UiO66-Cl, UiO66-NH₂-defects6, UiO66-Zr, UiO66-Zr(OH)₂, UiO66-Zr(CO₂H), UiO66-Zr-defects3, UiO-67, UiO-68 and Zr-AzoBDC.

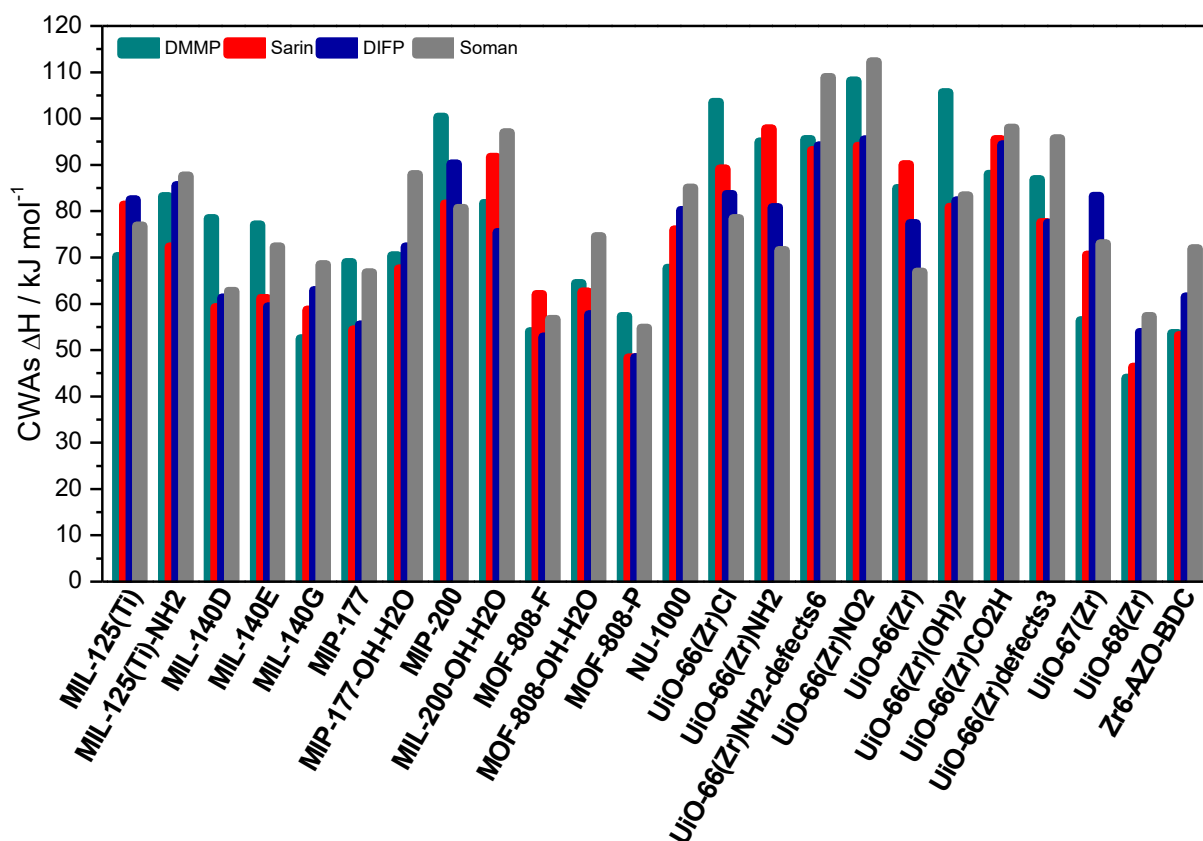


Source: Elaborated by the author (2019).

Interestingly, the calculated CWA adsorption enthalpies (Figure 4.8) were shown to be spread in a relatively large domain reaching for some MOFs very high values up to -110 kJ mol^{-1} . The highest values were obtained for soman, DIFP and DMMP in UiO-66(Zr)NO₂, which

has the lower cavity diameter (5.725 Å) of the studied MOFs, and for sarin in UiO-66(Zr)NH₂ (6.825 Å). On the other hand, the lowest values are gotten for DMMP and sarin in UiO-68(Zr) (13.775 Å) and DIFP and soman in MOF-808-P (13.525 Å) (c.f Table 4.1 and Figure 4.8).

Figure 4.8 - GCMC simulated adsorption enthalpy at 298 K for all MOFs with respect to sarin, soman, DMMP and DIFP calculated at low coverage.



Source: Elaborated by the author (2019).

The strength of interactions obtained for these screened MOFs is significantly higher than the unique value reported so far for a MOF, i.e. $-44.8 \text{ kJ mol}^{-1}$ for DIFP in Zn-DMCP (MONTORO *et al.*, 2011). This result emphasizes MOFs combining large uptake and very strong MOF/CWA interactions at low coverage can be selected to strongly bind the CWA molecules. This very high affinity is a crucial prerequisite for further use of this family of materials as CWA filters to ensure an immediate capture of the CWA once it is adsorbed in the pores and to limit the potential risk of CWA released under operating conditions. This is a clear advantage compared to the other porous adsorbents which have been shown to establish weaker interactions with the CWA. Typically, Kowalczyk *et al.* (KOWALCZYK *et al.*, 2005) reported the DMMP adsorption enthalpies ranging from -55 to -61 kJ mol^{-1} for diverse carbonaceous

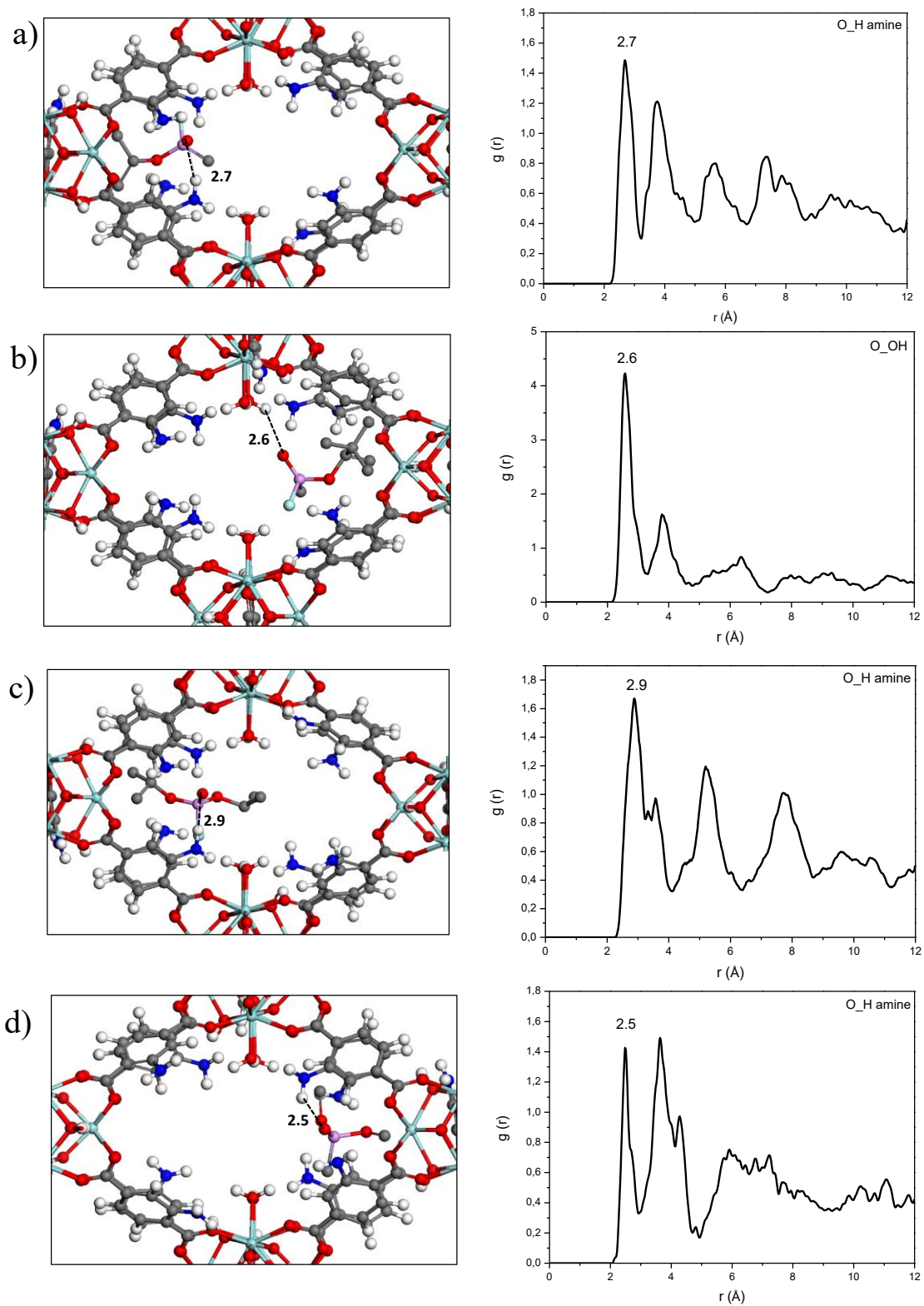
materials including pitch-based P7 ACF and commercialized granular activated carbons (Norit and D55/2) while Loven *et al* (LOVEN, A.W. & VERMILION, 1964) evidenced that the PCC coal-based carbon (KOWALCZYK *et al.*, 2013; LOVEN, A.W. & VERMILION, 1964) with a smaller pore width of ~ 5 Å shows a slightly higher adsorption enthalpy of -84 kJ mol⁻¹ but still lower than the values simulated here for certain MOFs.

4.2 UNDERSTANDING OF THE CWA/MOFs INTERACTIONS

To gain more insight into the microscopic origin of the potentially high CWA/MOF interactions, a carefully analysis of the preferential adsorption sites for the CWAs was undertaken based on the calculations of the RDFs for the corresponding pairs. Typically, the scenario is depicted for the defective UiO-66-(Zr)-NH₂ which is one of the MOFs showing the strongest interactions with soman, DMMP, sarin and DIFP associated with adsorption enthalpies of -108 , -95 , -93 and -94 kJ mol⁻¹ respectively. It is be noted that these values converge well with the interaction energies calculated at the DFT-level. This observation validates the set of LJ potential parameters and atomic partial charges used to describe the CWA/MOF interactions.

Figure 4.9a shows that sarin is preferentially located in the vicinity of the amino function grafted to the organic linker via an interaction between its oxygen atom of the P=O group and the hydrogen atom of the amino group with a characteristic distance of 2.7 Å. Such a range of interacting distance suggests a van der Waals-type interaction between CWA and the pore wall of the MOFs and thus a physisorption-based process. The same preferential interactions with the NH₂-group of the MOF were also observed for the simulants DMMP and DIFP (Figure 4.9c and d) while the adsorption behavior of soman only slightly deviates with an interaction between its oxygen atom of the P=O group and the hydrogen atom of the hydroxyl group bounded to the Zr atom (Figure 4.9b). Relatively similar strength of CWA/MOFs and microscopic adsorption mechanisms were also observed for the other best MOFs including for instance MOF-808s.

Figure 4.9 - A typical illustration of the preferential sittings for (a) Sarin, (b) Soman, (c) DIFP and (d) DMMP in the pores of the defective UiO-66(Zr)-NH₂ and the corresponding CWA/MOF radial distribution functions averaged over all the MC configurations.



Source: Elaborated by the author (2019).

In order to confirm that the CWA adsorption proceeds in these MOFs via physisorption-type interactions, further DFT analysis were performed. As a typical example, it was specifically treated the case of CWA adsorbed in the defective UiO-66(Zr)-NH₂. The analysis of Bader charges revealed that there is no significant change when one compares the charges of the isolated and confined CWA as summarized in Table 4.2. This result clearly supports that there is no significant charge transfer between the CWA and the host framework which excludes the existence of a chemisorption process.

Table 4.2 - Bader charge analysis for the isolated and adsorbed CWAs in the defective UiO-66(Zr)-NH₂.

Charges	Isolated Soman	Confined Soman	Isolated Sarin	Confined Sarin	Isolated DMMP	Confined DMMP	Isolated DIFP	Confined DIFP
O=(P)	-1.87	-1.88	-1.88	-1.88	-1.88	-1.87	-1.88	-1.88
O-CH	-1.71	-1.71	-1.71	-1.71	-	-1.70	-1.71	-1.70
P	4.86	4.86	4.86	4.86	4.86	4.86	4.86	4.87
F	-1.03	-1.01	-1.01	-1.01	-	-	-1.01	-1.01
CH ₃ -P	-1.27	-1.24	-1.26	-1.26	-1.21	-1.25	-	-
O-CH ₃	-	-	-	-	-1.73	-1.72	-	-

Source: Elaborated by the author (2019).

4.3 COMPARISON BETWEEN THE ADSORPTION BEHAVIORS OF CWAs AND THEIR SIMULANTS

From an experimental standpoint, simulant molecules, with physical or chemical properties similar to the real CWAs, are usually considered to avoid working with the highly toxic agents. DMMP and DIFP are the most common simulants employed to mimic soman and sarin, however it is crucial to make sure that they accurately capture the adsorption behaviour of the real molecules and this issue has been only rarely discussed so far in the literature. In this concern, Agrawal *et al.* (AGRAWAL *et al.*, 2018) showed that dimethyl p-nitrophenyl phosphate is a suitable simulant to mimic the adsorption of Soman while DMMP, DIFP and diethyl chlorophosphite are more appropriate to reproduce the behavior of Sarin. To address this question in the case of MOFs, it was considered the comparison of the adsorption behaviours of DIFP, DMMP, soman and sarin in two representative MOFs, namely the MOF-

808-OH-H₂O and the MIP-177-OH-H₂O. The simulated adsorption uptakes and adsorption enthalpies for all four molecules are represented in Table 4.3. It can be clearly stated that while DMMP and DIFP accurately reproduce the behavior of sarin in terms of uptake and energetics this is far to be the case for soman. Therefore, I searched for an alternative simulant that can mimic more accurately soman. Indeed, the PMP molecule showing similar backbone than the real molecule (see Figure 4.1) was thus considered.

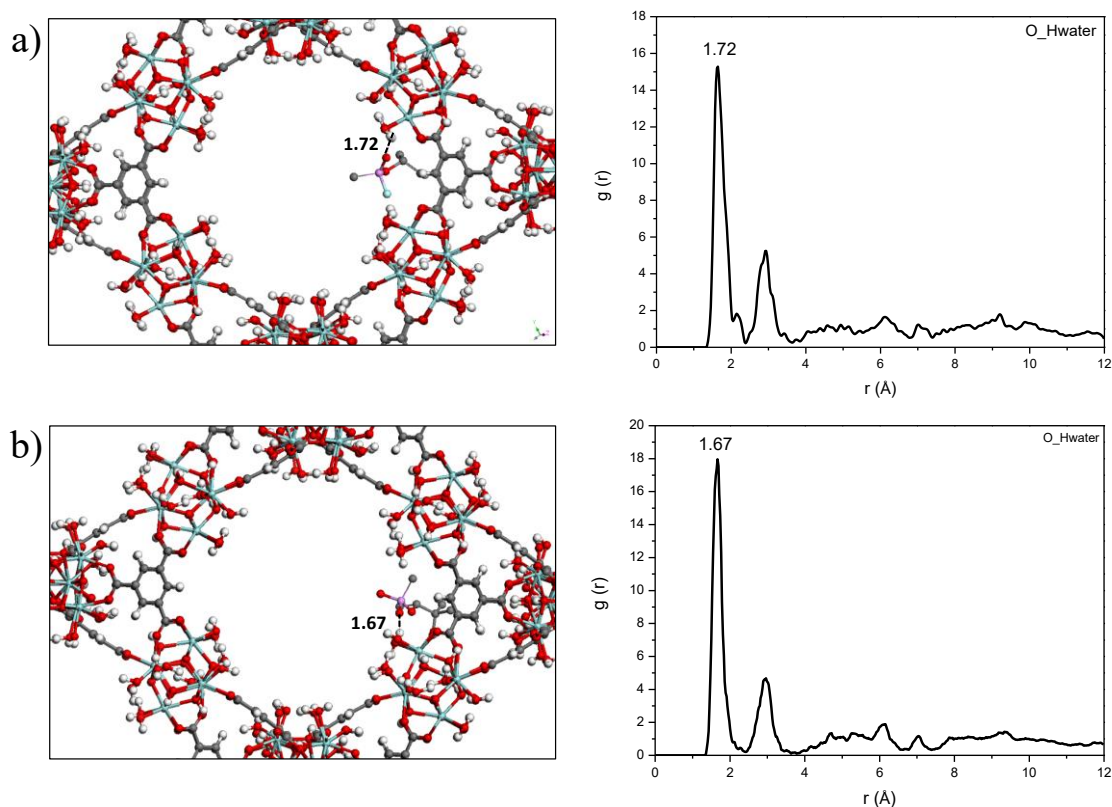
Table 4.3 indicates that this simulant reproduces much better the adsorption behavior of soman (in terms of both uptake and energetics), while Figure 4.10 shows that this molecule occupies a preferential sitting in the pores similar to the real molecule. This observation suggests that this simulant of low toxicity should be considered as an alternative simulant to the standard DMMP and DIFP molecules to explore the performances of MOFs regarding soman.

Table 4.3 - Simulated adsorption uptakes and enthalpies for sarin, soman, DMMP, DIFP and PMP in two representative MOF materials investigated in this study.

Uptake / mmol g ⁻¹					ΔH / kJ mol ⁻¹				
sarin	DMMP	DIFP	soman	PMP	sarin	DMMP	DIFP	soman	PMP
MIP-177-OH-H ₂ O									
1.695	1.977	1.212	1.122	1.110	67.63	70.30	71.26	88.26	83.89
MOF-808-OH-H ₂ O									
6.685	7.95	4.839	4.716	4.509	62.90	64.65	57.79	74.71	72.05

Source: Elaborated by the author (2019).

Figure 4.10 - GCMC simulations at low loading. A typical illustration with the preferential sittings for a) Soman and b) DIFP in the pores of MOF-808-OH-H₂O and the radial distribution functions between all the hydrogen atom of the active sites and the oxygen of guest molecules.



Source: Elaborated by the author (2019).

4.4 CONCLUSION

This chapter describes a computational evaluation of the CWA capture performances of robust MOFs. The GCMC simulations evidenced that a series of water stable Zr and Ti MOFs show outstanding adsorption uptakes for soman, sarin and their simulants combined with high adsorption enthalpies. This level of performance makes these materials potentially attractive as CWA filters with great promises in large payload and limitation of release under operating conditions. Force field and quantum-calculations were coupled to clarify the microscopic adsorption mechanisms. Although the CWA adsorption enthalpies reached for some MOFs values higher than -100 kJ mol^{-1} , complementary DFT analysis precluded the existence of charge transfer between the CWA and the host framework consistent with a physisorption-based process involving mostly van der Waals interactions. Structure-CWA adsorption

performances relationship was established with the definition of a geometric descriptor based on the free pore volume of the MOF and the molecular dimension of the CWAs. Finally, it was evidenced that a special attention needs to be paid when one selects the simulants to mimic the adsorption of real CWAs in MOFs. While the standard DMMP and DIFP simulants reproduce well the behavior of sarin, this is not anymore true for soman and an alternative simulant established in this work, namely the PMP molecule, needs to be considered.

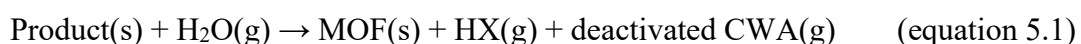
5 COMPUTATIONAL EXPLORATION OF THE CATALYTIC DEGRADATION OF CWAs BY Ti- AND Zr- MOFs

A considerable number of studies has been dedicated so far to probe the catalytic degradation performances of MOFs for diverse CWAs, however the microscopic mechanisms in play are still not fully understood. Therefore, in this chapter three distinct mechanisms of CWA decomposition were explored in a series of MOFs that have been revealed as promising candidates in terms of adsorption uptakes and energetics for these toxic molecules, i.e. MIP-177(Ti), MIP-200(Zr), UiO-66(Zr) and UiO-66(Zr)-NH₂ (see chapter 4). The selected CWAs include soman, sarin, sulfur mustard as well as their respective simulants.

In this context, DFT calculations were performed with periodic boundary conditions to accurately assess the main states of the degradation reaction (reactants, transition state and products) and the associated activation energy barriers for each degradation reaction (MOMENI; CRAMER, 2018a). The Quantum-Espresso package (GIANNOZZI et al., 2009) was employed with the use of pseudopotentials to describe ion cores and plane-wave basis sets (KOHN; SHAM, 1965) while the generalized gradient approximation GGA-PBE for the exchange-correlation functional (PERDEW; BURKE; ERNZERHOF, 1996) and the Vanderbilt ultra-soft pseudopotentials (VANDERBILT, 1990) to describe the ion cores of Ti, Zr, P, C, O, H and F atoms were considered. The energy cutoff for the plane wave basis set was fixed to 50 Ry (400 eV) and the electron density was obtained at the Γ point in the first Brillouin zone (PACK; MONKHORST, 1977). The atomic positions and cell parameters of all MOFs were taken from the crystal structures previously reported (CAVKA et al., 2008; ROGGE et al., 2016; WANG et al., 2018a, 2018b). All the structures containing pending Ti- or Zr- atoms were saturated by –OH and –H₂O groups. The corresponding structures were fully DFT-geometry optimized (both cell parameters and atomic positions relaxed) until all force components were smaller than 0.001 Ry/Bohr and the convergence criterion of 10⁻⁴ Ry was reached for the total energy.

Starting with these DFT-optimized empty structures, 1 molecule of CWA or its simulants were introduced in the pore of each MOF by means of Monte Carlo simulations following the methodology (force field parameters, charges, number of MC steps) detailed in Chapter 4. The resulting guest-loaded structures were further optimized at the DFT-level. Minimum energy paths (MEPs) (HENKELMAN; UBERUAGA; JÓNSSON, 2000) for the different envisaged catalytic degradation mechanisms were further computed to identify the transition state and products, evaluate the corresponding reaction barrier and characterize the

main structural modifications along the reaction. The geometries of eleven images used to compute each MEP were optimized to establish the minimum-energy path on the potential surface of the system until the energy variation was below 0.05 eV/Å. The convergence criterion was satisfied when all components of the forces were smaller than 10⁻⁴ Ry/Bohr. The energy involved in the process of desorption of the molecules, thought the adsorption of one water molecule in the MOFs was further calculated according to the reaction as schematized by equation 5.1.



For soman, sarin and sulfur mustard (HD) the molecules involved in the process of desorption are Pinacolyl methylphosphonic acid (PMP), Isopropyl methyl phosphonic acid (IMPA) and Half mustard (half_HD), respectively. HX is hydrofluoric acid for sarin and soman while hydrochloridric acid is obtained for HD.

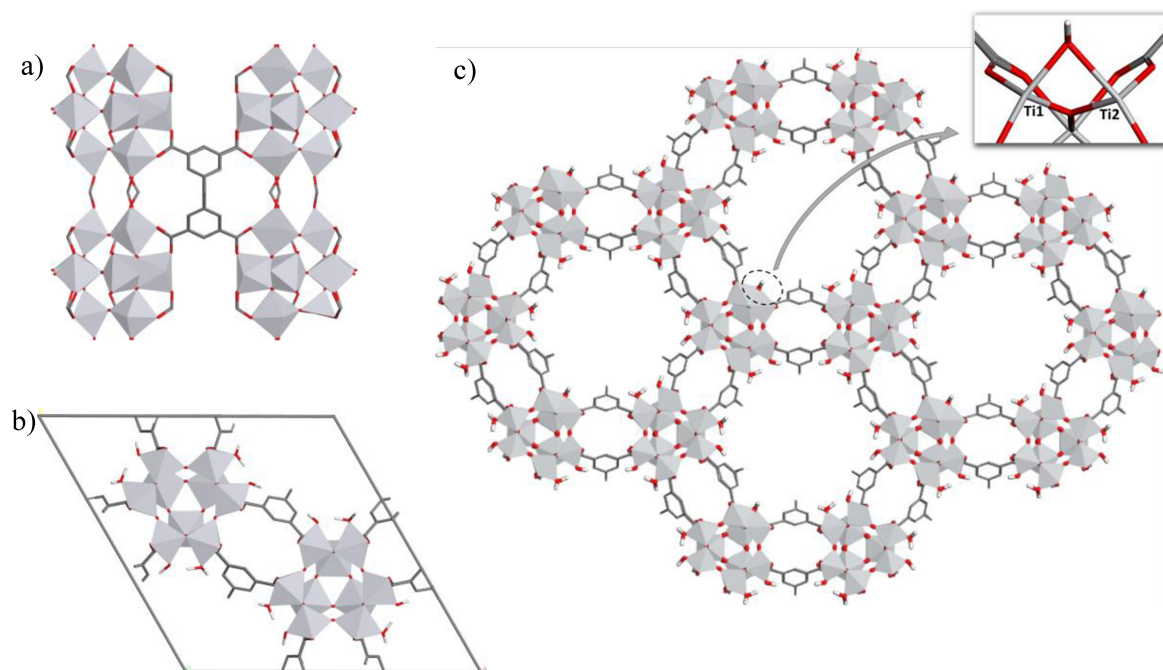
In this thesis, several possible hydrolysis mechanisms on the activated Ti site of a recently discovered highly stable Ti-MOF, MIP-177(Ti) were for the first time explored (WANG et al., 2018b), in the presence/absence of water, considering Sarin and its simulants Dimethyl methylphosphonate and diisopropyl phosphorofluoridate. The hydrolysis mechanisms on the activated Ti site were considered with the aim to carefully characterize the main states of the degradation reaction (reactants, transition state and products), the minimum energy reaction path and the resulting activation energy barriers required to initiate the catalytic degradation and hence the most probable reaction pathway. These whole set of data were further compared with the corresponding data reported in the literature for the whole series of Zr-MOFs (CHEN et al., 2018; HARVEY; GREATHOUSE; SAVA GALLIS, 2018; MOMENI; CRAMER, 2018a, 2018b; TROYA, 2016; WANG et al., 2017) in order to assess the promises of MIP-177(Ti) as CWA catalyst. The Soman and Sarin degradation mechanisms were further studied in the Zr-MOFs as well as the hydrolysis reaction of sulfur mustard and its simulant 2-Chloroethyl ethyl sulfide, also known as half-mustard (CEES).

5.1 DEGRADATION OF SARIN ON THE ACTIVATED Ti SITE OF MIP-177(Ti)

As mentioned before, the catalytic degradation of CWAs into less toxic products by MOFs have been exclusively focused on Zr-based materials so far although Ti-MOFs, might be also of interest owing to the well-known capacity of Ti-compounds to efficiency hydrolyze CWAs. Indeed, the use of titanium oxides as catalysts for the degradation of toxic industrial compounds is well documented (SCHNEIDER et al., 2014). Nanotubular Titania were demonstrated to be attractive for the catalytic degradation of a series of CWAs including Sarin, Soman, Sulfur mustard and VX (LEE et al., 2017; LEMAIRE et al., 2017; MCCARTHY et al., 2017). Furthermore, recent works reported the incorporation of Ti compounds such as $\text{Ti}(\text{OH})_4$, TiO_2 and TiCl_4 into MOFs to enhance the efficiency of the hydrolysis of CWA (LEE et al., 2017; MCCARTHY et al., 2017; VELLINGIRI; PHILIP; KIM, 2017; ZHAO et al., 2016). All together, this experimental observation encouraged us to envisage for the first time a Ti-MOF as a potential candidate for the degradation of Sarin and its simulants DMMP and DIFP. The carboxylate Ti-MOF labeled as MIP-177(Ti) (Figure 5.1) in its low temperature and formate free form (MIP stands for the Materials of the Institute of Porous Materials of Paris) (WANG et al., 2018b) was selected owing to its attractive predicted performances in terms of adsorption uptakes and energetics (VIEIRA SOARES; MAURIN; LEITÃO, 2019a) for a series of CWAs including soman, sarin, DMMP and DIFP (chapter 4), as well as its high chemical stability, its favorable 1D-type channel large enough (11 Å) to accommodate the CWA molecules and its optimal chemical environment that incorporates free Ti metal sites on its formate-free version able to act as active sites for catalysis.

This MOF has highly ordered crystalline structures, integrating the properties of existing Ti–O compounds with those of ordered porous materials. It crystallizes in a hexagonal space group P6/mmm with unit cell parameters of $a = b = 22.59 \text{ \AA}$ and $c = 12.31 \text{ \AA}$. This robust structure comprises a $\text{Ti}_{12}\text{O}_{15}$ oxocluster and a tetracarboxylate ligand (H_4mdip), with the associated chemical formula $\text{Ti}_{12}\text{O}_{15}(\text{mdip})_3(\text{formate})_6$. Each H_4mdip linker connects four Ti-oxoclusters and the formates play the role to ensure the linkage of SBUs along the c-axis (Figure 5.1a). The resulting 3D pore system features large (11 Å) accessible hexagonal channels running along the c-axis (WANG et al., 2018b).

Figure 5.1 - a) Adjacent SBUs with bridging formates connected by 3,3',5,5'-tetracarboxydiphenylmethane (H4mdip) linkers. b) Unit cell and c) Illustration of the crystal structure of MIP-177(Ti). The creation of the Ti open site through dehydration leads to a hydroxyl group coordinated in a bidentate manner to the Ti1 and Ti2.

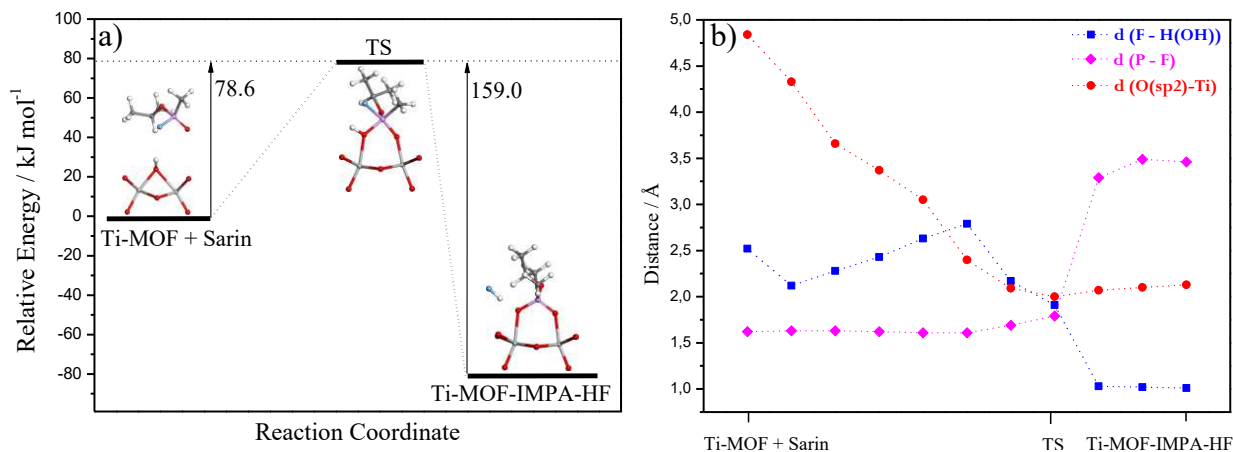


Source: Elaborated by the author (2019).

The structure was considered in its formate-free form, the corresponding linkers connecting two Ti sites being replaced by one terminal -OH and $\text{-H}_2\text{O}$ respectively. The DFT-geometry optimization of the empty MIP-177(Ti) converged towards a structure characterized by the formation of a bridging OH group bounded to two neighbor Ti sites as illustrated in the inset of Figure 5.1c. Among all the Ti-pairs, we considered the creation of one activated Ti site by removing its bounded $\text{-H}_2\text{O}$ molecule while the neighbor Ti keeps its -OH group.

The **first investigated degradation mechanism** corresponds to the nucleophilic addition of the -OH function, initially bridging two neighbors Ti sites, to the phosphorus atom of Sarin. This activates the phosphate ester function and further leads to the formation of a phosphonate product and the release of hydrogen fluoride (TROYA, 2016). The simulated MEP of the corresponding reaction is reported in Figure 5.2a with the identification of the initial reactant, TS and the resulting product.

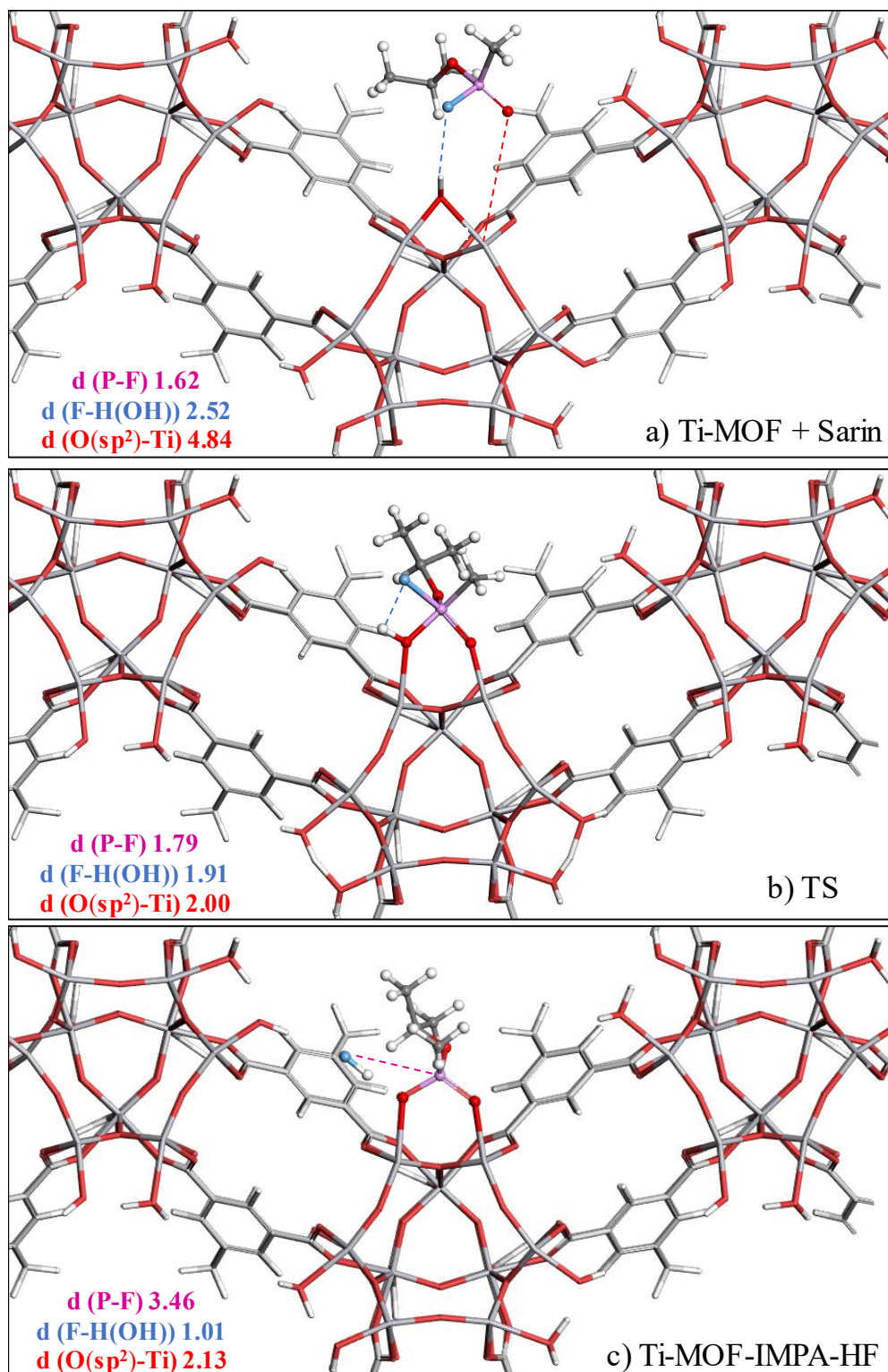
Figure 5.2 - Simulated Minimum Energy Path corresponding to the degradation mechanism of Sarin on the Ti activated site. b) Evolution of the main characteristic distances involving the atoms of Sarin (F, P and O(sp²)) and of Ti-MOF (Ti, H(OH)) along the reaction coordinate.



Source: Elaborated by the author (2019).

Figure 5.3a illustrates the most stable DFT-optimized configuration of Sarin initially adsorbed in the pore of the Ti-MOF corresponding to the reactant. Sarin adopts a preferential conformation in such a way than its fluorine atom interacts with the bridging -OH group of MIP-177(Ti) with a separating F-H(OH) distance of 2.52 Å. During the first step of the reaction, this bridging -OH group moves away from one titanium site, creating an extra-space for the toxic molecule to access the activated Ti site, and consequently the distance between the O(sp²) atom of Sarin (the oxygen atom bounded to the phosphorus atom) and this titanium atom becomes shorter (see red line in Figure 5.2b). As the reaction proceeds through the transition state, there is a bond formation between the O(sp²) atom of Sarin and the Ti site and this leads to a 5-coordinated geometry of Sarin as evidenced in Figure 5.2b. Beyond TS, a progressive increase of the distance separating the phosphorus and fluorine atoms of Sarin (Figure 5.2b) that finally results to a breaking of the corresponding bond and consequently the formation of HF can be observe. This gives rise to a stable configuration for the product where the organophosphorus fragment, namely the isopropyl methyl phosphonic acid (IMP A), is coordinated in a bidentate manner to the inorganic node of the Ti-MOF (Figure 5.3c).

Figure 5.3 - Illustration of the degradation mechanism of Sarin on the Ti activated site of MIP-177(Ti). a) Reactant (Ti-MOF + Sarin), b) Transition state (TS) and c) Product (Ti-MOF-IMPA-HF). The main distances involved in the degradation process, P-F (pink), F-H(OH) (blue) and O(sp²)-Ti (red) are represented and expressed in Å.

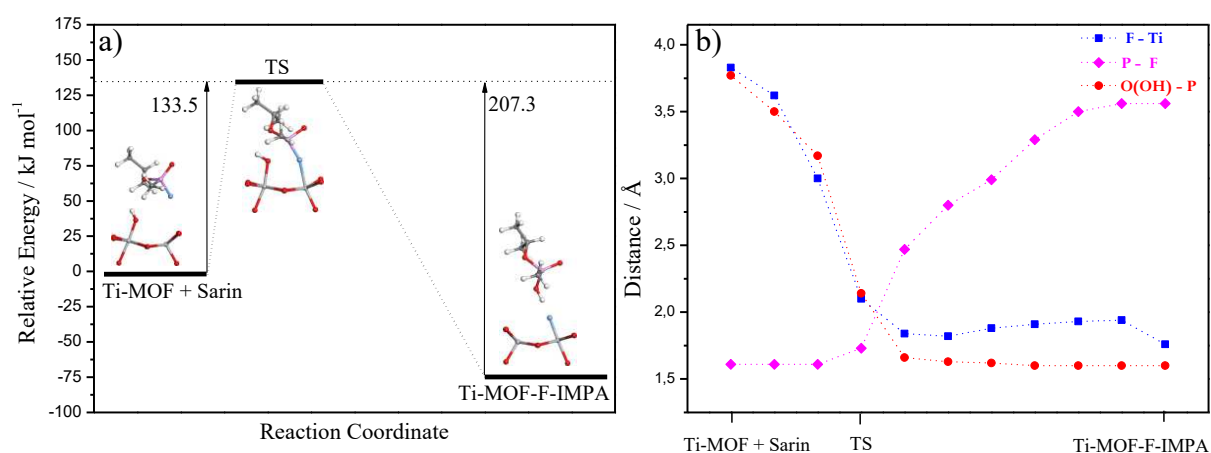


Source: Elaborated by the author (2019).

The MEP reported in Figure 5.2a implies an activation energy barrier of 78.6 kJ mol⁻¹. This range of value is similar to the free energy previously reported (MOMENI; CRAMER, 2018a) for the hydrolysis of Sarin in diverse Zr-MOFs including MOF-808 (79.1 kJ mol⁻¹), NU-1000 (75.3 kJ mol⁻¹) and UiO-66(Zr) (71.5 kJ mol⁻¹). This observation suggests that this Ti-MOF is expected to perform as good as the best Zr-MOFs explored so far for the catalytic degradation of Sarin. One can also note that the product represents the most stable configuration along the whole reaction path (-80.5 kJ mol⁻¹). This indicates that the coordination of IMPA to the inorganic node of the MIP-177(Ti) leads to the formation of a stable complex. Finally, the desorption energy of IMPA and HF from the product calculated by using equation 5.1 is predicted to be relatively high, i.e. 131.6 kJ mol⁻¹. This observation emphasizes that MIP-177(Ti) not only allows the degradation of Sarin but also a strong retention of the resulting IMPA product into their pores.

The **second degradation mechanism** examined corresponds to a scenario where the Ti active site binds to the fluorine atom of Sarin leading to the formation of the deactivated IMPA molecule (Figure 5.4a). To do so, the molecule was initially slightly tilted from its most stable configuration reported in Figure 5.3a in such a way to favor an interaction between its F-atom and the inorganic node of MIP-177(Ti).

Figure 5.4 - a) Simulated Minimum Energy Path corresponding to the degradation mechanism where the Ti active site binds to the fluorine atom of Sarin. b) Evolution of the main characteristic distances involving the atoms of Sarin (F, P) and of Ti-MOF (Ti, O(OH)) along the reaction coordinate.

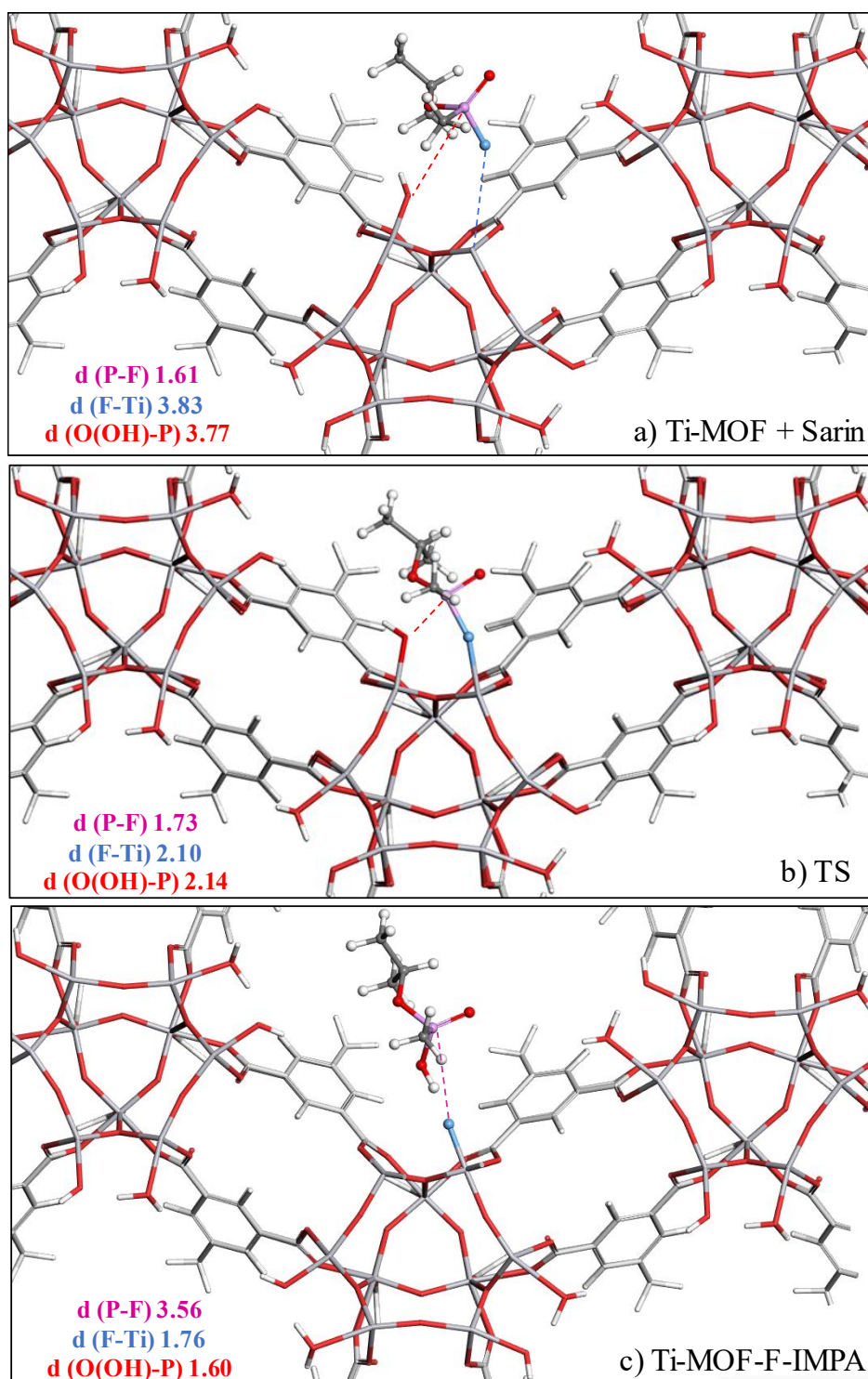


Source: Elaborated by the author (2019).

A further geometry optimization led to a local minimum energy where the OH-group does not anymore bridge the two Ti neighbors allowing the F-atom of Sarin to face the Ti-active site (Figure 5.5a). The reaction path leads to a transition state involving the coordination of the -F atom towards the Ti active site while the phosphorous atom of Sarin interacts with the oxygen atom of the -OH group (Figures 5.4b and 5.5b). Finally, the product (Ti-MOF-F-IMPA) implies the formation of a bond between the F-atom and the Ti-active site while the OH group of the Ti-MOF is transferred to the molecule via the formation of a P-OH bond (Figures 5.4b and 5.5c).

The MEP reported in Figure 5.4a implies an activation energy barrier of $133.5 \text{ kJ mol}^{-1}$ which is much higher compared to the value obtained for the first mechanism (Figure 5.2a - 78.6 kJ mol^{-1}). This clearly reveals that the degradation of Sarin through the coordination of F-atom towards the Ti-active site is much less probable, consistent with the previous findings reported in the case of Zr-MOFs (BERMUDEZ, 2007b; HARVEY; GREATHOUSE; SAVA GALLIS, 2018; TROYA, 2016).

Figure 5.5 - Illustration of the degradation mechanism of Sarin on the Ti activated site of MIP-177(Ti) where the Ti active site binds to the fluorine atom of Sarin. a) Reactant (Ti-MOF + Sarin), b) Transition state (TS) and c) Product (Ti-MOF-F-IMPA). The main distances involved in the degradation process, P-F (pink), F-Ti (blue) and O(OH)-P (red) are represented and expressed in Å.



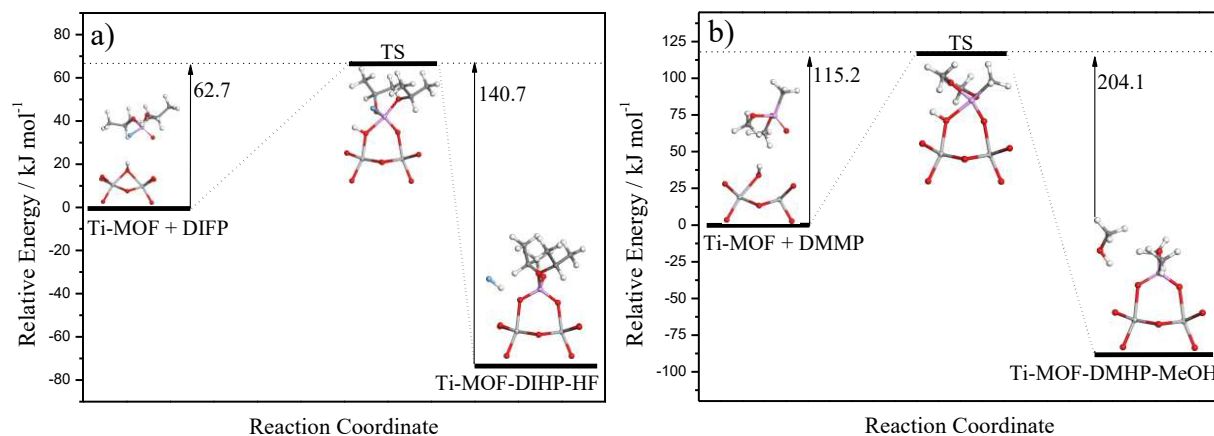
Source: Elaborated by the author (2019).

5.1.1 Degradation of the simulants of sarin on the activated Ti site of MIP-177(Ti)

The degradation mechanisms of DMMP and DIFP considered as simulants of Sarin involving the formation of CH_3OH and HF respectively were explored since this mechanism was demonstrated to be the most probable mechanism in the case of Sarin (Figures 5.2 and 5.3). Indeed, the two molecules were first individually loaded in MIP-177(Ti) using preliminary Monte Carlo simulations (VIEIRA SOARES; MAURIN; LEITÃO, 2019a) and the resulting geometries were further optimized at the DFT level.

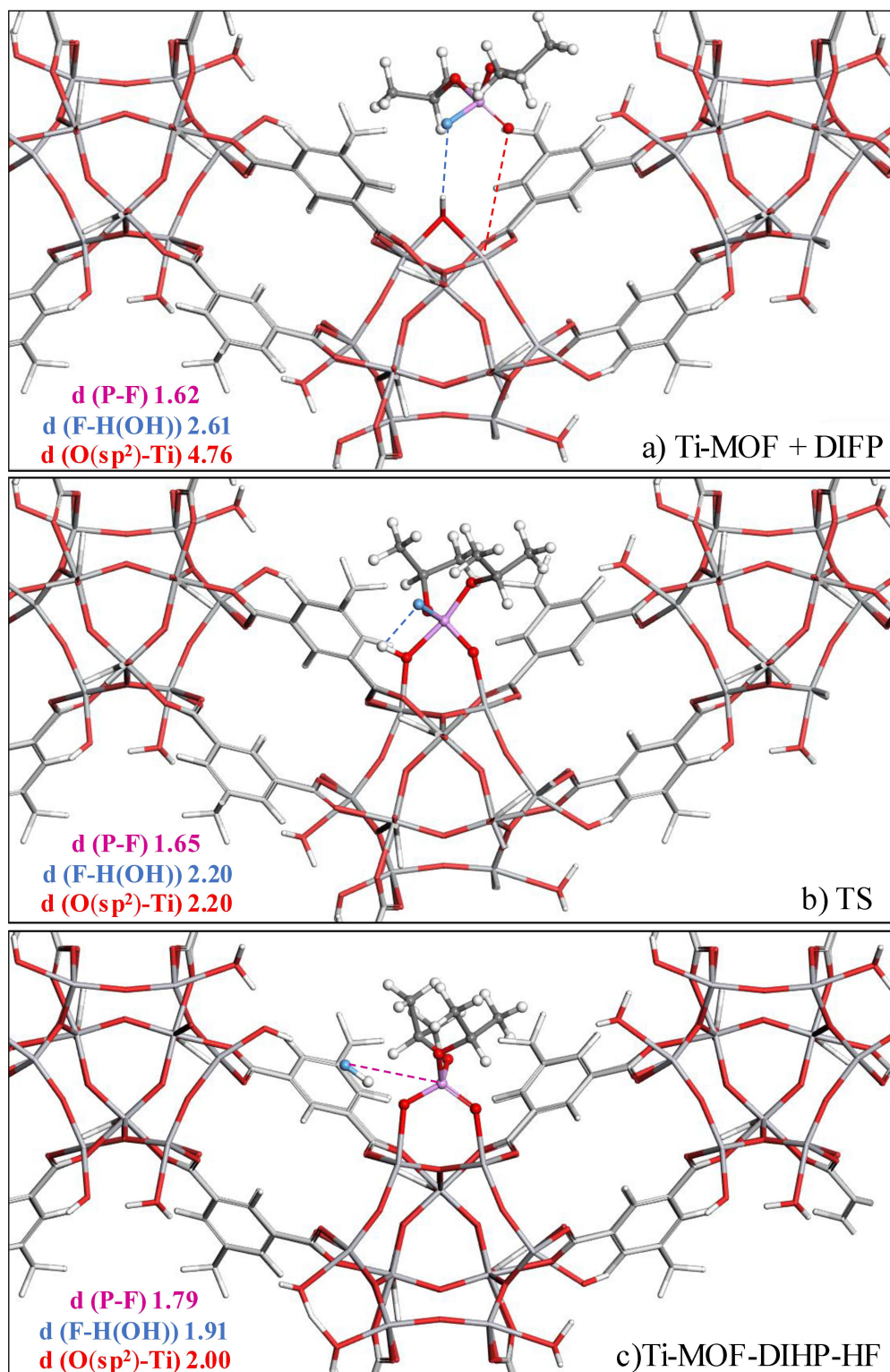
The corresponding minimum energy paths for the catalytic degradation mechanism of DIFP and DMMP are plotted in Figure 5.6a and Figure 5.6b respectively. Regarding DIFP, the TS and products formed during the reaction are very similar than that evidenced for Sarin, with in this case the formation of the deactivated diisopropyl hydrogen phosphate (DHFP) molecule (cf. Figure 5.7 and Figure 5.5). This observation is consistent with an energy barrier associated with the degradation mechanism of DIFP (67.2 kJ mol^{-1}) (Figure 5.6a) relatively similar to the value calculated for Sarin (78.6 kJ mol^{-1}) (Figure 5.4a).

Figure 5.6 - Simulated Minimum Energy Paths corresponding to the degradation mechanism of (a) DIFP and (b) DMMP on the Ti activated site.



Source: Elaborated by the author (2019).

Figure 5.7 - Illustration of the degradation mechanism of DIFP on the Ti activated site of MIP-177(Ti). a) Reactant (Ti-MOF + DIFP), b) Transition state (TS) and c) Product (Ti-MOF-DIHP-HF). The main distances involved in the degradation process, P-F (pink), F-H(OH) (blue) and O(sp²)-Ti (red) are represented and expressed in Å.

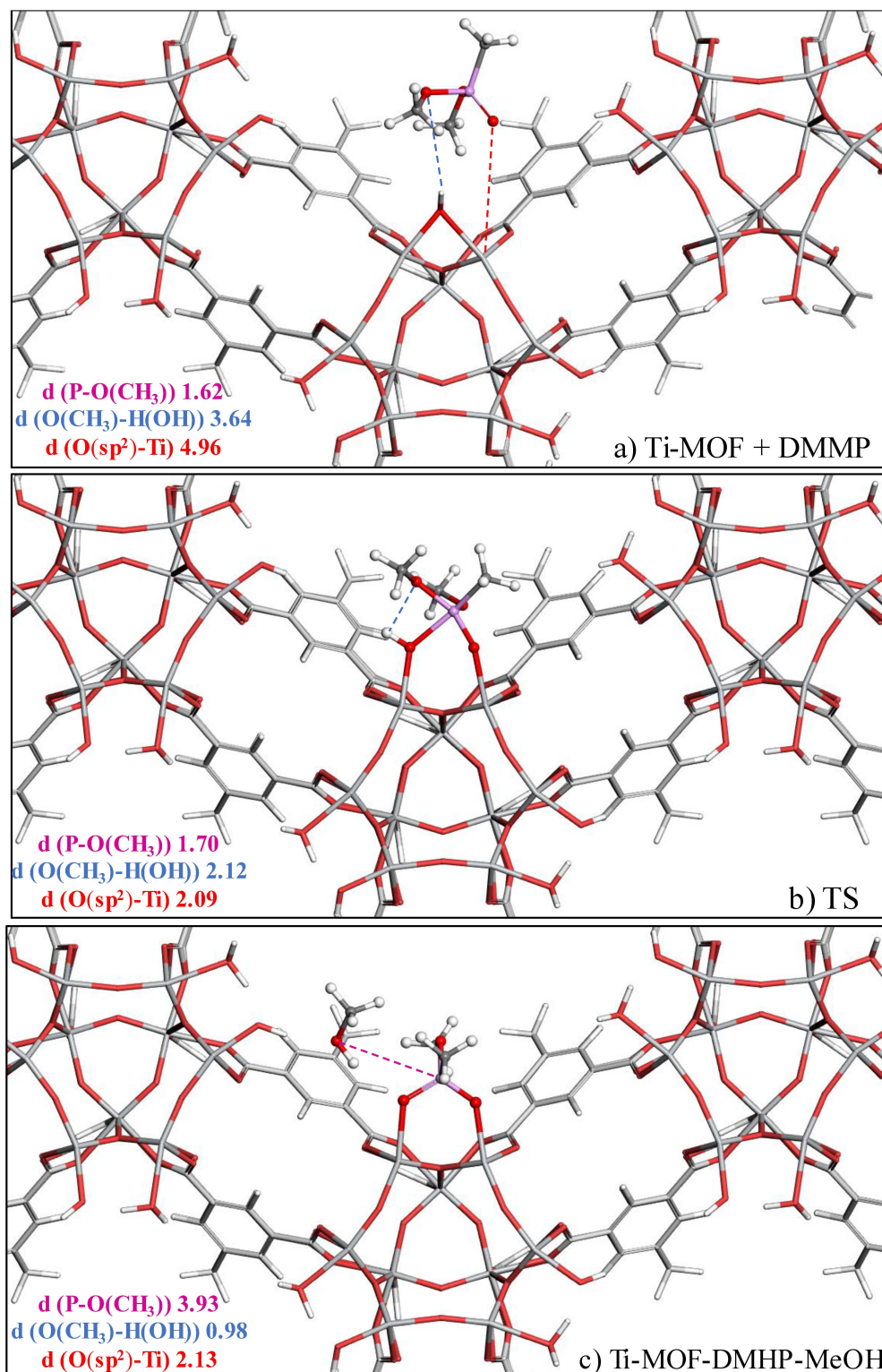


Source: Elaborated by the author (2019).

When one switches to DMMP, Figure 5.8a evidences that the initial configuration implies an interaction between its -OCH₃ function and the bridging -OH group of MIP-177(Ti) at longer distance compared to the scenario implying the interactions between the -F atom of both Sarin and DIFP with the hydroxyl group of the MOF. The transition state shows that the P-OCH₃ bond becomes collinear to the P-OH bond and the nucleophilic addition of the bridging -OH group to the DMMP molecule results to the cleavage of the P-OCH₃ bond leading to the formation of methanol and the deactivated dimethyl hydrogen phosphate (DMHP) molecule as it can be illustrated in Figures 5.8b and Figure 5.8c.

The resulting activation energy barrier for the degradation of DMMP (115.2 kJ mol⁻¹) (Figure 5.6b) is significantly higher than the value calculated for Sarin (78.6 kJ mol⁻¹). This trend that can be associated with the subsequent elimination of methanol instead of HF is consistent with what has been reported previously for UiO-67(Zr) by Troya *et al.* (TROYA, 2016) and Wang *et al.* (WANG *et al.*, 2017) for the degradation of Sarin and DMMP respectively. Interestingly, this calculation performed on the two simulants emphasizes that DIFP mimics better Sarin in terms of the TS and products obtained during the reaction as well as of the activation energy required to achieve their degradation.

Figure 5.8 - Illustration of the degradation mechanism of DMMP on the Ti activated site of MIP-177(Ti). a) Reactant (Ti-MOF + DMMP), b) Transition state (TS) and c) Product (Ti-MOF-DMHP-MeOH). The main distances involved in the degradation process, P-O(CH₃) (pink), O(CH₃)-H(OH) (blue) and O(sp²)-Ti (red) are represented and expressed in Å.



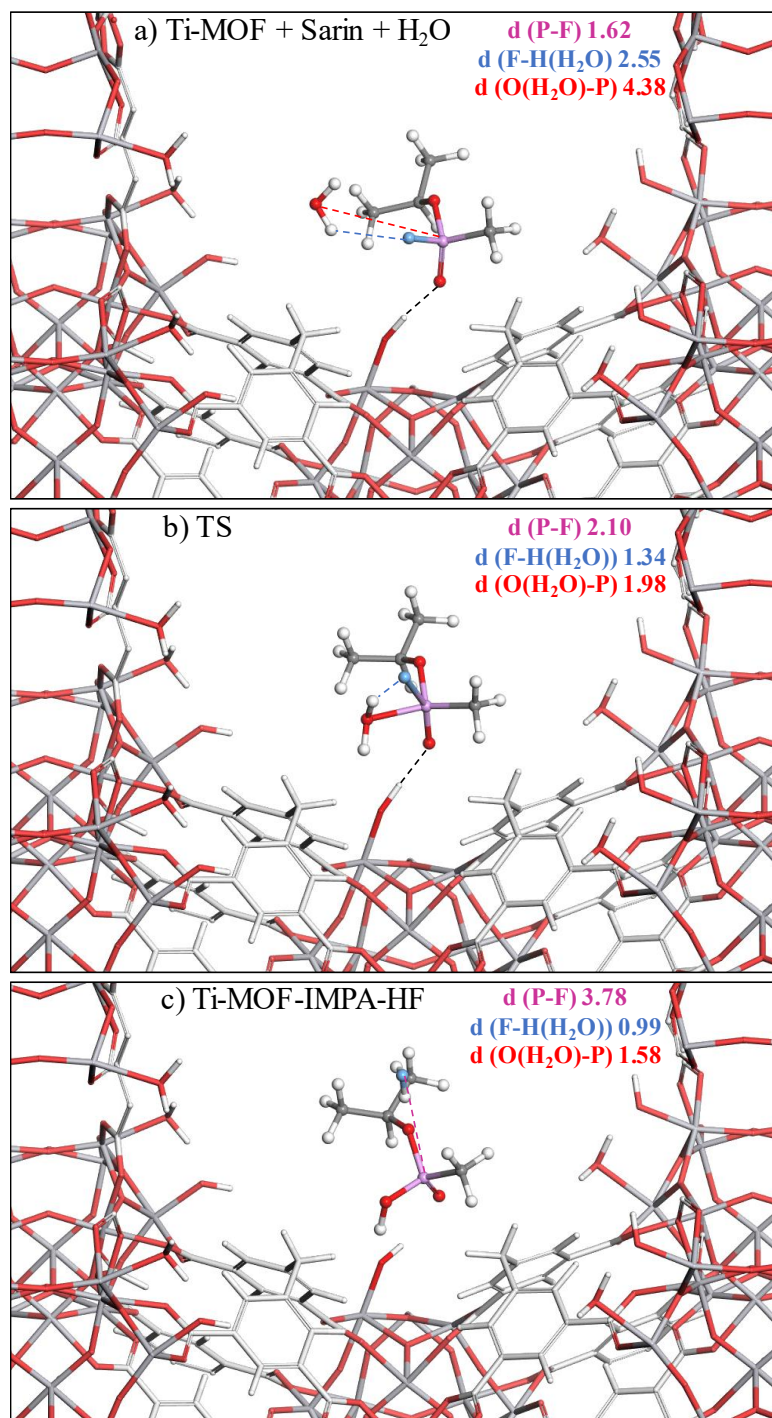
Source: Elaborated by the author (2019).

5.2 DEGRADATION OF SARIN IN THE PRESENCE OF WATER ON THE ACTIVATED Ti SITE OF MIP-177(Ti)

Since the catalyst is expected to operate under atmospheric condition, e.g. potentially under a given relative humidity, the degradation mechanism of Sarin in the presence of water confined in the pore of MIP-177(Ti) was also investigated. Starting with the configuration reported in Figure 5.2a corresponding to the most stable arrangement of Sarin in MIP-177(Ti), the incorporation of 1 extra-water molecule was considered by testing different initial positions. These resulting configurations were further geometry optimized and the two most stable reported in Figure 5.9a and Figure 5.10a were subsequently selected for further exploration of the degradation mechanism. Figure 5.9a illustrates that the Sarin forming a strong hydrogen bond with the -OH group of the MOF $\text{H(OH)-O(sp}^2\text{)}$ (1.75 \AA – black dashed line). The degradation mechanism ensues via nucleophilic attack of water molecule on P atom of Sarin, resulting in a pentacoordinate phosphorus where fluorine forming a hydrogen bond with the H of water, as it can be observed in the transition state reported in Figure 5.9b, similar to that already reported by Troya et al. (TROYA, 2016) for Zr-MOFs. Thus, the water molecule dissociated and its proton migrates to the fluor atom to the oxygen atom of the OH^- anion coordinates the P-atom of Sarin while its proton generating HF and IMPA, as reported in Figure 5.9c.

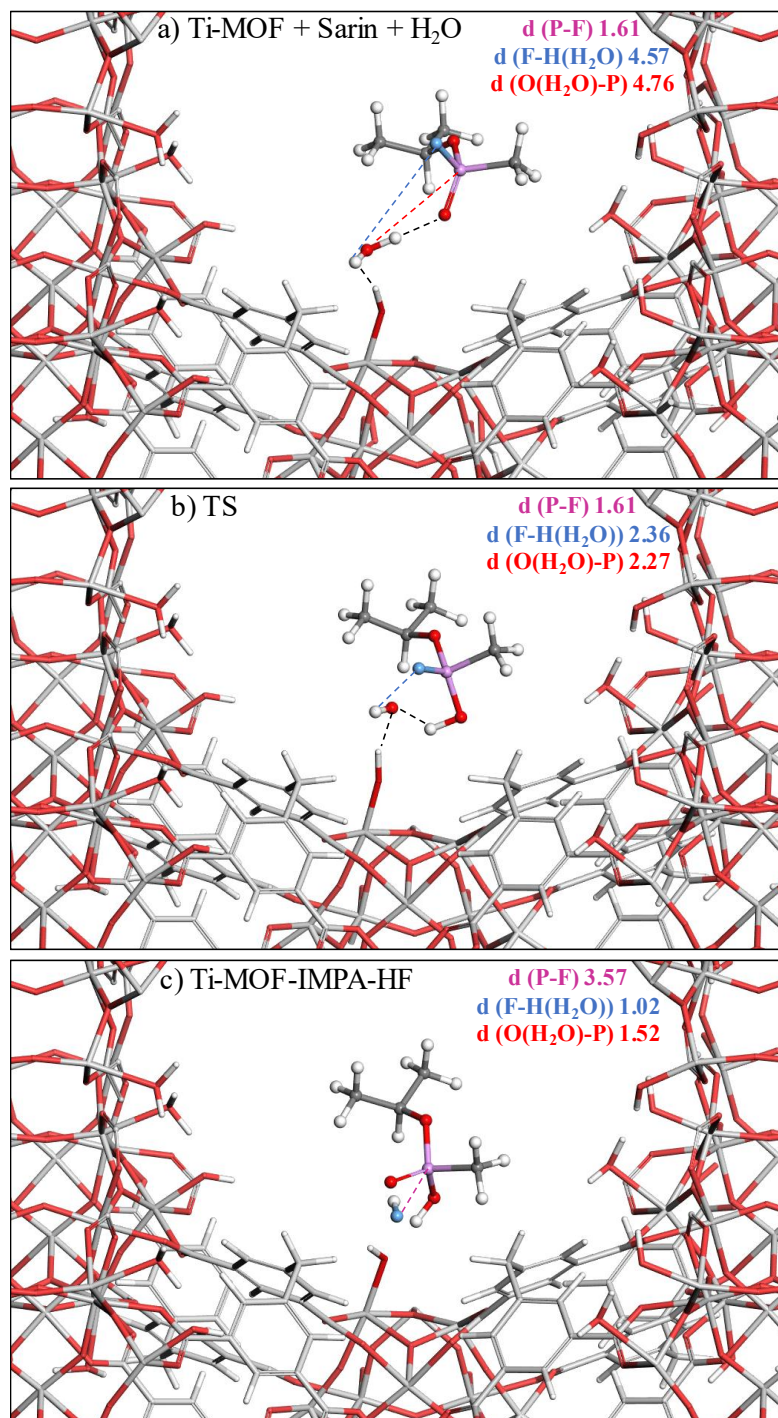
In the second case, the water molecule interacts with both Sarin and the -OH group of the MOF forming in both cases relatively strong $\text{H(H}_2\text{O)-O(sp}^2\text{)}$ (1.73 \AA – black dashed line) and $\text{H(H}_2\text{O)-O(OH)}$ (1.69 \AA – black dashed line) hydrogen bonds (see Figure 5.10a). Such an interaction makes the -OH group bonded to only 1 Ti site. The degradation mechanism further proceeds via the dissociation of water with one proton transferred to the $\text{O(sp}^2\text{)}$ atom of Sarin, the resulting OH^- anion remaining in strong hydrogen bond interactions with the -OH group of MIP-177(Ti) (1.71 \AA – black dashed line) and with the P-OH group (1.44 \AA – black dashed line) as it can be observed in the transition state reported in Figure 5.10b. Finally, the oxygen atom of the OH^- anion coordinates the P-atom of Sarin while its proton participates concertedly to the degradation of the toxic molecule into IMPA and the subsequent release of HF as reported in Figure 5.10c.

Figure 5.9 - Illustration of the degradation mechanism of sarin on the activated Ti site of MIP-177(Ti) in the presence of water where sarin interacts predominantly with the MOF framework. (a) Reactant (Ti- MOF + sarin + H₂O), (b) transition state (TS), and (c) product (Ti- MOF-IMPA-HF). The main distances involved in the degradation process, P–F (pink), F–H(H₂O)) (blue), and O(H₂O)–P (red) are represented and expressed in Å. The black dashed lines indicate the interaction between the molecules (water and IMPA) and the framework.



Source: Elaborated by the author (2019).

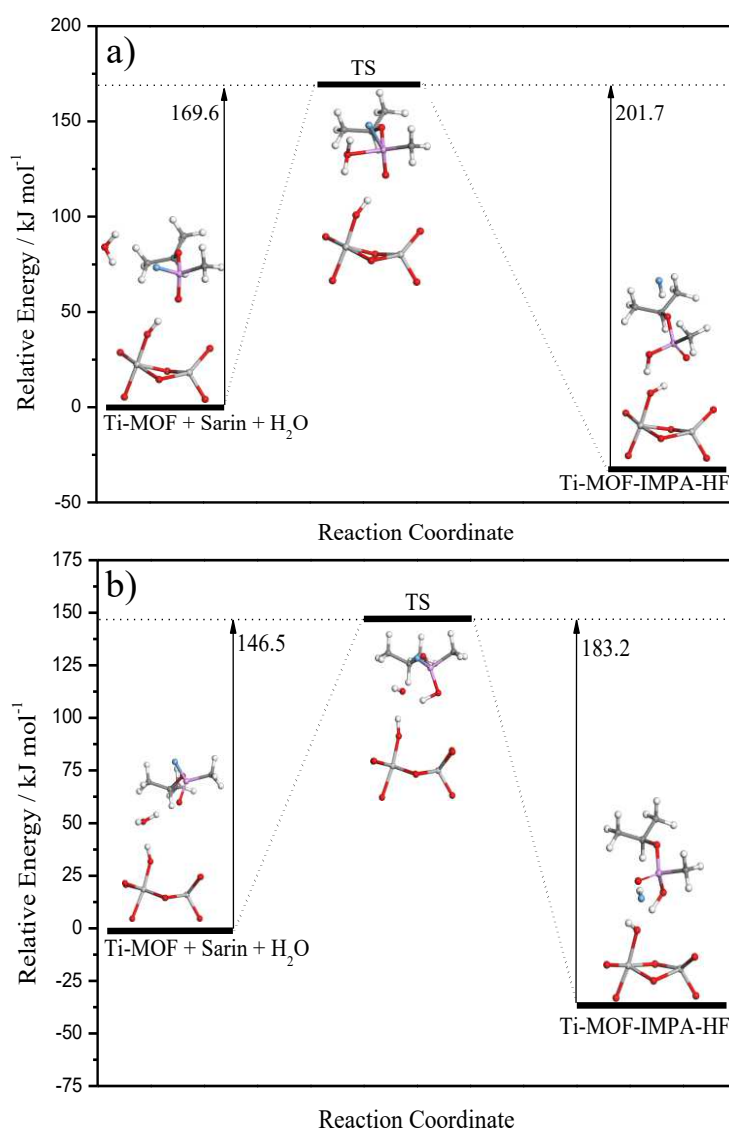
Figure 5.10 - Illustration of the degradation mechanism of Sarin on the Ti activated site of MIP-177(Ti) in the presence of water. a) Reactant (Ti-MOF + Sarin + H₂O), b) Transition state (TS) and c) Product (Ti-MOF-IMPA-HF). The main distances involved in the degradation process, P-F (pink), F-H(H₂O) (blue) and O(H₂O)-P (red) are represented and expressed in Å. The black dashed lines indicate the interaction between the molecules (water and IMPA) and the framework.



Source: Elaborated by the author (2019).

Figure 5.11 reports the corresponding minimum energy paths for the reaction in the presence of water starting with two different arrangements of water and Sarin (Figure 5.9a and 5.10a). The associated energy barriers of $146.5 \text{ kJ mol}^{-1}$ and $169.6 \text{ kJ mol}^{-1}$ are significantly higher than the value obtained in the absence of water (see Figure 5.3a). This observation emphasizes that the degradation performance of MIP-177(Ti) is expected to be less attractive under humidity conditions.

Figure 5.11 - Simulated Minimum Energy Paths corresponding to the degradation mechanism of Sarin on the Ti activated site in the presence of water. (a) Related to the configurations reported on Figure 5.9 and (b) Related to the configurations reported on Figure 5.10.



Source: Elaborated by the author (2019).

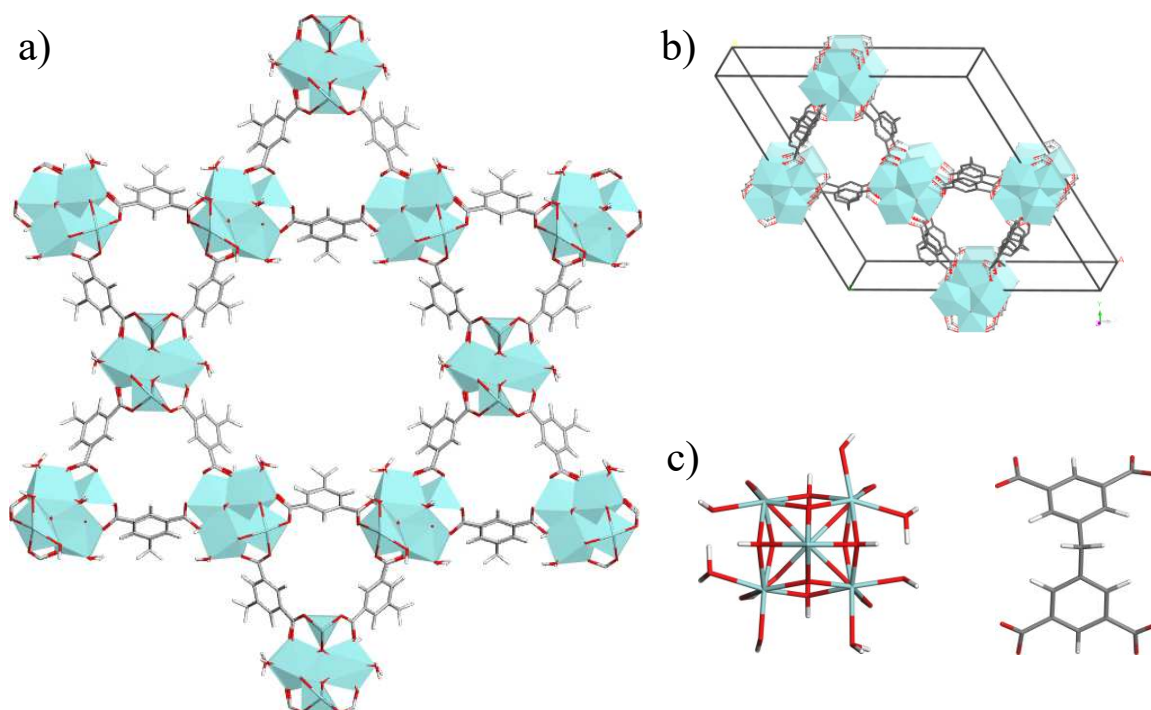
It is to be noted that MIP-177(Ti) demonstrated to be a promising candidate for an efficient degradation of Sarin and retention of the resulting products with a level of performance as attractive as the best Zr-MOFs reported so far. Furthermore, the simulations performed on the two simulants emphasized that diisopropyl phosphorofluoridate mimics better Sarin in terms of the transition states and products obtained during the reaction as well as of the activation energy required to achieve their degradation. It can be explained by the presence of the P-F bond in this simulant, since the hydrolysis reaction of the neurotoxic bond occurs between the same atoms and results in a formation of the same molecule (HF).

5.3 DEGRADATION OF SARIN ON THE ACTIVATED Zr SITE OF Zr-MOFs

The catalytic degradation of Sarin was further explored in MIP-200(Zr) and UiO-66(Zr).

MIP-200(Zr) [$Zr_6(\mu_3-O)_4(\mu_3-OH)_4(\text{mdip})_2(\text{formate})_4$] is a Zr-carboxylate constructed from a Zr_6 oxocluster and tetracarboxylate linker (3,3',5,5'-tetracarboxydiphenylmethane; $H_4\text{mdip}$) and presents remarkable advantages such as the scalable synthesis involving simple, cheap and green chemicals and exceptional chemical and mechanical stability (WANG et al., 2018a). Figure 5.12 reports the constitutive 8-connected $Zr_6(\mu_3-O)_4(\mu_3-OH)_4$ oxocluster secondary building unit with eight carboxylate groups and four terminal hydroxyl and water groups interconnected with $H_4\text{mdip}$ molecules, resulting in a three-dimensional (3D) framework with separated hexagonal and triangular channels along the *c*-axis. The 1D hexagonal channels have a nano-sized free diameter of 14 Å, while the diameter of the smaller triangular tunnels is 6.8 Å. A structural model by replacing all the formates attached to the Zr_6 SBUs with H_2O and OH groups was constructed. Then, the creation of one activated Zr site was considered by removing its bounded $-H_2O$ molecule, however, one can note that the -OH group does not bridge the two metal sites as observed for MIP-177(Ti) (see Figure 5.1c). The DFT-geometry optimization of this formate free model remains almost identical to the pristine structure consisting of four formates per Zr_6 nodes.

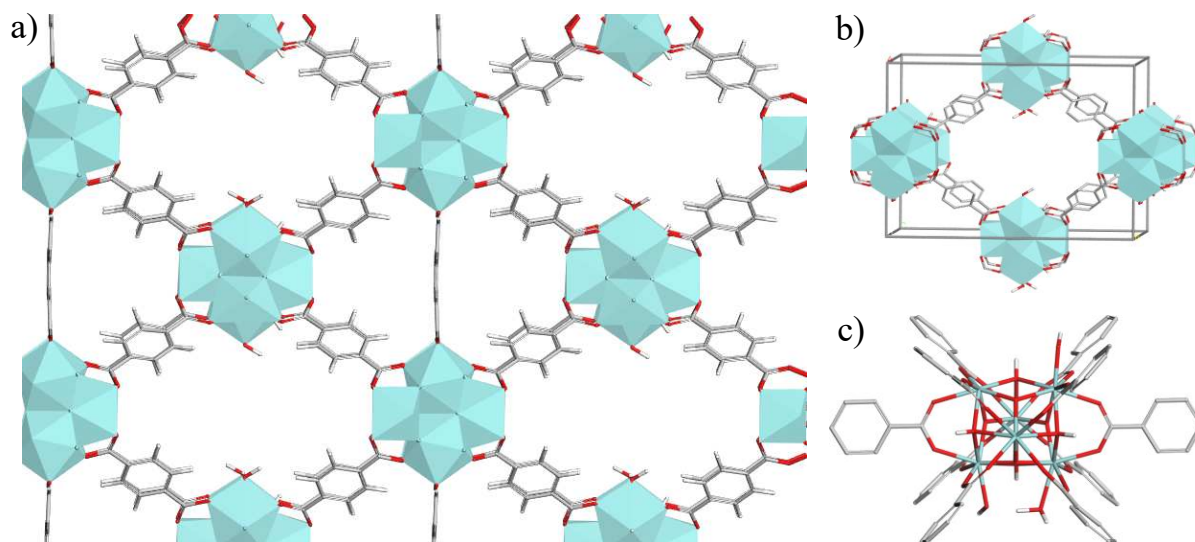
Figure 5.12 - a) Illustration of the crystal structure of MIP-200(Zr), b) Unit cell and c) A single 8-connected SBU and a 4-coordinated H4mdip linker.



Source: Elaborated by the author (2019).

UiO-66(Zr) (UiO stands for University of Oslo) consists of an inner $Zr_6O_4(OH)_4$ where one square face is formed by oxygen atoms supplied by carboxylates while the second square face is formed by oxygen atoms coming from the μ_3-O and μ_3-OH groups. The structure UiO-66(Zr) is constructed by linking 12-connected $[Zr_6(\mu_3-O)_4(\mu_3-OH)_4(COO)_{12}]$ clusters with benzene-1,4-dicarboxylate (BDC) linkers and each zirconium atom is eight-coordinated (Figure 4.13) (CAVKA et al., 2008). However, aiming to use this material for CWA degradation a defective material was chosen in order to facilitate the access of the molecules to the activated sites. The corresponding defective UiO-66(Zr) (also called UiO-66(Zr)-defects6 along the manuscript) was obtained by withdrawing two of the 24 BDC ligands present in the pristine UiO-66(Zr) unit cell, creating an average coordination number of 11 instead of 12 in the ideal structure (ROGGE et al., 2016). This MOF exhibits interesting features as an exceptionally high thermal stability (DECOSTE et al., 2013b) and retain its crystal structure under high pressures (YOT et al., 2016) as well as in relatively harsh acidic environments (LEUS et al., 2016). As was previously described the defects generate by the missing linker in the Zr_6 SBUs were saturated by H_2O and OH groups and one activated Zr site was created by removing its bounded $-H_2O$ molecule.

Figure 5.13 - a) Illustration of the crystal structure of UiO-66(Zr)-defects6, b) Unit cell. c) A single 10-connected SBU.

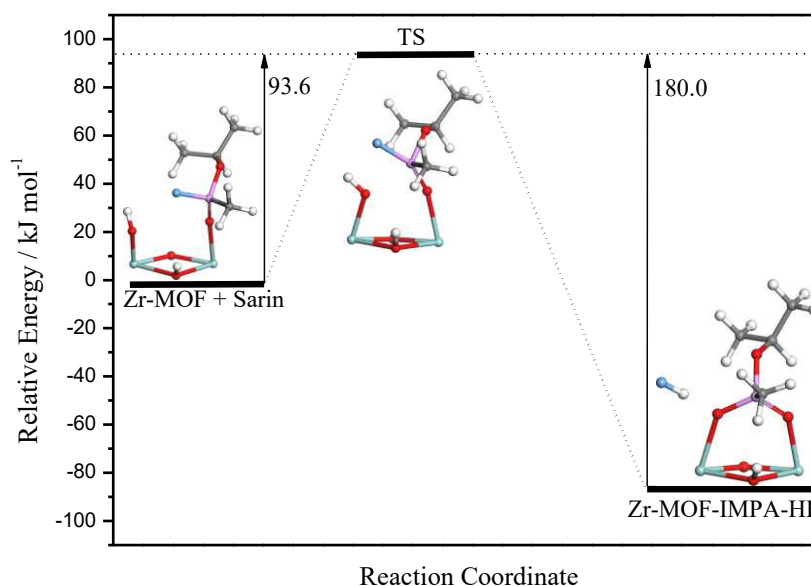


Source: Elaborated by the author (2019).

Considering that the mechanism which corresponds to the nucleophilic addition of the $-OH$ function to the phosphorus atom of Sarin was shown to be the most probable one in the case of MIP-177(Ti) (see section 5.1), I proceeded only with this mechanism to investigate the CWAs degradation using Zr-MOFs. The initial configurations reported in this section were collected from the preliminary Monte Carlo simulations (see chapter 4) (VIEIRA SOARES; MAURIN; LEITÃO, 2019a), and then these geometries were optimized at the DFT level.

Figure 5.14 illustrates the degradation reaction path of Sarin in the cavity of MIP-200(Zr) with the identification of the initial reactant, the transition state and the resulting product.

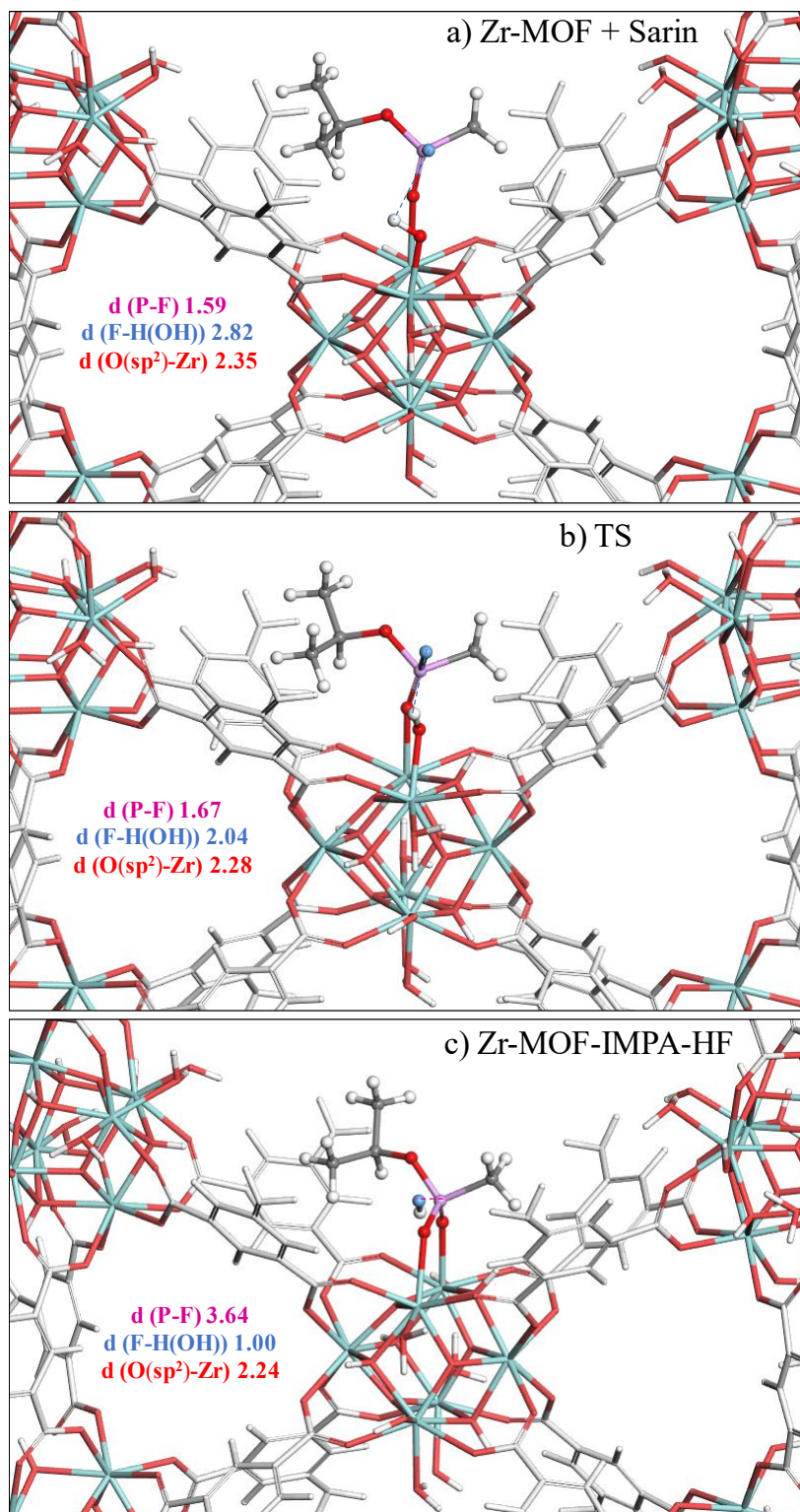
Figure 5.14 - Simulated Minimum Energy Path corresponding to the degradation mechanism of Sarin on the MIP-200(Zr).



Source: Elaborated by the author (2019).

The most stable DFT-optimized configuration of Sarin adsorbed in the cavity of MIP-200(Zr) is shown in Figure 5.15a, where the molecule stays in a preferential conformation in such a way that its oxygen atom interacts with the uncoordinated zirconium with a distance of 2.35 Å while the fluorine atom interacts with the hydroxyl group of the Zr MOF with a separating F-H(OH) distance of 2.82 Å. Along the reaction, one can observe a bond formation between the P atom of Sarin and the O(OH) bonded to the Zr leading to a 5-coordinated geometry of Sarin in the transition state, as evidenced in Figure 5.15b. The energy barrier associated with this process is 93.6 kJ mol⁻¹ (Figure 5.14). After overtaking the transition state, an increase of the distance between phosphorus and fluorine atoms and decrease of the distance separating the oxygen of Sarin and zirconium atom resulting in a stable configuration where the isopropyl methyl phosphonic acid is coordinated in a bidentate manner to the inorganic node of the MIP-200(Zr) (Figure 5.15c).

Figure 5.15 - Illustration of the degradation mechanism of Sarin on the Zr activated site of MIP-200(Zr). a) Reactant (Zr-MOF + Sarin), b) Transition state (TS) and c) Product (Zr-MOF-IMPA-HF). The main distances involved in the degradation process, P-F (pink), F-H(OH) (blue) and O(sp²)-Zr (red) are represented and expressed in Å.

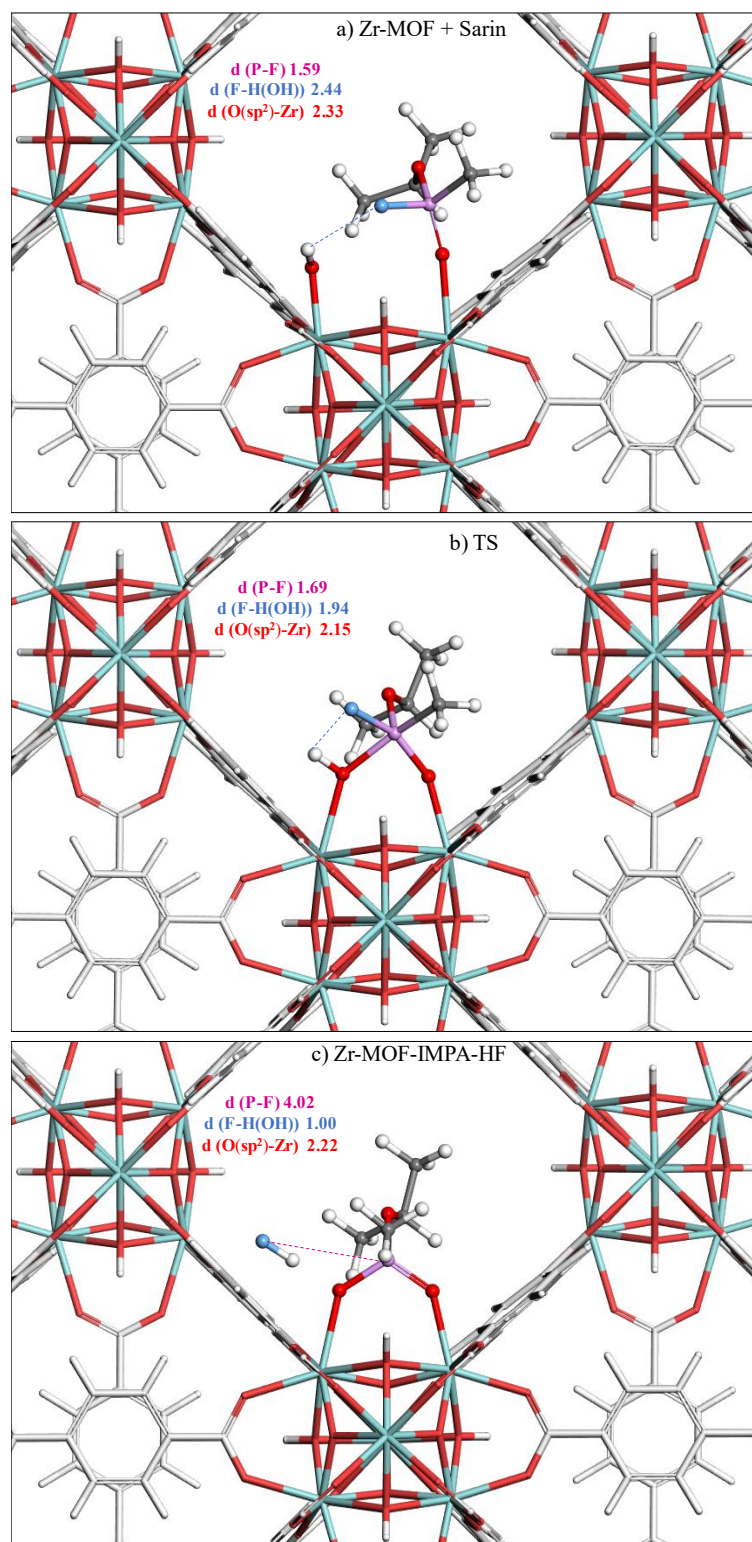


Source: Elaborated by the author (2019).

Figure 5.16 illustrates the degradation mechanism of Sarin by UiO-66(Zr) starting with the first optimized configuration, where sarin is interacting with the $-OH$ group $H(OH)-F$ (2.34 Å, blue dashed line – see Figure 5.16b) and with the Zr site $O(\text{sarin})-Zr$ (2.33 Å). The configuration along the degradation reaction is similar to that already described above for MIP-200(Zr) (cf. Figure 5.15 and Figure 5.16), however it is to be noted that Sarin shows closer distances to the activated site in the structures formed by Zr atom than by Ti atom (MIP-177(Ti)). It occurs due to the space available for the molecule adsorption, i.e. the missing linkers in the UiO-66(Zr) make easily the access of the molecules to the activated sites. Moreover, the manner of the coordination of the H4mdip ligands to the Ti-SBU becomes some adsorption modes, near the activated sites, sterically hindered even when compared with MIP-200(Zr), which is formed by the same ligand. It can be explained by the fact that the coordination of the ligands and the consequential spare space near to the activated sites is directly correlated to the topology of the SBU, which is the same for the MOFs MIP-200(Zr) and UiO66-defects6(Zr).

Then, the next reaction step is the decomposition of the CWA via the coordination of the molecule to the SBU indicated in the transition state (see Figure 5.16b) with a subsequent elimination of HF (see Figure 5.16c).

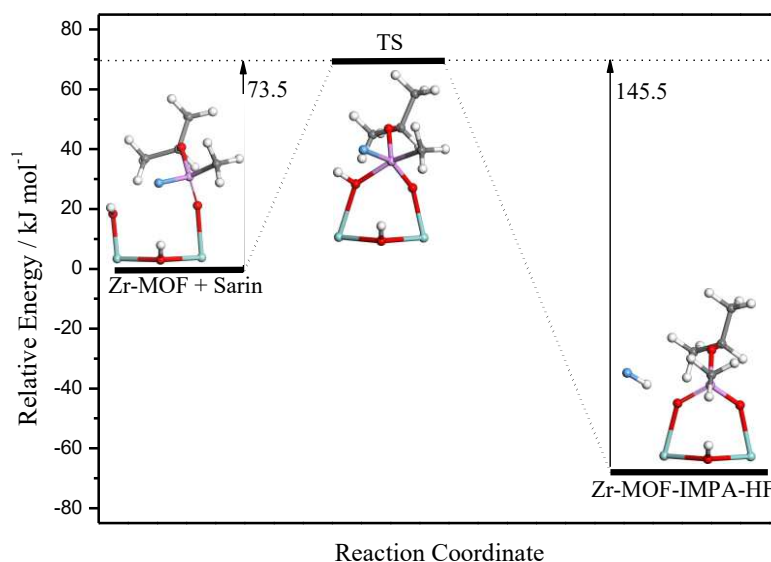
Figure 5.16 - Illustration of the degradation mechanism of Sarin on the Zr activated site of UiO-66(Zr). a) Reactant (Zr-MOF + Sarin), b) Transition state (TS) and c) Product (Zr-MOF-IMPA-HF). The main distances involved in the degradation process, P-F (pink), F-H(OH) (blue) and O(sp²)-Zr (red) are represented and expressed in Å.



Source: Elaborated by the author (2019).

The MEP associated with this reaction is illustrated in Figure 5.17, with the energy barrier of 73.5 kJ mol^{-1} .

Figure 5.17 - Simulated Minimum Energy Path corresponding to the degradation mechanism of Sarin on the UiO66-defects6(Zr).



Source: Elaborated by the author (2019).

The MEPs reported in Figures 5.14 and 5.17 reveal activation energy barriers of 93.6 kJ mol^{-1} and 73.5 kJ mol^{-1} for MIP-200(Zr) and UiO-66(Zr) respectively. This range of value is similar to the free energy previously reported (MOMENI; CRAMER, 2018a) for the hydrolysis of Sarin in diverse Zr-MOFs including MOF-808 (79.1 kJ mol^{-1}), NU-1000 (75.3 kJ mol^{-1}) and it is similar to the free energy described in section 5.1 for the Ti-MOF MIP-177(Ti) (78.6 kJ mol^{-1}). As it is already known both, the Ti and the Zr MOFs are expected to have a good performance for the catalytic degradation of Sarin, however the MIP-200(Zr) demands higher energy when compared to the MIP-177(Ti). It can be also noted that the products represent the most stable configuration along the whole reaction path $-86.4 \text{ kJ mol}^{-1}$ (for MIP-200(Zr)) and $-72.0 \text{ kJ mol}^{-1}$ (for UiO-66(Zr) as previously described for MIP-177(Ti) (see section 5.2). The desorption energy of IMPA and HF from the product (calculated by using equation 5.1) are $175.8 \text{ kJ mol}^{-1}$ (for MIP-200(Zr)) and $177.6 \text{ kJ mol}^{-1}$ (for UiO66-defects6(Zr)), which are higher values when compared with the Ti-MOF. These results suggest that UiO-66(Zr) is the most appropriate MOF for the degradation of Sarin, since it requires the less amount of energy to degrade sarin and also presented strong retention of the resulting IMPA product into their pores ensuring that the most toxic molecule will not be regenerated.

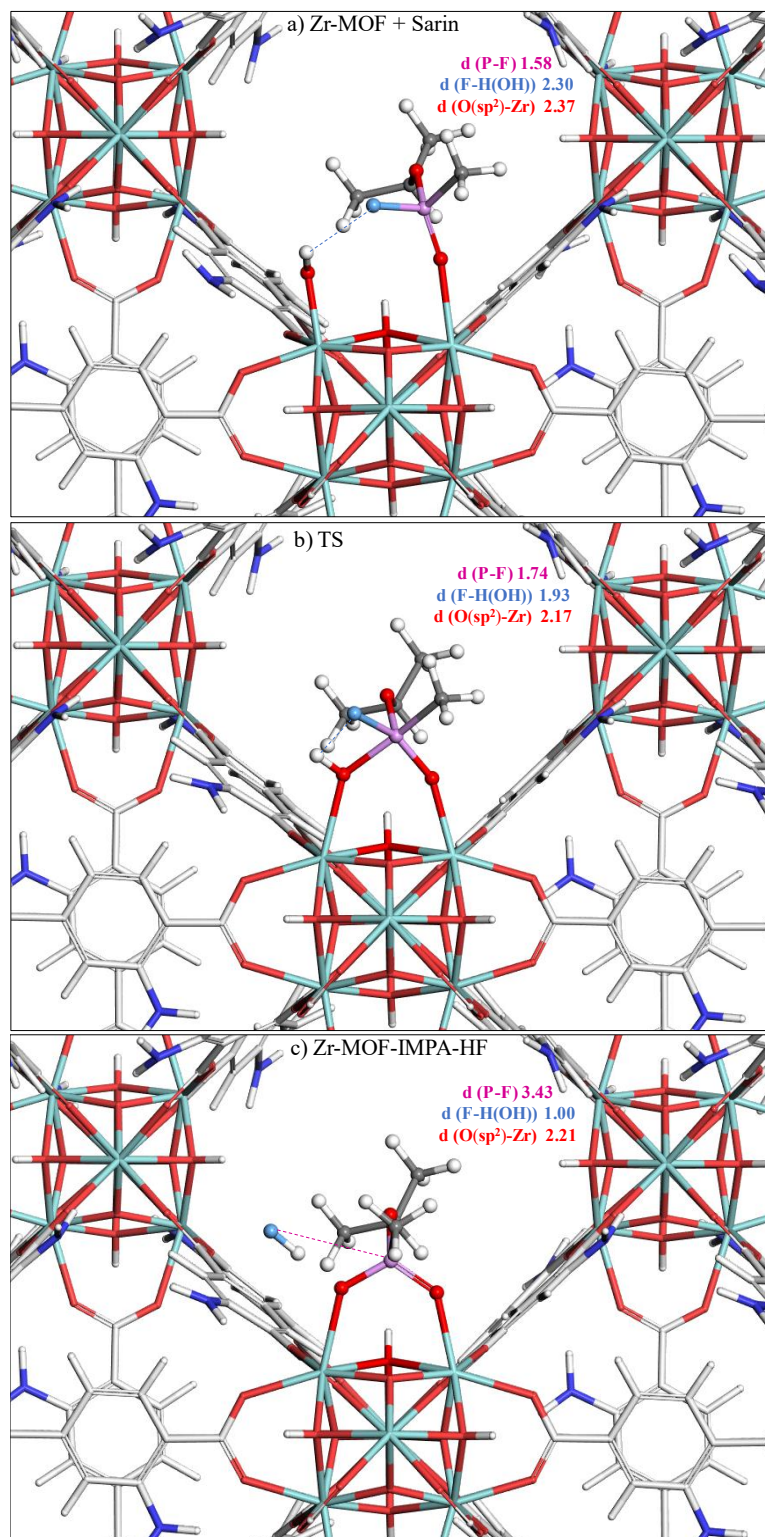
5.4 EFFECT OF THE MOF LINKER FUNCTIONALIZATION ON THE DEGRADATION OF SARIN AND SOMAN: CASE OF UiO-66(Zr) AND UiO-66(Zr)-NH₂

As a further stage, the effect of the functionalization of the organic linker of UiO-66(Zr) by amine groups was investigated for the hydrolysis reaction of Sarin and Soman. Figure 5.18 illustrates the resulting degradation mechanism of Sarin in UiO-66(Zr)-NH₂ starting with the DFT-optimized configuration, where sarin is coordinated towards Zr while it also interacts with the -OH group of the MOF via its fluorine atom (2.30 Å, blue dashed line).

The degradation mechanism proceeds with the decomposition of the CWA via the coordination of Sarin to the SBU as indicated in the TS reported in Figure 5.18, leading to the formation of IMPA, which is coordinated in a bidentate manner to the inorganic node of the Zr-MOF as well as HF (Figure 5.18c). It should be noted that the configurations along the degradation reaction are almost identical to that described above for Sarin on UiO-66(Zr) (cf. Figure 5.16 and Figure 5.18).

Figure 5.18 - Illustration of the degradation mechanism of Sarin in UiO66-defects6(Zr)-NH₂. a) Reactant (Zr-MOF + Sarin), b) Transition state (TS) and c) Product (Zr-MOF-IMPA-HF).

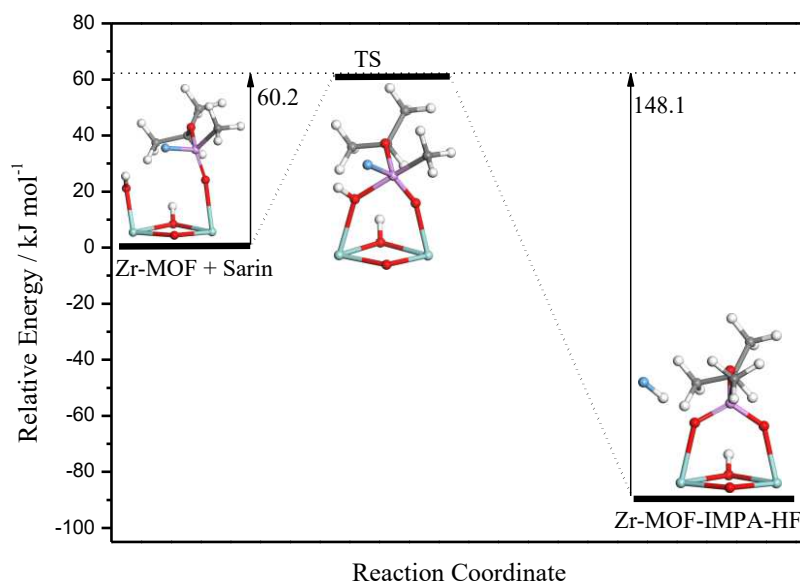
The main distances involved in the degradation process, P-F (pink), F-H(OH) (blue) and O(sp²)-Zr (red) are represented and expressed in Å.



Source: Elaborated by the author (2019).

The corresponding MEP reported in Figure 5.19 implies an activation energy barrier of 60.2 kJ mol^{-1} . Despite the similarity between the configurations along the degradation mechanism the energy barrier slightly decreases when the amino-functionalized MOF is considered (cf. Figure 5.19 and Figure 5.17).

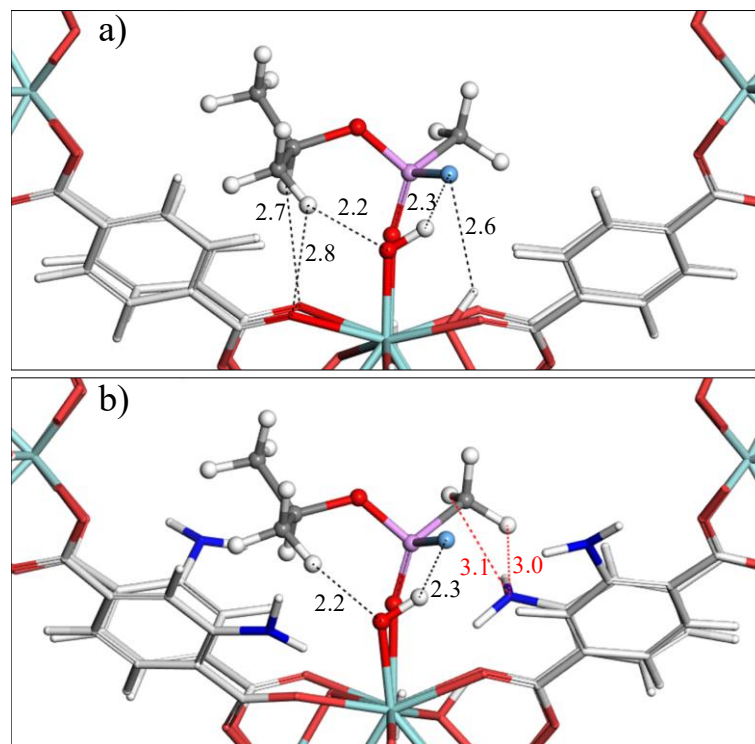
Figure 5.19 - a) Simulated Minimum Energy Path corresponding to the degradation mechanism of Sarin on the UiO66-defects6(Zr)-NH₂.



Source: Elaborated by the author (2019).

Noteworthy, Sarin is most stabilized in the non-functionalized UiO-66(Zr) because this molecule interacts slightly strongly with the SBU while in the functionalized structure there is a predominance of weak interactions between the nerve agent and the linkers, as illustrated in Figure 5.20. This scenario leads to a higher energy barrier of 71.5 kJ mol^{-1} to degrade Sarin in the absence of the amino groups. Therefore, these calculations suggest that UiO66-defects6(Zr)-NH₂ is expected to outperform the best Zr-MOFs explored so far for the degradation of Sarin.

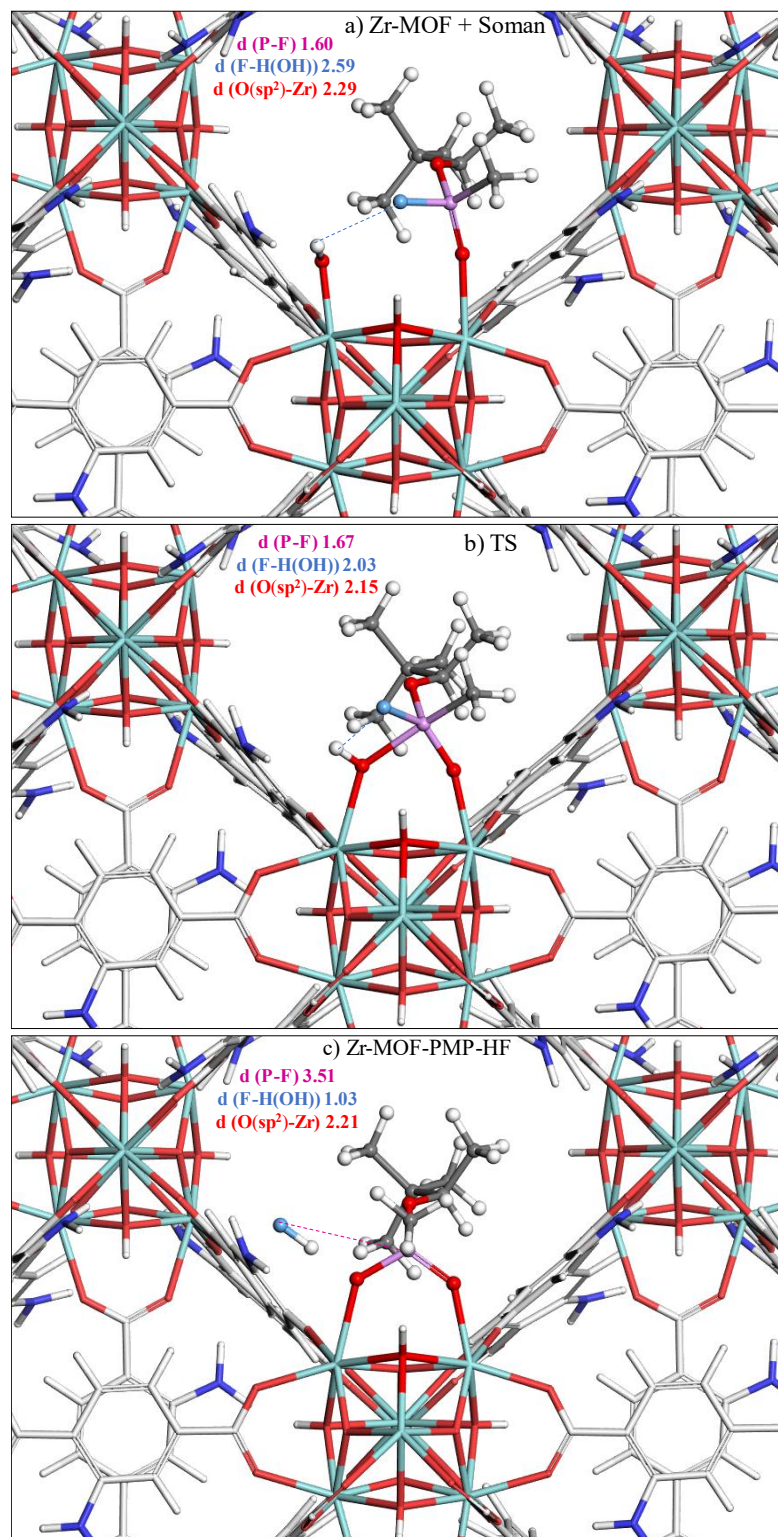
Figure 5.20 - Illustration of the adsorption configurations (Reactants) involved in the Sarin degradation process. a) UiO-66(Zr) and b) UiO-66(Zr)-NH₂. The main distances between Sarin and the SBU (black) and Sarin and the linker (red) are expressed in Å.



Source: Elaborated by the author (2019).

The most stable optimized configuration of Soman initially adsorbed in the pore of the UiO66-defects6(Zr)-NH₂ corresponding to the reactant is reported in Figure 5.21a. During the first step of the reaction, Soman coordinated to the Zr atom through its oxygen atom (sp²) while its fluorine atom interacts with the hydroxyl group of UiO66-defects6(Zr)-NH₂ with a separating F-H(OH) distance of 2.59 Å. As the reaction proceeds through the TS, there is a bond formation between the P atom of Soman and the terminal -OH group of the MOF and this leads to a 5-coordinated geometry of Soman as evidenced in Figure 5.21b. Beyond TS, one can observe a progressive increase of the distance separating the phosphorus and fluorine atoms of Soman (Figure 5.21) that finally results to a breaking of the corresponding bond and consequently the formation of HF. This gives rise to a stable configuration for the product where the Pinacolyl methylphosphonic acid is coordinated in a bidentate manner to the inorganic node of the Zr-MOF (Figure 5.21c). One can note in the degradation mechanism of Soman that the nucleophilic addition of the -OH function of UiO66-defects6(Zr)-NH₂ to the phosphorus atom activates the phosphate ester function and further leads to the formation of a phosphonate product and the release of hydrogen fluoride, as observed for Sarin.

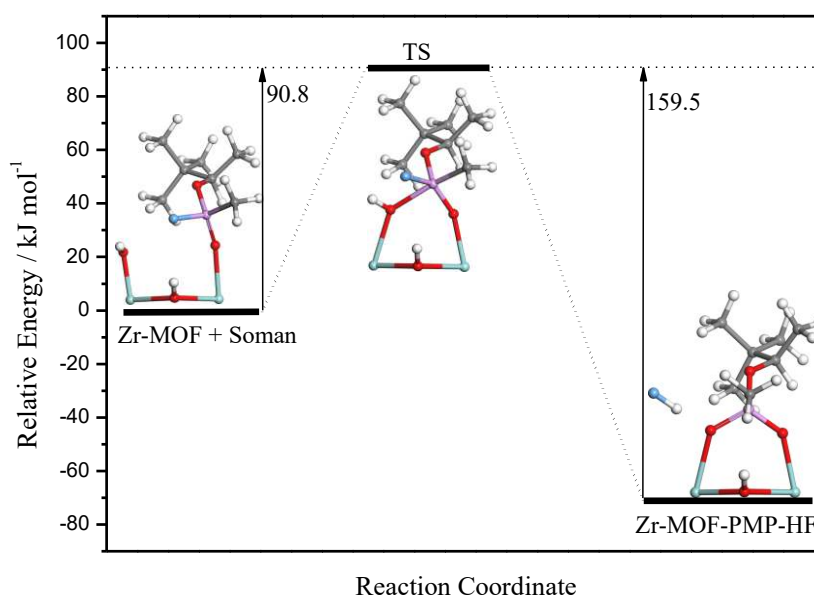
Figure 5.21 - Illustration of the degradation mechanism of Soman in UiO66-defects6(Zr)-NH₂. a) Reactant (Zr-MOF + Soman), b) Transition state (TS) and c) Product (Zr-MOF-PMP-HF). The main distances involved in the degradation process, P-F (pink), F-H(OH) (blue) and O(sp²)-Zr (red) are represented and expressed in Å.



Source: Elaborated by the author (2019).

The simulated MEP of the corresponding reaction is reported in Figure 5.22 with the identification of the initial reactant, TS and the resulting product. The activation energy barrier required for this hydrolysis reaction is 90.8 kJ mol^{-1} . One can also note that the product represents the most stable configuration along the whole reaction path ($-68.7 \text{ kJ mol}^{-1}$). This indicates that the coordination of PMP to the inorganic node of UiO66-defects6(Zr)-NH₂ leads to the formation of a stable complex. Finally, the desorption energy of PMP and HF from the product calculated by using equation 5.1 is predicted to be relatively high, i.e. $146.1 \text{ kJ mol}^{-1}$. This observation emphasizes that UiO66-defects6(Zr)-NH₂ not only allows the degradation of Soman but also a strong retention of the resulting IMPA product into its pore.

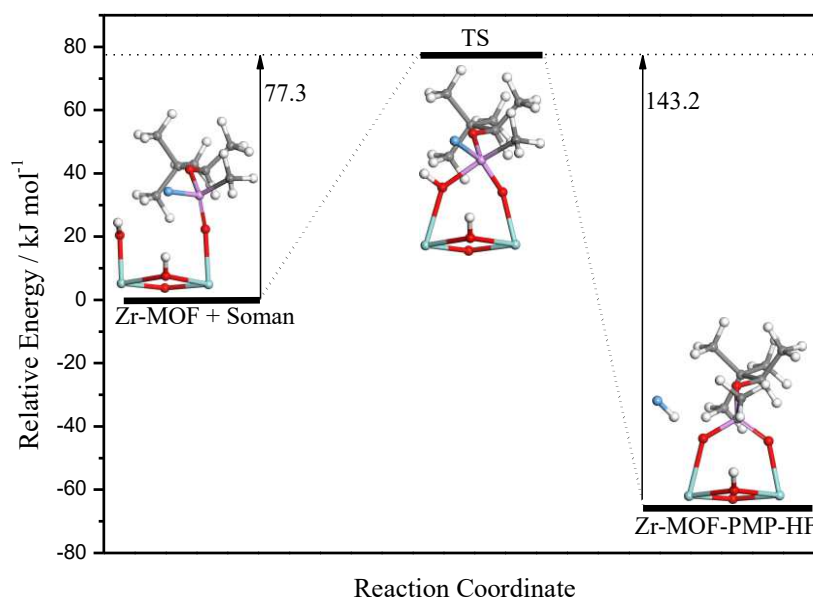
Figure 5.22 - Simulated Minimum Energy Path corresponding to the degradation mechanism of Soman in UiO66-defects6(Zr)-NH₂.



Source: Elaborated by the author (2019).

Figure 5.23 illustrates the degradation mechanism of Soman by UiO66-defects6(Zr) where the energy barrier is slightly lower than the value calculated for the degradation on the functionalized UiO-66(Zr) (Figure 5.22).

Figure 5.23 - Simulated Minimum Energy Path corresponding to the degradation mechanism of Soman in UiO66-defects6(Zr).



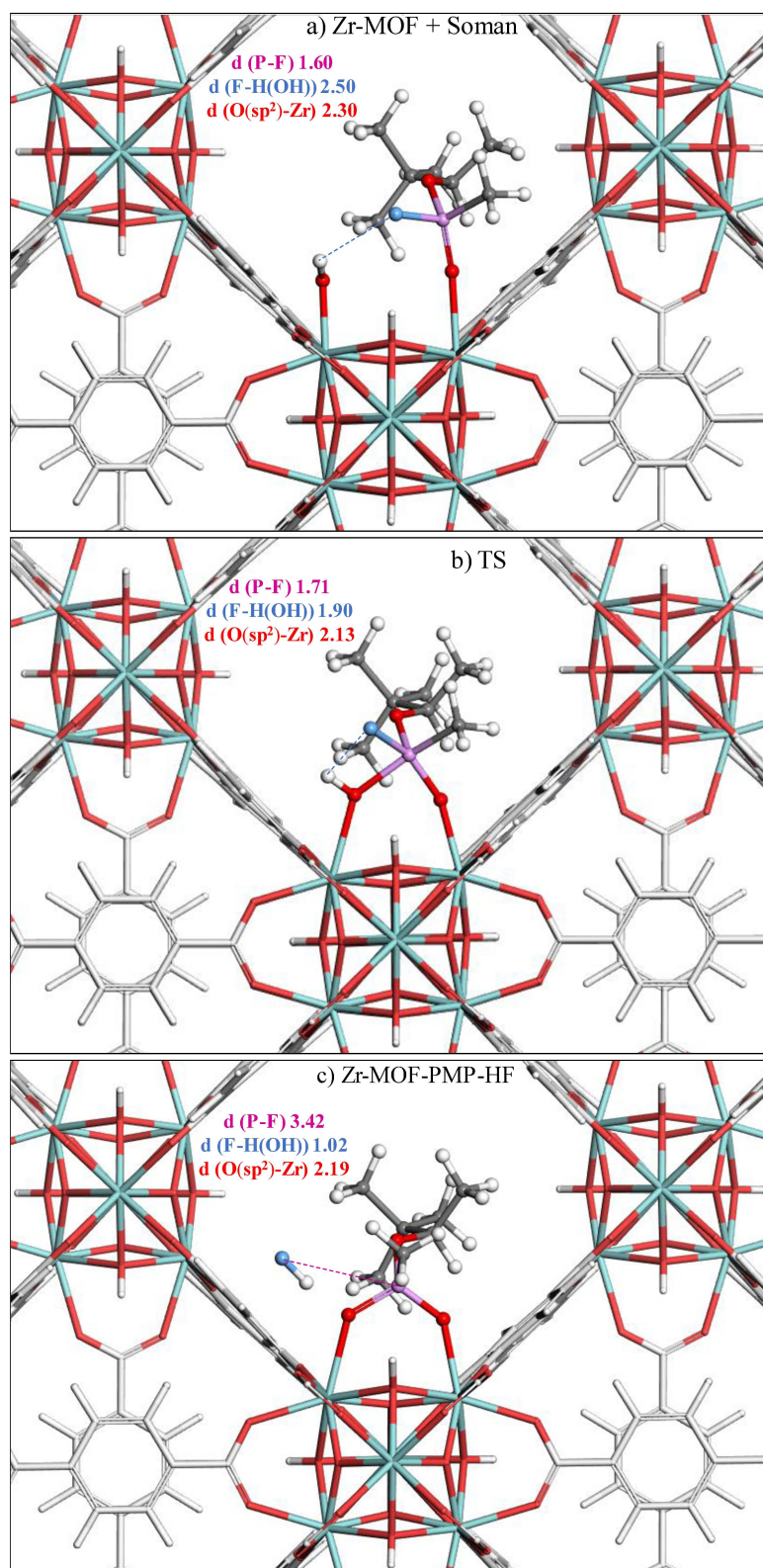
Source: Elaborated by the author (2019).

Figure 5.24 exhibits the main configurations along the degradation reaction. The reactant indicated that Soman interacts with the $-OH$ group $H(OH)-F$ (2.50 \AA , blue dashed line – see Figure 5.24b) and with the Zr site $O(\text{sarin})-Zr$ (2.30 \AA). It should be noted that the configurations of the reactant, TS and product are similar to that already described above for UiO66-defects6(Zr)- NH_2 (cf. Figure 5.21 and Figure 5.24).

It is known in the literature that is not obvious to control the guest adsorption strength through modifying the linker with different functional groups because these molecules typically interact strongly with the SBU rather than the linker. For example, strong interactions with the SBU are typically due to the presence of defects, however it was observed only for the degradation of Sarin on the non-functionalized UiO66-defects6(Zr). For Soman, the adsorption energies and the interactions with the pore wall indicated mostly the presence of weakly interactions between Soman and the linkers, but not necessarily with the amino groups, as can be observed in Figure 5.25. Another interesting point is that in the UiO66-defects6(Zr)- NH_2 Soman interacts with four different linkers, that makes difficult the approaching of phosphorus atom to the $-OH$ group for reaching the penta-coordinated configuration in the transition state and therefore it demands more energy for this process. All these factors can be directly associated with the bulkier volume of Soman when compared to Sarin.

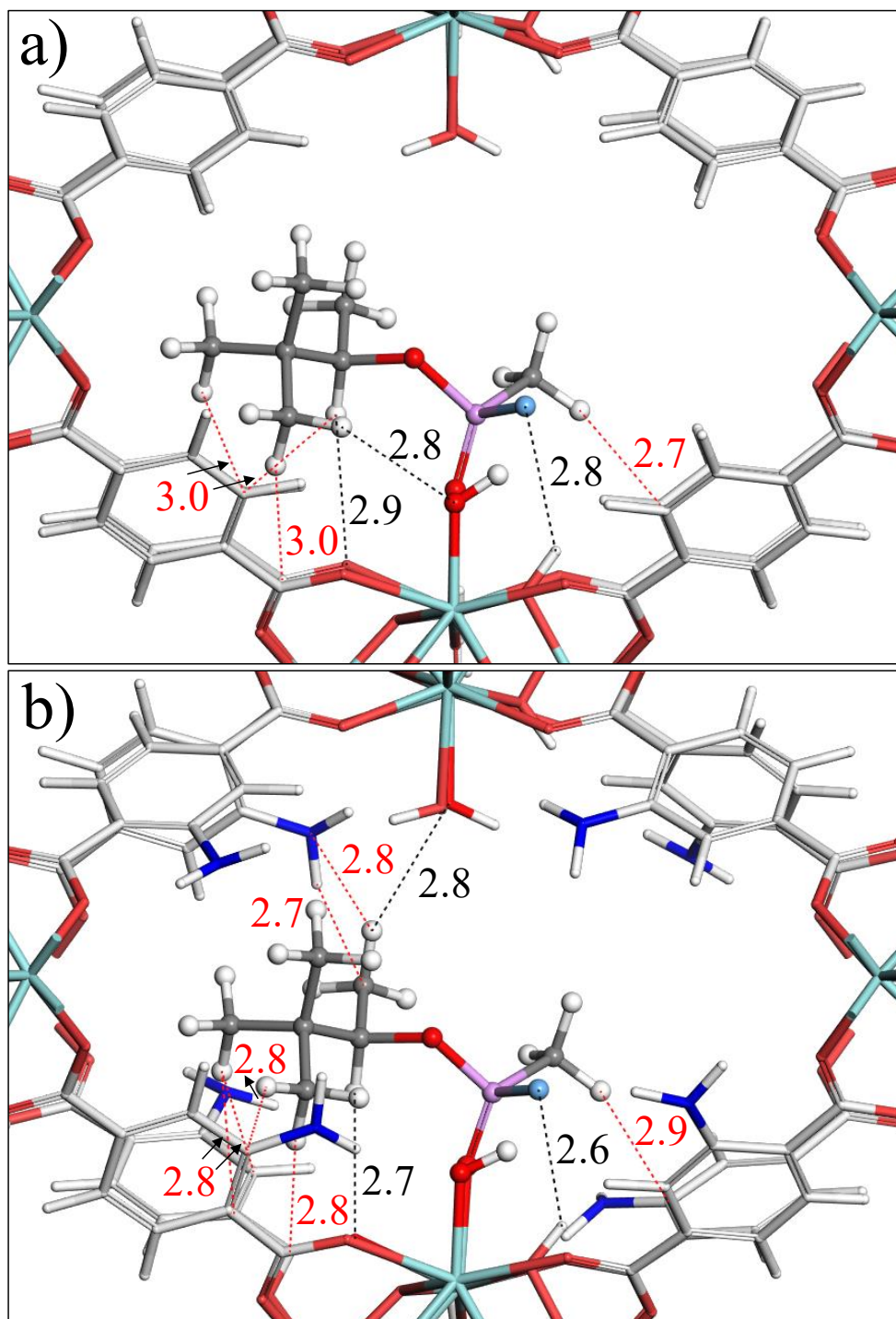
Figure 5.24 - Illustration of the degradation mechanism of Soman in UiO66-defects6(Zr). a) Reactant (Zr-MOF + Soman), b) Transition state (TS) and c) Product (Zr-MOF-PMP-HF).

The main distances involved in the degradation process, P-F (pink), F-H(OH) (blue), O(sp²)-Zr (red).



Source: Elaborated by the author (2019).

Figure 5.25 - Illustration of the adsorption configurations (Reactants) involved in the Soman degradation process. a) Non-functionalized UiO-66(Zr) and b) Functionalized UiO-66(Zr). The main distances between Soman and the SBU (black) and Sarin and the linker (red) are expressed in Å.



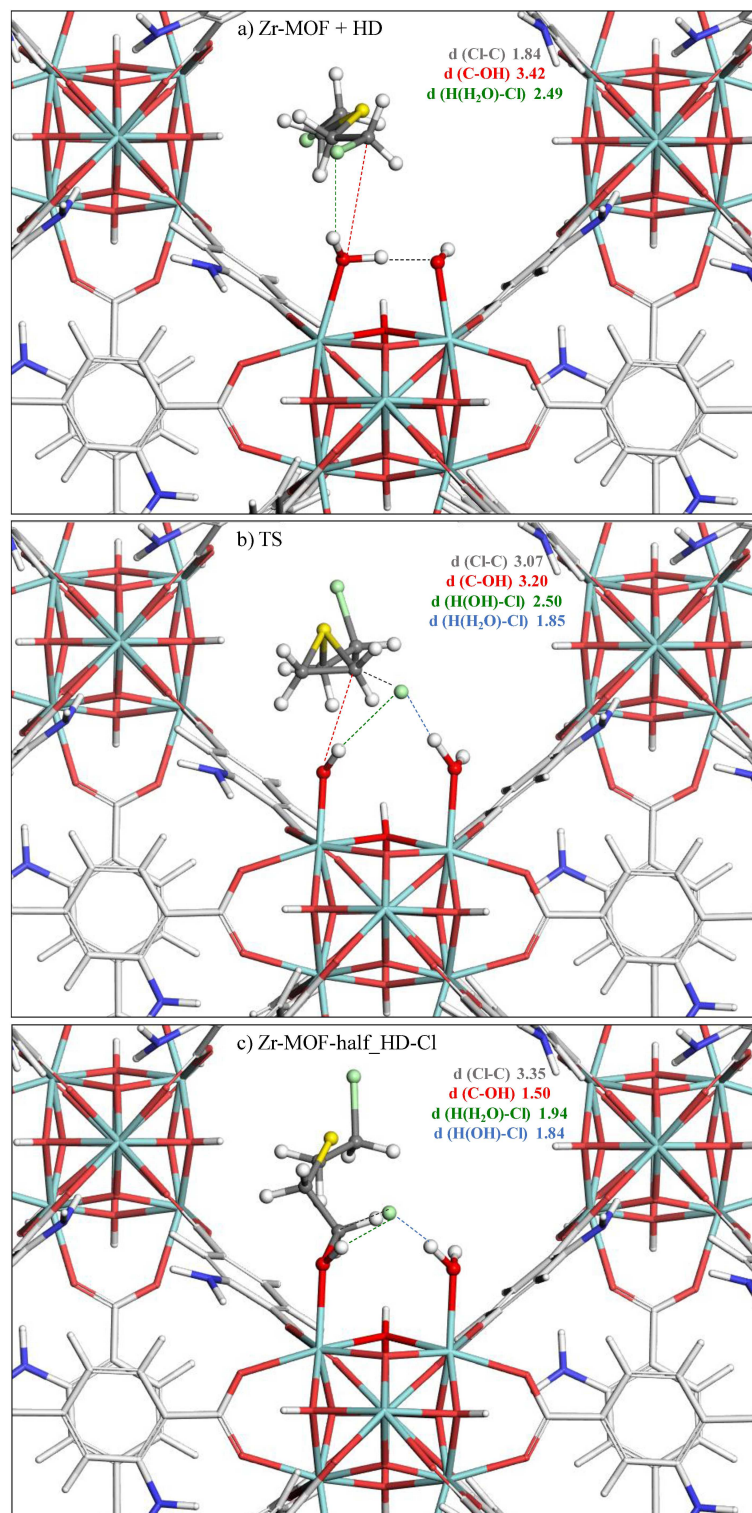
Source: Elaborated by the author (2019).

5.5 DEGRADATION OF HD ON THE ACTIVATED Zr SITE OF UiO-66(Zr) AND UiO-66(Zr)-NH₂

Considering the potential of UiO66-defects6(Zr) and UiO66-defects6(Zr)-NH₂ to degrade Sarin (see Figure 5.17 and Figure 5.19) and Soman (see Figure 5.22 and Figure 5.23) and the fact the Sulfur mustard (HD) is more commonly used during conflicts attacks, the hydrolysis reaction of this blister agent and its simulant 2-Chloroethyl ethyl sulfide, also known as half-mustard (CEES) were further investigated. The hydrolytic pathway, i.e. in the presence of water, was chosen since this is one of the most probable ways of remedying the contamination caused by this CWA.

The degradation profile of HD on UiO66-defects6(Zr)-NH₂ is summarized in Figure 5.26. The first arrangement indicates the most stable optimized configuration of HD adsorbed in the cavity of the material, where the molecule adopts a preferential conformation in such a way that the chlorine atom interacts with the water coordinated to Zr through with a distance of 2.49 Å (green dashed line). One can also note a strong hydrogen bond between this coordinated water and the neighbor terminal -OH group of the MOF (1.56 Å, black dashed line). At the transition state the hydrogen atom from water migrates to the hydroxyl moiety and both interact with the chlorine atom of HD with characteristic distances of 2.50 Å and 1.85 Å respectively (Figure 5.26b). The conformation observed at this stage was previously proposed by experimental studies (LÓPEZ-MAYA et al., 2015; PETERSON; WAGNER, 2014). Finally, the product shows a bond formation between the C atom of HD and the terminal OH group of the MOF. It is interesting to note that the chlorine atom is involved in a strong interaction with the OH group (1.94 Å) and coordinated water (1.84 Å), as evidenced in Figure 5.26c.

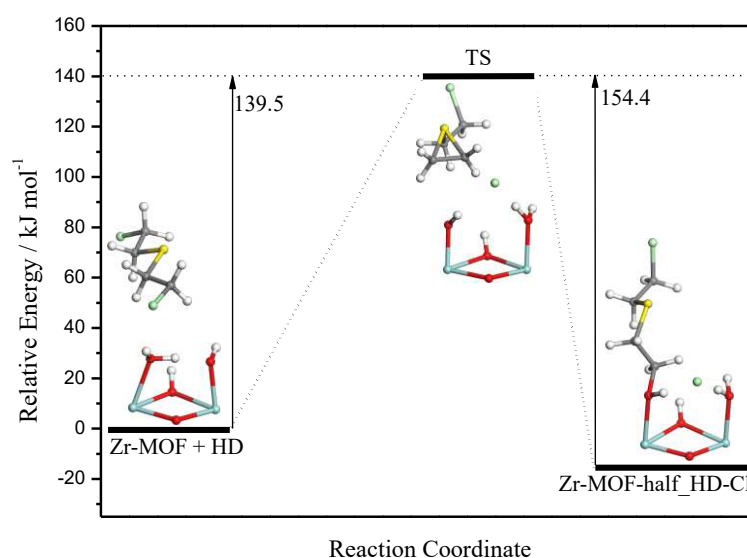
Figure 5.26 - Illustration of the degradation mechanism of HD on the UiO66-defects6(Zr)-NH₂. a) Reactant (Zr-MOF + HD), b) Transition state (TS) and c) Product (Zr-MOF-half_HD-Cl). The main distances involved in the degradation process, Cl-C (gray), C-OH (red), H(H₂O)-Cl (green) and H(OH)-Cl (blue) are represented and expressed in Å.



Source: Elaborated by the author (2019).

The energy barrier associated with the hydrolysis of HD is $139.5 \text{ kJ mol}^{-1}$ (Figure 5.27). Analyzing this pathway, one can note that the difference of the energy between the initial configuration and the product is rather low. This indicates that UiO66-defects6(Zr)-NH₂ shows good performance for the catalytic degradation of HD. The desorption energy of half mustard and HCl from the product calculated by using equation 5.1 is predicted to be 66.5 kJ mol^{-1} .

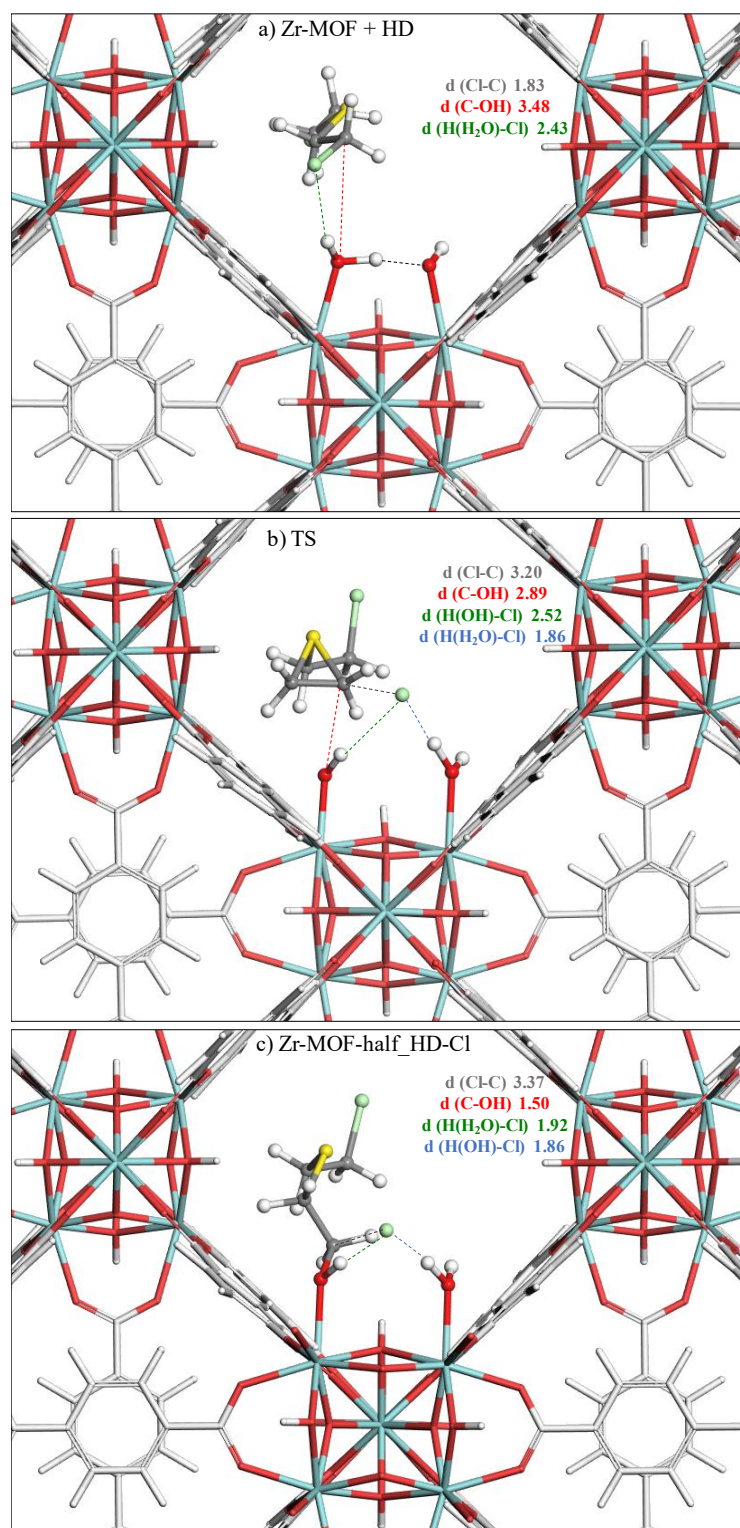
Figure 5.27 - Simulated Minimum Energy Path corresponding to the degradation mechanism of HD on the UiO66-defects6(Zr)-NH₂.



Source: Elaborated by the author (2019).

For comparison, the degradation mechanism of HD was also explored for the non-functionalized UiO-66(Zr). Figure 5.28 showed the conformation of sulfur mustard and the main distances between the molecule and the -OH group and water along the hydrolytic pathway. The initial configuration showed chlorine interacting with the hydrogen from the coordinated water with a distance of 2.43 \AA (Figure 5.28a, green dashed line) and a strong hydrogen bond between this water molecule and the -OH group of UiO-66(Zr) (1.51 \AA , black dashed line) leading to a proton transfer from water to the hydroxyl moiety (Figure 5.28b). The molecule adopts the same conformation observed for the mechanism on the functionalized UiO-66(Zr) reported above, where sulfur forms a three-membered ring with the carbons and the chlorine atom is getting close to the SBU until be stabilized for two hydrogen bonds with the OH (1.92 \AA) and coordinated water (1.86 \AA), as demonstrated in Figure 5.28c.

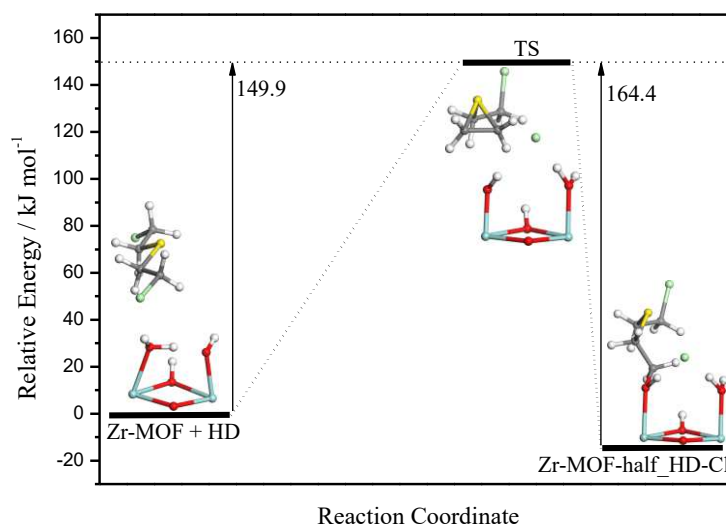
Figure 5.28 - Illustration of the degradation mechanism of HD on the UiO66-defects6(Zr). a) Reactant (Zr-MOF + HD), b) Transition state (TS) and c) Product (Zr-MOF-half_HD-Cl). The main distances involved in the degradation process, Cl-C (gray), C-OH (red), H(H₂O)-Cl (green) and H(OH)-Cl (blue) are represented and expressed in Å.



Source: Elaborated by the author (2019).

The MEP reported in Figure 5.29 implies an activation energy barrier of $149.9 \text{ kJ mol}^{-1}$, which is slightly higher compared to the value obtained for the mechanism where the BDC linkers were functionalized with amino groups (Figure 5.27). It is to be noted that the effect on the functionalization did not affect the adsorption of the molecule, where the interactions between HD and the MOF are only with the atoms from the SBU, as reported for Sarin, however here the interactions are exactly the same when compared the MOF functionalized with the non-functionalized one.

Figure 5.29 - Simulated Minimum Energy Path corresponding to the degradation mechanism of HD on the UiO66-defects6(Zr).

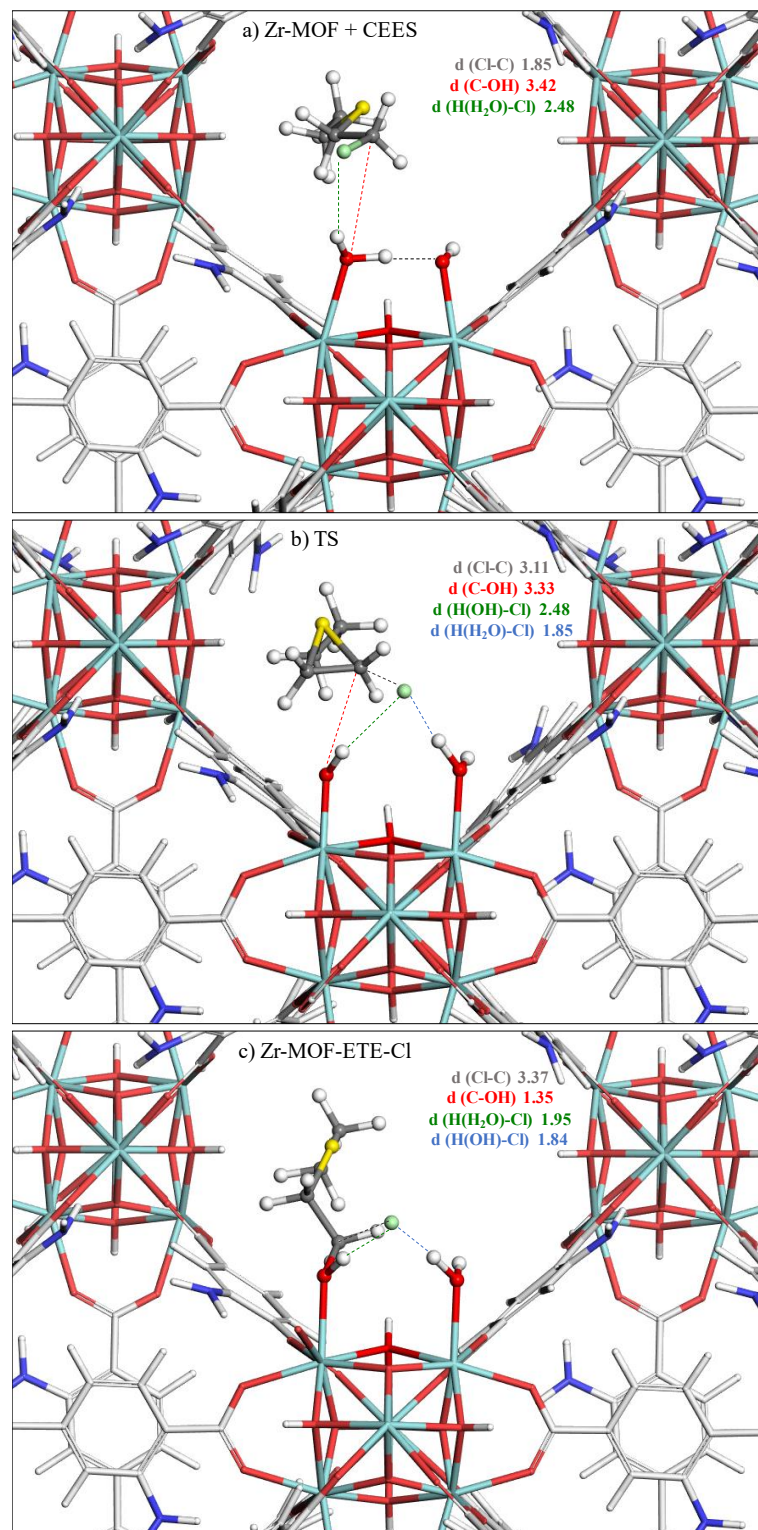


Source: Elaborated by the author (2019).

5.5.1 Degradation of the simulant of HD on the activated Zr site of UiO-66(Zr) and UiO-66(Zr)-NH₂

The degradation mechanism of the simulant CEES was further explored for UiO66-defects6(Zr) and UiO66-defects6(Zr)-NH₂, however how both demonstrated the same behavior only the comparison for the functionalized UiO66-defects6(Zr) is described in this thesis. Figure 5.30 shows the main configurations involved in this reaction pathway. The initial configuration, the TS and the product formed during the reaction are very similar than that evidenced for HD, with in this case the formation of the deactivated 2-(Ethythio)ethanol (ETE) molecule (cf. Figure 5.30 and Figure 5.27). This observation is consistent with an energy barrier associated with the degradation mechanism of 2-Chloroethyl ethyl sulfide ($126.0 \text{ kJ mol}^{-1}$) (Figure 5.31) relatively similar to the value calculated for HD ($139.5 \text{ kJ mol}^{-1}$) (Figure 5.27).

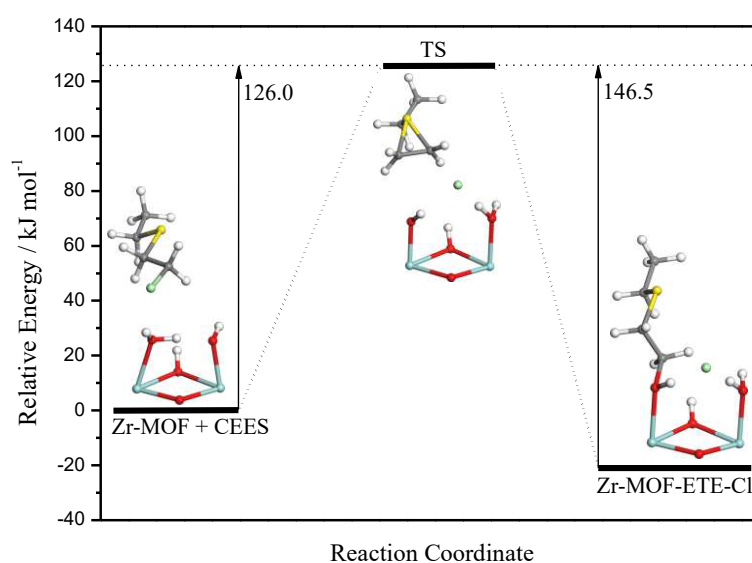
Figure 5.30 - Illustration of the degradation mechanism of CEES on the UiO66-defects6(Zr)-NH₂. a) Reactant (Zr-MOF + CEES), b) Transition state (TS) and c) Product (Zr-MOF-ETE-Cl). The main distances involved in the degradation process, Cl-C (gray), C-OH (red), H(H₂O)-Cl (green) and H(OH)-Cl (blue) are represented and expressed in Å.



Source: Elaborated by the author (2019).

The calculation performed on the CEES simulant revealed its potential to mimic a real scenario of the sulfur mustard in terms of the configurations obtained during the reaction as well as of the activation energy required to achieve their degradation. Interestingly, for HD and CEES one can observe that the product and the initial state have similar energies, indeed it seems that it is possible to regenerate the sites. This is not possible for Sarin or Soman, where the products represent the most stable configurations in the entire mechanism.

Figure 5.31 - Simulated Minimum Energy Path corresponding to the degradation mechanism of CEES in UiO66-defects6(Zr)-NH₂.



Source: Elaborated by the author (2019).

5.6 CONCLUSION

The periodic DFT calculations explored for the first time the ability of a Ti-MOF, namely the MIP-177(Ti) for the catalytic degradation of Sarin and also the deactivation of Sarin, Soman and Sulfur mustard on the activated Zr-site of MIP-200(Zr) and UiO66-defects6(Zr) and UiO66-defects6(Zr)-NH₂.

These simulations demonstrated the attractiveness of MIP-177(Ti) to degrade Sarin with a level of performance similar than the best Zr-MOFs explored so far. The mostly probable degradation mechanism proceeds with a coordination of Sarin towards the activated Ti site via its oxygen atom, leading to the formation of isopropyl methyl phosphonic acid coordinated in a bidentate manner to the inorganic node of the Ti-MOF and the release of HF. The resulting product was shown to be highly stable and associated with a high energy required to desorb the

so-formed IMPA. This observation emphasizes that MIP-177(Ti) is able to strongly retain the IMPA molecule once fixed to the Ti site. The exploration of the same degradation mechanism for two standard simulants of Sarin, revealed that DIFP reproduces much better the catalytic behavior of Sarin than DMMP not only in terms of degradation mechanisms but also in terms of activation energy required to proceed the corresponding reaction.

The Zr-MOFs (MIP-200(Zr) and UiO-66(Zr)) also showed a good performance to degradate Sarin, Soman and Sulfur mustard. Besides that, the effect of the functionalization of the linkers with amino group did not present a satisfactory improving in the activation energy. The adsorbed Sarin was most stabilized in the non-functionalized UiO-66(Zr) because it interacts strongly with the SBU while Soman interacts more with the linkers in the functionalized structure while the adsorption of Sulfur mustard was not affected by the presence of the amino groups. The simulant of Sulfur mustard CEES also showed an excellent performance to mimic this blister agent in terms of degradation mechanisms and activation energy in the hydrolytic pathway as DIFP did for Sarin. This conclusion is of importance for the future experimental exploration that should proceed with the most reliable simulants to further extrapolate the behavior of the real toxic molecules.

This overall computational study led to the publication of one article (VIEIRA SOARES; MAURIN; LEITÃO, 2019b) and another manuscript is being prepared with our collaborators from Korea Research Institute of Chemical Technology (KRICT) who performed the experimental exploration of CWA adsorption and degradation in MOFs.

6 COMPUTATIONAL EXPLORATION OF THE STABILITY OF MOFs UNDER HUMIDITY

As mentioned in chapter 2, most relevant applications of MOFs such as gas storage and separation, catalysis and proton conduction require retention of porosity in the presence of water (WANG et al., 2016). Particularly, the family of MOFs has been widely considered for, adsorption-driven heat pump and chiller (CADIAU et al., 2015; DE LANGE et al., 2015), water purification (HASAN; JHUNG, 2015), dehumidification (SEO et al., 2012), indoor moisture control (ABDULHALIM et al., 2017), etc. In this context researchers have turned their efforts to synthesize robust MOFs to be effectively used in these processes. Recently, Yuan et al. (YUAN et al., 2018) highlighted that since the stability of MOFs depends on the bond formed between the inorganic node and the organic ligand, a strategy to enhance the stability of MOFs is to use high-valent metal cations, which strengthen the inorganic-organic linkage therefore preventing the attack of the framework by water molecules.

A few papers investigating the structural factors that govern water stability in MOFs has been published so far. In terms of experiments, Levan et al. (LIU et al., 2011) have noted for MOF-74 series that Ni-MOF-74 is more stable than Mg-MOF-74, because Mg is more easily oxidized. Kang et al. (KANG et al., 2011) reported that the stability of MIL-53(Al, Cr) and MIL-47(V) is governed by the inertness of the central metal ions, suggesting that MOFs composed by Cr(III) or Al(III) may be very stable. In addition, the hydrophobicity of the ligand was indicated to be responsible for the stability of the DMOF-1(Zn), material formed by tetramethylated ligands (JASUJA; HUANG; WALTON, 2012), MOF-508, made up of Me-bipy pillars (MA; LI; LI, 2011) and CALF-25, containing phosphonate monoesters as linkers (TAYLOR et al., 2012). It was also mentioned that the steric hindrance caused by the presence of the alkyl groups in the organic linkers make the critical site (metal-ligand) hardly accessible to water. Indeed, through a joint computational and experimental study of a series of MOFs (IRMOF-1, MOF-69C, Zn-MOF-74, MOF-508b, Zn-BDC-DABCO, Cr-MIL-101, Al-MIL-110, Al-MIL-53 and ZIF-8), Low et al. (LOW et al., 2009) suggested that the strength of the bond between the metal oxide cluster and the bridging linker is important in determining the hydrothermal stability of the corresponding architectures.

Despite the important features cited in the literature in determining the stability of MOFs such as the bond strength between metal–ligand bond, the degree of coordination for protecting the inorganic node against water coordination and the hydrophobicity of the pore surface area, there is still a crucial need to rationalize the main driving force responsible of the water stability

of MOFs. Furthermore, in real conditions, the humidity is always present in protective materials due to the breath of the users. Based on this, envisaging the industrial application of MOFs in this field, the stability under humidity of the promising candidates for the capture/degradation of CWAs should be well understood. Therefore, in this chapter, a systematic exploration of the water stability of series of Zr and Ti-MOFs (MIP-200(Zr), UiO-66(Zr), UiO-67(Zr), NU-800(Zr) and MIP-177(Ti)) was performed DFT calculations with periodic boundary conditions (KOHNSHAM, 1965; RAJAGOPAL; CALLAWAY, 1973) in order to explore the hydrolysis mechanism with a careful characterization of the reactant, transition states and intermediates. As a further step, the activation energy barriers involved in the hydrolysis mechanism were compared with the standard MOFs, UiO-66(Zr), UiO-67(Zr), NU-800(Zr) and MIP-177(Ti) in order to identify the pivotal parameter that drives the stability of the MOFs under humidity.

These calculations were achieved using the codes available in the Quantum-Espresso package (GIANNOZZI et al., 2009), the exchange-correlation potential being described by the PBE Generalized Gradient Approximation (GGA) (PERDEW; WANG, 1992), and the core electrons being treated with Vanderbilt ultrasoft pseudopotentials (VANDERBILT, 1990). Kohn-Sham orbitals were expanded in a plane wave basis set up to a kinetic energy cutoff of 60 Ry and with a cutoff of 480 Ry for the charge density. The electron density was obtained at the Γ point in the first Brillouin-Zone (PACK; MONKHORST, 1977) for the investigated MOFs. The structural models for all MOFs: UiO-66(Zr) and UiO-67(Zr) (CAVKA et al., 2008); NU-800(Zr) (GOMEZ-GUALDRON et al., 2014); MIP-200-OH-H₂O(Zr) (WANG et al., 2018a) and MIP-177-OH-H₂O(Ti) (WANG et al., 2018b) taken from the literature were fully optimized, where both cell parameters and atomic positions relaxed, until all of the force components were smaller than 0.001 Ry/Bohr and the convergence criterion was 10^{-4} Ry for total energy.

The so-explored hydrolysis mechanism consists of two steps: (1) a non-dissociative adsorption of water in the pores of the materials at the vicinity of the bond between the inorganic node and the ligand, (2) a dissociation of water leading to a bond break between the metal oxide and the linker according to equation 6.1.



The minimum energy path (MEP) was constructed in order to obtain the transition state (TS), the reaction barrier and the main structural modifications involved in the process of dissociation of the water molecule in the structures according to the model reaction as

schematized in equation 6.1. The calculation of the MEP connecting different minimum geometries is based on the nudged elastic band (NEB) method that is known to accurately describe the MEP between the initial and the final states of a reaction and thus to evaluate the transition state and the energy barrier (HENKELMAN; UBERUAGA; JÓNSSON, 2000). A total of 11 images were used to compute each MEP, their geometries were optimized to establish the minimum-energy path on the potential surface of the system until energy variations were less than 0.05 eV/Å.

6.1 STABILITY OF Zr-MOFs

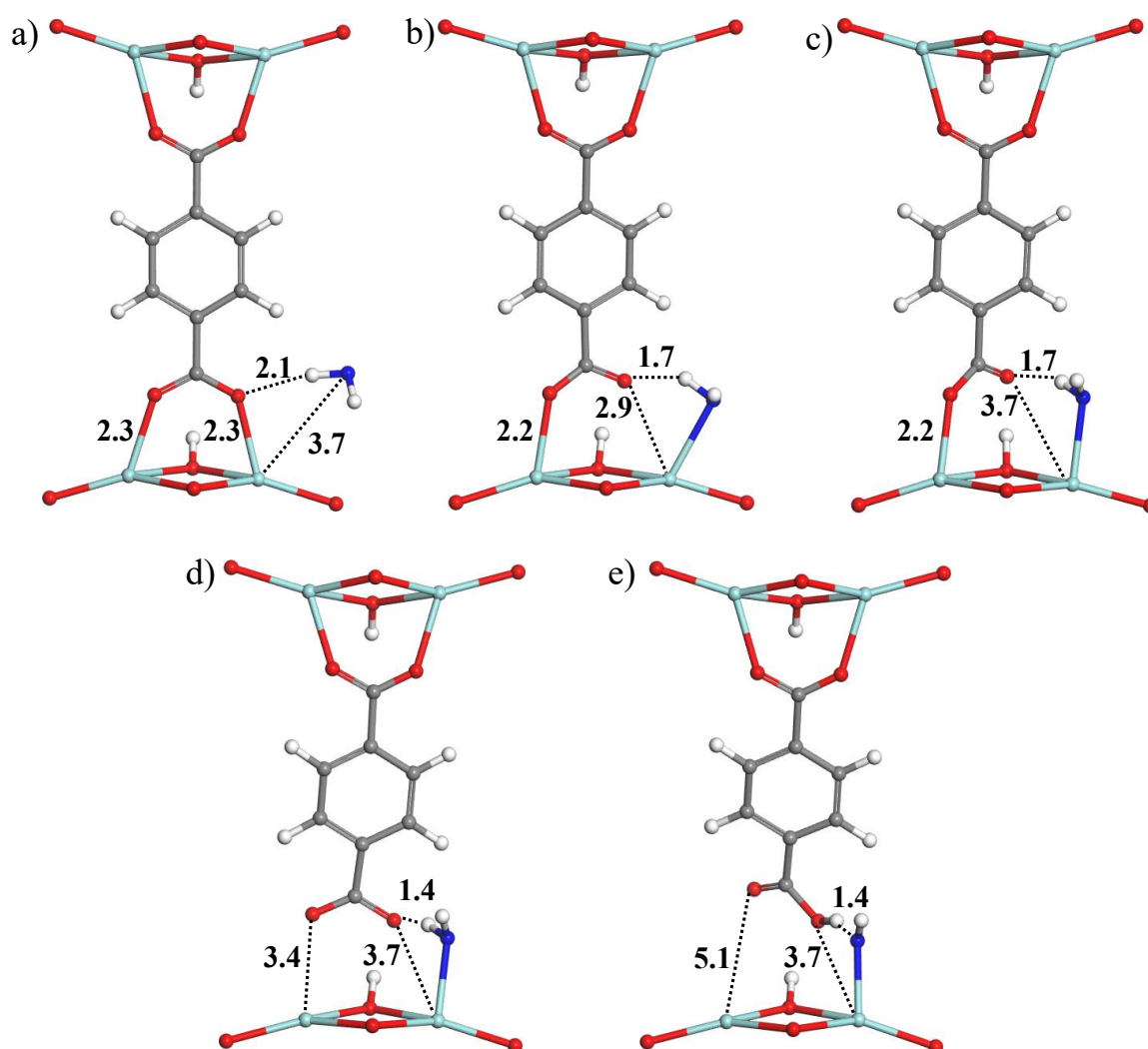
6.1.1 UiO-66(Zr)

As a preliminary step, the hydrolysis mechanism of UiO-66(Zr) was explored since this MOF is well-known for its ability to maintain the network structure upon water adsorption/desorption cycles (CAVKA et al., 2008). Besides this, UiO-66(Zr) was also shown to be a very promising MOF to capture and degrade CWAs. As mentioned in the previous chapter, this structure is constructed by linking 12-connected $[\text{Zr}_6(\mu_3\text{-O})_4(\mu_3\text{-OH})_4(\text{COO})_{12}]$ clusters with linear 1,4 benzenedicarboxylate (BDC) linkers, where each zirconium atom is eight-coordinated.

Figure 6.1a reports the most preferential arrangement of water adsorbed near to the metal-ligand node of UiO-66(Zr) corresponding to the reactant. The water molecule interacts via its hydrogen atom (Hw) towards the oxygen atom of the carboxylate group (Oc) with a characteristic distance (Hw-Oc) of 2.1 Å. Thereafter, at the first transition state, the water molecule coordinates to the zirconium atom and consequently, this leads to a breaking of the bond between the linker and the metal, as evidenced in Figure 6.1b. It is important to emphasize that at the intermediate 1 the water molecule has not dissociated yet (Figure 6.1c). The main difference when one compares the transition state with the intermediate 1 is an increasing in the Zr- Oc distance (from 2.9 Å to 3.7 Å), while the Oc-Hw distance does not change. The simulated MEP of the hydrolysis of UiO-66(Zr) is reported in Figure 6.2 with the identification of the initial reactant, the first transition state, the intermediate 1, the second transition state and the intermediate 2. Thus, the first step of the hydrolysis reaction implies an activation energy barrier of 47.3 kJ mol⁻¹. As the reaction proceeds through the second transition state, there is a progressive decrease of the Hw-Oc distance and the breaking of the other metal-ligand bond. Subsequently, H₂O dissociates into H⁺ and OH⁻. The OH⁻ keep attached to the Zr, while the

H^+ attaches to the oxygen atom of the BDC, as represented in Figure 6.1e. The resulting activation energy barrier for the second step of the hydrolysis reaction is 80.5 kJ mol^{-1} .

Figure 6.1 - Illustration of the hydrolysis mechanism of UiO-66(Zr). a) Reactant (UiO-66(Zr) + H_2O), b) First transition state (TS1), c) Intermediate 1, d) Second transition state (TS2) and e) Intermediate 2 (UiO-66(Zr): $[OH^-][H^+]$). The main distances involved in the dissociative chemisorption of water are represented and expressed in Å. Color scheme: MOF (Zr: blue, C: gray, O: red and H: white) and water (O: dark blue and H: white).

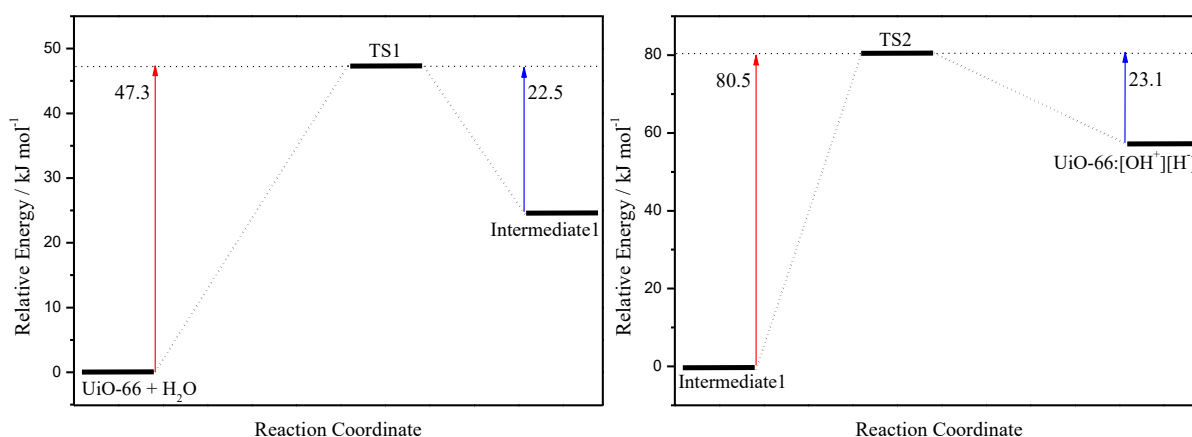


Source: Elaborated by the author (2019).

It is to be noted that at the intermediate 1 the reaction can proceed in two ways: (i) the regeneration of the material back to the reactant, which implies an energy barrier of 22.5 kJ mol^{-1} or (ii) the dissociation of water requiring about four times more energy, 80.5 kJ mol^{-1} . So,

even if water coordinates to the metal, the lower energy barrier of 22.5 kJ mol^{-1} suggests an easy bond regeneration of UiO-66(Zr). Moreover, the breaking of the Zr-Oc bond and the water dissociation both destabilize the system, leading to the second intermediate (Figure 6.1e), less stable than the reactant (Figure 6.1a), as it can be observed in Figure 6.2 through the comparison of the energies along the simulated MEP.

Figure 6.2 - Simulated Minimum Energy Path corresponding to the dissociative chemisorption of 1 water molecule per unit cell of UiO-66(Zr).



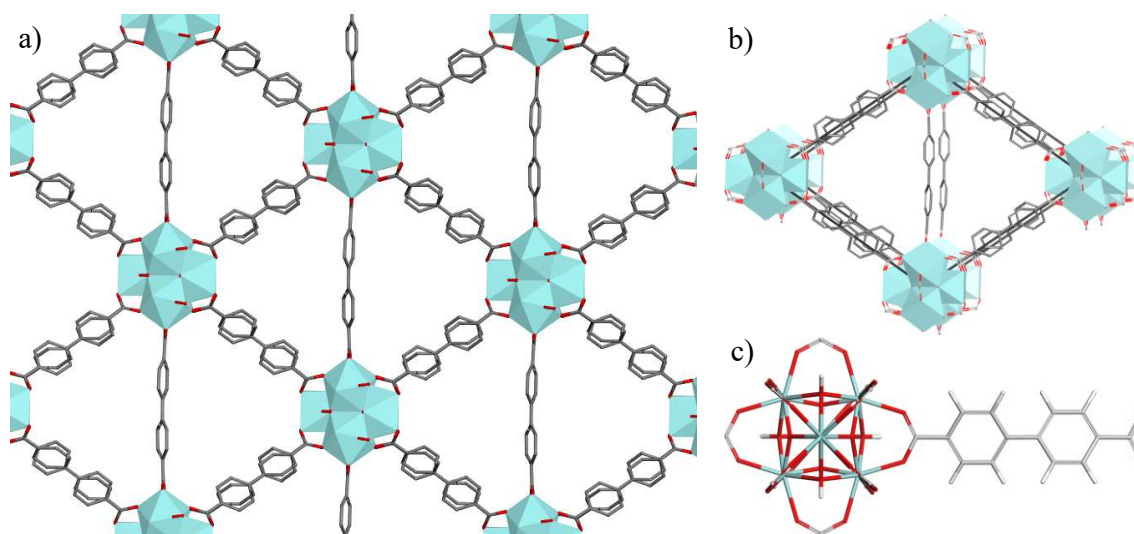
Source: Elaborated by the author (2019).

6.1.2 UiO-67(Zr)

The same procedure was applied to UiO-67(Zr), which is isoreticular to UiO-66(Zr) with elongated linkers, 4,4'-biphenyldicarboxylate (BPDC) (Figure 6.3). This MOF has been reported to be less stable than UiO-66(Zr) (DECOSTE et al., 2013a; SHEARER et al., 2013).

Five different initial positions and orientations of the confined water molecule next to metal-ligand node of UiO-67(Zr) were initially considered. The three most stable optimized configurations converged toward similar arrangements, as indicated in Figure 6.4. One can notice that the water adsorption causes the disruptions of the coordination bonds between the organic ligands and the inorganic moieties, besides the substantial distortions of the BPDC ligands. The optimized structures, reported in Figure 6.4b, c and d, illustrate that water molecules are further apart from the metal-ligand node. The interacting distances between Hw and Oc are 2.5 \AA (Figure 6.4b), 3.2 \AA (Figure 6.4c) and 3.9 \AA (Figure 6.4d) for the 3 configurations respectively. While, the Ow/Zr distances are in the order of 4.7 \AA (Figure 6.4b), 5.5 \AA (Figure 6.4c) and 6.2 \AA (Figure 6.4d).

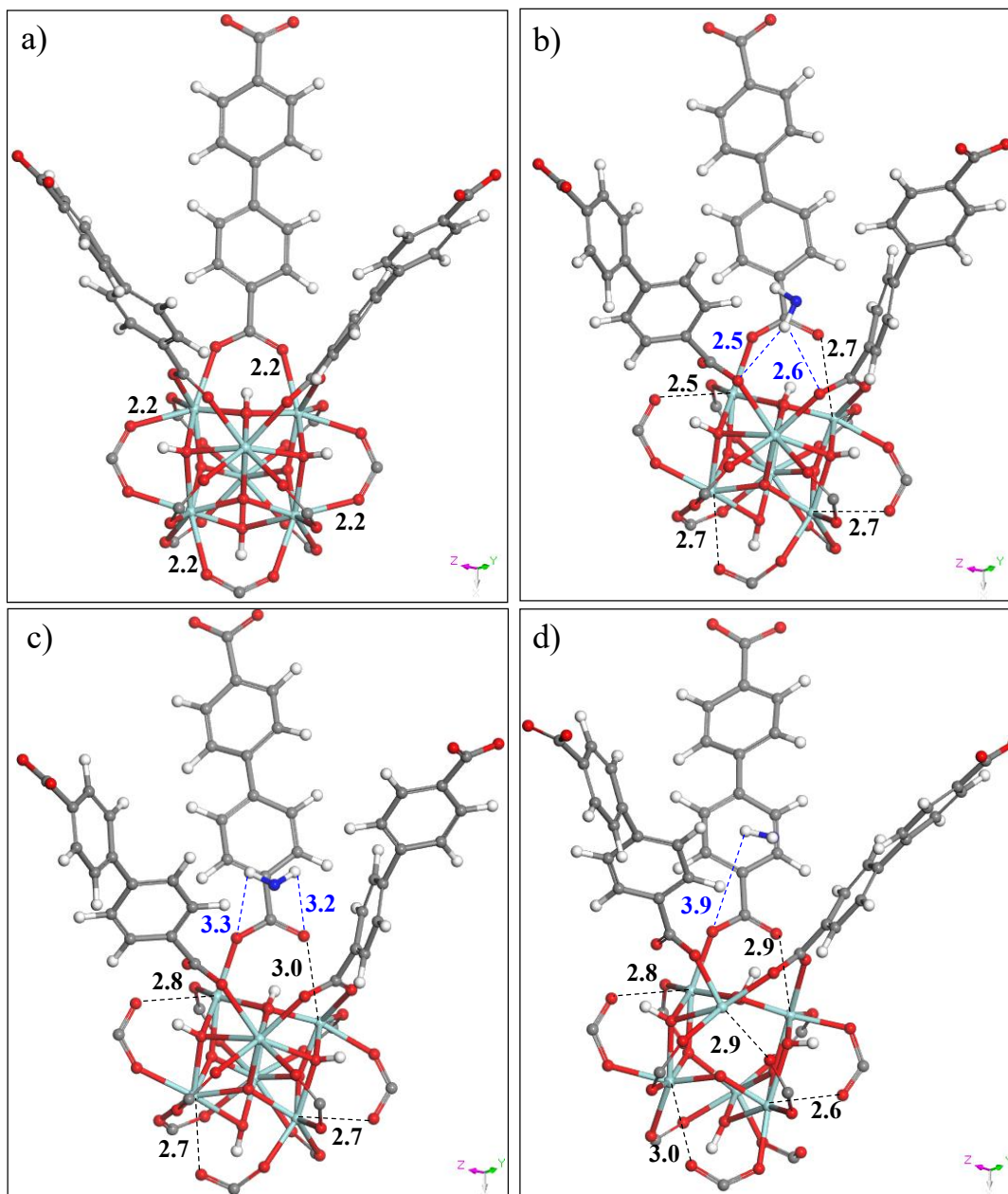
Figure 6.3 - a) Illustration of the crystal structure of UiO-67(Zr), b) Unit cell. c) A single 12-connected SBU and a 4,4'-biphenyldicarboxylate linker to clarify the bond between them.



Source: Elaborated by the author (2019).

The adsorption energies calculated showed values in the range of -39 to -41 kJ mol^{-1} for H_2O confined in UiO-67(Zr), which are low and within the same range of value than the H_2O vaporization enthalpy (-44.0 kJ mol^{-1}). Furthermore, the difference of electronic density was calculated and the absence of electronic transfer from the water molecule to the MOF confirms that the mechanism in play is a physisorption-based process. Therefore, despite it is unexpected, the presence of weak interactions between water molecule and MOF is enough to cause the break of several chemical bonding (Oc-Zr) and, making UiO-67(Zr) more susceptible to structural breakdown. However, the minimum energy path corresponding to the dissociative chemisorption of water molecule, as calculated for UiO-66(Zr), could not be converged due to the complex reorganization of the structure along the calculation. Thus, other mechanisms should be investigated to gain a deeper knowledge of the details of the water reaction mechanism for this MOF.

Figure 6.4 - DFT optimized water loaded UiO-67(Zr). The most stable arrangements of water in the pores of UiO-67(Zr). Structures for the 3 corresponding configurations (b, c and d) compared to the DFT optimized structure for the empty UiO-67(Zr). Color scheme: MOF (Zr: blue, C: gray, O: red and H: white) and water (O: dark blue and H: white).

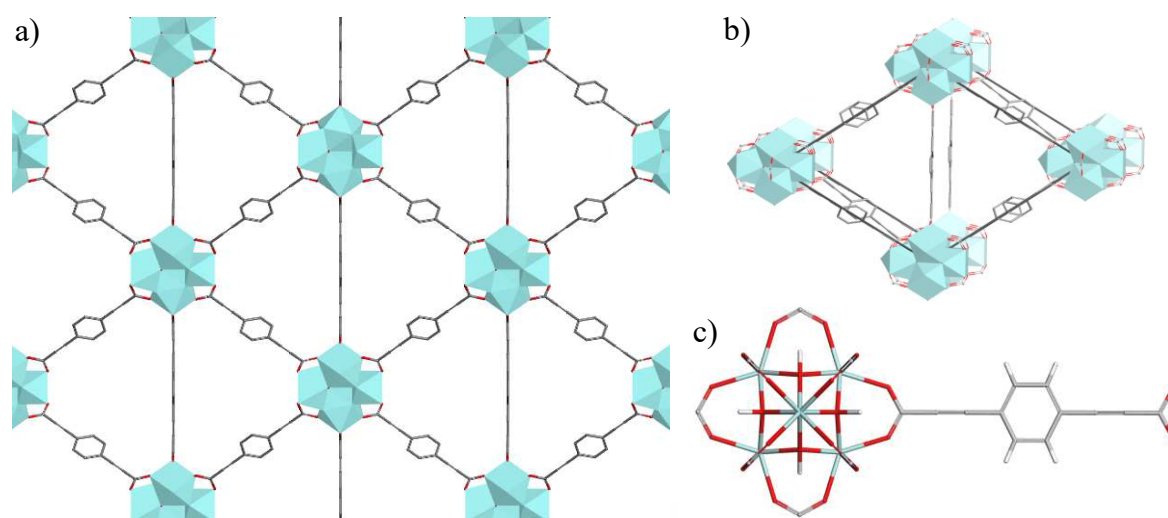


Source: Elaborated by the author (2019).

6.1.3 NU-800(Zr)

This structure is formed by the ligand 1,4-benzenedipropynoic acid (TPT), which features terminal triple bond (Figure 6.5), and has octahedral cages formed by 12 linkers and 6 zirconium nodes, surrounded by tetrahedral cages formed by 6 linkers and 4 zirconium nodes, these pores being about 16.5 and 7.5 Å, respectively (GOMEZ-GUALDRON et al., 2014).

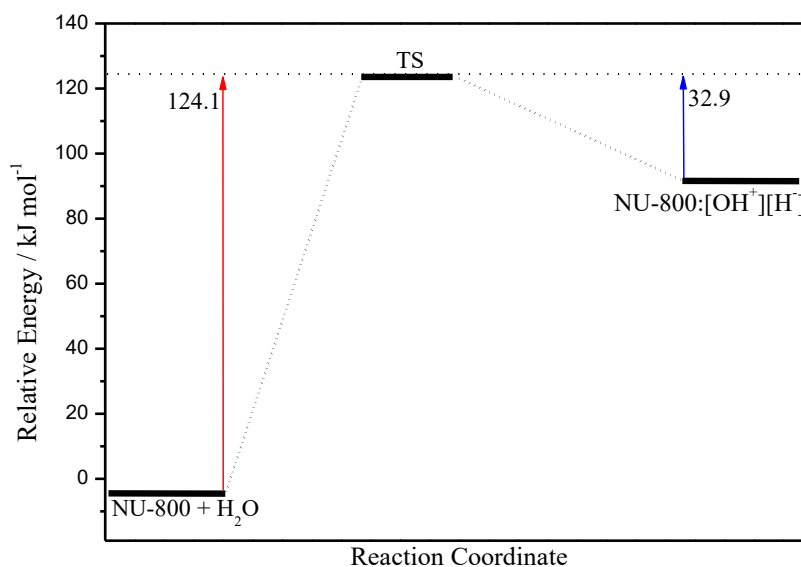
Figure 6.5 - a) Illustration of the crystal structure of NU-800(Zr), b) Unit cell. c) A single 12-connected SBU and a TPT linker to clarify the bond between them.



Source: Elaborated by the author.

Figure 6.6 shows the simulated minimum energy path corresponding to the dissociative chemisorption of one water molecule in NU-800(Zr). It is to be noted that compared to the scenario encountered for UiO-66(Zr) (Figure 6.1) the water molecule is already dissociated in the transition state (Figure 6.7b) as it was previously reported for MIL-140A(Zr) (VIEIRA SOARES et al., 2016). The energy barriers corresponding to the hydrolysis mechanism are $124.1 \text{ kJ mol}^{-1}$ and $139.7 \text{ kJ mol}^{-1}$ while the reverse barriers are much lower 32.9 kJ mol^{-1} and 27.6 kJ mol^{-1} , for NU-800(Zr) and MIL-140A(Zr), respectively. As can be observed, the energy barrier from the reactant (NU-800(Zr) + H₂O) to the intermediate (NU-800(Zr):[OH⁻][H⁺]) is much higher than the reverse barrier. Therefore, these energy values emphasize the stability of NU-800(Zr) and suggest that the reconstruction of the structure would be expected even if the water dissociation and consequently the breaking of the Zr-Oc bond would be feasible.

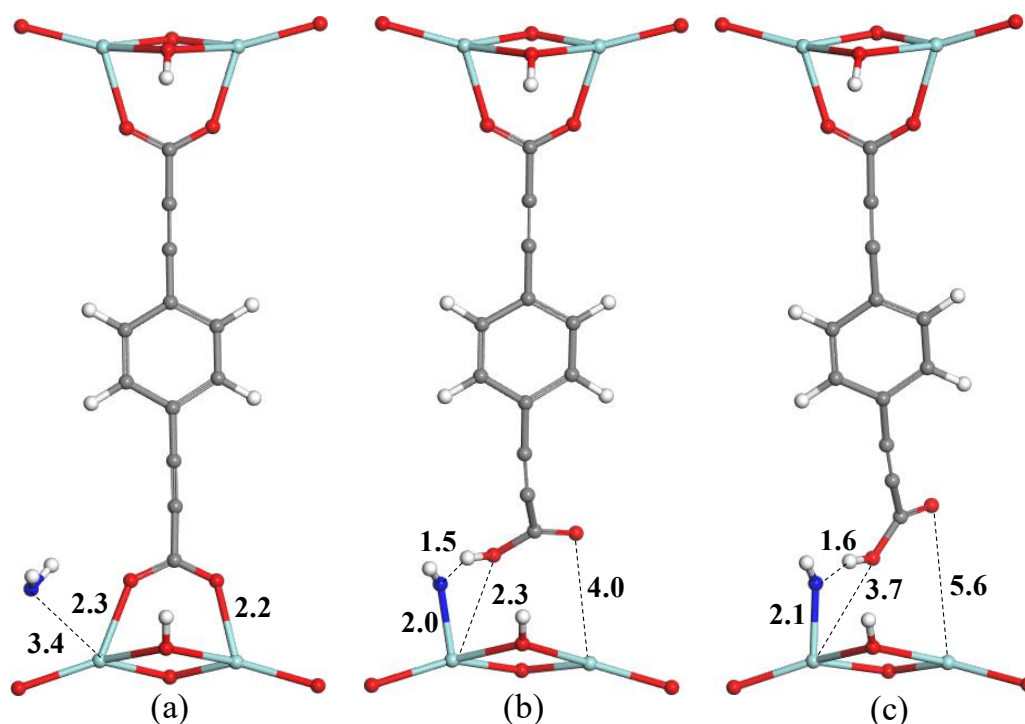
Figure 6.6 - Simulated Minimum Energy Path corresponding to the dissociative chemisorption of 1 water molecule per unit cell of NU-800(Zr).



Source: Elaborated by the author (2019).

The hydrolysis reaction of NU-800(Zr) occurs without the prior coordination of the water to the metal site, as can be observed in Figure 6.7. In this mechanism the water molecule dissociates into H⁺ and OH⁻, concomitantly the hydroxyl migrates to the Zr atom and the proton migrates to the Oc of the TPT ligand. Thus, NU-800(Zr) loses its original structure and after surpassing the transition state, the organic linker undergoes a significant distortion moving away from the inorganic node, where the distances between Oc-Zr goes from 2.3 Å and 4.0 Å to 3.7 Å and 5.6 Å (c.f Figure 6.7b and Figure 6.7c).

Figure 6.7 - Illustration of the hydrolysis mechanism of NU-800(Zr). a) Reactant (NU-800(Zr) + H₂O), b) First transition state (TS) and c) Intermediate (NU-800(Zr):[OH]⁻[H]⁺). The main distances involved in the dissociative chemisorption of water are represented and expressed in Å. Color scheme: MOF (Zr: blue, C: gray, O: red and H: white) and water (O: dark blue and H: white).



Source: Elaborated by the author (2019).

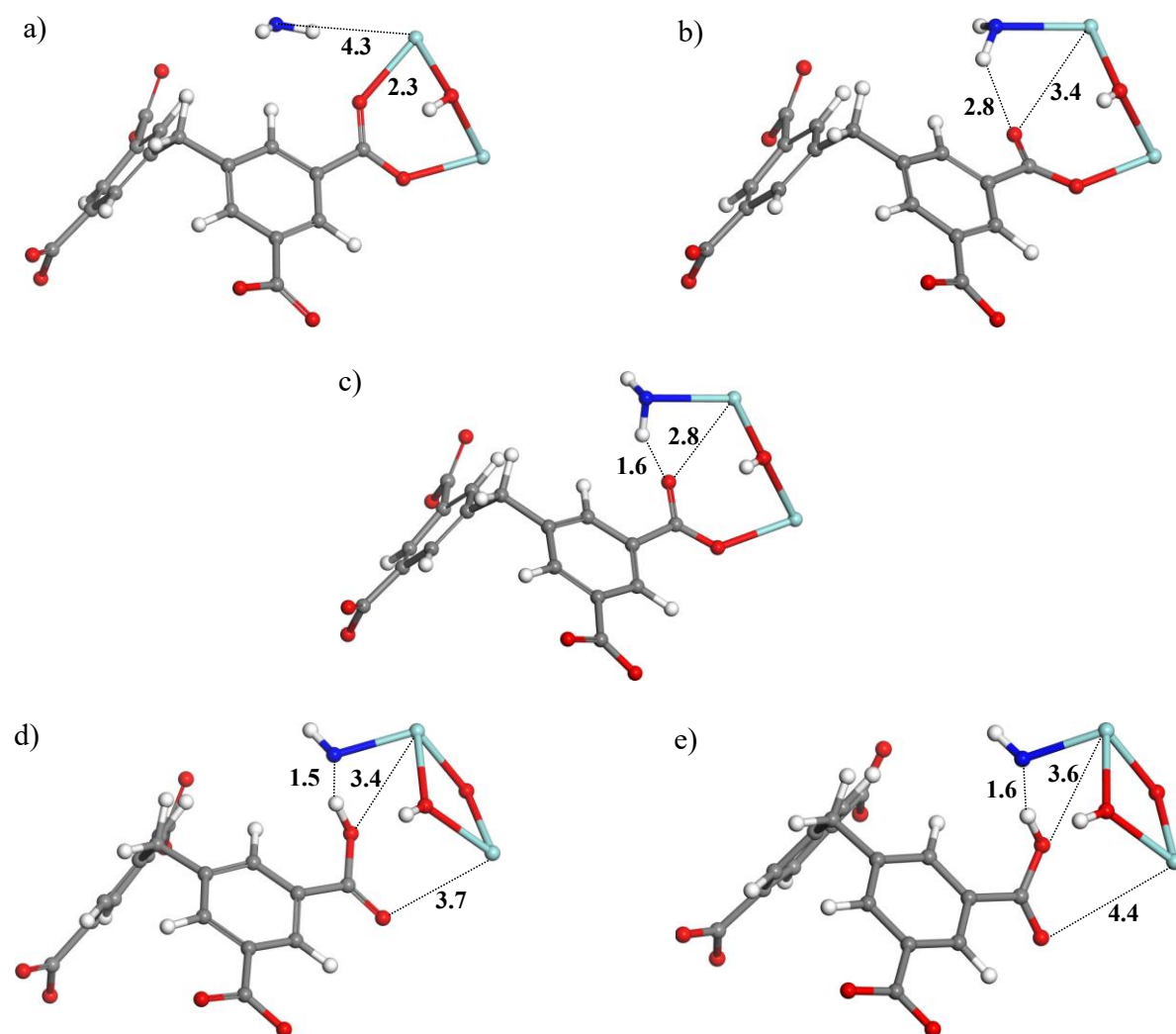
6.1.4 MIP-200(Zr)

One of the most recent Zr-MOFs namely, the MIP-200(Zr) (WANG et al., 2018a), was selected owing to its exceptional water stability that has been experimentally demonstrated but not understood yet.

It was previously shown by Monte Carlo simulations that water molecules are preferentially located in the hexagonal pores (WANG et al., 2018a). Therefore, the optimized configuration of one water molecule initially adsorbed in the large pore of the MIP-200(Zr) was considered as the initial state for the hydrolysis mechanism, as illustrated in Figure 6.8a. During the first step of the reaction, the water moves in direction to the zirconium site, and consequently the bond between this zirconium atom and the oxygen atom of the carboxylate ligand is broken, as indicated in the first transition state in Figure 6.8b. Thus, the proton migrates to a nearby oxygen atom of the carboxylate giving rise to the first intermediate state, where the water

molecule is coordinated to the Zr and the ligand still remains bound to the inorganic node (Figure 6.8c).

Figure 6.8 - Illustration of the hydrolysis mechanism of MIP-200(Zr). a) Reactant (MIP-200(Zr) + H₂O), b) First transition state (TS1), c) Intermediate 1, d) Second transition state (TS2) and e) Intermediate 2 (MIP-200(Zr):[OH⁻][H⁺]). The main distances involved in the dissociative chemisorption of water are represented and expressed in Å. Color scheme: MOF (Zr: blue, C: gray, O: red and H: white) and water (O: dark blue and H: white).

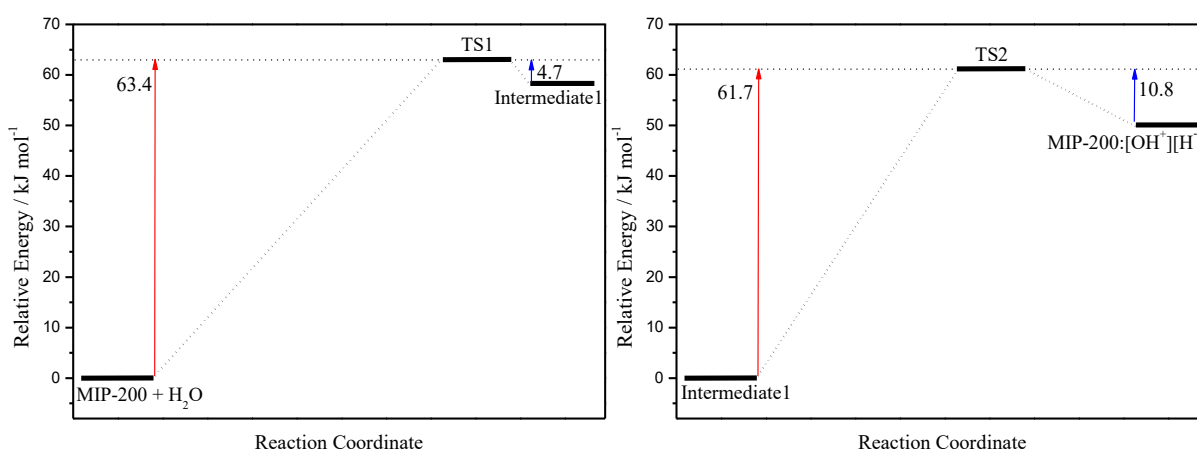


Source: Elaborated by the author (2019).

Figure 6.9 reports the water dissociation path and the associated energy barrier corresponding to the decomposition of MIP-200(Zr). The resulting energy barrier is slightly lower (63.4 kJ mol⁻¹) than the energies barriers reported for UiO-66(Zr) and NU-800(Zr), however the reverse barrier is very small (4.7 kJ mol⁻¹). The intermediate state, represented in

Figure 6.8c, shows that water does not dissociate but coordinates to zirconium atom, as observed for UiO-66(Zr).

Figure 6.9 - Simulated Minimum Energy Path corresponding to the dissociative chemisorption of 1 water molecule per unit cell of MIP-200(Zr).



Source: Elaborated by the author (2019).

The hydrolysis reaction further occurs via a molecular dissociative chemisorption of water giving rise to the fragments Zr-OH and H₄mdip-CO₂H, as illustrated by the second transition state (Figure 6.8d). One can note that the water dissociation occurs after overcoming a second energy barrier of 61.7 kJ mol⁻¹ (Figure 6.9), however a much lower energy barrier (4.7 kJ mol⁻¹) emphasizes an easy bond regeneration in the MIP-200(Zr). In addition, the second intermediate (Figure 6.8e) is less stable, so consequently, the water dissociation and the metal-oxygen bond breaking destabilize the system, the energy difference between the reactant (MIP-200(Zr) + H₂O) and the intermediate 2 (MIP-200(Zr):[OH⁻][H⁺]) being 109.6 kJ mol⁻¹. Therefore, the very high stability attributed to MIP-200(Zr) can be stated from the following points: (i) the MOF structure remains intact due to the absence of water dissociation after the first energy barrier (63.4 kJ mol⁻¹) and (ii) a very low energy barrier (4.7 kJ mol⁻¹) is required to regenerate the Zr-Oc bond compared with the energy necessary (61.7 kJ mol⁻¹) to dissociate the water molecule.

6.2 RATIONALIZATION OF THE STABILITY OF Zr-MOFs

Table 6.1 reports the average of angles (Cc-C2-C3) of the ligand affected by the presence of water. The angle is formed between the carbon atom of the carboxylate group (Cc) and the two carbon atoms (C2 and C3), which are collinear with the Cc, as indicated by the blue line. The measurements were performed for the corresponding reactant (MOF+H₂O) and the final intermediate reported in Figures 6.1, 6.4, 6.7, and 6.8, respectively compared to those present in the empty structure.

It is to be noted that the ligand BDC and TPT do not show a significant deviation of the angles (Cc-C2-C3) upon water adsorption compared to the scenario observed for the most stable configuration reported for UiO-67(Zr) in section 6.1.2 (see Figure 6.4b). Furthermore, the instability of UiO-67(Zr) can be explained by the torsional strain of the biphenyl ring (GÖLLER; GRUMMT, 2000) that is experienced in the crystalline structure, making this structure less robust. The BDC and TPT ligands undergo a deformation after the complete dissociation of water, as it can be observed in Figure 6.1e and Figure 6.7c, respectively. Thus, one possible explanation is that the rigidity of the ligand makes the MOF more stable under humidity.

It is important to highlight that the mdip ligand has a different topology when compared with BDC, BPDC and TPT and is one of the most complex tetratopic linker used to synthesize Zr-MOFs. Table 6.1 shows that the Cc-C2-C3 angles of MIP-200(Zr) does not present a considerable distortion after water adsorption. Furthermore, comparing the reactant with the intermediate 2 one can note that the water dissociation causes only a small reorientation in the organic linker. This analysis shows that the very small deviation of the angle, which indicates the linker cannot be so easily distorted, indeed prevents the water to access the metal-ligand node, making the material more stable. In order to support this conclusion, the stability of the titanium-carboxylate framework denoted MIP-177(Ti) formed by the same ligand, mdip (WANG et al., 2018), was further explored .

Table 6.1 - The average of the measurements of the angles for the linkers in the presence of the water molecule compared with the MOF without water in the pore cavity.

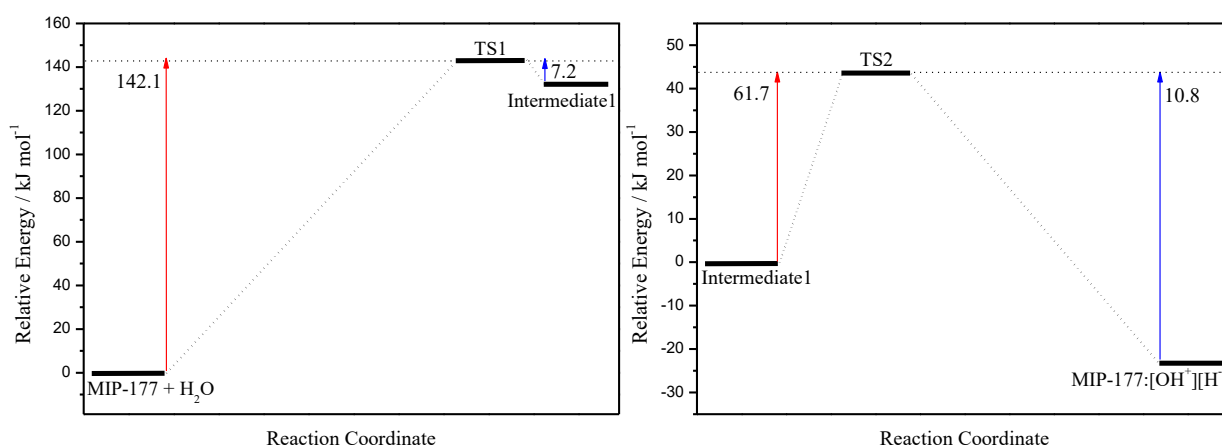
	Angle(C-C-C)	Ligand
UiO-66(Zr)	178.44	
UiO-66 + H ₂ O (Fig. 6.1a)	178.28	
Intermediate 2 (Fig. 6.1e)	173.76	
UiO-67(Zr) (Fig. 6.4a)	178.81	
UiO-67 + H ₂ O (Fig. 6.4b)	168.64	
UiO-67 + H ₂ O (Fig. 6.4c)	168.80	
UiO-67 + H ₂ O (Fig. 6.4d)	169.43	
NU-800(Zr)	178.88	
NU-800 + H ₂ O (Fig. 6.7a)	177.93	
Intermediate (Fig. 6.7c)	172.78	
MIP-200(Zr)	173.76	
MIP-200 + H ₂ O (Fig. 6.8a)	173.80	
Intermediate 2 (Fig. 6.8e)	176.79	

Source: Elaborated by the author (2019).

6.3 STABILITY OF THE Ti-MOFs

Figure 6.10 reports the water dissociation path and the energy barrier involved in the hydrolysis mechanism of MIP-177(Ti). One can see that MIP-177(Ti) shows a high water stability as illustrated by the very high energy barrier from the reactant (Figure 6.11a) to the intermediate 1 (Figure 6.11c) ($142.1 \text{ kJ mol}^{-1}$), and the very low reverse energy barrier (7.2 kJ mol^{-1}). This observation suggests that even if the water molecule dissociates, the reconstruction of the structure would be achievable due to the very low energy barrier required for this process.

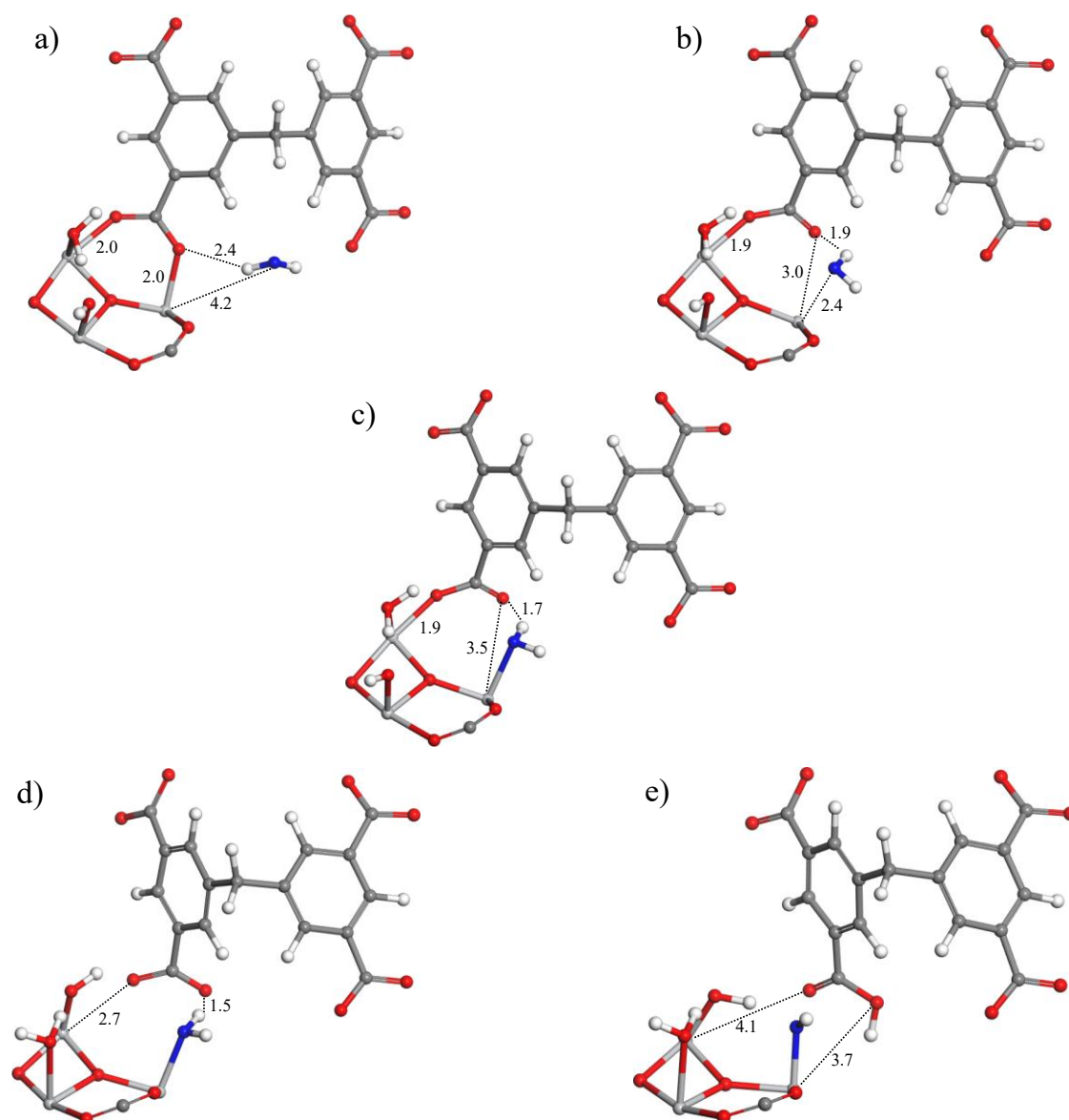
Figure 6.10 - Simulated Minimum Energy Path corresponding to the dissociative chemisorption of 1 water molecule per unit cell of MIP-177(Ti).



Source: Elaborated by the author (2019).

It is to be noted that the hydrolysis mechanism occurs through the coordination of the water to the metal and that in the transition state (Figure 6.11b) the water molecule is not dissociated, as was observed for UiO-66(Zr) and MIP-200(Zr). Further to this, the main difference when one compares the second transition state with the intermediate 2 is that the proton migrates to the carboxylate and the organic linker moves away from the inorganic node. The measurement of the Cc-C2-C3 angles corresponding to the main configurations (Figure 6.11) for the hydrolysis reaction of MIP-177(Ti) is: 178.19° (Figure 6.11a) and 173.61° (Figure 6.11e). There is no angle deformation after the adsorption of water, when compared with the empty structure 178.17° , and the distortion associated to the dissociation of water showed the same trend than for MIP-200(Zr). Therefore, this analysis clearly confirms the role of the linker in the degradation mechanism of MOFs in the presence of water.

Figure 6. 11 - Illustration of the hydrolysis mechanism of MIP-177(Zr). a) Reactant (MIP-177(Zr) + H₂O), b) First transition state (TS1), c) Intermediate 1, d) Second transition state (TS2) and e) Intermediate 2 (MIP-177(Zr):[OH⁻][H⁺]). The main distances involved in the dissociative chemisorption of water are represented and expressed in Å. Color scheme: MOF (Ti: light gray, C: gray, O: red and H: white) and water (O: dark blue and H: white).



Source: Elaborated by the author (2019).

6.4 CONCLUSION

UiO-66(Zr), UiO-67(Zr) and NU-800(Zr) present similar $(Zr_6O_4)(OH)_4(CO_2)_n$ inorganic building blocks. Furthermore, a variety of MOFs with these inorganic building blocks have been found to be highly stable, suggesting that their stability is linked to the presence of

this type of building unit. However, there are significant changes in chemical stability of Zr-MOFs due to the incorporation of different organic linkers. The instability of UiO-67(Zr) towards water is attributed to the linker distortions engendered by water physisorption near the Zr₆-based node, that are mostly attributed to the rotation of the biphenyl rings. On the other hand, the structures UiO-66(Zr) and NU-800(Zr) revealed to be more robust which can be directly correlated with the rigidity of BDC and TPT ligands, respectively.

The DFT calculations confirmed that MIP-200(Zr) is one of the most stable MOFs reported so far, since the mechanism implies that the water dissociation must overcome two reaction barriers of 63.4 kJ mol⁻¹ and 61.7 kJ mol⁻¹ (see Figure 6.9), while a much lower energy barrier (4.7 kJ mol⁻¹) is required to reverse the process suggesting an easy bond regeneration. Besides that, the high stability of the MOF can be attributed to the rigidity of the ligand, 3,3',5,5'-tetracarboxydiphenyl-methane (mdip) that reinforces the link between the organic and inorganic nodes. Its structure-property relationship encouraged us to investigate another MOF formed by a titanium tetravalent metal cation and the same ligand (mdip), and indeed the analysis for MIP-177(Ti) confirmed the role of the ligand in the degradation mechanism of MOFs in water paving the way towards future guidance for the synthesis of water robust architectures.

In summary, the values of the energy barrier relative to the dissociative chemisorption of one water molecule as well as that associated with the regeneration of the broken bond can allow to assess the stability of the MOF structures. Furthermore, the Cc-C2-C3 angle is an important parameter that not only points out the rigidity of the ligand but also correlates with the accessibility of the water molecules to the metal-ligand bond. Our calculations allowed to define the following stability sequence: BPDC (UiO-67) < TPT (NU-800) < BDC (UiO-66) < mdip (MIP-200-OH-H₂O) and mdip (MIP-177-OH-H₂O). The highly stability of MOFs formed by mdip ligand, MIP-200-OH-H₂O and MIP-177-OH-H₂O, were proven by the requirement of two energy barriers to dissociate water, the lower reversible barrier and the very small deviation of the angle (Cc-C2-C3), indicating that mdip cannot be so easily distorted. Moreover, the mode of coordination of the ligand should also be taken into account, since the more bonds there are between SBU and ligand the harder it will be to completely remove the ligand and consequently to lead to the structure collapse.

7 CONCLUSION AND PERSPECTIVES

This thesis was dedicated to the evaluation of MOFs for their adsorption and degradation performances with respect to nerve agents, vesicant agents as well as their simulants through the combination of quantum and force-field based molecular simulations.

Initially, the CWA adsorption properties of the nerve agents sarin and soman as well as their simulants were explored by GCMC simulations. A series of Zr and Ti-based MOFs were predicted to show CWA capture uptakes that outperform the standard porous solids reported so far. The CWA adsorption enthalpies were found to be very high. Thus, to gain more insight into these CWA/MOF interactions, further analysis was deployed including the calculations of the Bader charges using DFT. The junction of these molecular simulations culminated in two important conclusions: (i) there is no significant charge transfer between the CWAs and the host frameworks which excludes the existence of a chemisorption process and (ii) the similarity between the energies calculated by DFT and GCMC validate the set of LJ potential parameters and atomic partial charges used to describe the CWA/MOF interactions. The correlation of the CWA uptake/energetics with a geometric descriptor α , which is based on the free pore volume of the MOF and the molecular dimension of the CWAs, indicated that the capacity of stockpiling CWA in MOFs and the adsorption enthalpies are predominantly governed by the space available in the pores. Lastly, the ability of simulant molecules (DMMP and DIFP) to predict the adsorption properties of Sarin or Soman evidenced that these simulants reproduce well the behavior of Sarin, however they have poor predictive power to mimic Soman. Therefore, the alternative simulant PMP, proposed in this work, should be carefully considered by experimentalists. As a perspective, we plan to apply this computational strategy in order to explore the adsorption performances of MOFs with respect to different families of CWAs and toxic industrial compounds (TICs).

As a further step, the systematic examination conducted with the twenty-five MOFs leads toward to some promising materials, which are expected to overcome the current limitation of the commercialized protection devices against CWAs. Besides that, some factors, such as: feasible and low-cost synthesis, presence of activated sites, sites truly available for the access of CWAs and structures studied by experimental collaborators were considered. Thus, the degradation reaction was further explored for the MIP-177(Ti), MIP-200(Zr) and UiO66-defects6(Zr) and UiO66-defects6(Zr)-NH₂. Three possible hydrolysis mechanisms of CWAs by a Ti-MOF were for the first time explored here in this work. The most probable mechanism shows that the deactivated molecule, namely IMPA remains coordinated in a bidentate manner

to the Ti-sites and its desorption energy was predicted to be very high, which emphasizes that MIP-177(Ti) not only allows the degradation of Sarin but also a strong retention of the resulting IMPA product into their pores. The degradation mechanism performed on the two simulants demonstrated that DIFP mimics better Sarin in terms of the TS and products obtained during the reaction as well as of the activation energy required to achieve their degradation. Thus, this computational work emphasizes that two important points need to be considered by the experimentalist, on hand the highest toxicity of DIFP than DMMP, on the other hand, the most reliability of DIFP to further extrapolate the behavior of the real toxic molecule, Sarin. As a follow up of this work, some experiments are being undergone and this might allow us to validate and/or refine our simulations.

The nucleophilic addition of the $-OH$ functions to the phosphorus atom of Sarin and Soman using the Zr-MOFs (MIP-200(Zr) and UiO-66(Zr)) also demonstrated a good performance. It is important to highlight that UiO-66(Zr)-NH₂ is the most appropriate MOF for the degradation of Sarin, since it requires the less amount of energy to degrade Sarin when compared with MIP-177(Ti), MIP-200(Zr) and UiO-66(Zr) and also presents strong retention of the resulting IMPA product into their pores ensuring that the most toxic molecule will not be regenerated. At this point, it is important to mention that this computational work guided further experimental development of our collaborators in KRICT. The degradation reaction for Soman was Tested by Agency for Defense Development in Korea using the textile made of the composite UiO-66(Zr)-NH₂ and polyacrylonitrile.

The hydrolytic pathway, chosen to deactivate the sulfur mustard, revealed good performance of UiO66-defects6(Zr)-NH₂ for the catalytic degradation of this blister agent. Furthermore, the simulant CEES perfectly mimics the behavior of HD, considering the degradation mechanism on the activated Zr site of UiO-66(Zr)-NH₂. Finally, the effect of the MOF linker functionalization on the degradation of Sarin, Soman and HD considering the MOFs UiO-66(Zr) and UiO-66(Zr)-NH₂ did not cause a substantial impact in the activation energy. It can be explained by the presence of strong interactions with the activated sites of the SBU and/or the presence of weakly interactions between the molecules and the linkers, but not necessarily with the amino groups, where these interactions vary for each molecule due to their volume.

One significant obstacle found during the investigation of the degradation mechanisms was the lack of resources in terms of machines. Thus, the effect of the temperature, as well as the confirmation of the transition states, could not be accomplished. However, we can be confident regarding the reliability of the energies barriers and the transition states presented in

this work owing to the robustness of the CI-NEB methodology and considering that some computational works published in the literature reported configurations of the transition state similar that those reported here.

The last part of this thesis was dedicated to the deep investigation of the stability of MOFs under humidity. The NEB calculations confirmed the very good water stability of this family of materials, UiO-66(Zr), NU-800(Zr), MIP-200(Zr) and MIP-177(Ti). The analyses of the (Cc-C2-C3) angles showed that the very small deviation of the angle indicates the linker cannot be so easily distorted, which prevents the water to access the metal-ligand node. Therefore, the rigidity of the ligand makes the MOF more stable under humidity. Thus, the instability of UiO-67(Zr) can be attributed to the biphenyl rings, which undergoes significant reorientation upon water adsorption leading to the disruption of the coordination bonds between the organic ligands and the inorganic moieties. In contrast, the robustness of UiO-66(Zr), NU-800(Zr), MIP-200(Zr) and MIP-177(Ti) can be assigned to the rigidity of BDC, TPT and mdip ligands, respectively. In summary three factors should be examined to assess the stability of the MOF structures: (i) the values of the energy barrier relative to the dissociative chemisorption of one water molecule, (ii) the energy associated with the regeneration of the broken bond and (iii) the Cc-C2-C3 angle, which can be correlated to the rigidity of the ligand but also to the non-accessibility of the water molecules to the metal-ligand bond. Thus, it is possible to define the following stability sequence: BPDC (UiO-67) < TPT (NU-800) < BDC (UiO-66) < mdip (MIP-200-OH-H₂O) and mdip (MIP-177-OH-H₂O). The highly stability of MIP-200-OH-H₂O and MIP-177-OH-H₂O, both formed by mdip ligand, indicates that the mode of coordination of the ligand should also be taken into account, since the more bonds there are between SBU and ligand the harder it will be to completely remove the ligand and consequently to lead to the structure collapse. Therefore, the understanding of the stability of MOFs under humidity, provided in this thesis, can be used to future guide the synthesis of water robust architectures.

REFERENCES

- AAS, Pål. The Threat of Mid-Spectrum Chemical Warfare Agents. **Prehospital and Disaster Medicine**, v. 18, n. 4, p. 306–312, 2003.
- ABDULHALIM, Rasha G.; BHATT, Prashant M.; BELMABKHOUT, Youssef; SHKURENKO, Aleksander; ADIL, Karim; BARBOUR, Leonard J.; EDDAOUDI, Mohamed. A Fine-Tuned Metal–Organic Framework for Autonomous Indoor Moisture Control. **Journal of the American Chemical Society**, v. 139, n. 31, p. 10715–10722, 2017.
- AGRAWAL, Mayank; SAVA GALLIS, Dorina F.; GREATHOUSE, Jeffery A.; SHOLL, David S. How Useful Are Common Simulants of Chemical Warfare Agents at Predicting Adsorption Behavior? **The Journal of Physical Chemistry C**, v. 122, n. 45, p. 26061–26069, 2018.
- AHMADPOUR, A.; OKHOVAT, A.; DARABI MAHBOUB, M. J. Pore size distribution analysis of activated carbons prepared from coconut shell using methane adsorption data. **Journal of Physics and Chemistry of Solids**, v. 74, n. 6, p. 886–891, 2013.
- ALVIM, Raphael S.; VAISS, Viviane S.; LEITÃO, Alexandre A.; BORGES, Itamar. Hydrolysis of a VX-like Organophosphorus Compound through Dissociative Chemisorption on the MgO(001) Surface. **The Journal of Physical Chemistry C**, v. 117, n. 40, p. 20791–20801, 2013.
- ANDERSSON, Y.; LANGRETH, D. C.; LUNDQVIST, B. I. van der Waals Interactions in Density-Functional Theory. **Physical Review Letters**, v. 76, n. 1, p. 102–105, 1996.
- ASHA, P.; SINHA, Mekhola; MANDAL, Sukhendu. Effective removal of chemical warfare agent simulants using water stable metal–organic frameworks: mechanistic study and structure–property correlation. **RSC Advances**, v. 7, n. 11, p. 6691–6696, 2017.
- ASCROFT, Neil. W.; Mermin, N. D. Níveis eletrônicos em um potencial periódico: propriedades gerais. In: ASCROFT, N. W.; MERMIN, N. D. **Física do Estado Sólido**. São Paulo: Cengage Learning, 2011. p. 141-163.
- BANDOSZ, Teresa J.; LASKOSKI, Matt; MAHLE, John; MOGILEVSKY, Gregory; PETERSON, Gregory W.; ROSSIN, Joseph A.; WAGNER, George W. Reactions of VX, GD, and HD with Zr(OH) 4 : Near Instantaneous Decontamination of VX. **The Journal of Physical Chemistry C**, v. 116, n. 21, p. 11606–11614, 2012.
- BARTELT-HUNT, Shannon L.; KNAPPE, Detlef R. U.; BARLAZ, Morton A. A Review of Chemical Warfare Agent Simulants for the Study of Environmental Behavior. **Critical Reviews in Environmental Science and Technology**, v. 38, n. 2, p. 112–136, 2008.
- BASHKOVA, Svetlana; BANDOSZ, Teresa J. The effects of urea modification and heat treatment on the process of NO₂ removal by wood-based activated carbon. **Journal of Colloid and Interface Science**, v. 333, n. 1, p. 97–103, 2009.

BERMUDEZ, V. M. Adsorption on carbon nanotubes studied using polarization-modulated infrared reflection-absorption spectroscopy. **Journal of Physical Chemistry B**, v. 109, n. 20, p. 9970–9979, 2005.

BERMUDEZ, V. M. Computational study of the adsorption of trichlorophosphate, dimethyl methylphosphonate, and sarin on amorphous SiO₂. **Journal of Physical Chemistry C**, v. 111, n. 26, p. 9314–9323, 2007. a.

BERMUDEZ, V. M. Quantum-chemical study of the adsorption of DMMP and Sarin on γ -Al₂O₃. **Journal of Physical Chemistry C**, v. 111, n. 9, p. 3719–3728, 2007. b.

BERMUDEZ, V. M. Computational Study of Environmental Effects in the Adsorption of DMMP, Sarin, and VX on γ -Al₂O₃: Photolysis and Surface Hydroxylation. **The Journal of Physical Chemistry C**, v. 113, p. 1917–1930, 2009.

BOBBITT, N. Scott; MENDONCA, Matthew L.; HOWARTH, Ashlee J.; ISLAMOGLU, Timur; HUPP, Joseph T.; FARHA, Omar K.; SNURR, Randall Q. Metal-organic frameworks for the removal of toxic industrial chemicals and chemical warfare agents. **Chemical Society Reviews**, v. 46, n. 11, p. 3357–3385, 2017. a.

BOBBITT, N. Scott; MENDONCA, Matthew L.; HOWARTH, Ashlee J.; ISLAMOGLU, Timur; HUPP, Joseph T.; FARHA, Omar K.; SNURR, Randall Q. Metal-organic frameworks for the removal of toxic industrial chemicals and chemical warfare agents. **Chem. Soc. Rev.**, v. 46, n. 11, p. 3357–3385, 2017. b.

BONHOMME, Christian et al. First-Principles Calculation of NMR Parameters Using the Gauge Including Projector Augmented Wave Method: A Chemist's Point of View. **Chemical Reviews**, v. 112, n. 11, p. 5733–5779, 2012.

BORN, M., & OPPENHEIMER, R. Zur quantentheorie der molekeln. **Annalen der Physik**, v. 389, n. 20, p. 457–484, 1927.

BRITT, David; TRANCHEMONTAGNE, David; YAGHI, Omar M. Metal-organic frameworks with high capacity and selectivity for harmful gases. **Proceedings of the National Academy of Sciences**, v. 105, n. 33, p. 11623–11627, 2008.

BROMBERG, Lev; KLICHKO, Yaroslav; CHANG, Emily P.; SPEAKMAN, Scott; STRAUT, Christine M.; WILUSZ, Eugene; HATTON, T. Alan. Alkylaminopyridine-modified aluminum aminoterephthalate metal-organic frameworks as components of reactive self-detoxifying materials. **ACS Applied Materials and Interfaces**, v. 4, n. 9, p. 4595–4602, 2012.

CADIAU, Amandine et al. Design of Hydrophilic Metal Organic Framework Water Adsorbents for Heat Reallocation. **Advanced Materials**, v. 27, n. 32, p. 4775–4780, 2015.

CAPELLE, Klaus. A bird's-eye view of density-functional theory. **Brazilian Journal of Physics**, v. 36, n. 4a, p. 1318–1343, 2006.

CASPERSEN, Kyle J.; CARTER, Emily A. Finding transition states for crystalline solid-solid phase transformations. **Proceedings of the National Academy of Sciences**, v. 102, n.

19, p. 6738–6743, 2005.

CAVKA, Jasmina Hafizovic; JAKOBSEN, Søren; OLSBYE, Unni; GUILLOU, Nathalie; LAMBERTI, Carlo; BORDIGA, Silvia; LILLERUD, Karl Petter. A New Zirconium Inorganic Building Brick Forming Metal Organic Frameworks with Exceptional Stability. **Journal of the American Chemical Society**, v. 130, n. 42, p. 13850–13851, 2008.

CHEN, Haoyuan; LIAO, Peilin; MENDONCA, Matthew L.; SNURR, Randall Q. Insights into Catalytic Hydrolysis of Organophosphate Warfare Agents by Metal-Organic Framework NU-1000. **Journal of Physical Chemistry C**, v. 122, p. 12362–12368, 2018.

CHEN, Wei; WU, Chunsheng. Synthesis, functionalization, and applications of metal-organic frameworks in biomedicine. **Dalton Transactions**, v. 47, n. 7, p. 2114–2133, 2018.

COLOMBO, Valentina; GALLI, Simona; CHOI, Hye Jin; HAN, Ggoch Ddeul; MASPERO, Angelo; PALMISANO, Giovanni; MASCIOCCHI, Norberto; LONG, Jeffrey R. High thermal and chemical stability in pyrazolate-bridged metal-organic frameworks with exposed metal sites. **Chemical Science**, v. 2, n. 7, p. 1311–1319, 2011.

DACRE, Jack C.; GOLDMAN, Max. Toxicology and pharmacology of the chemical warfare agent sulfur mustard. **Pharmacological Reviews**, v. 48, n. 2, p. 289–326, 1996.

DAN-HARDI, Meenakshi; SERRE, Christian; ROZES, Laurence; MAURIN, Guillaume. A New Photoactive Crystalline Highly Porous Titanium (IV) Dicarboxylate. **Journal of the American Chemical Society**, v. 131, n. 31, p. 1–15, 2009.

DE LANGE, Martijn F.; VEROUDEN, Karlijn J. F. M.; VLUGT, Thijs J. H.; GASCON, Jorge; KAPTEIJN, Freek. Adsorption-Driven Heat Pumps: The Potential of Metal-Organic Frameworks. **Chemical Reviews**, v. 115, n. 22, p. 12205–12250, 2015.

DECOSTE, Jared B.; BROWE, Matthew A.; WAGNER, George W.; ROSSIN, Joseph A.; PETERSON, Gregory W. Removal of chlorine gas by an amine functionalized metal–organic framework via electrophilic aromatic substitution. **Chemical Communications**, v. 51, n. 62, p. 12474–12477, 2015.

DECOSTE, Jared B.; PETERSON, Gregory W. Metal–Organic Frameworks for Air Purification of Toxic Chemicals. **Chemical Reviews**, v. 114, n. 11, p. 5695–5727, 2014.

DECOSTE, Jared B.; PETERSON, Gregory W.; JASUJA, Himanshu; GLOVER, T. Grant; HUANG, You-gui; WALTON, Krista S. Stability and degradation mechanisms of metal–organic frameworks containing the Zr₆O₄(OH)₄ secondary building unit. **Journal of Materials Chemistry A**, v. 1, n. 18, p. 5642, 2013. a.

DECOSTE, Jared B.; PETERSON, Gregory W.; SCHINDLER, Bryan J.; KILLOPS, Kato L.; BROWE, Matthew A.; MAHLE, John J. The effect of water adsorption on the structure of the carboxylate containing metal–organic frameworks Cu-BTC, Mg-MOF-74, and UiO-66. **Journal of Materials Chemistry A**, v. 1, n. 38, p. 11922, 2013. b.

DELFINO, Reinaldo T.; RIBEIRO, Tatiana S.; FIGUEROA-VILLAR, José D. Organophosphorus Compounds as Chemical Warfare Agents: a Review. **J. Braz. Chem.**

Soc., v. 20, n. 3, p. 407–428, 2009.

DELLEY, B. From molecules to solids with the DMol3 approach. **The Journal of Chemical Physics**, v. 113, n. 18, p. 7756–7764, 2000.

DICHTWALD, Sara; WEINBROUM, Avi A. Bioterrorism and the anaesthesiologist's perspective. **Best Practice and Research: Clinical Anaesthesiology**, v. 22, n. 3, p. 477–502, 2008.

DION, M.; RYDBERG, H.; SCHRÖDER, E.; LANGRETH, D. C.; LUNDQVIST, B. I. Van der Waals density functional for general geometries. **Physical Review Letters**, v. 92, n. 24, p. 22–25, 2004.

DRASCH, Gustav; KRETSCHMER, Elisabeth; KAUERT, Gerold; VON MEYER, Ludwig. Concentrations of Mustard Gas [Bis(2-Chloroethyl)Sulfide] in the Tissues of a Victim of a Vesicant Exposure. **Journal of Forensic Sciences**, v. 32, n. 6, p. 11235J, 1987.

EASTON, D. F.; PETO, J.; DOLL, R. Cancers of the respiratory tract in mustard gas workers. **British Journal of Industrial Medicine**, v. 45, n. 10, p. 652–659, 1988.

EVANS, Arwyn; LUEBKE, Ryan; PETIT, Camille. The use of metal-organic frameworks for CO purification. **Journal of Materials Chemistry A**, v. 6, n. 23, p. 10570–10594, 2018.

EWALD, P. P. Die Berechnung optischer und elektrostatischer Gitterpotentiale. **Annalen der Physik**, v. 369, n. 3, p. 253–287, 1921.

FÉREY, Gérard. Hybrid porous solids: past, present, future. **Chem. Soc. Rev.**, v. 37, n. 1, p. 191–214, 2008.

FÉREY, Gérard et al. Why hybrid porous solids capture greenhouse gases? **Chem. Soc. Rev.**, v. 40, n. 2, p. 550–562, 2011.

FIDDER, Alex; MOES, Gerrit W. H.; SCHEFFER, Annehieke G.; VAN DER SCHANS, Govert P.; BAAN, Robert A.; DE JONG, Leo P. A.; BENSCHOP, Hendrik P. Synthesis, Characterization, and Quantitation of the Major Adducts Formed between Sulfur Mustard and DNA of Calf Thymus and Human Blood. **Chemical Research in Toxicology**, v. 7, n. 2, p. 199–204, 1994.

FIOLHAIS, Carlos; FERNANDO Nogueira; MIGUEL Al M. **A Primer in Density Functional Theory**. Springer Science & Business Media. v. 620, 2003.

FRENKEL, Daan; SMIT, Berend; RATNER, Mark A. Understanding Molecular Simulation: From Algorithms to Applications. **Physics Today**, v. 50, n. 7, p. 66–66, 1997.

GERACI, Matthew J. Mustard gas: Imminent danger or eminent threat? **Annals of Pharmacotherapy**, v. 42, n. 2, p. 237–246, 2008.

GHABILI, Kamyar; AGUTTER, Paul S.; GHANEI, Mostafa; ANSARIN, Khalil; PANAHI, Yunes; SHOJA, Mohammadali M. Sulfur mustard toxicity: History, chemistry, pharmacokinetics, and pharmacodynamics. **Critical Reviews in Toxicology**, v. 41, n. 5, p.

384–403, 2011.

GIANNOZZI, Paolo et al. QUANTUM ESPRESSO: a modular and open-source software project for quantum simulations of materials. **Journal of Physics: Condensed Matter**, v. 21, n. 39, p. 395502, 2009.

GÖLLER, Andreas; GRUMMT, Ulrich-Walter. Torsional barriers in biphenyl, 2,2'-bipyridine and 2-phenylpyridine. **Chemical Physics Letters**, v. 321, n. 5–6, p. 399–405, 2000.

GOMEZ-GUALDRON, Diego A.; GUTOV, Oleksii V.; KRUNGLEVICIUTE, Vaiva; BORAH, Bhaskarjyoti; MONDLOCH, Joseph E.; HUPP, Joseph T.; YILDIRIM, Taner; FARHA, Omar K.; SNURR, Randall Q. Computational Design of Metal–Organic Frameworks Based on Stable Zirconium Building Units for Storage and Delivery of Methane. **Chemistry of Materials**, v. 26, n. 19, p. 5632–5639, 2014.

GORDON, Wesley O.; TISSUE, Brian M.; MORRIS, John R. Adsorption and decomposition of dimethyl methylphosphonate on Y 2O₃ nanoparticles. **Journal of Physical Chemistry C**, v. 111, n. 8, p. 3233–3240, 2007.

GRANT GLOVER, T.; PETERSON, Gregory W.; SCHINDLER, Bryan J.; BRITT, David; YAGHI, Omar. MOF-74 building unit has a direct impact on toxic gas adsorption. **Chemical Engineering Science**, v. 66, n. 2, p. 163–170, 2011.

GREATHOUSE, Jeffery A.; OCKWIG, Nathan W.; CRISCENTI, Louise J.; GUILINGER, T. R.; POHL, Phil; ALLENDORF, Mark D. Computational screening of metal–organic frameworks for large-molecule chemical sensing. **Physical Chemistry Chemical Physics**, v. 12, n. 39, p. 12621, 2010.

GRIMME, Stefan. Accurate description of van der Waals complexes by density functional theory including empirical corrections. **Journal of Computational Chemistry**, v. 25, n. 12, p. 1463–1473, 2004.

GRIMME, Stefan. Semiempirical GGA-type density functional constructed with a long-range dispersion correction. **Journal of Computational Chemistry**, v. 27, n. 15, p. 1787–1799, 2006.

GRIMME, Stefan; ANTONY, Jens; EHRLICH, Stephan; KRIEG, Helge. A consistent and accurate ab initio parametrization of density functional dispersion correction (DFT-D) for the 94 elements H–Pu. **Journal of Chemical Physics**, v. 132, n. 15, 2010.

GUILLERM, V. et al. A series of isorecticular, highly stable, porous zirconium oxide based metal-organic frameworks. **Angewandte Chemie - International Edition**, v. 51, n. 37, p. 9267–9271, 2012.

GUO, X.; YOSHINOBU, J.; YATES, J. T. Decomposition of an organophosphonate compound (dimethylmethylphosphonate) on the nickel(111) and palladium(111) surfaces. **The Journal of Physical Chemistry**, v. 94, n. 17, p. 6839–6842, 1990.

HAFIZ, A. A. Metallosurfactants of Cu(II) and Fe(III) complexes as catalysts for the destruction of paraoxon. **Journal of Surfactants and Detergents**, v. 8, n. 4, p. 359–363,

2005.

HAFIZ, A. A.; AWADI, M. Y.; BADAWI, A. M.; MOKHAR, S. M. Catalytic destruction of paraoxon by metallomicelle layers of Co(II) and Cr(III). **Journal of Surfactants and Detergents**, v. 8, n. 2, p. 203–206, 2005.

HARVEY, S.P., SZAFRANIEC, L.L., BEAUDRY, W.T., EARLEY, J.T., AND IRVINE, R. L. **Neutralization and Biodegradation of Sulfur Mustard**. Disponível em: <http://oai.dtic.mil/oai/oai?verb=getRecord&metadataPrefix=html&identifier=ADA322638>. Acesso em 15 fev. 2019.

HARVEY, Jacob A.; GREATHOUSE, Jeffery A.; SAVA GALLIS, Dorina F. Defect and Linker Effects on the Binding of Organophosphorous Compounds in UiO-66 and Rare-Earth MOFs. **The Journal of Physical Chemistry C**, v. 122, n. 47, p. 26889–26896, 2018.

HARVEY, Jacob A.; MCENTEE, Monica L.; GARIBAY, Sergio J.; DURKE, Erin M.; DECOSTE, Jared B.; GREATHOUSE, Jeffery A.; SAVA GALLIS, Dorina F. Spectroscopically Resolved Binding Sites for the Adsorption of Sarin Gas in a Metal–Organic Framework: Insights beyond Lewis Acidity. **The Journal of Physical Chemistry Letters**, v. 10, n. 17, p. 5142–5147, 2019.

HASAN, Zubair; JHUNG, Sung Hwa. Removal of hazardous organics from water using metal-organic frameworks (MOFs): Plausible mechanisms for selective adsorptions. **Journal of Hazardous Materials**, v. 283, p. 329–339, 2015.

HAYES, Antoinette N.; GILBERT, Steven G. **Historical milestones and discoveries that shaped the toxicology sciences**. v. 99, p. 1-35, 2009.

HEGDE, R. I.; GREENLIEF, C. M.; WHITE, J. M. Surface chemistry of dimethyl methylphosphonate on Rh(100). **Journal of Physical Chemistry**, v. 89, n. 13, p. 2886–2891, 1985.

EHRE, W. J.; DITCHFIELD, K.; POPLE, J. A. Self-consistent molecular orbital methods. XII. Further extensions of gaussian-type basis sets for use in molecular orbital studies of organic molecules. **The Journal of Chemical Physics**, v. 56, n. 5, p. 2257–2261, 1972.

HENDERSON, M. A.; JIN, T.; WHITE, J. M. A TPD/AES study of the interaction of dimethyl methylphosphonate with iron oxide (α -Fe₂O₃) and silicon dioxide. **The Journal of Physical Chemistry**, v. 90, n. 19, p. 4607–4611, 1986.

HENDERSON, M. A.; WHITE, J. M. Adsorption and Decomposition of Dimethyl Methylphosphonate on Platinum(111). **Journal of the American Chemical Society**, v. 110, n. 21, p. 6939–6947, 1988.

HENKELMAN, Graeme; ARNALDSSON, Andri; JÓNSSON, Hannes. A fast and robust algorithm for Bader decomposition of charge density. **Computational Materials Science**, v. 36, n. 3, p. 354–360, 2006.

HENKELMAN, Graeme; JÓHANNESSON, Gísli; JÓNSSON, Hannes. Methods for finding

saddle points and minimum energy paths. In: **Theoretical methods in condensed phase chemistry**. Springer, Dordrecht, 2002. p. 269-302.

HENKELMAN, Graeme; JÓNSSON, Hannes. Improved tangent estimate in the nudged elastic band method for finding minimum energy paths and saddle points. **The Journal of Chemical Physics**, v. 113, n. 22, p. 9978–9985, 2000.

HENKELMAN, Graeme; UBERUAGA, Blas P.; JÓNSSON, Hannes. A climbing image nudged elastic band method for finding saddle points and minimum energy paths. **The Journal of Chemical Physics**, v. 113, n. 22, p. 9901–9904, 2000.

HOSKINS, Bernard F.; ROBSON, Richard. Infinite Polymeric Frameworks Consisting of Three Dimensionally Linked Rod-like Segments. **Journal of the American Chemical Society**, v. 111, n. 15, p. 5962–5964, 1989.

INANC, Ibrahim; YAZAYDIN, Ozgur. **Screening of Zeolitic Imidazolate Frameworks for Preconcentration of Hazardous Chemicals**. Dordrecht: Springer Netherlands, 2015. Disponível em: <http://link.springer.com/10.1007/978-94-017-7218-1>.

ISLAMOGLU, Timur et al. Presence versus Proximity: The Role of Pendant Amines in the Catalytic Hydrolysis of a Nerve Agent Simulant. **Angewandte Chemie - International Edition**, v. 57, n. 7, p. 1949–1953, 2018.

ISLAMOGLU, Timur; ATILGAN, Ahmet; MOON, Su Young; PETERSON, Gregory W.; DECOSTE, Jared B.; HALL, Morgan; HUPP, Joseph T.; FARHA, Omar K. Cerium(IV) vs Zirconium(IV) Based Metal-Organic Frameworks for Detoxification of a Nerve Agent. **Chemistry of Materials**, v. 29, n. 7, p. 2672–2675, 2017.

JACOBY, Mitch. Air filters for the face. **C&EN CHICAGO**, v. 92, n. 49, p. 34–38, 2014.

JASUJA, Himanshu; HUANG, You Gui; WALTON, Krista S. Adjusting the stability of metal-organic frameworks under humid conditions by ligand functionalization. **Langmuir**, v. 28, n. 49, p. 16874–16880, 2012.

JAVADI, Mohammad Ali; YAZDANI, Shahin; SAJJADI, Hamid; JADIDI, Khosro; KARIMIAN, Farid; EINOLLAHI, Bahram; JA'FARINASAB, Mohammad Reza; ZARE, Mohammad. Chronic and delayed-onset mustard gas keratitis: Report of 48 patients and review of literature. **Ophthalmology**, v. 112, n. 4, p. 617- 625.e2, 2005.

KALAJ, Mark; MOMENI, Mohammad R.; BENTZ, Kyle C.; BARCUS, Kyle S.; PALOMBA, Joseph M.; PAESANI, Francesco; COHEN, Seth M. Halogen bonding in UiO-66 frameworks promotes superior chemical warfare agent simulant degradation. **Chemical Communications**, n. 1, p. 3481–3484, 2019.

KANAN, Sofian M.; TRIPP, Carl P. An infrared study of adsorbed organophosphonates on silica: A prefiltering strategy for the detection of nerve agents on metal oxide sensors. **Langmuir**, v. 17, n. 7, p. 2213–2218, 2001.

KANG, In Joong; KHAN, Nazmul Abedin; HAQUE, Enamul; JHUNG, Sung Hwa. Chemical and Thermal Stability of Isotypic Metal–Organic Frameworks: Effect of Metal Ions.

Chemistry – A European Journal, v. 17, n. 23, p. 6437–6442, 2011.

KATZ, Michael J.; KLET, Rachel C.; MOON, Su-Young; MONDLOCH, Joseph E.; HUPP, Joseph T.; FARHA, Omar K. One Step Backward Is Two Steps Forward: Enhancing the Hydrolysis Rate of UiO-66 by Decreasing $[\text{OH}^-]$. **ACS Catalysis**, v. 5, n. 8, p. 4637–4642, 2015. a.

KATZ, Michael J.; MONDLOCH, Joseph E.; TOTTEN, Ryan K.; PARK, Jin K.; NGUYEN, Sonbinh T.; FARHA, Omar K.; HUPP, Joseph T. Simple and compelling biomimetic metal-organic framework catalyst for the degradation of nerve agent simulants. **Angewandte Chemie - International Edition**, v. 53, n. 2, p. 497–501, 2014.

KATZ, Michael J.; MOON, Su-Young; MONDLOCH, Joseph E.; BEYZAVI, M. Hassan; STEPHENSON, Casey J.; HUPP, Joseph T.; FARHA, Omar K. Exploiting parameter space in MOFs: a 20-fold enhancement of phosphate-ester hydrolysis with UiO-66-NH₂. **Chemical Science**, v. 6, n. 4, p. 2286–2291, 2015. b.

KEHE, Kai; SZINICZ, Ladislaus. Medical aspects of sulphur mustard poisoning. **Toxicology**, v. 214, n. 3, p. 198–209, 2005.

KENAR, Levent; KARAYILANOĞLU, Turan; KOSE, Songul. Laboratory Conditions and Safety in a Chemical Warfare Agent Analysis and Research Laboratory. **Military Medicine**, v. 167, n. 8, p. 628–633, 2002.

KHATERI, Shahriar; GHANEI, Mostafa; KESHAVARZ, Saeed; SOROUSH, Mohammad; HAINES, David. Incidence of Lung, Eye, and Skin Lesions as Late Complications in 34,000 Iranians with Wartime Exposure to Mustard Agent. **Journal of Occupational and Environmental Medicine**, [S. l.], v. 45, n. 11, p. 1136–1143, 2003. DOI: 10.1097/01.jom.0000094993.20914.d1.

KINGERY, Andrew F.; ALLEN, Herbert E. The environmental fate of organophosphorus nerve agents: A review. **Toxicological & Environmental Chemistry**, v. 47, n. 3–4, p. 155–184, 1995.

KNAGGE, Kevin; JOHNSON, Matthew; GRASSIAN, Vicki H.; LARSEN, Sarah C. Adsorption and thermal reaction of DMMP in nanocrystalline NaY. **Langmuir**, v. 22, n. 26, p. 11077–11084, 2006.

KOHN, W. Nobel Lecture: Electronic structure of matter—wave functions and density functionals. **Reviews of Modern Physics**, v. 71, n. 5, p. 1253–1266, 1999.

KOHN, W.; SHAM, L. J. Self-consistent equations including exchange and correlation effects. **Physical Review**, v. 140, n. 4A, p. A1133–A1138, 1965.

KOHN, W.; SHAM, L. J.; VANDERBILT, David; RAJAGOPAL, A. K.; CALLAWAY, J. Soft self-consistent pseudopotentials in a generalized eigenvalue formalism. **Physical Review B**, v. 7, n. 5, p. 7892–7895, 1965.

KONDO, Mitsuru; YOSHITOMI, Tomomichi; MATSUZAKA, Hiroyuki; KITAGAWA, Susumu; SEKI, Kenji. Three-Dimensional Framework with Channeling Cavities for Small

Molecules: $\{[M_2(4, 4'\text{-bpy})_3(\text{NO}_3)_4] \cdot x\text{H}_2\text{O}\}_n$ ($M = \text{Co, Ni, Zn}$). **Angewandte Chemie International Edition in English**, v. 36, n. 16, p. 1725–1727, 1997.

KORKMAZ, Ahmet; TAN, Dun Xian; REITER, Russel J. Acute and delayed sulfur mustard toxicity; novel mechanisms and future studies. **Interdisciplinary Toxicology**, v. 1, n. 1, p. 22–26, 2008.

KOWALCZYK, Piotr; GAUDEN, Piotr A.; TERZYK, Artur P.; NEIMARK, Alexander V. Screening of carbonaceous nanoporous materials for capture of nerve agents. **Phys. Chem. Chem. Phys.**, v. 15, n. 1, p. 291–298, 2013.

KOWALCZYK, Piotr; TANAKA, Hideki; KANEKO, Katsumi; TERZYK, Artur P.; DO, Duong D. Grand canonical Monte Carlo simulation study of methane adsorption at an open graphite surface and in slitlike carbon pores at 273 K. **Langmuir**, v. 21, n. 12, p. 5639–5646, 2005.

KUPPLER, Ryan J. et al. Potential applications of metal-organic frameworks. **Coordination Chemistry Reviews**, v. 253, n. 23–24, p. 3042–3066, 2009.

KÜSGENS, Pia; ROSE, Marcus; SENKOVSKA, Irena; FRÖDE, Heidrun; HENSCHHEL, Antje; SIEGLE, Sven; KASKEL, Stefan. Characterization of metal-organic frameworks by water adsorption. **Microporous and Mesoporous Materials**, v. 120, n. 3, p. 325–330, 2009.

LEACH, Andrew R. Molecular modelling: principles and applications. **Pearson Education Limited**, 2001.

LEE, Dennis T.; ZHAO, Junjie; OLDHAM, Christopher J.; PETERSON, Gregory W.; PARSONS, Gregory N. UiO-66-NH₂ Metal–Organic Framework (MOF) Nucleation on TiO₂, ZnO, and Al₂O₃ Atomic Layer Deposition-Treated Polymer Fibers: Role of Metal Oxide on MOF Growth and Catalytic Hydrolysis of Chemical Warfare Agent Simulants. **ACS Applied Materials & Interfaces**, v. 9, n. 51, p. 44847–44855, 2017.

LEE, J. H.; HOUK, R. T. J.; ROBINSON, A.; GREATHOUSE, J. A.; THORNBERG, S. M.; ALLENDORF, M. D.; HESKETH, P. J. Investigation of microcantilever array with ordered nanoporous coatings for selective chemical detection. *In*: (Thomas George, M. Saif Islam, Achyut K. Dutta, Eds.) **Micro- and nanotechnology sensors, systems, and applications II**, 2010.

LEE, Kyuho; MURRAY, Éamonn D.; KONG, Lingzhu; LUNDQVIST, Bengt I.; LANGRETH, David C. Higher-accuracy van der Waals density functional. **Physical Review B - Condensed Matter and Materials Physics**, v. 82, n. 8, p. 3–6, 2010.

LEMAIRE, Paul C.; LEE, Dennis T.; ZHAO, Junjie; PARSONS, Gregory N. Reversible Low-Temperature Metal Node Distortion during Atomic Layer Deposition of Al₂O₃ and TiO₂ on UiO-66-NH₂ Metal-Organic Framework Crystal Surfaces. **ACS Applied Materials and Interfaces**, v. 9, n. 26, p. 22042–22054, 2017.

LEUS, Karen; BOGAERTS, Thomas; DE DECKER, Jeroen; DEPAUW, Hannes; HENDRICKX, Kevin; VRIELINCK, Henk; VAN SPEYBROECK, Veronique; VAN DER

VOORT, Pascal. Systematic study of the chemical and hydrothermal stability of selected “stable” Metal Organic Frameworks. **Microporous and Mesoporous Materials**, v. 226, p. 110–116, 2016.

LI, Peng et al. Synthesis of nanocrystals of Zr-based metal–organic frameworks with csq-net: significant enhancement in the degradation of a nerve agent simulant. **Chem. Commun.**, v. 51, n. 54, p. 10925–10928, 2015.

LIANG, Weibin; CHEVREAU, Hubert; RAGON, Florence; SOUTHON, Peter D.; PETERSON, Vanessa K.; D’ALESSANDRO, D. M. Electronic Supporting Information Tuning pore size in a zirconium-tricarboxylate metal-organic framework. **CrystEngComm**, v. 16, n. 29, p. 6530–6533, 2014.

LIU, Jian; BENIN, Annabelle I.; FURTADO, Amanda M. B.; JAKUBCZAK, Paulina; WILLIS, Richard R.; LEVAN, M. Douglas. Stability effects on CO₂ adsorption for the DOBDC series of metal-organic frameworks. **Langmuir**, v. 27, n. 18, p. 11451–11456, 2011.

LIU, Yangyang; MOON, Su Young; HUPP, Joseph T.; FARHA, Omar K. Dual-Function Metal-Organic Framework as a Versatile Catalyst for Detoxifying Chemical Warfare Agent Simulants. **ACS Nano**, v. 9, n. 12, p. 12358–12364, 2015.

LÓPEZ-MAYA, Elena; MONTORO, Carmen; RODRÍGUEZ-ALBELO, L. Marleny; AZNAR CERVANTES, Salvador D.; LOZANO-PÉREZ, A. Abel; CENÍS, José Luis; BAREA, Elisa; NAVARRO, Jorge A. R. R. Textile/Metal-Organic-Framework Composites as Self-Detoxifying Filters for Chemical-Warfare Agents. **Angewandte Chemie International Edition**, v. 54, n. 23, p. 6790–6794, 2015.

LORENTZ, H. A. Ueber die Anwendung des Satzes vom Virial in der kinetischen Theorie der Gase. **Annalen der Physik**, v. 248, n. 1, p. 127–136, 1881.

LOVEN, A.W. & VERMILION, J. Adsorption-Desorption Properties of Sorbents. **West virginia pulp and paper co New York**, p.1-27, 1964.

LOW, John J.; BENIN, Annabelle I.; JAKUBCZAK, Paulina; ABRAHAMIAN, Jennifer F.; FAHEEM, Syed A.; WILLIS, Richard R. Virtual High Throughput Screening Confirmed Experimentally: Porous Coordination Polymer Hydration. **Journal of the American Chemical Society**, v. 131, n. 43, p. 15834–15842, 2009.

LUDLUM, David B.; AUSTIN-RITCHIE, Paula; HAGOPIAN, Miasnig; NIU, Tian Qi; YU, Dong. Detection of sulfur mustard-induced DNA modifications. **Chemico-Biological Interactions**, v. 91, n. 1, p. 39–49, 1994.

MA, Deyun; LI, Yingwei; LI, Zhong. Tuning the moisture stability of metal-organic frameworks by incorporating hydrophobic functional groups at different positions of ligands. **Chemical Communications**, v. 47, n. 26, p. 7377–7379, 2011.

MA, Feng-Ji; LIU, Shu-Xia; SUN, Chun-Yan; LIANG, Da-Dong; REN, Guo-Jian; WEI, Feng; CHEN, Ya-Guang; SU, Zhong-Min. A Sodalite-Type Porous Metal–Organic Framework with Polyoxometalate Templates: Adsorption and Decomposition of Dimethyl Methylphosphonate. **Journal of the American Chemical Society**, v. 133, n. 12, p. 4178–

4181, 2011.

MAHAN, Gerald D. Homogeneous Electron Gas. *In: Many-Particle Physics*. Boston, MA: Springer MA, p. 295–374, 2000.

MAKOV, G.; PAYNE, M. C. Periodic boundary conditions in ab initio calculations. **Physical Review B**, v. 51, n. 7, p. 4014–4022, 1995.

MANGUN, C. L.; YUE, Z.; ECONOMY, J.; MALONEY, S.; KEMME, P.; CROPEK, D. Adsorption of organic contaminants from water using tailored ACFs. **Chemistry of Materials**, v. 13, n. 7, p. 2356–2360, 2001.

MARTIN, Marcus G.; SIEPMANN, J. Ilja. Transferable Potentials for Phase Equilibria. 1. United-Atom Description of n -Alkanes. **The Journal of Physical Chemistry B**, v. 102, n. 97, p. 2569–2577, 1998.

MATITO-MARTOS, Ismael; MOGHADAM, Peyman Z.; LI, Aurelia; COLOMBO, Valentina; NAVARRO, Jorge A. R.; CALERO, Sofia; FAIREN-JIMENEZ, David. Discovery of an Optimal Porous Crystalline Material for the Capture of Chemical Warfare Agents. **Chemistry of Materials**, v. 30, n. 14, p. 4571–4579, 2018.

MAURIN, Guillaume; SERRE, Christian; COOPER, Andrew; FÉREY, Gérard. The new age of MOFs and of their porous-related solids. **Chemical Society Reviews**, v. 46, n. 11, p. 3104–3107, 2017.

MAYO, Stephen L.; OLAFSON, Barry D.; III, William a Goddard; EB, Eva; EL, E. a E. T.; GODDARD, William A. DREIDING: A generic force field for molecular simulations. **Journal of Physical chemistry**, v. 94, n. Suite 540, p. 8897–8909, 1990.

MCCARTHY, Danielle L.; LIU, Jian; DWYER, Derek B.; TROIANO, Jennifer L.; BOYER, Steven M.; DECOSTE, Jared B.; BERNIER, William E.; JONES, Wayne E.; JONES, JR, Wayne E. Electrospun metal-organic framework polymer composites for the catalytic degradation of methyl paraoxon. **New Journal of Chemistry**, v. 41, n. 17, p. 8748–8753, 2017.

MCQUARRIE, Donald Alan AND SIMON, John Douglas. **McQuarrie: Physical Chemistry: A molecular approach**. Sausalito, California: University science books, Sterling Publishing Company, 1997.

METROPOLIS, Nicholas; ROSENBLUTH, Arianna W.; ROSENBLUTH, Marshall N.; TELLER, Augusta H.; TELLER, Edward. Equation of state calculations by fast computing machines. **The Journal of Chemical Physics**, v. 21, n. 6, p. 1087–1092, 1953.

MICHAEL A. Wartell, MICHAEL T. Kleinman, BEVERLY M. Huey, And Laura M. Duffy. Strategies to Protect the Health of Deployed U.S. Forces. Washington, D.C.: **National Academies Press**, 1999.

MOMENI, Mohammad R.; CRAMER, Christopher J. Structural Characterization of Pristine and Defective $[Zr_{12}(\mu_3-O)_8(\mu_3-OH)_8(\mu_2-OH)_6]^{18+}$ Double-Node Metal-Organic

Framework and Predicted Applications for Single-Site Catalytic Hydrolysis of Sarin. **Chemistry of Materials**, v. 30, n. 13, p. 4432–4439, 2018. a.

MOMENI, Mohammad R.; CRAMER, Christopher J. Dual Role of Water in Heterogeneous Catalytic Hydrolysis of Sarin by Zirconium-Based Metal–Organic Frameworks. **ACS Applied Materials & Interfaces**, v. 10, n. 22, p. 18435–18439, 2018. b.

MOMENI, Mohammad R.; CRAMER, Christopher J. Computational Screening of Roles of Defects and Metal Substitution on Reactivity of Different Single- vs Double-Node Metal–Organic Frameworks for Sarin Decomposition. **Journal of Physical Chemistry C**, v. 123, n. 24, p. 15157–15165, 2019.

MONDAL, Suvendu Sekhar; HOLDT, Hans Jürgen. Breaking Down Chemical Weapons by Metal–Organic Frameworks. **Angewandte Chemie - International Edition**, v. 55, n. 1, p. 42–44, 2016.

MONDLOCH, Joseph E. et al. Vapor-Phase Metalation by Atomic Layer Deposition in a Metal–Organic Framework. **Journal of the American Chemical Society**, v. 135, n. 28, p. 10294–10297, 2013.

MONDLOCH, Joseph E. et al. Destruction of chemical warfare agents using metal–organic frameworks. **Nature Materials**, v. 14, n. 5, p. 512–516, 2015.

MONTORO, Carmen; LINARES, Fátima; QUARTAPELLE PROCOPIO, Elsa; SENKOVSKA, Irena; KASKEL, Stefan; GALLI, Simona; MASCIOCCHI, Norberto; BAREA, Elisa; NAVARRO, Jorge A. R. Capture of Nerve Agents and Mustard Gas Analogues by Hydrophobic Robust MOF-5 Type Metal–Organic Frameworks. **Journal of the American Chemical Society**, v. 133, n. 31, p. 11888–11891, 2011.

MOON, Su Young; LIU, Yangyang; HUPP, Joseph T.; FARHA, Omar K. Instantaneous Hydrolysis of Nerve-Agent Simulants with a Six-Connected Zirconium-Based Metal–Organic Framework. **Angewandte Chemie - International Edition**, v. 66, p. 6795–6799, 2015.

MORRILL, L.G., REED, L.W., AND CHINN, K. S. K. **Toxic Chemicals in the Soil Environment / Interaction of some Toxic Chemicals/CWAs and Soils**. v.2, p.1-55, 1985.

MOSS, John A.; SZCZEPANKIEWICZ, Steven H.; PARK, Eleanor; HOFFMANN, Michael R. Adsorption and photodegradation of dimethyl methylphosphonate vapor at TiO₂ surfaces. **Journal of Physical Chemistry B**, v. 109, n. 42, p. 19779–19785, 2005.

MULLIKEN, R. S. Electronic Population Analysis on LCAO–MO Molecular Wave Functions. I. **The Journal of Chemical Physics**, v. 23, n. 10, p. 1833–1840, 1955.

MUNRO, N. B.; AMBROSE, K. R.; WATSON, A. P. Toxicity of the organophosphate chemical warfare agents GA, GB, and VX: Implications for public protection. **Environmental Health Perspectives**, v. 102, n. 1, p. 18–38, 1994.

MUNRO, Nancy B.; TALMAGE, Sylvia S.; GRIFFIN, Guy D.; WATERS, Larry C.; WATSON, Annetta P.; KING, Joseph F.; HAUSCHILD, Veronique. The Sources, Fate, and Toxicity of Chemical Warfare Agent Degradation Products. v. 107, n. 12, p. 933–974, 1999.

NATIONAL RESEARCH COUNCIL. **Chemical and Biological Terrorism: Research and Development to Improve Civilian Medical Response**. National Academy, 1999.

NAZARIAN, Dalar; CAMP, Jeffrey S.; SHOLL, David S. A Comprehensive Set of High-Quality Point Charges for Simulations of Metal-Organic Frameworks. **Chemistry of Materials**, v. 28, n. 3, p. 785–793, 2016.

NI, Zheng; JERRELL, John P.; CADWALLADER, Keith R.; MASEL, Richard I. Metal-organic frameworks as adsorbents for trapping and preconcentration of organic phosphonates. **Analytical Chemistry**, v. 79, n. 4, p. 1290–1293, 2007.

NORADOUN, C. E.; MEKMAYSY, C. S.; HUTCHESON, R. M.; CHENG, I. F. Detoxification of malathion a chemical warfare agent analog using oxygen activation at room temperature and pressure. **Green Chemistry**, v. 7, p. 426–430, 2005.

NOWICKI, Piotr; PIETRZAK, Robert. Effect of ammoxidation of activated carbons obtained from sub-bituminous coal on their NO₂ sorption capacity under dry conditions. **Chemical Engineering Journal**, v. 166, n. 3, p. 1039–1043, 2011.

OPCW. **Assistance and Protection Against Attack with Chemical Weapons**. The Hague, The Netherlands, 2019. Disponível em: <https://www.opcw.org/work/responding-use-chemical-weapons>. Acesso em 25 de jan. 2019.

OPCW. **Chemical weapons convention**. The Hague, The Netherlands, 2005. Disponível em: <https://www.opcw.org/chemical-weapons-convention>. Acesso em: 20 de jan. 2019.

OUDEJANS, Lukas. **Adsorption and Desorption of Chemical Warfare Agents on Activated Carbon: Impact of Temperature and Relative Humidity Adsorption and Desorption of Chemical Warfare Agents on Activated Carbon: Impact of Temperature and Relative Humidity**. U.S. Environmental Protection Agency (MD-E343-06), 2014.

PACK, James D.; MONKHORST, Hendrik J. “Special points for Brillouin-zone integrations”—a reply. **Physical Review B**, v. 16, n. 4, p. 1748–1749, 1977.

PADIAL, Natalia M. et al. Highly hydrophobic isorecticular porous metal-organic frameworks for the capture of harmful volatile organic compounds. **Angewandte Chemie - International Edition**, v. 52, n. 32, p. 8290–8294, 2013.

PANAHI, Yunes; ABDOLGHAFARI, Amir H.; SAHEBKAR, Amirhossein. A review on symptoms, treatments protocols, and proteomic profile in sulfur mustard-exposed victims. **Journal of Cellular Biochemistry**, v. 119, n. 1, p. 197–206, 2018.

PANAYOTOV, Dimitar A.; MORRIS, John R. Catalytic degradation of a chemical warfare agent simulant: Reaction mechanisms on TiO₂-supported Au nanoparticles. **Journal of Physical Chemistry C**, v. 112, n. 19, p. 7496–7502, 2008.

PANAYOTOV, Dimitar A.; MORRIS, John R. Uptake of a chemical warfare agent simulant (DMMP) on TiO₂: Reactive adsorption and active site poisoning. **Langmuir**, v. 25, n. 6, p. 3652–3658, 2009.

PAPIRMEISTER, Bruno; GROSS, Clark L.; MEIER, Henry L.; PETRALI, John P.; JOHNSON, John B. Molecular basis for mustard-induced vesication. **Toxicological Sciences**, v. 5, n. 6, p. 134–149, 1985.

PAROMOV, Victor; SUNTRES, Zacharias; SMITH, Milton; STONE, William L. Sulfur mustard toxicity following dermal exposure: role of oxidative stress, and antioxidant therapy. **Journal of burns and wounds**, v. 7, p. e7, 2007.

PAYNE, M. C.; TETER, M. P.; ALLAN, D. C.; ARIAS, T. A.; JOANNOPOULOS, J. D. Iterative minimization techniques for ab initio total-energy calculations: molecular dynamics and conjugate gradients. **Reviews of Modern Physics**, v. 64, n. 4, p. 1045–1097, 1992.

PERDEW, J. P.; ZUNGER, Alex. Self-interaction correction to density-functional approximations for many-electron systems. **Physical Review B**, v. 23, n. 10, p. 5048–5079, 1981.

PERDEW, John P.; BURKE, Kieron; ERNZERHOF, Matthias. Generalized gradient approximation made simple. **Physical Review Letters**, v. 77, n. 18, p. 3865–3868, 1996.

PERDEW, John P.; WANG, Yue. Accurate and simple analytic representation of the electron-gas correlation energy. **Physical Review B**, [S. l.], v. 45, n. 23, p. 13244–13249, 1992.

PETERSON, Gregory W.; BRITT, David K.; SUN, Daniel T.; MAHLE, John J.; BROWE, Matthew; DEMASKY, Tyler; SMITH, Shirmonda; JENKINS, Amanda; ROSSIN, Joseph A. Multifunctional purification and sensing of toxic hydride gases by CUBTC metal-organic framework. **Industrial and Engineering Chemistry Research**, v. 54, n. 14, p. 3626–3633, 2015.

PETERSON, Gregory W.; MOON, Su Young; WAGNER, George W.; HALL, Morgan G.; DECOSTE, Jared B.; HUPP, Joseph T.; FARHA, Omar K. Tailoring the Pore Size and Functionality of UiO-Type Metal-Organic Frameworks for Optimal Nerve Agent Destruction. **Inorganic Chemistry**, v. 54, n. 20, p. 9684–9686, 2015.

PETERSON, Gregory W.; WAGNER, George W. Detoxification of chemical warfare agents by CuBTC. **Journal of Porous Materials**, v. 21, n. 2, p. 121–126, 2014.

PETIT, Camille. Present and future of MOF research in the field of adsorption and molecular separation. **Current Opinion in Chemical Engineering**, v. 20, p. 132–142, 2018.

PLONKA, Anna M. et al. In Situ Probes of Capture and Decomposition of Chemical Warfare Agent Simulants by Zr-Based Metal Organic Frameworks. **Journal of the American Chemical Society**, v. 139, n. 2, p. 599–602, 2017.

RABER, Ellen; MCGUIRE, Raymond. Oxidative decontamination of chemical and biological warfare agents using L-Gel. **Journal of Hazardous Materials**, v. 93, n. 3, p. 339–352, 2002.

RAJAGOPAL, A. K.; CALLAWAY, J. Inhomogeneous Electron Gas. **Physical Review B**, v. 7, n. 5, p. 1912–1919, 1973.

RAPPÉ, A. K.; CASEWIT, C. J.; COLWELL, K. S.; GODDARD, W. A.; SKIFF, W. M.

UFF, a Full Periodic Table Force Field for Molecular Mechanics and Molecular Dynamics Simulations. **Journal of the American Chemical Society**, v. 114, n. 25, p. 10024–10035, 1992.

ROGGE, Sven M. J.; WIEME, Jelle; VANDUYFHUYS, Louis; VANDENBRANDE, Steven; MAURIN, Guillaume; VERSTRAELEN, Toon; WAROQUIER, Michel; VAN SPEYBROECK, Veronique. Thermodynamic Insight in the High-Pressure Behavior of UiO-66: Effect of Linker Defects and Linker Expansion. **Chemistry of Materials**, v. 28, n. 16, p. 5721–5732, 2016.

ROUQUEROL, F.; ROUQUEROL, J.; SING, K. S. W.; LLEWELLYN, P.; MAURIN, G. **Adsorption by Powders and Porous Solids Principles, Methodology and Applications**. Aix Marseille University-CNRS, MADIREL Laboratory, Marseille, France and University of Montpellier 2, Institute Charles Gerhardt, Montpellier, France: Academic press, 2014.

ROY, Anuradha; SRIVASTAVA, Avanish K.; SINGH, Beer; SHAH, Dilip; MAHATO, T. H.; GUTCH, P. K.; HALVE, A. K. Degradation of sarin, DECIP and DECNP over Cu-BTC metal organic framework. **Journal of Porous Materials**, v. 20, n. 5, p. 1103–1109, 2013.

ROY, Anuradha; SRIVASTAVA, Avanish K.; SINGH, Beer; SHAH, Dilip; MAHATO, Timir Haran; SRIVASTAVA, Anchal. Kinetics of degradation of sulfur mustard and sarin simulants on HKUST-1 metal organic framework. **Dalton Transactions**, v. 41, n. 40, p. 12346–12348, 2012.

RUFFLEY, Jonathan P.; GOODENOUGH, Isabella; LUO, Tian-Yi; RICHARD, Melissandre; BORGUET, Eric; ROSI, Nathaniel L.; JOHNSON, J. Karl. Design, Synthesis, and Characterization of Metal–Organic Frameworks for Enhanced Sorption of Chemical Warfare Agent Simulants. **The Journal of Physical Chemistry C**, v. 123, n. 32, p. 19748–19758, 2019.

RUSU, Camelia N.; YATES, John T. Photooxidation of dimethyl methylphosphonate on TiO₂ powder. **Journal of Physical Chemistry B**, v. 104, n. 51, p. 12299–12305, 2000.

SAVA GALLIS, Dorina F.; HARVEY, Jacob A.; PEARCE, Charles J.; HALL, Morgan G.; DECOSTE, Jared B.; KINNAN, Mark K.; GREATHOUSE, Jeffery A. Efficient MOF-based degradation of organophosphorus compounds in non-aqueous environments. **Journal of Materials Chemistry A**, v. 6, n. 7, p. 3038–3045, 2018.

SAXENA, Amit; SRIVASTAVA, Avanish K.; SINGH, Beer; GOYAL, Anshu. Removal of sulphur mustard, sarin and simulants on impregnated silica nanoparticles. **Journal of Hazardous Materials**, v. 211–212, p. 226–232, 2012.

SCHAATE, Andreas; DÜHNEN, Simon; PLATZ, Georg; LILIENTHAL, Sebastian; SCHNEIDER, Andreas M.; BEHRENS, Peter. A novel Zr-based porous coordination polymer containing azobenzenedicarboxylate as a linker. **European Journal of Inorganic Chemistry**, n. 5, p. 790–796, 2012.

SCHNEIDER, Jenny; MATSUOKA, Masaya; TAKEUCHI, Masato; ZHANG, Jinlong; HORIUCHI, Yu; ANPO, Masakazu; BAHNEMANN, Detlef W. Understanding TiO₂ Photocatalysis: Mechanisms and Materials. **Chemical reviews**, v. 114, n. 19, p. 9919–9986,

2014.

ŠEČKUTE, Jolita; MENKE, Jessica L.; EMNETT, Ryan J.; PATTERSON, Eric V.; CRAMER, Christopher J. Ab initio molecular orbital and density functional studies on the solvolysis of sarin and O,S-dimethyl methylphosphonothiolate, a VX-like compound. **Journal of Organic Chemistry**, v. 70, n. 22, p. 8649–8660, 2005.

SEO, You-Kyong et al. Energy-Efficient Dehumidification over Hierarchically Porous Metal-Organic Frameworks as Advanced Water Adsorbents. **Advanced Materials**, v. 24, n. 6, p. 806–810, 2012.

SEREDYCH, Mykola; DELIYANNI, Eleni; BANDOSZ, Teresa J. Role of microporosity and surface chemistry in adsorption of 4,6-dimethyldibenzothiophene on polymer-derived activated carbons. **Fuel**, v. 89, n. 7, p. 1499–1507, 2010.

SERRE, C. A private communication. 2018.

SHEARER, Greig C.; FORSELV, Stian; CHAVAN, Sachin; BORDIGA, Silvia; MATHISEN, Karina; BJØRGEN, Morten; SVELLE, Stian; LILLERUD, Karl Petter. In Situ Infrared Spectroscopic and Gravimetric Characterisation of the Solvent Removal and Dehydroxylation of the Metal Organic Frameworks UiO-66 and UiO-67. **Topics in Catalysis**, v. 56, n. 9–10, p. 770–782, 2013.

SHOLL, David; STECKEL, Janice. **Density functional theory - A Practical Introduction**. John Wiley & Sons, Inc., 2011.

SIDELL, F. R.; TAKAFUJI, E. T.; FRANZ, D. R. **MEDICAL ASPECTS OF CHEMICAL AND BIOLOGICAL WARFARE**. Office of The Surgeon General Department of the Army, United States of America Editor, 1997.

SILVA, Patrícia; VILELA, Sérgio M. F.; TOMÉ, João P. C.; ALMEIDA PAZ, Filipe A. Multifunctional metal-organic frameworks: From academia to industrial applications. **Chemical Society Reviews**, v. 44, n. 19, p. 6774–6803, 2015.

SINGER, Brett C.; HODGSON, Alfred T.; DESTAILLATS, Hugo; HOTCHI, Toshifumi; REVZAN, Kenneth L.; SEXTRO, Richard G. Indoor sorption of surrogates for sarin and related nerve agents. **Environmental Science and Technology**, v. 39, n. 9, p. 3203–3214, 2005.

SINGH, BEER; PRASAD, GANGAVARAPU KRISHNA; PANDEY, K S; DANIKHEL, R K; VIJAYARAGHAVAN, R. Decontamination of Chemical Warfare Agents. **Decontamination of Warfare Agents**, Weinheim, Germany, v. 60, n. 4, p. 428–441, 2010.

SMENTKOWSKI, V. S.; HAGANS, P.; YATES, J. T. Study of the catalytic destruction of dimethyl methylphosphonate: oxidation over Mo(110). **Journal of physical chemistry**, v. 92, n. 22, p. 6351–6357, 1988.

SMITH, B. M. Catalytic methods for the destruction of chemical warfare agents under ambient conditions. **Chemical Society Reviews**, v. 37, n. 3, p. 470–478, 2008. a.

SOKKALINGAM, Nandhini; KAMATH, Ganesh; COSCIONE, Maria; POTOFF, Jeffrey J. Extension of the transferable potentials for phase equilibria force field to dimethylmethyl phosphonate, sarin, and soman. **Journal of Physical Chemistry B**, v. 113, n. 30, p. 10292–10297, 2009.

SOLBERG, Yoram; ALCALAY, Menachem; BELKIN, Michael. Ocular injury by mustard gas. **Survey of Ophthalmology**, v. 41, n. 6, p. 461–466, 1997.

STASSEN, I. et al. Towards metal–organic framework based field effect chemical sensors: UiO-66-NH₂ for nerve agent detection. **Chem. Sci.**, v. 7, n. 9, p. 5827–5832, 2016.

STEINRITZ, Dirk; THIERMANN, Horst. Sulfur Mustard. *In*: BRENT, Jeffrey; BURKHART, Keith; DARGAN, Paul; HATTEN, Benjamin; MEGARBANE, Bruno; PALMER, Robert. **Critical Care Toxicology**. Cham: Springer International Publishing, p. 1–30, 2016.

SZINICZ, L. History of chemical and biological warfare agents. **Toxicology**, v. 214, n. 3, p. 167–181, 2005.

TAN, Peng; JIANG, Yao; SUN, Lin-Bing; LIU, Xiao-Qin; ALBAHILY, Khalid; RAVON, Ugo; VINU, Ajayan. Design and fabrication of nanoporous adsorbents for the removal of aromatic sulfur compounds. **Journal of Materials Chemistry A**, v. 6, n. 47, p. 23978–24012, 2018.

TAVERNELLI, Ivano; LIN, I. Chun; ROTHLSBERGER, Ursula. Multicenter-type corrections to standard DFT exchange and correlation functionals. **Physical Review B**, v. 79, n. 4, p. 045106, 2009.

TAYLOR, Jared M.; VAIDHYANATHAN, Ramanathan; IREMONGER, Simon S.; SHIMIZU, George K. H. Enhancing water stability of metal-organic frameworks via phosphonate monoester linkers. **Journal of the American Chemical Society**, v. 134, n. 35, p. 14338–14340, 2012.

TEMPLETON, M. K.; WEINBERG, W. H. Adsorption and Decomposition of Dimethyl Methylphosphonate on an Aluminum Oxide Surface. **Journal of the American Chemical Society**, v. 107, n. 1, p. 97–108, 1985.

TKATCHENKO, Alexandre; SCHEFFLER, Matthias. Accurate molecular van der Waals interactions from ground-state electron density and free-atom reference data. **Physical Review Letters**, v. 102, n. 7, p. 6–9, 2009.

TOTTEN, Ryan K.; KIM, Ye Seong; WESTON, Mitchell H.; FARHA, Omar K.; HUPP, Joseph T.; NGUYEN, Sonbinh T. Enhanced catalytic activity through the tuning of micropore environment and supercritical CO₂ processing: Al(Porphyrin)-based porous organic polymers for the degradation of a nerve agent simulant. **Journal of the American Chemical Society**, v. 135, n. 32, p. 11720–11723, 2013. a.

TOTTEN, Ryan K.; RYAN, Patrick; KANG, Byungman; LEE, Suk Joong; BROADBELT, Linda J.; SNURR, Randall Q.; HUPP, Joseph T.; NGUYEN, Sonbinh T. Enhanced catalytic decomposition of a phosphate triester by modularly accessible bimetallic porphyrin dyads and

dimers. **Chemical Communications**, v. 48, n. 35, p. 4178–4180, 2012.

TOTTEN, Ryan K.; WESTON, Mitchell H.; PARK, Jin Kuen; FARHA, Omar K.; HUPP, Joseph T.; NGUYEN, Sonbinh T. Catalytic solvolytic and hydrolytic degradation of toxic methyl paraoxon with la(catecholate)-functionalized porous organic polymers. **ACS Catalysis**, v. 3, n. 7, p. 1454–1459, 2013. b.

TROYA, Diego. Reaction Mechanism of Nerve-Agent Decomposition with Zr-Based Metal Organic Frameworks. **The Journal of Physical Chemistry C**, v. 120, n. 51, p. 29312–29323, 2016.

TRUBITSYN, Dmitry A.; VORONTSOV, Alexander V. Experimental study of dimethyl methylphosphonate decomposition over anatase TiO₂. **Journal of Physical Chemistry B**, v. 109, n. 46, p. 21884–21892, 2005.

VAISS, Viviane S.; BORGES, Itamar; LEITÃO, Alexandre A. Sarin degradation using brucite. **Journal of Physical Chemistry C**, v. 115, n. 50, p. 24937–24944, 2011.

VALDEZ, Carlos A.; LEIF, Roald N.; HOK, Saphon; HART, Bradley R. Analysis of chemical warfare agents by gas chromatography-mass spectrometry: methods for their direct detection and derivatization approaches for the analysis of their degradation products. **Reviews in Analytical Chemistry**, v. 37, n. 1, p. 1–26, 2018.

VANDERBILT, David. Soft self-consistent pseudopotentials in a generalized eigenvalue formalism. **Physical Review B**, v. 41, n. 11, p. 7892–7895, 1990.

VELLINGIRI, Kowsalya; PHILIP, Ligy; KIM, Ki Hyun. Metal–organic frameworks as media for the catalytic degradation of chemical warfare agents. **Coordination Chemistry Reviews**, v. 353, p. 159–179, 2017.

VERMA, Aniza K.; SRIVASTAVA, Avanish K.; SINGH, Beer; SHAH, Dilip; SHRIVASTAVA, Smriti; SHINDE, Chandra Kant P. Alumina-supported oxime for the degradation of sarin and diethylchlorophosphate. **Chemosphere**, v. 90, n. 8, p. 2254–2260, 2013.

VIEIRA SOARES, C. et al. Adsorption of Small Molecules in the Porous Zirconium-Based Metal Organic Framework MIL-140A (Zr): A Joint Computational-Experimental Approach. **The Journal of Physical Chemistry C**, v. 120, n. 13, p. 7192–7200, 2016.

VIEIRA SOARES, C.; MAURIN, G.; LEITÃO, A. A. Computational Exploration of the Catalytic Degradation of Sarin and Its Simulants by a Titanium Metal–Organic Framework. **The Journal of Physical Chemistry C**, v. 123, n. 31, p. 19077–19086, 2019. a.

VIEIRA SOARES, C.; MAURIN, G.; LEITÃO, A. A. Computational Exploration of the Catalytic Degradation of Sarin and Its Simulants by a Titanium Metal–Organic Framework. **The Journal of Physical Chemistry C**, v. 123, n. 31, p. 19077–19086, 2019. b.

VISHNYAKOV, Aleksey; GOR, Gennady Yu; LEE, Ming Tsung; NEIMARK, Alexander V. Molecular modeling of organophosphorous agents and their aqueous solutions. **Journal of Physical Chemistry A**, v. 115, n. 20, p. 5201–5209, 2011.

VLUGT, T. J. H.; GARCÍA-PÉREZ, E.; DUBBELDAM, D.; BAN, S.; CALERO, S. Computing the Heat of Adsorption using Molecular Simulations: The Effect of Strong Coulombic Interactions. **Journal of Chemical Theory and Computation**, v. 4, n. 7, p. 1107–1118, 2008.

VON LILIENFELD, O. Anatole; TAVERNELLI, Ivano; ROTHLSBERGER, Ursula; SEBASTIANI, Daniel. Optimization of Effective Atom Centered Potentials for London Dispersion Forces in Density Functional Theory. **Physical Review Letters**, v. 93, n. 15, p. 153004, 2004.

VOSKO, S. H.; WILK, L.; NUSAIR, M. Accurate spin-dependent electron liquid correlation energies for local spin density calculations: a critical analysis. **Canadian Journal of Physics**, v. 58, n. 8, p. 1200–1211, 1980.

WAGNER, G. W.; PROCELL, L. R.; O'CONNOR, R. J.; MUNAVALLI, S.; CARNES, C. L.; KAPOOR, P. N.; KLABUNDE, K. J. Reactions of VX, GB, GD, and HD with nanosize AL₂O₃. Formation of aluminophosphonates. **Journal of the American Chemical Society**, v. 123, n. 8, p. 1636–1644, 2001.

WAGNER, George W.; BARTRAM, Philip W.; KOPER, Olga; KLABUNDE, Kenneth J. Reactions of VX, GD, and HD with Nanosize MgO. **The Journal of Physical Chemistry B**, [S. l.], v. 103, n. 16, p. 3225–3228, 1999.

WAGNER, George W.; CHEN, Qiang; WU, Yue. Reactions of VX, GD, and HD with nanotubular titania. **Journal of Physical Chemistry C**, v. 112, n. 31, p. 11901–11906, 2008.

WAGNER, George W.; KOPER, O. B.; LUCAS, E.; DECKER, S.; KLABUNDE, Kenneth J. Reactions of VX, GD, and HD with Nanosize CaO: Autocatalytic Dehydrohalogenation of HD. **Journal of Physical Chemistry B**, v. 104, n. 410, p. 5118–5123, 2000.

WAGNER, George W.; MACIVER, Brian K. Degradation and fate of mustard in soil as determined by ¹³C MAS NMR. **Langmuir**, v. 14, n. 24, p. 6930–6934, 1998.

WAGNER, George W.; PETERSON, Gregory W.; MAHLE, John J. Effect of adsorbed water and surface hydroxyls on the hydrolysis of VX, GD, and HD on titania materials: The development of self-decontaminating paints. **Industrial and Engineering Chemistry Research**, v. 51, n. 9, p. 3598–3603, 2012.

WANG, Chenghong; LIU, Xinlei; KESER DEMIR, Nilay; CHEN, J. Paul; LI, Kang. Applications of water stable metal–organic frameworks. **Chem. Soc. Rev.**, v. 45, n. 18, p. 5107–5134, 2016.

WANG, G. et al. Mechanism and Kinetics for Reaction of the Chemical Warfare Agent Simulant, DMMP(g), with Zirconium(IV) MOFs: An Ultrahigh-Vacuum and DFT Study. **Journal of Physical Chemistry C**, v. 121, n. 21, p. 11261–11272, 2017.

WANG, Hao; LUSTIG, William P.; LI, Jing. Sensing and capture of toxic and hazardous gases and vapors by metal-organic frameworks. **Chemical Society Reviews**, v. 47, n. 13, p. 4729–4756, 2018.

- WANG, Sa; BROMBERG, Lev; SCHREUDER-GIBSON, Heidi; HATTON, T. Alan. Organophosphorous ester degradation by chromium(III) terephthalate metal-organic framework (MIL-101) chelated to N, N-dimethylaminopyridine and related aminopyridines. **ACS Applied Materials and Interfaces**, v. 5, n. 4, p. 1269–1278, 2013.
- WANG, Sujing et al. A robust large-pore zirconium carboxylate metal–organic framework for energy-efficient water-sorption-driven refrigeration. **Nature Energy**, v. 3, n. 11, p. 985–993, 2018. a.
- WANG, Sujing et al. A phase transformable ultrastable titanium-carboxylate framework for photoconduction. **Nature Communications**, v. 9, n. 1, p. 1660, 2018. b.
- WARD, J. Richard; YANG, Yu Chu; WILSON, Robert B.; BURROWS, Wesley D.; ACKERMAN, Lori L. Base-catalyzed hydrolysis of 1,2,2-trimethylpropyl methylphosphonofluoridate-An examination of the saturation effect. **Bioorganic Chemistry**, v. 16, n. 1, p. 12–16, 1988.
- WITKIEWICZ, Zygfryd; NEFFE, Slawomir; SLIWKA, Ewa; QUAGLIANO, Javier. Analysis of the Precursors, Simulants and Degradation Products of Chemical Warfare Agents. **Critical Reviews in Analytical Chemistry**, v. 48, n. 5, p. 337–371, 2018.
- YAGHI, O. M.; LI, Hailian. Hydrothermal Synthesis of a Metal-Organic Framework Containing Large Rectangular Channels. **Journal of the American Chemical Society**, v. 117, n. 41, p. 10401–10402, 1995.
- YANG, Li; TAYLOR, Ramona; DE JONG, Wibe A.; HASE, William L. A model DMMP/TiO₂ (110) intermolecular potential energy function developed from ab initio calculations. **Journal of Physical Chemistry C**, v. 115, n. 25, p. 12403–12413, 2011. a.
- YANG, Li; TUNEGA, Daniel; XU, Lai; GOVIND, Niranjan; SUN, Rui; TAYLOR, Ramona; LISCHKA, Hans; DEJONG, Wibe A.; HASE, William L. Comparison of cluster, slab, and analytic potential models for the dimethyl methylphosphonate (DMMP)/TiO₂(110) intermolecular interaction. **Journal of Physical Chemistry C**, v. 117, n. 34, p. 17613–17622, 2013.
- YANG, Qingyuan; WIERSUM, Andrew D.; LLEWELLYN, Philip L.; GUILLERM, Vincent; SERRE, Christian; MAURIN, Guillaume. Functionalizing porous zirconium terephthalate UiO-66(Zr) for natural gas upgrading: a computational exploration. **Chemical Communications**, v. 47, n. 34, p. 9603, 2011. b.
- YANG, Yu C.; BAKER, James A.; WARD, J. Richard. decontamination of Chemical Warfare Agents. **Chemical Reviews**, v. 92, n. 8, p. 1729–1743, 1992.
- YOT, Pascal G.; YANG, Ke; RAGON, Florence; DMITRIEV, Vladimir; DEVIC, Thomas; HORCAJADA, Patricia; SERRE, Christian; MAURIN, Guillaume. Exploration of the mechanical behavior of metal organic frameworks UiO-66(Zr) and MIL-125(Ti) and their NH₂ functionalized versions. **Dalton Transactions**, v. 45, n. 10, p. 4283–4288, 2016.
- YUAN, Shuai; QIN, Jun-Sheng; LOLLAR, Christina T.; ZHOU, Hong-Cai. Stable Metal–Organic Frameworks with Group 4 Metals: Current Status and Trends. **ACS Central Science**,

v. 4, n. 4, p. 440–450, 2018.

YUAN, Weixin; BANDOSZ, Teresa J. Removal of hydrogen sulfide from biogas on sludge-derived adsorbents. **Fuel**, v. 86, n. 17–18, p. 2736–2746, 2007.

YUE, Zhongren; MANGUN, Christian; ECONOMY, James; KEMME, Patricia; CROPEK, Donald; MALONEY, Stephen. Removal of chemical contaminants from water to below USEPA MCL using fiber glass supported activated carbon filters. **Environmental Science and Technology**, v. 35, n. 13, p. 2844–2848, 2001.

ZHANG, Qi et al. Multivariable Sieving and Hierarchical Recognition for Organic Toxics in Nonhomogeneous Channel of MOFs. **Chem**, v. 5, n. 5, p. 1337–1350, 2019.

ZHAO, Junjie et al. Ultra-Fast Degradation of Chemical Warfare Agents Using MOF-Nanofiber Kebabs. **Angewandte Chemie International Edition**, v. 55, n. 42, p. 13224–13228, 2016.

ZHOU, Hong-Cai “Joe”; KITAGAWA, Susumu. Metal–Organic Frameworks (MOFs). **Chem. Soc. Rev.**, v. 43, n. 16, p. 5415–5418, 2014.

ZILKER, Thomas. Medical management of incidents with chemical warfare agents. **Toxicology**, v. 214, n. 3, p. 221–231, 2005.

ZOU, Ruqiang et al. A porous metal-organic replica of α -PbO₂ for capture of nerve agent surrogate. **Journal of the American Chemical Society**, v. 132, n. 51, p. 17996–17999, 2010.

ANNEX A - Atomic partial charges of MOFs

1. Atomic partial charges of MOFs

1.1 MIL-125(Ti)

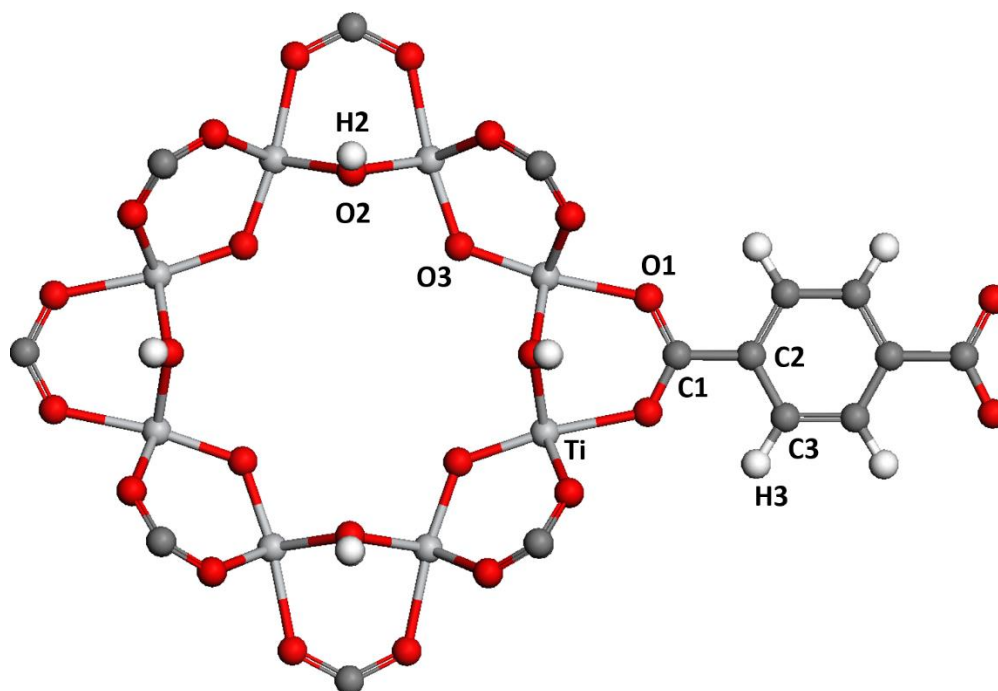
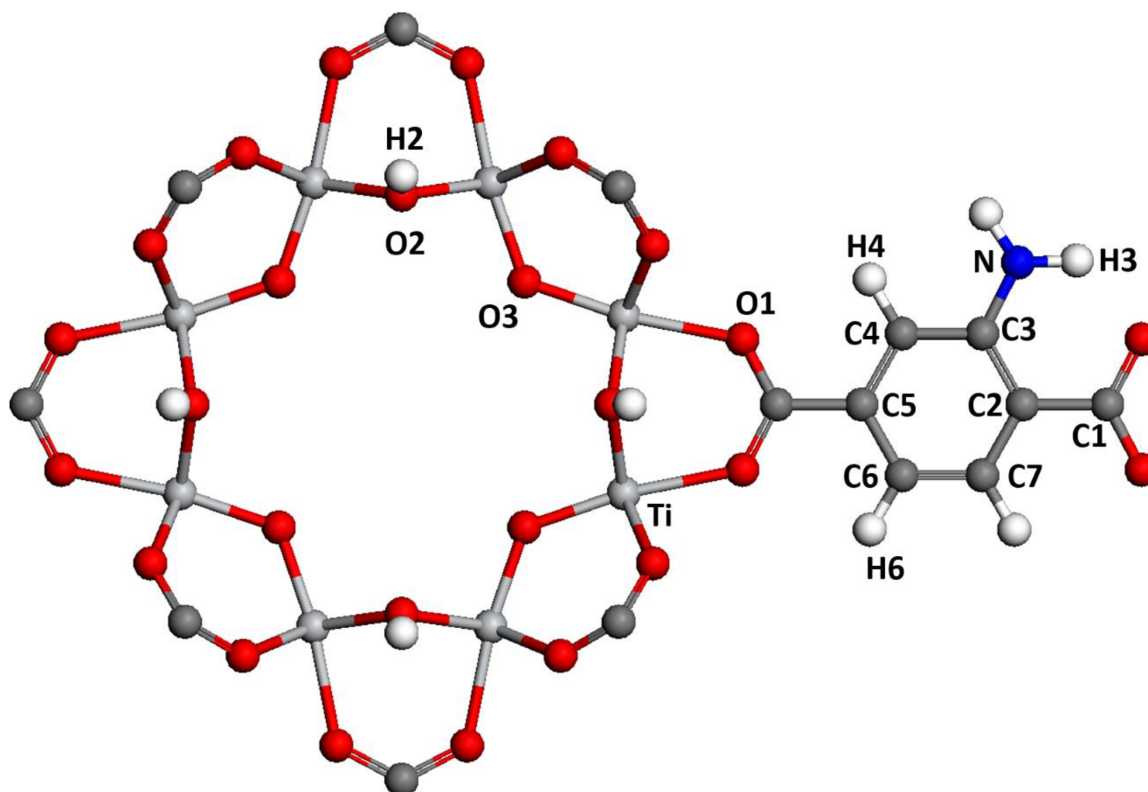


Figure S1. Labels of the atoms for the inorganic and organic parts of MIL-125(Ti).

Table S1: Partial charges for the MIL-125(Ti) structure derived at the DFT/PBE Level.

Atomic Types	Ti	O1	O2	O3	C1	C2	C3	H2	H3
Charge (e)	1.384	-0.5425	-0.67075	-0.718	0.6105	-0.077	-0.0745	0.278	0.1395

1.2 MIL-125(Ti)-NH₂Figure S2. Labels of the atoms for the inorganic and organic parts of MIL-125(Ti)-NH₂.Table S2: Atomic partial charges for the MIL-125(Ti)-NH₂ structure derived at the DFT/PBE Level.

Atomic Types	Ti	O1	O2	O3	C1	C2	C3	C4
Charge (e)	1.3784	-0.5725	-0.6665	-0.7227	0.6142	-0.1093	0.192	-0.1293
Atomic Types	C5	C6	C7	H2	H3	H4	H6	N
Charge (e)	-0.0785	-0.0823	-0.0958	0.2865	0.254	0.133	0.1337	-0.393

1.3 MIL-140D(Zr)

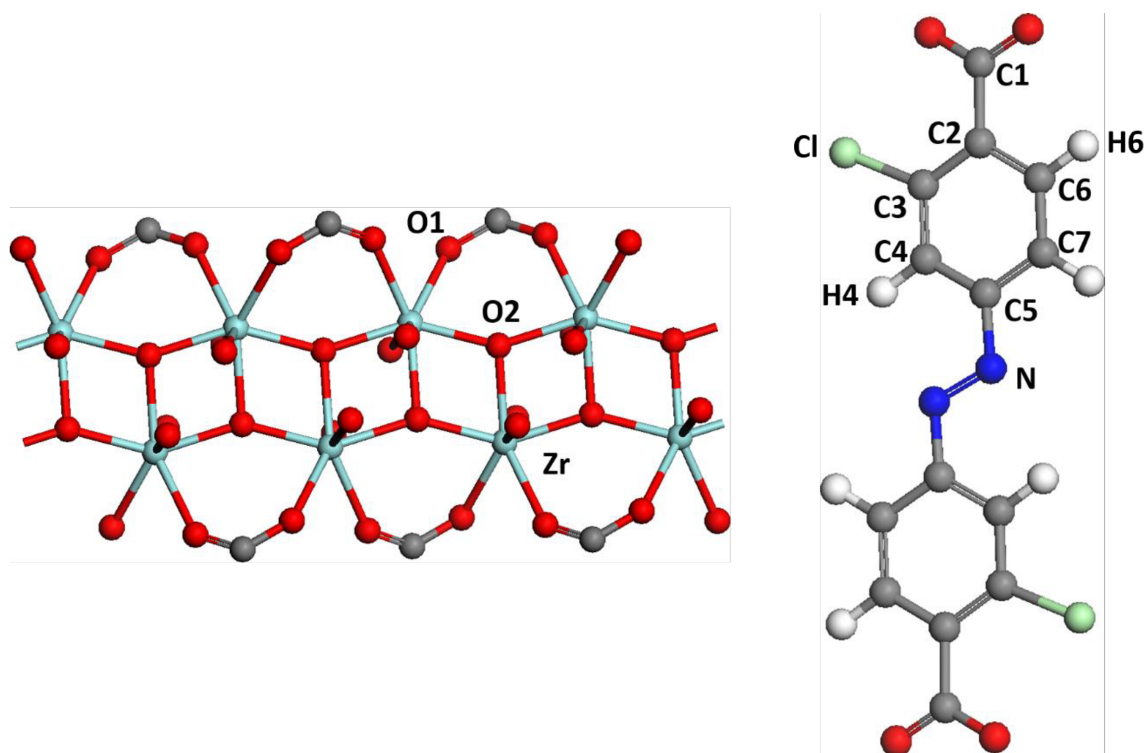


Figure S3. Labels of the atoms for the inorganic and organic parts of MIL-140D(Zr).

Table S3: Atomic partial charges for the MIL-140D(Zr) structure derived at the DFT/PBE Level.

Atomic Types	Zr	O1	O2	C1	C2	C3	C4
Charge (e)	2.016	-0.588	-1.033	0.642	-0.054	-0.0147	-0.0619
Atomic Types	C5	C6	C7	H4	H6	N	Cl
Charge (e)	0.102	-0.083	-0.0702	0.15	0.133	-0.1795	-0.0122

1.4 MIL-140E(Zr)

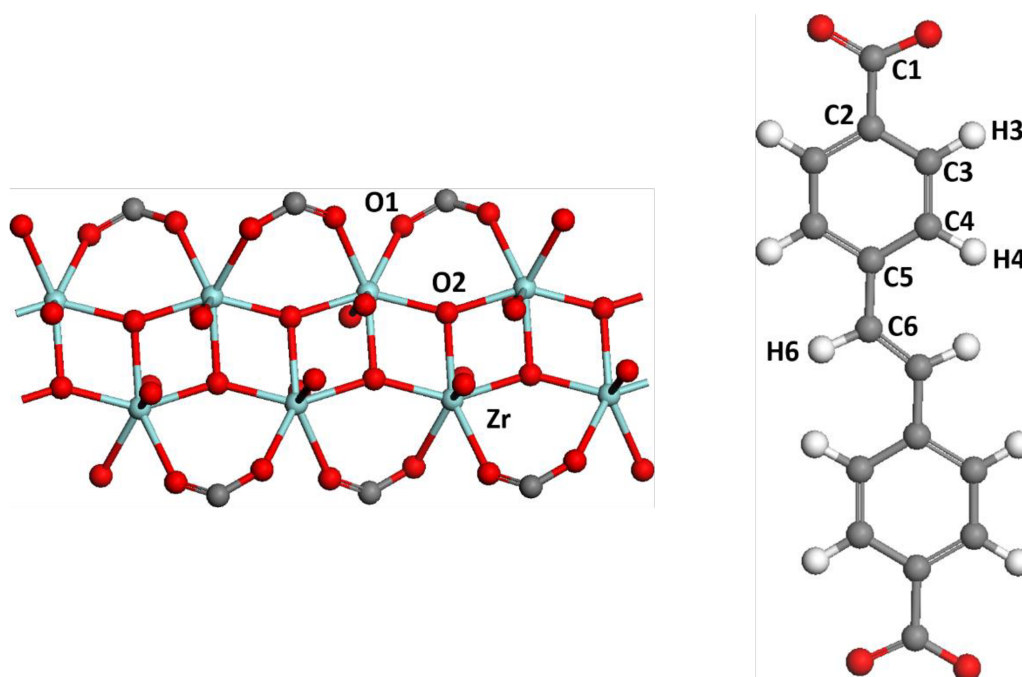


Figure S4. Labels of the atoms for the inorganic and organic parts of MIL-140E(Zr).

Table S4: Atomic partial charges for the MIL-140E(Zr) structure derived at the DFT/PBE Level.

Atomic Types	Zr	O1	O2	C1	C2	C3
Charge (e)	2.013	-0.5915	-1.043	0.6305	-0.0855	-0.07
Atomic Types	C4	C5	C6	H3	H4	H6
Charge (e)	-0.1005	0.0245	-0.0985	0.142	0.0955	0.093

1.5 MIL-140G(Zr)

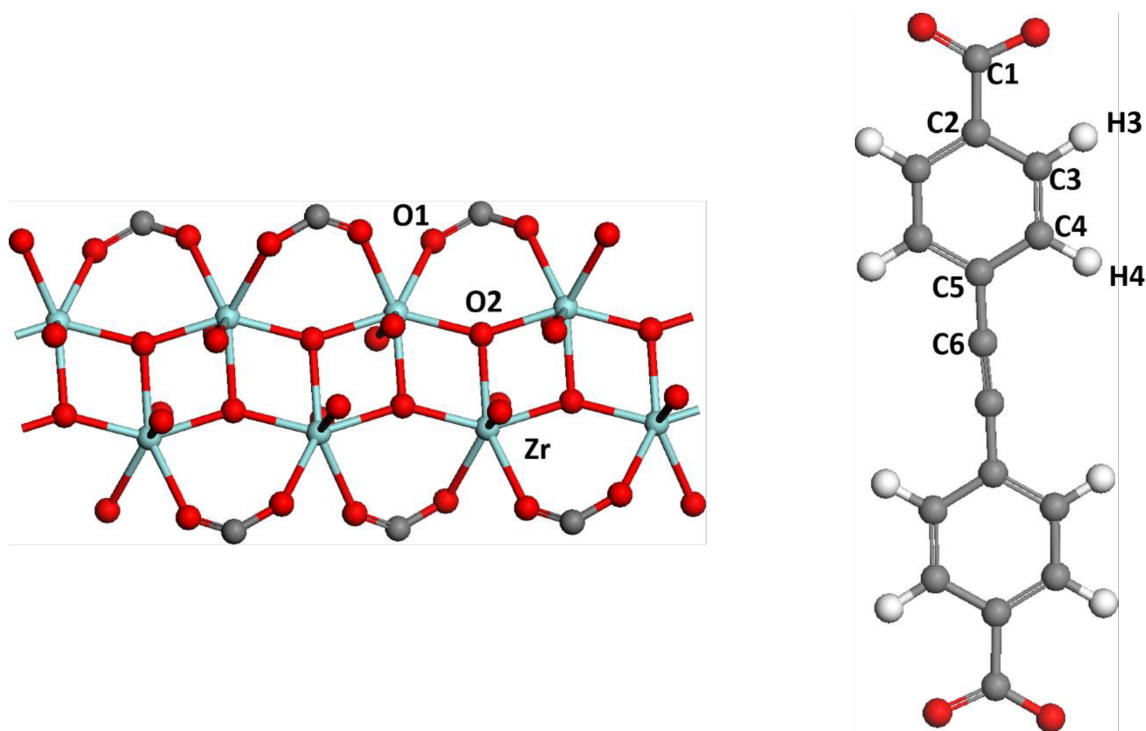


Figure S5. Labels of the atoms for the inorganic and organic parts of MIL-140G(Zr).

Table S5: Atomic partial charges for the MIL-140E(Zr) structure derived at the DFT/PBE Level.

Atomic Types	Zr	O1	O2	C1	C2	C3
Charge (e)	2.017	-0.591	-1.045	0.6301	-0.086	-0.0735
Atomic Types	C4	C5	C6	H3	H4	
Charge (e)	-0.0975	-0.0635	0.057	0.1435	0.1067	

1.6 MIP-177(Ti)

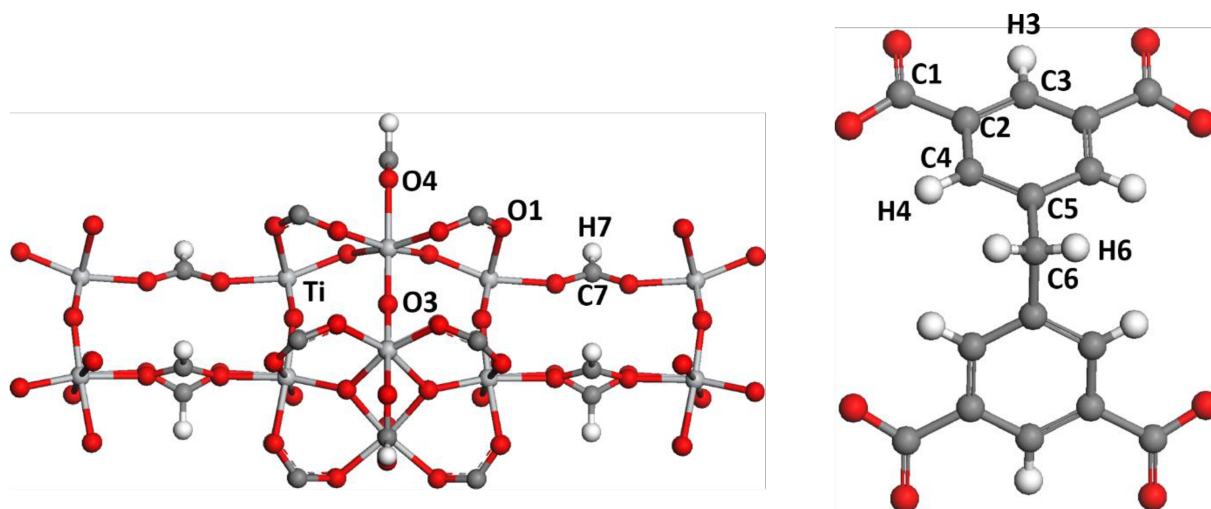
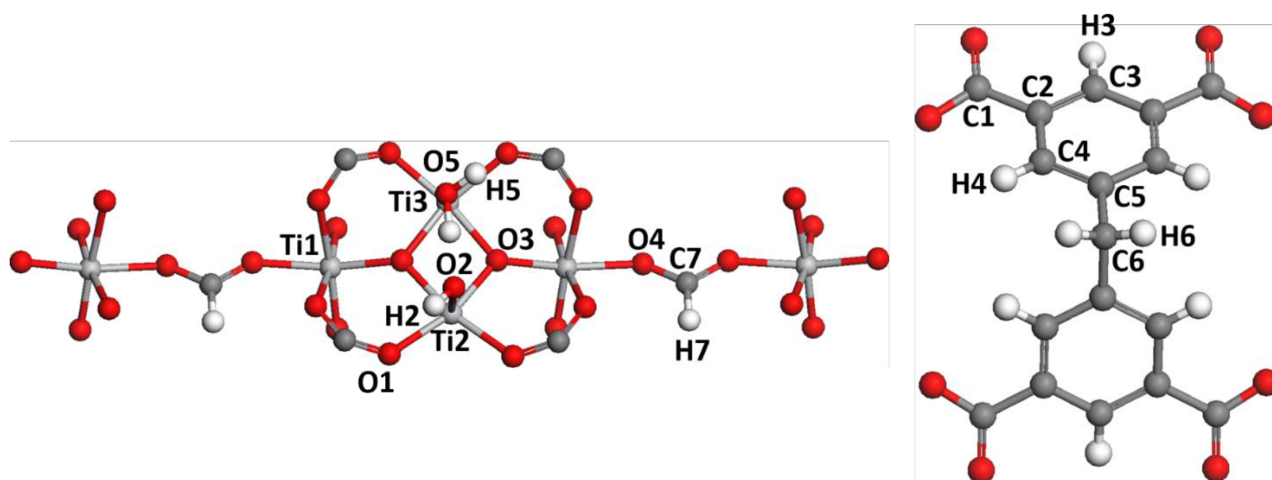


Figure S6. Labels of the atoms for the inorganic and organic parts of MIP-177(Ti).

Table S6: Atomic partial charges for the MIP-177(Ti) structure derived at the DFT/PBE Level.

Atomic Types	Ti	O1	O3	O4	C1	C2	C3	C4
Charge (e)	1.512	-0.5227	-0.7886	-0.4581	0.618	-0.0515	-0.0625	-0.0685
Atomic Types	C5	C6	C7	H3	H4	H6	H7	
Charge (e)	0.0295	-0.295	0.4955	0.1735	0.0135	0.1295	0.0705	

1.7 MIP-177-OH-H₂O(Ti)Figure S7. Labels of the atoms for the inorganic and organic parts of MIP-177-OH-H₂O(Ti).Table S7: Atomic partial charges for the MIP-177-OH-H₂O(Ti) structure derived at the DFT/PBE Level.

Atomic Types	Ti1	Ti2	Ti3	O1	O2	O3	O4
Charge (e)	1.50067	1.5033	1.54633	-0.52138	-0.676	-0.78843	-0.449835
Atomic Types	O5	C1	C2	C3	C4	C5	C6
Charge (e)	-0.558	0.608	-0.059	-0.08075	-0.06867	0.0275	-0.29383
Atomic Types	C7	H2	H3	H4	H5	H6	H7
Charge (e)	0.5085	0.281	0.1716	0.1359	0.3378	0.1289	0.06817

1.8 MIP-200(Zr)

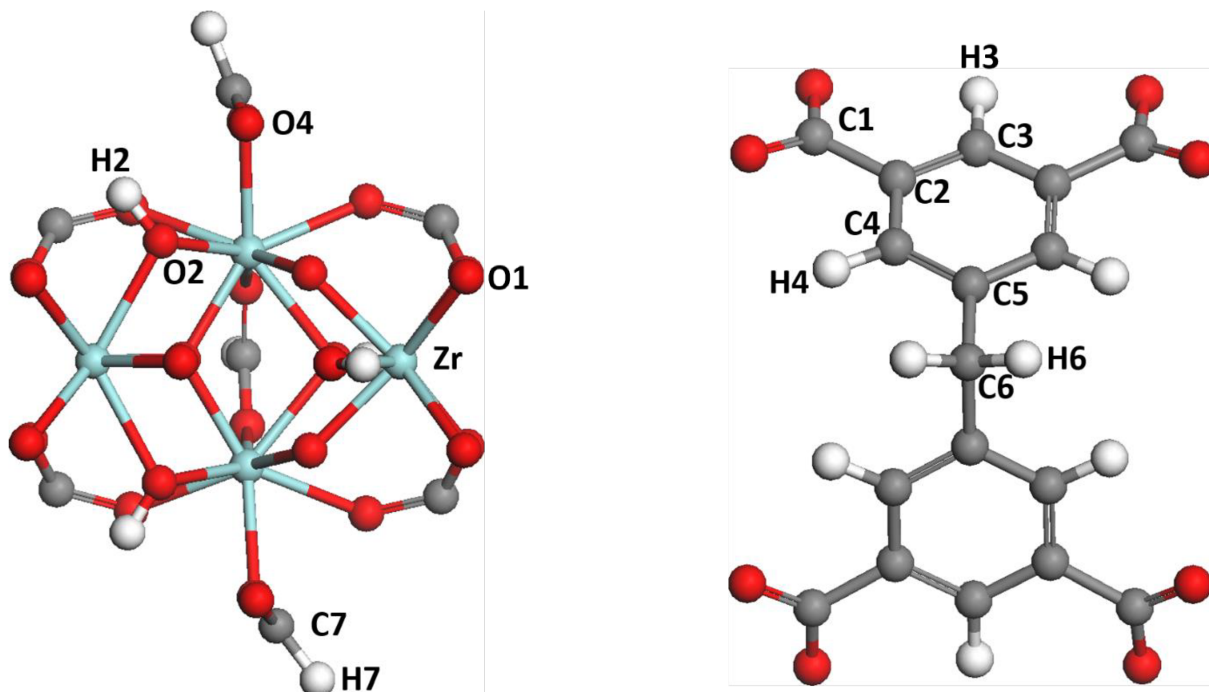
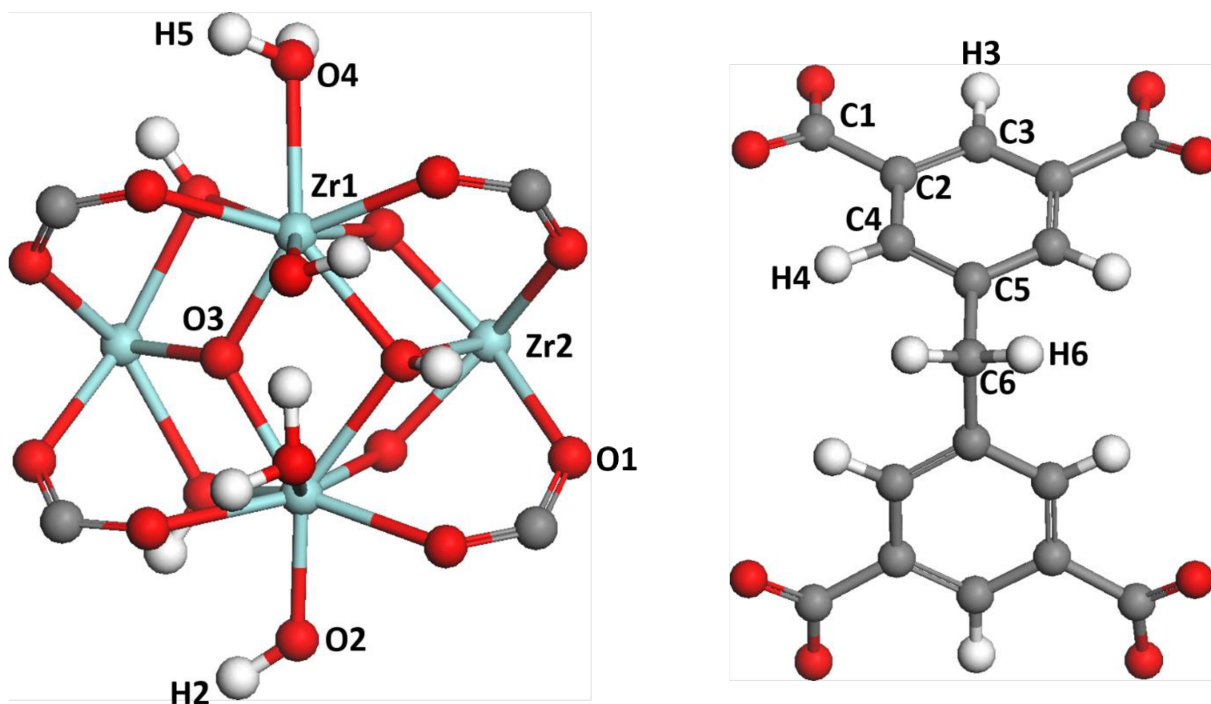


Figure S8. Labels of the atoms for the inorganic and organic parts of MIP-200(Zr).

Table S8: Atomic partial charges for the MIP-200(Zr) structure derived at the DFT/PBE Level.

Atomic Types	Zr	O1	O2	O3	O4	C1	C2	C3	C4
Charge (e)	1.945	-0.572	-0.776	-1.0075	-0.5128	0.589	-0.0657	-0.0646	-0.0593
Atomic Types	C5	C6	C7	H2	H3	H4	H6	H7	
Charge (e)	0.0197	-0.2713	0.45	0.351	0.156	0.132	0.128	0.0794	

1.9 MIP-200-OH-H₂O(Zr)Figure S9. Labels of the atoms for the inorganic and organic parts of MIP-200-OH-H₂O(Zr).Table S9: Atomic partial charges for the MIP-200-OH-H₂O(Zr) structure derived at the DFT/PBE Level.

Atomic Types	Zr1	Zr2	O1	O2	O3	O4	C1	C2	C3
Charge (e)	1.923	1.9365	-0.578	-0.753	-1.017	-0.584	0.587	-0.067	-0.0666
Atomic Types	C4	C5	C6	H2	H3	H4	H5	H6	
Charge (e)	-0.0657	0.024	-0.273	0.306	0.159	0.116	0.336	0.121	

1.10 MOF-808-A(Zr)

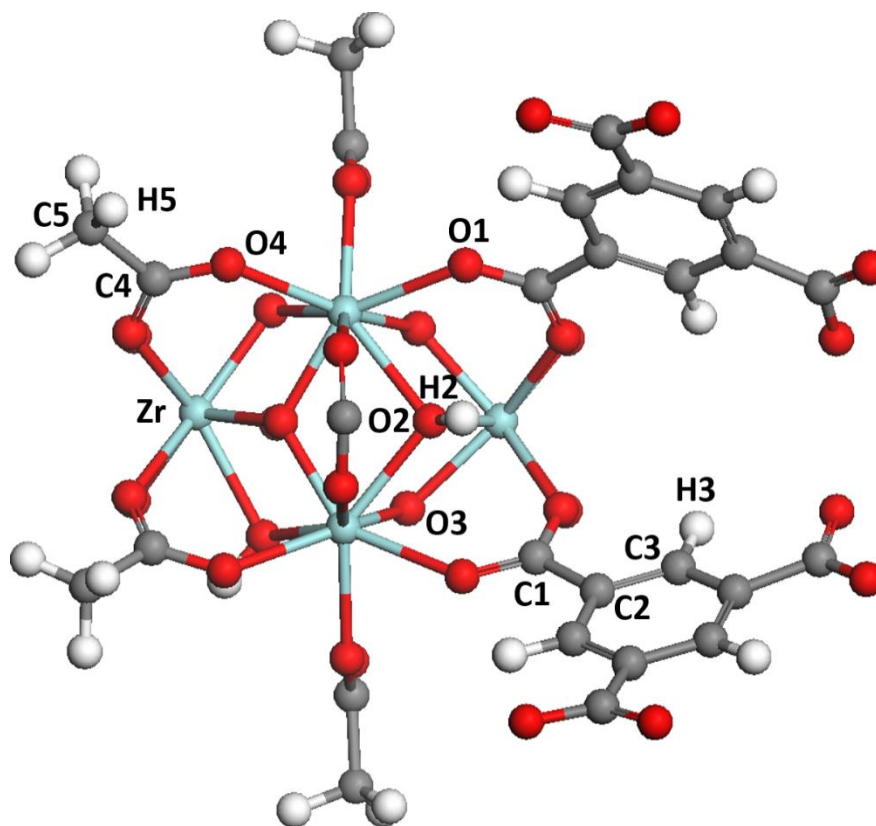


Figure S10. Labels of the atoms for the inorganic and organic parts of MIL-808-A(Zr).

Table S10: Atomic partial charges for the MIL-808-A(Zr) structure derived at the DFT/PBE Level.

Atomic Types	Zr	O1	O2	O3	O4	C1	C2
Charge (e)	1.938	-0.568	-0.7823	-0.9803	-0.549	0.571	-0.0752
Atomic Types	C3	C4	C5	H2	H3	H5	
Charge (e)	-0.0564	0.559	-0.326	0.361	0.165	0.131	

1.11 MOF-808-F(Zr)

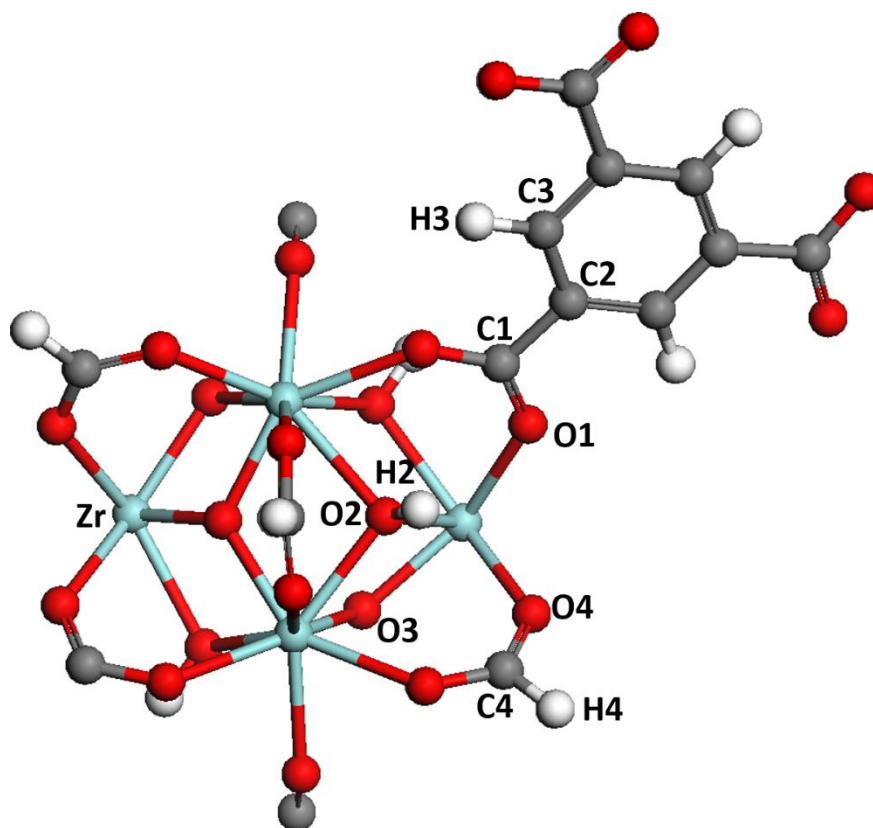


Figure S11. Labels of the atoms for the inorganic and organic parts of MOF-808-F(Zr).

Table S11: Atomic partial charges for the MOF-808-F(Zr) structure derived at the DFT/PBE Level.

Atomic Types	Zr	O1	O2	O3	O4	C1
Charge (e)	1.936	-0.568	-0.78735	-0.983	-0.515	0.575
Atomic Types	C2	C3	C4	H2	H3	H4
Charge (e)	-0.0738	-0.0529	0.479	0.362	0.169	0.0726

1.12 MOF-808-P(Zr)

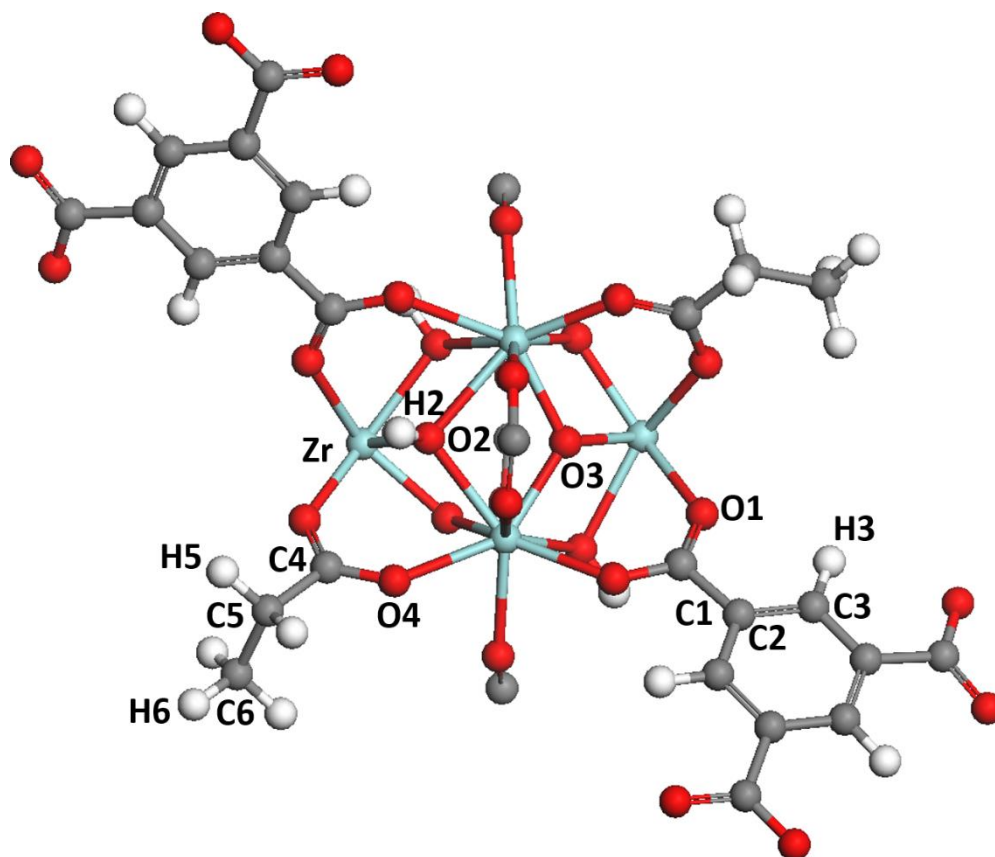


Figure S12. Labels of the atoms for the inorganic and organic parts of MOF-808-P(Zr).

Table S12: Atomic partial charges for the MOF-808-P(Zr) structure derived at the DFT/PBE Level.

Atomic Types	Zr	O1	O3	O4	C1	C2	C3
Charge (e)	1.94	-0.568	-0.786	-0.9828	-0.557	0.571	-0.0747
Atomic Types	C4	C5	C6	H2	H3	H5	H6
Charge (e)	0.599	-0.285	-0.284	0.361	0.165	0.14	0.115

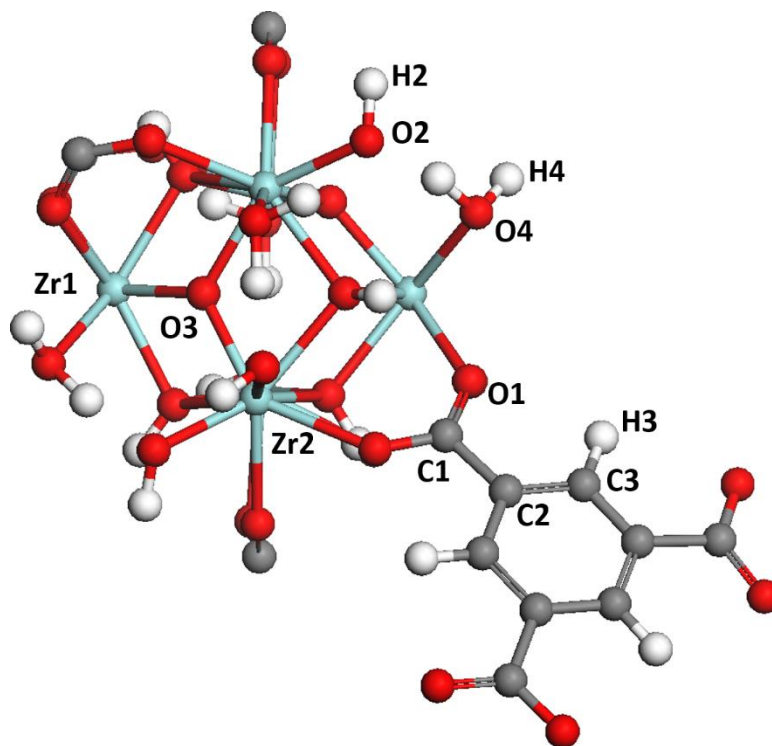
1.13 MOF-808-OH-H₂O(Zr)

Figure S13. Labels of the atoms for the inorganic and organic parts of MOF-808-OH-H₂O(Zr).

Table S13: Atomic partial charges for the MOF-808-OH-H₂O(Zr) structure derived at the DFT/PBE level.

Atomic Types	Zr1	Zr2	O1	O2	O3	O4
Charge (e)	1.913	1.91	-0.581	-0.77198	-0.995	-0.573
Atomic Types	C1	C2	C3	H2	H3	H4
Charge (e)	0.567	-0.0739	-0.0568	0.31	0.156	0.332

1.14NU-1000(Zr)

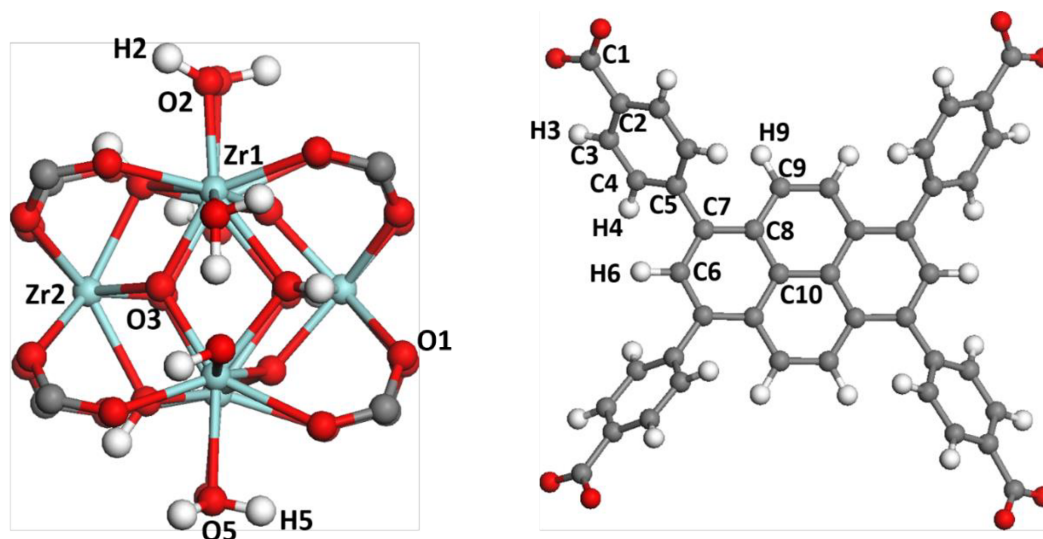


Figure S14. Labels of the atoms for the inorganic and organic parts of NU-1000(Zr).

Table S14: Atomic partial charges for the NU-1000(Zr) structure derived at the DFT/PBE level.

Atomic Types	Zr1	Zr2	O1	O2	O3
Charge (e)	1.918333333	1.9855	-0.592875	-0.761666667	-1.02475
Atomic Types	O5	C1	C2	C3	C4
Charge (e)	-0.561916667	0.605125	-0.087	-0.059916667	-0.101333333
Atomic Types	C5	C6	C7	C8	C9
Charge (e)	-0.031	-0.10575	-0.001958333	-0.000958333	-0.10875
Atomic Types	C10	H2	H3	H4	H5
Charge (e)	0.019083333	0.302	0.125041667	0.106270833	0.325875
Atomic Types	H6	H9			
Charge (e)	0.125416667	0.122375000			

1.15 UiO-66(Zr)

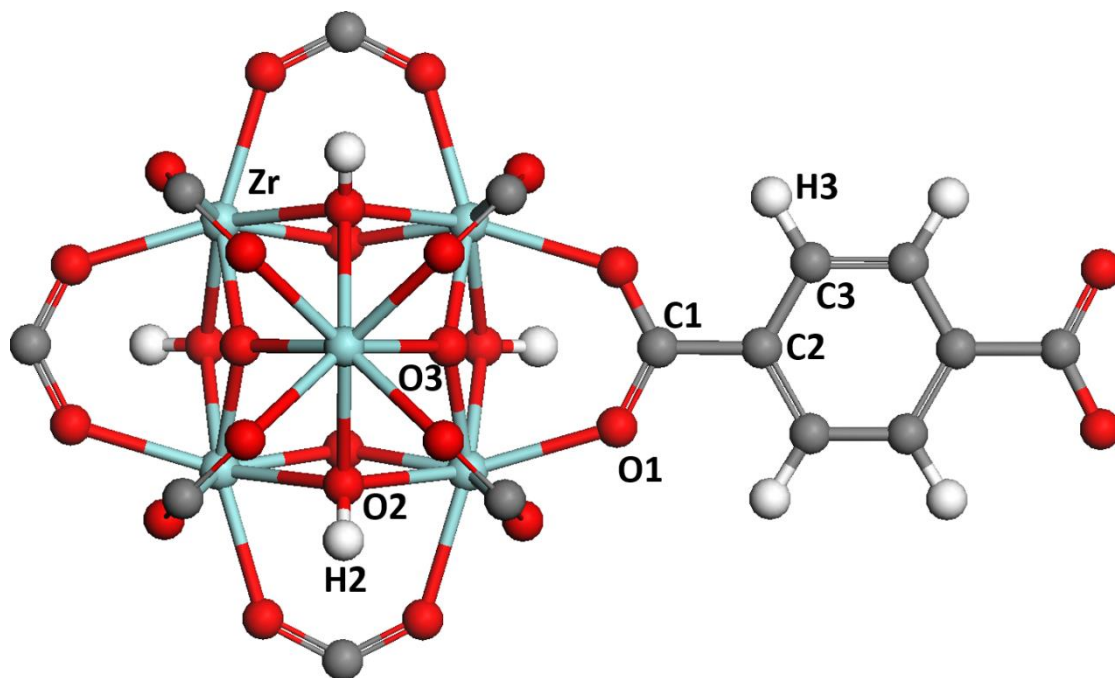


Figure S15. Labels of the atoms for the inorganic and organic parts of UiO-66(Zr).

Table S15: Atomic partial charges for the UiO-66(Zr) structure derived at the DFT/PBE level.

Atomic Types	Zr	O1	O2	O3	C1	C2	C3	H2	H3
Charge (e)	1.972	-0.577	-0.788	-1.008	0.599	-0.075	-0.064	0.356	0.126

1.16 UiO-66(Zr)-Cl

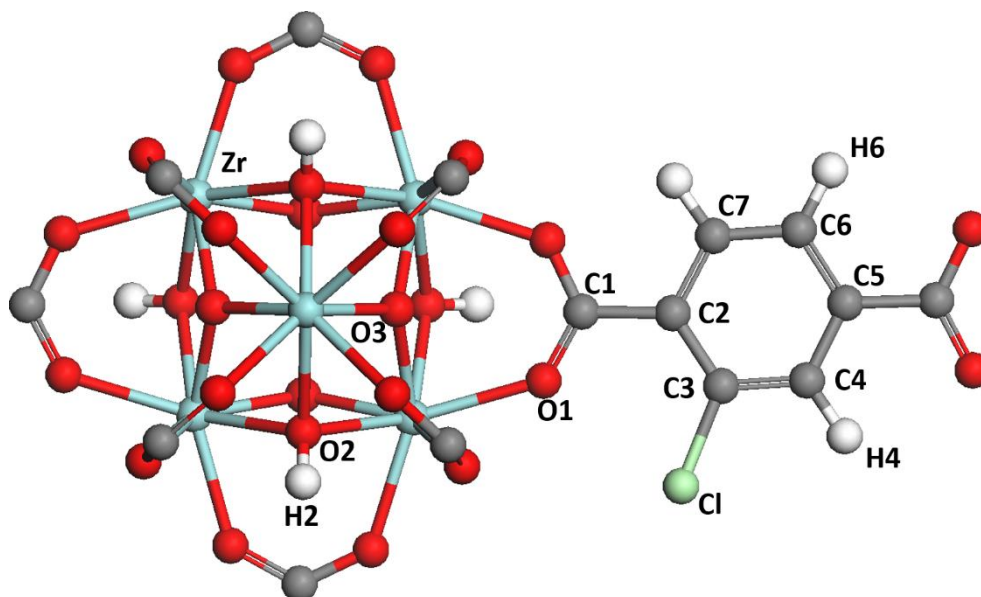
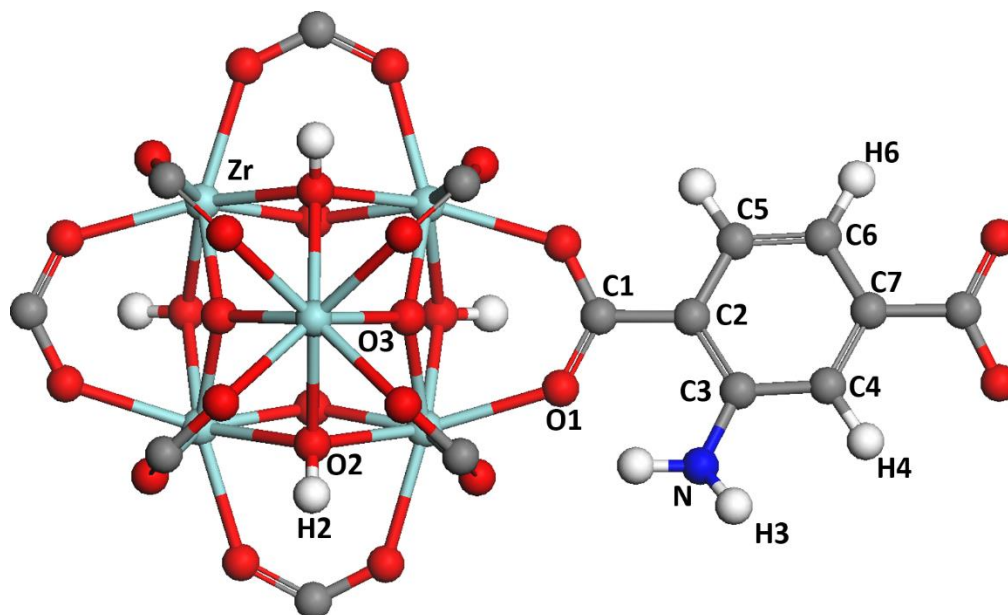


Figure S16. Labels of the atoms for the inorganic and organic parts of UiO-66(Zr)-Cl.

Table S16: Atomic partial charges for the UiO-66(Zr)-Cl structure derived at the DFT/PBE Level.

Atomic Types	Zr	O1	O2	O3	C1	C2	C3	C4
Charge (e)	1.969	-0.576	-0.77705	-1.011	0.605	-0.0753	-0.0308	-0.018
Atomic Types	C5	C6	C7	H2	H4	H6	Cl	
Charge (e)	-0.0557	-0.0645	-0.0635	0.35	0.159	0.1395	-0.0465	

1.17 UiO-66-(Zr)-NH₂Figure S17. Labels of the atoms for the inorganic and organic parts of UiO-66-(Zr)-NH₂.Table S17: Atomic partial charges for the UiO-66-(Zr)-NH₂ structure derived at the DFT/PBE level.

Atomic Types	Zr	O1	O2	O3	C1	C2	C3	C4
Charge (e)	1.956	-0.600	-0.7607	-0.9967	0.6035	-0.113	0.1765	-0.109
Atomic Types	C5	C6	C7	H2	H3	H4	H6	N
Charge (e)	-0.067	-0.0927	-0.0672	0.348	0.253	0.131	0.109	-0.406

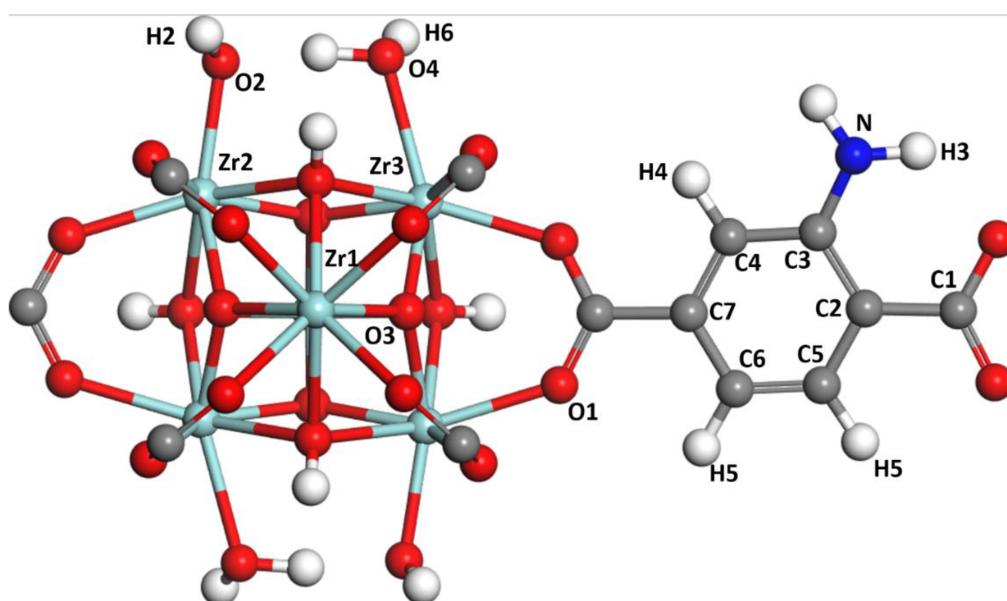
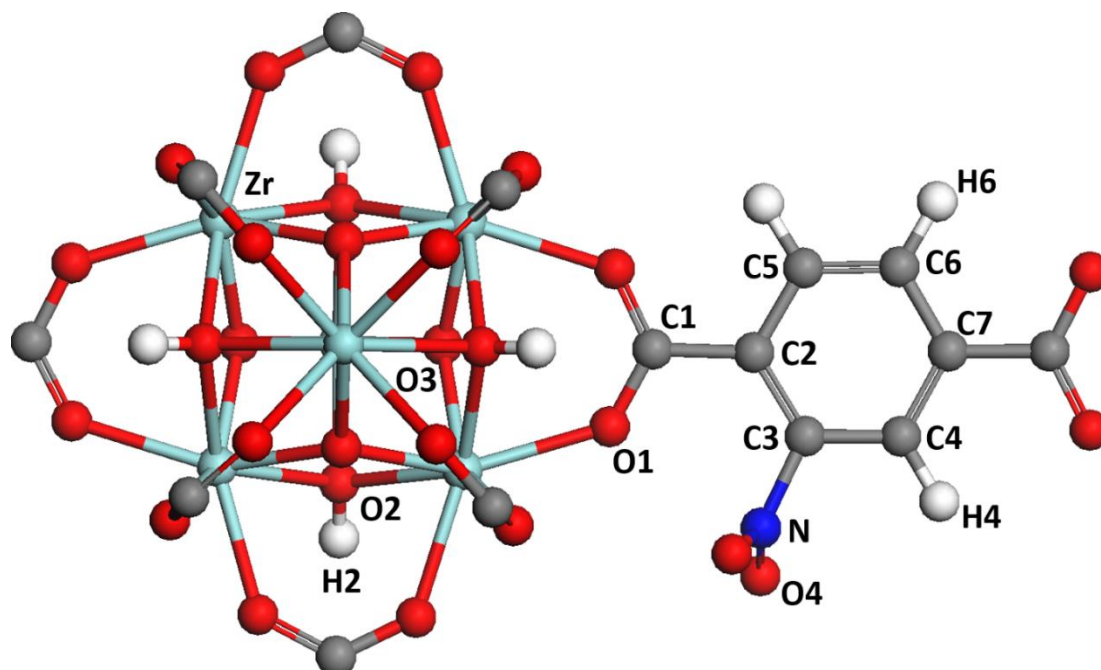
1.18 Defective UiO-66-(Zr)-NH₂

Figure S18. Labels of the atoms for the inorganic and organic parts of the defective UiO-66-(Zr)-NH₂.

Table S18: Atomic partial charges for the defective UiO-66-(Zr)-NH₂ structure derived at the DFT/PBE Level.

Atomic Types	Zr	Zr2	Zr3	O1	O2	O3	O4
Charge (e)	1.952	1.946	1.959	-0.599	-0.774	-1.015	-0.55865
Atomic Types	C1	C2	C3	C4	C5	C6	C7
Charge (e)	0.603	-0.114	0.182	-0.119	-0.0816	-0.0664	-0.0687
Atomic Types	H2	H3	H4	H5	H6	N	
Charge (e)	0.321	0.249	0.121	0.123	0.329	-0.405	

1.19 UiO-66-(Zr)-NO₂Figure S19. Labels of the atoms for the inorganic and organic parts of UiO-66-(Zr)-NO₂.Table S19: Atomic partial charges for the UiO-66-(Zr)-NO₂ structure derived at the DFT/PBE Level.

Atomic Types	Zr	O1	O2	O3	O4	C1	C2	C3
Charge (e)	1.941	-0.540	-0.7872	-1.0002	-0.318	0.585	-0.0513	0.0692
Atomic Types	C4	C5	C6	C7	H2	H4	H6	N
Charge (e)	-0.0445	-0.0605	-0.0473	-0.051	0.375	0.176	0.138	0.36

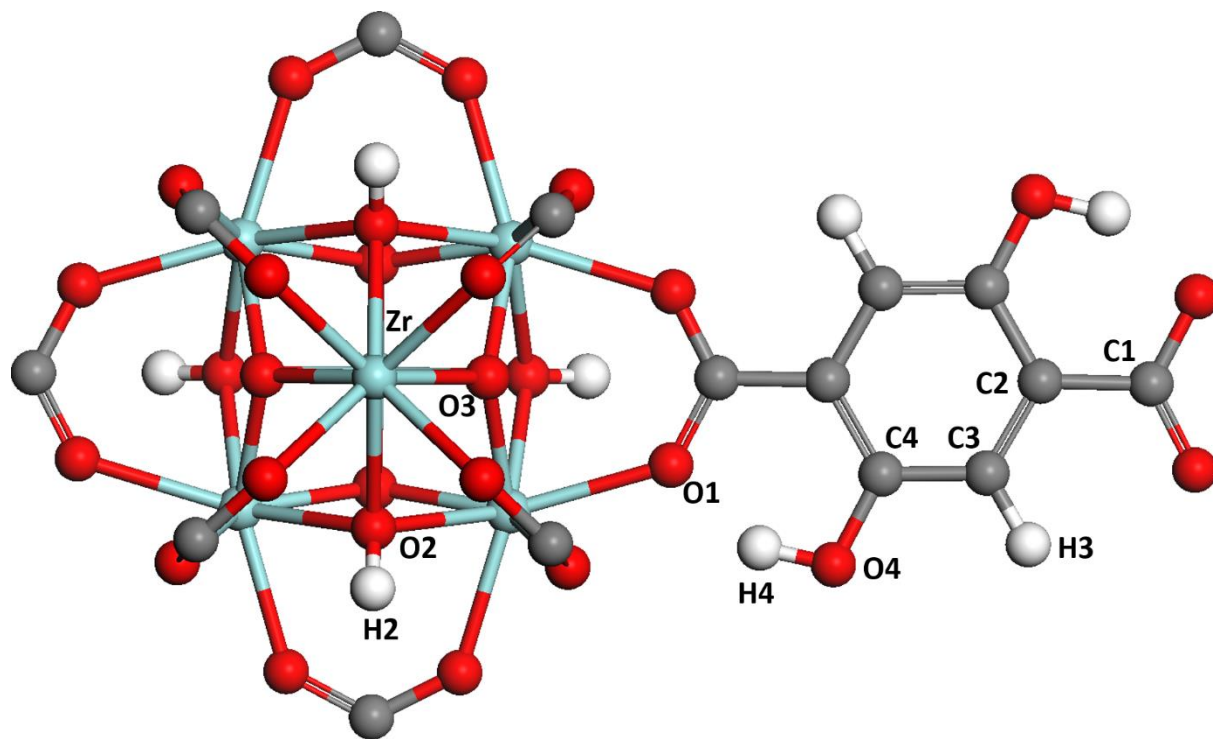
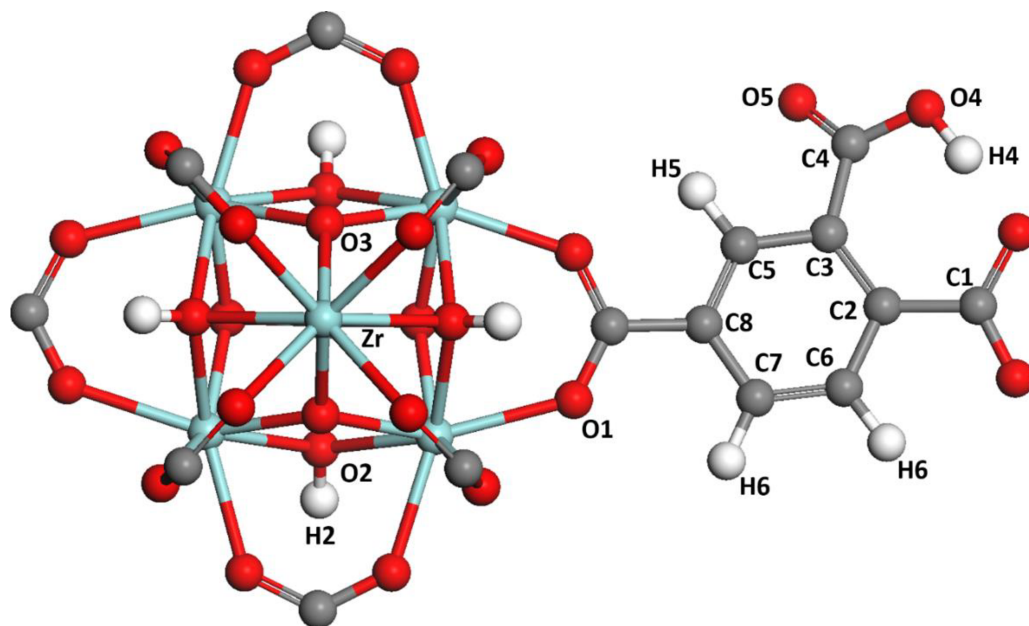
1.20 UiO-66-(Zr)-(OH)₂

Figure S20. Labels of the atoms for the inorganic and organic parts of UiO-66-(Zr)-2OH.

Table S20: Atomic partial charges for the UiO-66-(Zr)-2OH structure derived at the DFT/PBE level.

Atomic Types	Zr	O1	O2	O3	O4	C1
Charge (e)	1.97	-0.634	-0.7794	-1.02	-0.394	0.631
Atomic Types	C2	C3	C4	H2	H3	H4
Charge (e)	-0.136	-0.0932	0.244	0.348	0.154	0.361

1.21 UiO-66-(Zr)-CO₂HFigure S21. Labels of the atoms for the inorganic and organic parts of UiO-66(Zr)-(CO₂H).Table S21: Atomic partial charges for the UiO-66-(Zr)-(CO₂H) structure derived at the DFT/PBE Level.

Atomic Types	Zr	O1	O2	O3	O4	O5	C1	C2	C3
Charge (e)	1.969	-0.582	-0.7773	-1.0133	-0.396	-0.361	0.603	-0.052	-0.114
Atomic Types	C4	C5	C6	C7	C8	H2	H4	H5	H6
Charge (e)	0.472	-0.039	-0.0758	-0.0635	-0.0663	0.3515	0.332	0.168	0.154

1.22 Defective UiO-66-(Zr)

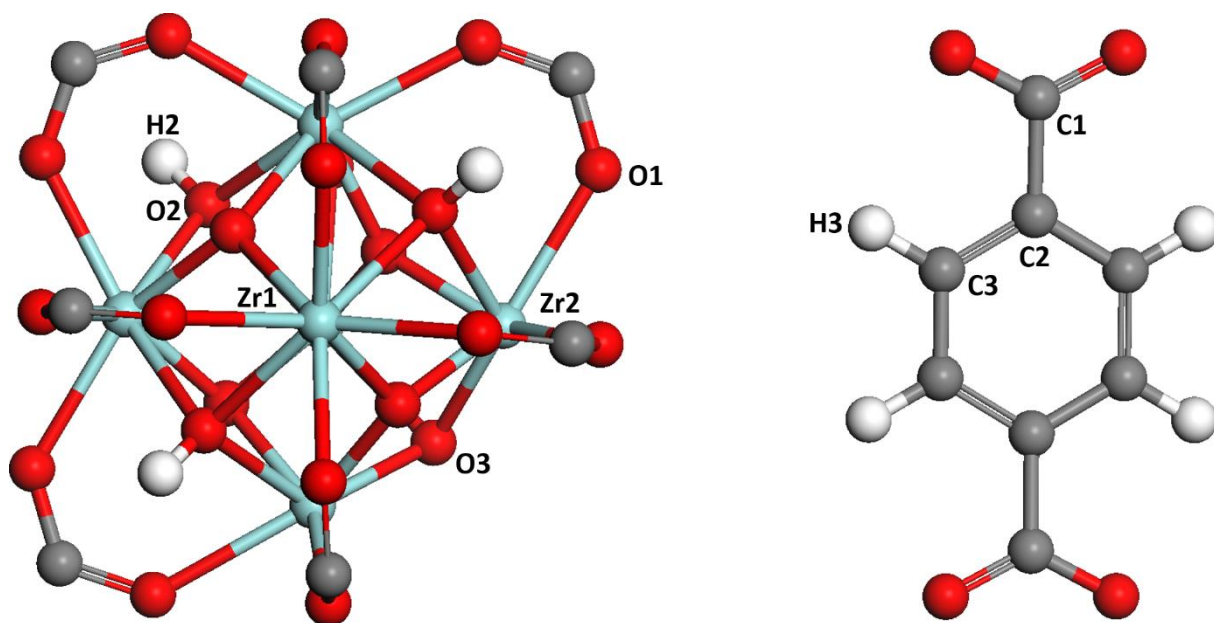


Figure S22. Labels of the atoms for the inorganic and organic parts of the defective UiO-66-(Zr).

Table S22: Atomic partial charges for the defective UiO-66-(Zr)- structure derived at the DFT/PBE Level.

Atomic Types	Zr1	Zr2	O1	O2	O3
Charge (e)	1.907	1.942	-0.566	-0.7557	-0.99364
Atomic Types	H2	H3	C1	C2	C3
Charge (e)	0.3477	0.1236	0.5963	-0.0891	-0.0546

1.23 UiO-67(Zr)

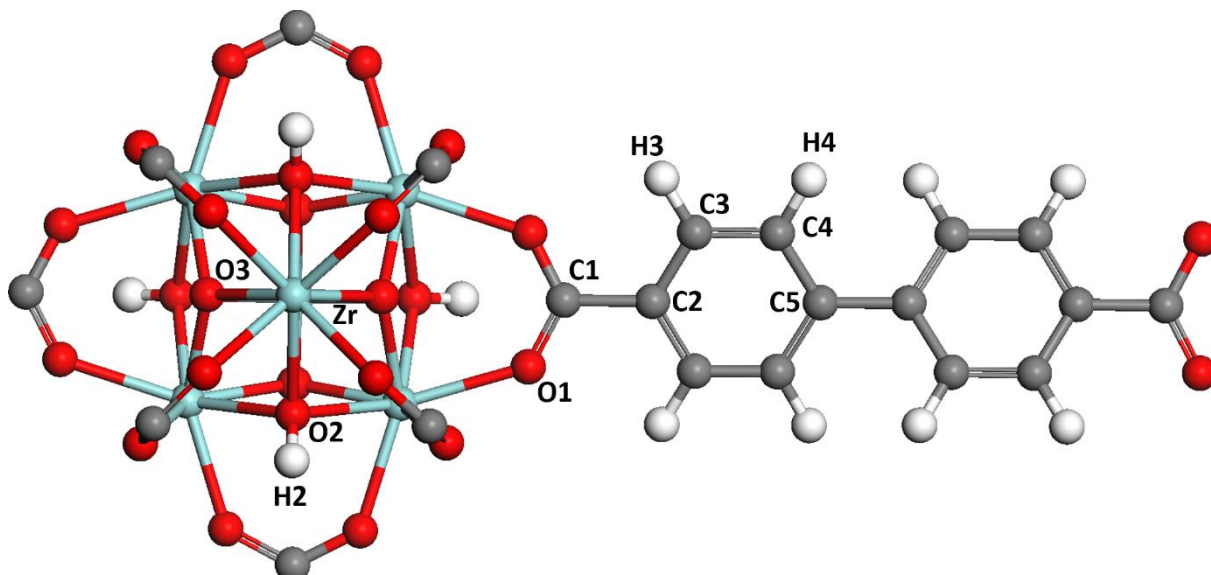


Figure S23. Labels of the atoms for the inorganic and organic parts of UiO-67(Zr).

Table S23: Atomic partial charges for the UiO-67(Zr) structure derived at the DFT/PBE Level.

Atomic Types	Zr	O1	O2	O3	C1	C2
Charge (e)	1.946	-0.5744	-0.764	-0.99	0.589	-0.087
Atomic Types	C3	C4	C5	H2	H3	H4
Charge (e)	-0.0601	-0.0955	0.006	0.347	0.126	0.098

1.24 UiO-68(Zr)

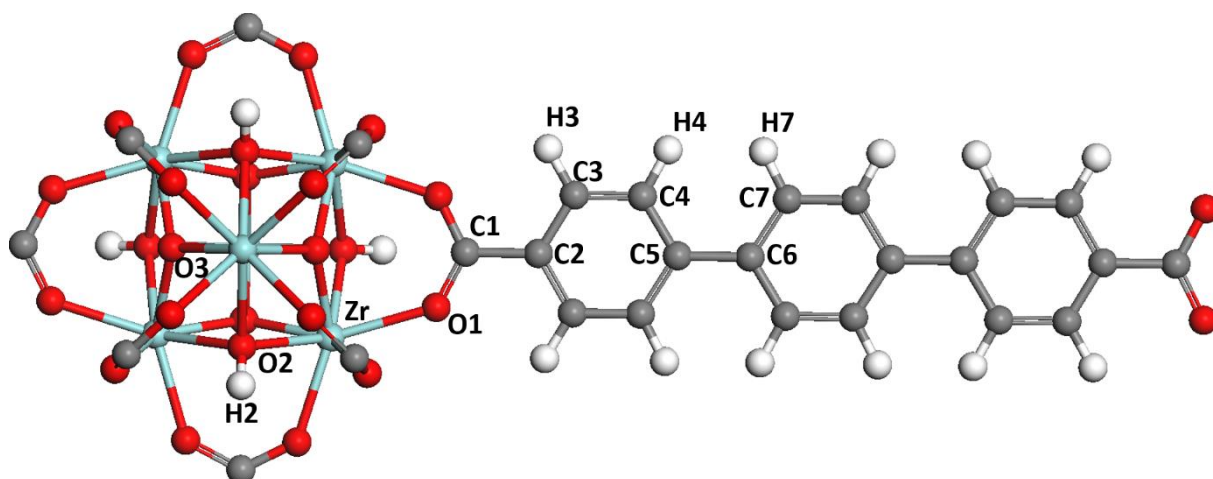


Figure S24. Labels of the atoms for the inorganic and organic parts of UiO-68(Zr).

Table S24: Atomic partial charges for the UiO-68(Zr) structure derived at the DFT/PBE level.

Atomic Types	Zr	O1	O2	O4	C1	C2	C3	C4
Charge (e)	1.948	-0.576	-0.766	-0.994	0.591	-0.09	-0.054	-0.091
Atomic Types	C5	C6	C7	H2	H3	H4	H7	
Charge (e)	0.015	0.007	-0.081	0.347	0.121	0.083	0.085	

1.25 Zr-Azo-BDC

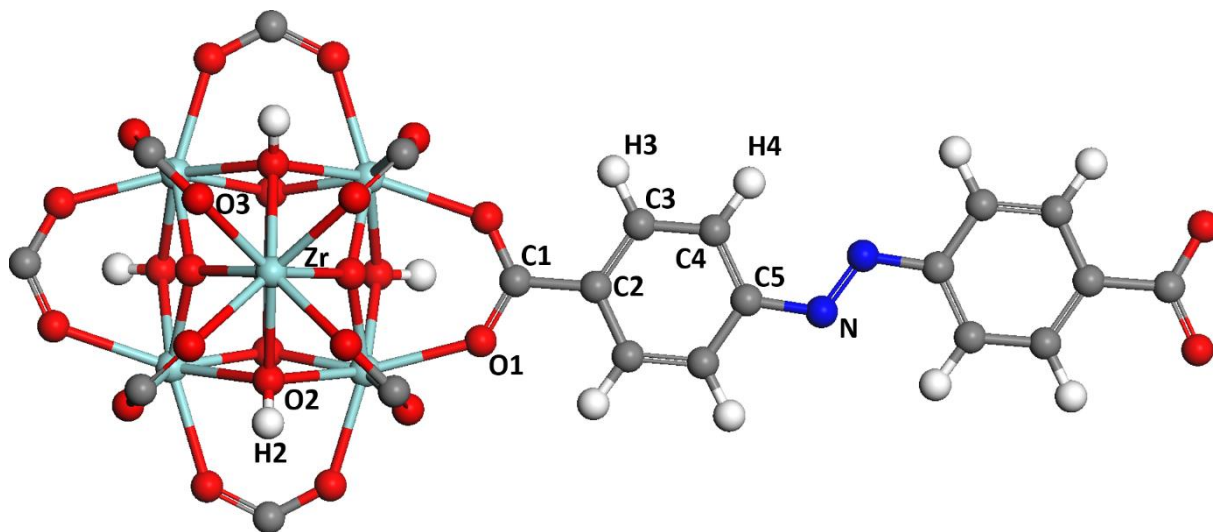


Figure S25. Labels of the atoms for the inorganic and organic parts of Zr-AZO-BDC.

Table S25: Atomic partial charges for the Zr-AZO-BDC structure derived at the DFT/PBE Level.

Atomic Types	Zr	O1	O2	O3	C1	C2	C3
Charge (e)	1.954	-0.575	-0.766	-0.993	0.595	-0.086	-0.0575
Atomic Types	C4	C5	H2	H3	H4	N	
Charge (e)	-0.0765	0.098	0.349	0.1255	0.112	-0.171	

ANNEX B - Articles



Computational evaluation of the chemical warfare agents capture performances of robust MOFs

C. Vieira Soares^{a,b}, A.A. Leitão^b, G. Maurin^{a,*}

^a Institut Charles Gerhardt Montpellier, UMR-5253, Université de Montpellier, ENSCM, Place E. Bataillon, Montpellier cedex 05, 34095, France

^b Departamento de Química, Universidade Federal de Juiz de Fora, Juiz de Fora, MG, 36036-330, Brazil

ARTICLE INFO

Keywords:

MOFs
Chemical warfare agents
Monte Carlo simulations
Density functional theory calculations

ABSTRACT

A series of stable MOFs containing zirconium or titanium ions as metal centers was screened to assess their capture performances for nerve agents including sarin and soman as well as their standard simulants, i.e. the dimethyl-methyl-phosphonate and diisopropyl fluorophosphate. These Monte Carlo simulations revealed that some of these MOFs show very high uptakes that significantly outperform those of other families of porous materials and interestingly they exhibit a very high affinity for these toxic molecules at low loading. These combined features make them potentially attractive to act as nerve agent filters. This set of adsorption data was further rationalized to establish structure-adsorption performances relationship and Monte Carlo simulations were combined with Density Functional Theory calculations to gain more insight into the adsorption mechanism in play. Finally, the choice of reliable simulants to accurately mimic the adsorption behavior of real toxic molecules in MOFs has been further discussed and in particular it has been established that soman is better described considering the pinacolyl methylphosphonate rather than the standard dimethyl-methyl-phosphonate and diisopropyl fluorophosphate simulants.

1. Introduction

Despite the chemical weapon convention of 1997, chemical warfare agents (CWAs) are still being employed throughout the world by terrorist groups and unscrupulous governments with most recently the reported use of CWAs in the Middle East [1]. This emphasizes that threat of exposure to CWAs is still considered as a major military issue. Several events such as the attack with sarin, in the Tokyo metro in 1995 [2], have also demonstrated that civilian populations may also be exposed to these toxic agents. Today's protection devices for the capture of CWA from air streams including gas masks and filters involve carbon materials (the so-called ASZM-TEDA [3]) impregnated with a mixture of nanoparticles of metal or metal oxides, salts and amines that act as specific adsorption sites for the targeted highly toxic molecules [4,5]. More recent developments have been also devoted to the detection of CWAs using notably pure or functionalized silica, zeolites, alumina or titania [6–8]. Although these existing adsorbents exhibit many desirable characteristics for the capture and the destruction of CWAs, they show relatively low adsorption capacities, rapid deactivation of their active sites and/or lack of tailorability. This leaves significant room to identify other porous materials with improved performances for such application. In this context, Metal-Organic Frameworks (MOFs) [9–13]

have been recently envisaged as promising candidates for the identification, adsorption and/or catalytic degradation of CWAs [14]. The attractiveness of this family of hybrid porous ordered solids, built up from inorganic sub-units and organic complexing linkers bearing or not functional polar or apolar groups, lies in the huge spectrum of physical properties and chemistries that can be explored, where almost all of the elements of the periodic table have been used in one material or another. This offers an unprecedented opportunity to identify porous adsorbents for CWA capture with the ability to capture a broad range of hazardous molecules to respond to diverse menaces and store high CWA. The large majority of studies related to the MOF/CWA topic has focused so far on the catalytic degradation purpose. The selected MOFs including Cu-BTC [15], MOF-5 [16], UiO-66s [17–19] UiO-67s [17,20], NU-1000 [17,21], PCN-222 [22], NENU-11 [23], Zn-DMCP [24], MIL-101(Al)-NH₂ [25] and MIL-53(Al)-NH₂ [25] revealed promising performances for the degradation of both G-type nerve agents, i.e. sarin, soman, VX and their standard simulants dimethyl-methyl-phosphonate (DMMP) and diisopropyl fluorophosphate (DIFP), and vesicant agents of which sulphur mustard and its simulant including 2-chloroethylsulfide (CEES). In terms of adsorption studies, only a very few studies have been reported. We can cite the experimental studies on the adsorption of DMMP in NENU-11 and MOF-5 [16] while a first

* Corresponding author.

E-mail address: guillaume.maurin1@umontpellier.fr (G. Maurin).

<https://doi.org/10.1016/j.micromeso.2019.01.046>

Received 17 December 2018; Received in revised form 15 January 2019; Accepted 28 January 2019

Available online 29 January 2019

1387-1811/ © 2019 Elsevier Inc. All rights reserved.

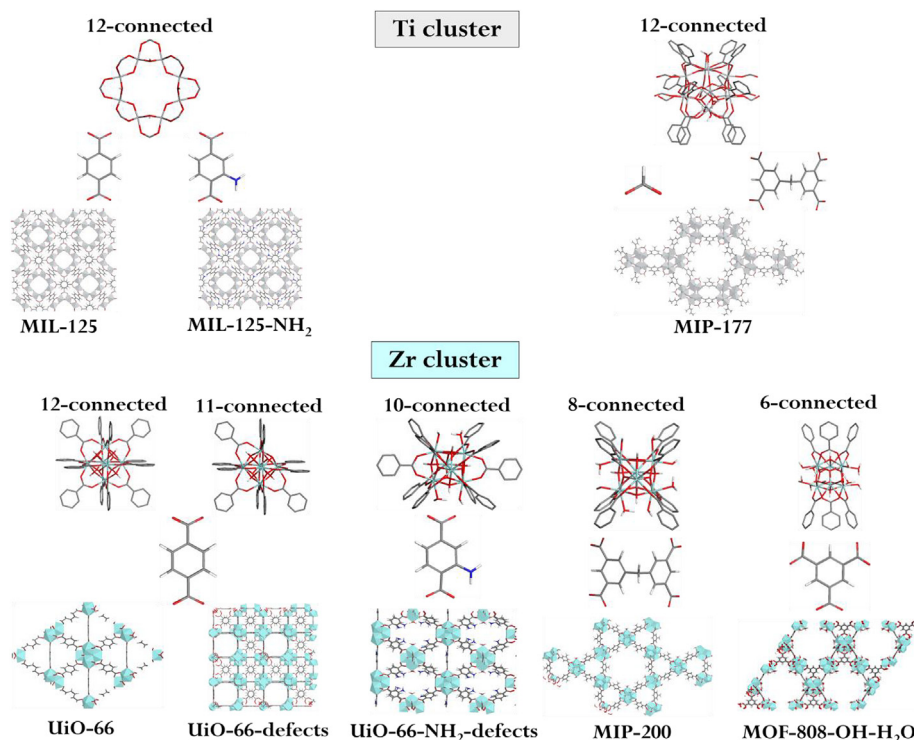


Fig. 1. Illustrations of the inorganic Zr and Ti building blocks present in a few representative 3D-MOFs considered in this work.

computational exploration has been very recently published by Matito-Martos et al. on the CWA removal capacity performances of a large series of MOFs [26]. Some of the tested MOFs for CWA-related applications are unstable in the presence of water which hampers their use for CWA capture since humidity in the air and in the breath is usually present in operating conditions.

In this context, priority has to be given to explore the CWA capture in chemical stable MOF containing high-valent cations, e.g. Al^{3+} , Zr^{4+} , Ti^{4+} , as metal centers to ensure that the performances can be maintained under operating conditions over prolonged periods. Another requirement is to favor MOFs incorporating relatively cheap commercially available organic linkers, easily scaled-up, and prepared via green synthesis routes in order to be cost-competitive with respect to the ASZM-TEDA active carbons currently used as filters. With these ideas in mind, here we report a systematic computational evaluation of the CWA capture performances of a series of Zr- and Ti- MOFs, showing different pore size/topology and incorporating diverse adsorption sites (Fig. 1), that have been proved to be water stable. This study aimed to explore sarin and soman as well as their most common simulants used in experiments, i.e. DMMP, DIFP and Pinacolyl methylphosphonate (PMP) (Fig. 2). Grand Canonical Monte Carlo (GCMC) simulations have been combined with Density Functional Theory (DFT) calculations to assess the adsorption uptakes and the energetics for each MOF/CWA pair and to evidence the preferential adsorption sites and the resulting CWA/MOF interactions. As a further step, this computational database has been used to build model structure-adsorption performances in order to identify the key parameters of the MOFs that drive the CWA capture. Finally, the comparison of the simulated adsorption behaviors of CWA and their simulants allowed us to define the most reliable simulant that mimics as fairly as possible the real molecules.

2. Computational details

The structural models for all MOFs were taken from the literature: MIL-125-(Ti) and MIL-125-(Ti)- NH_2 [27]; MIL-140-D [28], MIL-140-E and MIL-140G [29]; MIP-177 and MIP-177-OH- H_2O [30]; MIP-200 and

MIP-200-OH- H_2O [31]; MOF-808-A, MOF-808-F, MOF-808-P and MOF-808-OH- H_2O [32]; NU-1000 [33]; UiO-66-(Zr) [34]; UiO-66-(Zr)-Cl, UiO-66-(Zr)-(OH) $_2$, UiO-66-(Zr)- CO_2H , UiO-66-(Zr)- NO_2 and UiO-66-(Zr)- NH_2 [35]; defective UiO-66-(Zr) and UiO-66-(Zr)- NH_2 labelled as UiO-66-(Zr)-defects6 and UiO-66-(Zr)- NH_2 defects6 respectively in a previous study [36]; UiO-67-(Zr) [34], UiO-68-(Zr) [34] and Zr_6 -AZO-BDC [37] (Figs. S1–S25). The structures of MIP-177-OH- H_2O , MIP-200-OH- H_2O , MOF-808-OH- H_2O and defective UiO-66-(Zr) and UiO-66-(Zr)- NH_2 were preliminarily saturated by hydroxyl and water groups. These atoms were added to the metal atoms of the inorganic nodes. All crystal structures were further geometry optimized at the DFT level keeping the experimental unit cell parameters fixed. These calculations were performed using the Perdew Burke Ernzerhof (PBE) functional at generalized gradient approximation (GGA) [38] combined with the Double Numeric basis set with Polarization functions (DNP) [39] on all atoms as implemented in DMol³ package [40].

2.1. Force fields

The interactions between MOFs and CWAs were treated using the sum of a 12-6 Lennard-Jones (LJ) contribution and a Coulombic term. The Universal force field (UFF) [41] and DREIDING [42] force field were adopted to describe the Lennard-Jones (LJ) parameters of all atoms of the inorganic nodes and the organic linkers, respectively. The partial charges for all atoms of the MOF frameworks were extracted from our DFT calculations (see Tables S1–S25 and corresponding Figs. S1–S25). Regarding the CWAs, sarin, soman and DMMP molecules were described by a united atom representation including LJ point charges with parameters taken from the transferable potentials for phase equilibria (TraPPE) force field, reported by Sokkalingam et al. [43]. Same united atom representations were considered for the DIFP and PMP molecules with parameters taken from the previous work reported by Vishnyakov et al. [44] and Sokkalingam et al. [43] respectively. The LJ cross parameters corresponding to the interactions between the CWAs and the MOFs framework were obtained using the Lorentz-Berthelot mixing rules. Finally, the charges of these CWAs were taken from

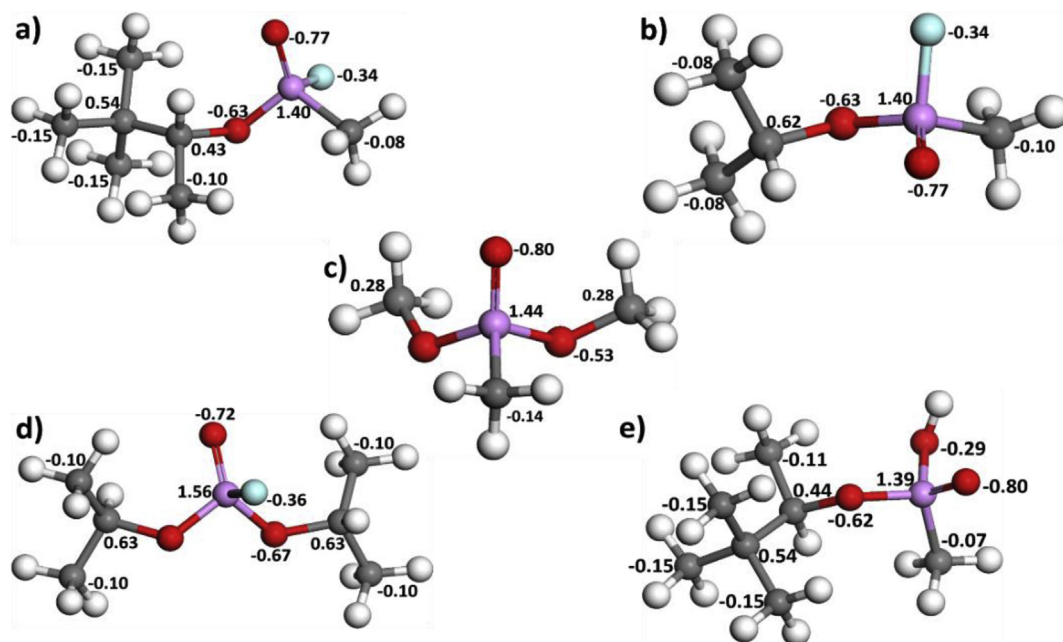


Fig. 2. Illustration of the CWAs molecules: (a) Soman, (b) Sarin, (c) DMMP, (d) DIFP and (e) PMP along with the partial charges used for the united-atom models considered in this work.

these previously reported United Atom models of these molecules as illustrated in Fig. 2.

2.2. Monte Carlo simulations

Grand Canonical Monte Carlo (GCMC) simulations were performed at 298 K for all MOFs and CWAs selected in this work for a series of fugacity for the CWAs up to 5000 kPa in order to estimate the saturation capacity for each molecule. The selection of this high range of pressure is to make sure that we can assess the maximum payload of all MOFs and there is no link with the pressure encountered under working condition of nerve agent filters. These calculations were performed using the Complex Adsorption and Diffusion Simulation Suite (CADSS) code implementing the configurational-bias Monte Carlo scheme that was used in this study to favor a more efficient sampling of the CWAs in the pores of the MOFs. This method includes insertion/deletion, translational, rotational, partial and full regrowth MC steps. The simulation box considered for all MOFs was defined in such a way that all a, b and c dimensions were longer than 24 Å. Short-range dispersion forces described by LJ potentials were thus truncated at a cutoff radius of 12 Å, whereas long-range electrostatic interactions were handled using the Ewald summation technique. For each state point, 2×10^8 Monte Carlo steps have been used for both equilibration and production runs. The adsorption enthalpies at low coverage (ΔH) for each molecule were calculated for all MOFs using the revised Widom's test particle insertion method [45]. To gain insight into the arrangement of the CWAs in the pores of the MOFs, the CWA/CWA and CWA/MOF radial distribution functions (RDFs) were obtained by averaging over the whole configurations generated during the GCMC simulations.

2.3. Density Functional Theory calculations

A Bader charge analysis was conducted on the MOF/CWA systems using a grid-based algorithm [46] to analyse the potential charge transfer between the CWAs and the MOFs. The charge in all atoms of the system was defined as the difference between the valence charge and the Bader charge. These calculations were performed using the codes available in the Quantum-Espresso package [47], which implements the Density Functional Theory (DFT) [48,49] with periodic

boundary conditions using plane wave functions as basis set [50]. We used the generalized gradient approximation (GGA/PBE) [51] for the exchange-correlation functional, and the ion cores of atoms were described by the Vanderbilt [52] ultrasoft pseudopotential. These calculations were performed using single point calculation on the configuration generated by the MC simulations.

3. Results and discussion

Fig. 3 reports the simulated CWA uptakes for all MOFs. One can observe that the best materials for CWA capture are MOF-808s, NU-1000, UiO-68(Zr) and Zr-Azo-BDC. This conclusion remains valid for all real CWAs and their simulants with adsorption uptakes above 6 mmol/g. This level of performances significantly surpasses that of previously reported MOFs and other standard porous materials. Typically, the carbons adsorb much lower amounts of CWAs. As an illustration Kowalczyk et al. [53], demonstrated that pitch-based P7 Activated Carbon Fiber (ACF) and the commercialized Norit activated carbons adsorb only respectively $0.806 \text{ mmol.g}^{-1}$ and $0.161 \text{ mmol.g}^{-1}$ of DMMP. In addition, the current activated carbon ASZM-TEDA showed a sarin adsorption uptake of 0.04 mg/m^3 [54]. Regarding MOFs, as mentioned in the introduction only a very few studies have been reported on their CWA adsorption performances. We can cite the sodalite-type MOF (NENU-11) [23] and MOF-5 [16] that were shown to adsorb 1.92 mmol.g^{-1} and 7.3 mmol.g^{-1} of DMMP respectively. As a further step, we concentrated our effort to identify the features of the MOFs at the origin of these high CWA uptakes. We evidenced that the uptake of each CWA considered individually correlates rather well with the N_2 -accessible surface area calculated for the MOFs (see Table S26 and Fig. S26 - correlation factors R^2 varying from 0.84 to 0.90). The correlation is even better using the free pore volume as a descriptor of the MOFs (see Fig. S27 with correlation factors higher than 0.96). In order to obtain a more generic expression, we introduced another geometric descriptor labelled as α which is given by the following expression:

$$\alpha = \left(\frac{V_{\text{MOF}}}{\nu_{\text{Soman}}} \right) / \nu_{\text{CWA}}$$

where V_{MOF} corresponds to the free pore volume of the MOF, ν_{Soman} and ν_{CWA} are the volume of the bulkier CWA, i.e. soman, and the other molecules respectively. Fig. 4 evidences an excellent correlation between the uptakes and α for all MOFs (correlation factor

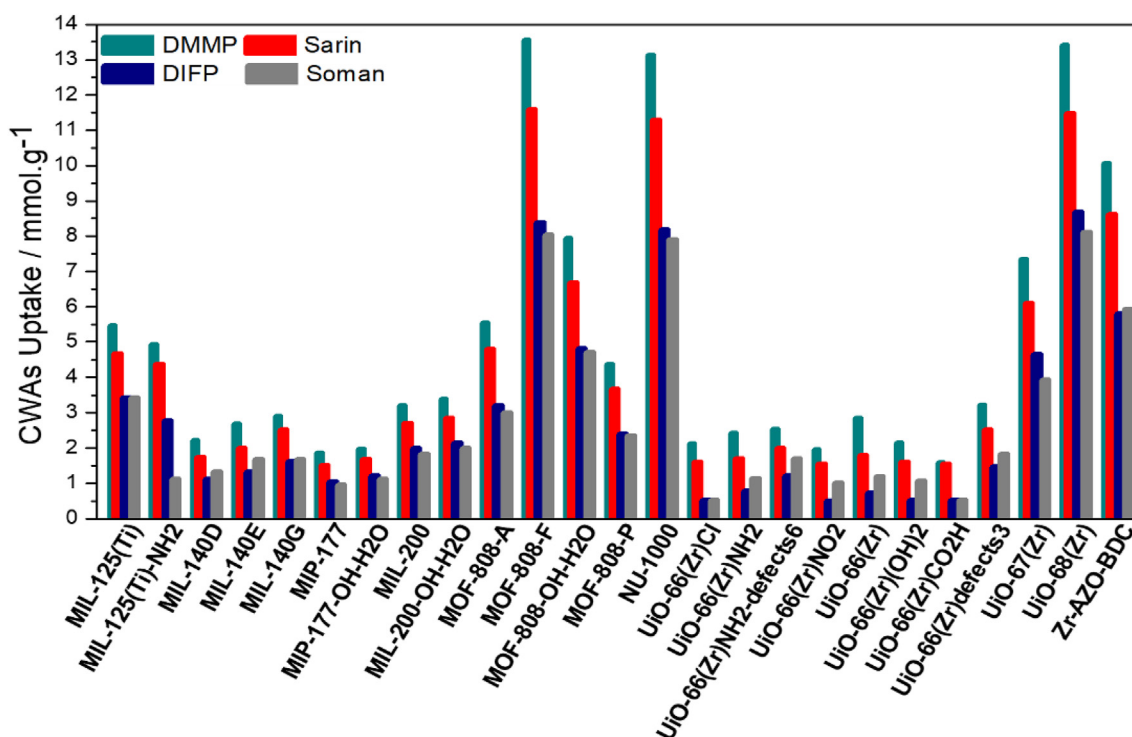


Fig. 3. GCMC simulated saturation uptakes at 298 K for all MOFs with respect to sarin, soman, DMMP and DIFP calculated using a pressure of 5000 kPa.

R^2 of 0.99). This structure-adsorption uptake performance relationship emphasizes that the capacity of stockpiling CWA in MOFs is predominantly governed by a pore filling mechanism, the higher porosity leading to the higher CWA uptake. This structure-adsorption uptake performance relationship emphasizes that the capacity of stockpiling CWA in MOFs is predominantly governed by a pore filling mechanism, the higher porosity leading to the higher CWA uptake. The predominance of this mechanism is also supported by the excellent correlation for all CWAs between the uptake capacity of the MOF with the fraction of the free pore volume of the MOF and the volume of the adsorbed molecule ($\frac{V_{MOF}}{V_{CWA}}$) as reported in Fig. S28. Typically, the best

materials UiO-68(Zr) and MOF-808s show the highest free pore volumes of 1.75 and 1.85 $\text{cm}^3 \cdot \text{g}^{-1}$ respectively (see Table S26).

We further evidenced that the calculated adsorption enthalpy is higher for all CWAs in the case of the MOFs showing the lower free pore volume although we do not find a direct correlation since the chemical features of the MOFs also impact the CWA/MOF interactions (see Fig. S29). This observation is consistent with the systematic computational study reported by Agrawal et al., which demonstrated that the MOFs with the pore limiting diameters in the range of 6–8 Å show the highest affinity for Sarin [55].

Interestingly the calculated CWA adsorption enthalpies were shown to be spread in a relatively large domain reaching for some MOFs very

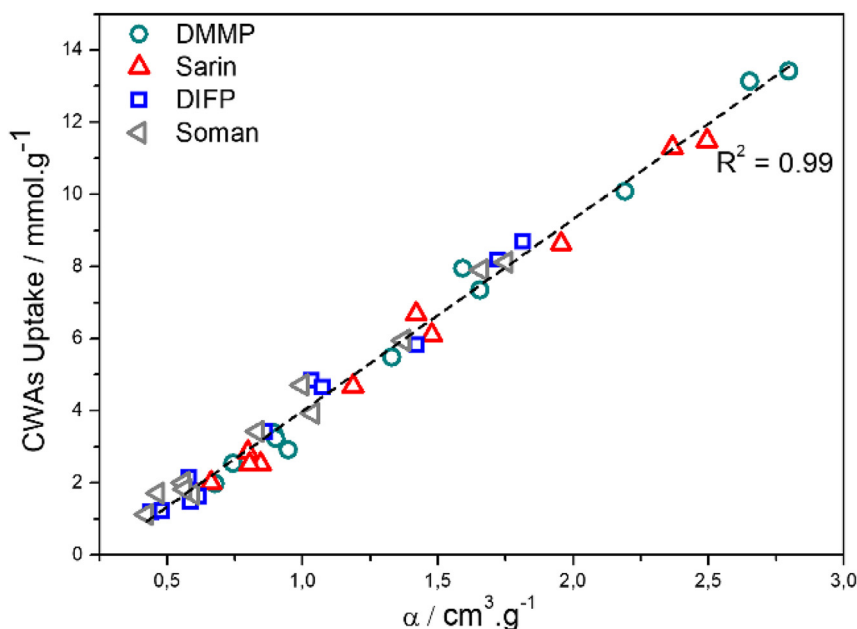


Fig. 4. Structure-adsorption uptake relationship for CWAs in MOFs.

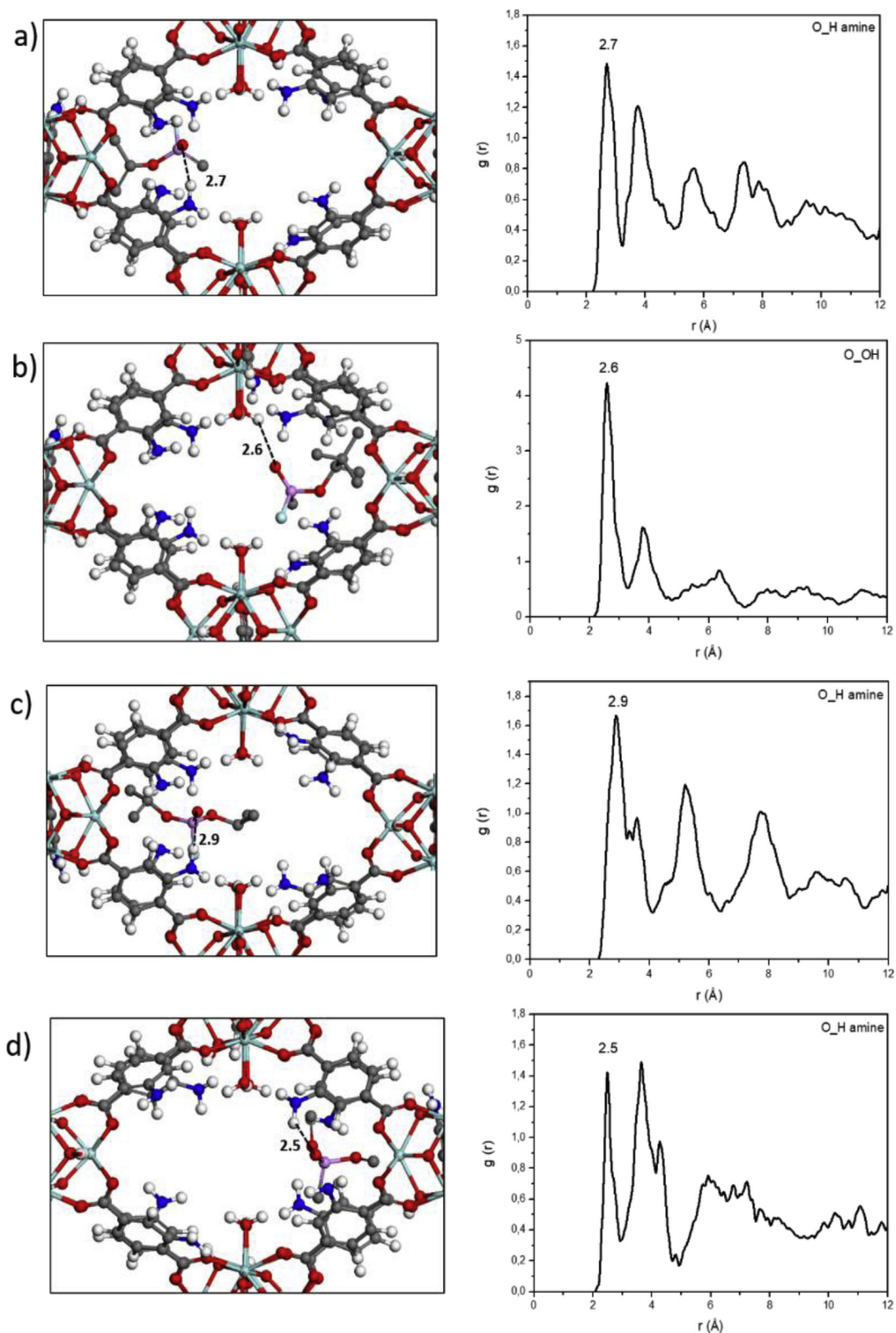


Fig. 5. A typical illustration of the preferential sittings for (a) Sarin, (b) Soman, (c) DIFP and (d) DMMP in the pores of the defective UiO-66(Zr)-NH₂ and the corresponding CWA/MOF radial distribution functions averaged over all the MC configurations.

high values up to -110 kJ/mol. The strength of interactions obtained for these screened MOFs is significantly higher than the unique experimental value reported so far for a MOF, i.e. -44.8 kJ/mol for DIFP in Zn-DMCP [24].

To gain more insight into the microscopic origin of the potentially

high CWA/MOF interactions, a carefully analysis of the preferential adsorption sites for the CWAs was undertaken based on the calculations of the radial distribution functions for the diverse CWA/MOF atom pairs averaged over the whole configurations generated by Monte Carlo simulations. Typically, we detailed the scenario for the defective UiO-

Table 1
Bader charge analysis for the isolated and adsorbed CWAs in the defective UiO-66(Zr)-NH₂.

Charges	Isolated Soman	Confined Soman	Isolated Sarin	Confined Sarin	Isolated DMMP	Confined DMMP	Isolated DIFP	Confined DIFP
O=(P)	-1.87	-1.88	-1.88	-1.88	-1.88	-1.87	-1.88	-1.88
O-CH	-1.71	-1.71	-1.71	-1.71	-	-1.70	-1.71	-1.70
P	4.86	4.86	4.86	4.86	4.86	4.86	4.86	4.87
F	-1.03	-1.01	-1.01	-1.01	-	-	-1.01	-1.01
CH ₃ -P	-1.27	-1.24	-1.26	-1.26	-1.21	-1.25	-	-
O-CH ₃	-	-	-	-	-1.73	-1.72	-	-

Table 2
Simulated adsorption uptakes and enthalpies for sarin, soman, DMMP, DIFP and PMP in two representative MOF materials investigated in this study.

	Uptake mmol.g ⁻¹					ΔH kJ.mol ⁻¹				
	sarin	DMMP	DIFP	soman	PMP	sarin	DMMP	DIFP	soman	PMP
MIP-177-OH-H ₂ O	1.695	1.977	1.212	1.122	1.110	67.63	70.30	71.26	88.26	83.89
MOF-808-OH-H ₂ O	6.685	7.951	4.839	4.716	4.509	62.90	64.65	57.79	74.71	72.05

66-(Zr)-NH₂ which is one of the MOFs showing the stronger interactions with sarin, soman, DMMP and DIFP associated with adsorption enthalpies of -108, -95, -93 and -94 kJ mol⁻¹ respectively. It is not be noted that these values converge well with the interaction energies calculated at the DFT-level (Table S27). This observation validates the set of LJ potential parameters and atomic partial charges used to describe the CWA/MOF interactions. Fig. 5a shows that sarin is preferentially located in the vicinity of the amino function grafted to the organic linker via an interaction between its oxygen atom of the P=O group and the hydrogen atom of the amino group with a characteristic distance of 2.7 Å. Such a range of interacting distance suggests a relatively moderated strength of interaction between CWA and the MOFs and thus a physisorption-based process. The same preferential interactions with the NH₂-group of the MOF were also observed for the simulants DMMP and DIFP (Fig. 5c and d) while the adsorption behavior of soman only slightly deviates with an interaction between its oxygen atom of the P=O group and the hydrogen atom of the hydroxyl group bounded to the Zr atom (Fig. 5b). Relatively similar strength of CWA/MOFs interactions and microscopic adsorption mechanisms were also observed for the other best MOFs including for instance MOF-808s (Fig. S30).

In order to confirm that the CWA adsorption proceeds in these MOFs via physisorption-type interactions, we performed further DFT analysis. As a typical example, we specifically treated the case of CWA adsorbed in the defective UiO-66(Zr)-NH₂. The analysis of Bader charges revealed that there is no significant change when one compares the charges of the isolated and confined CWA as summarized in Table 1. This result clearly supports that there is no charge transfer between the CWA and the host framework and this excludes the existence of a chemisorption process.

From an experimental standpoint, simulant molecules, with physical or chemical properties similar to the real CWAs are usually considered to avoid working with the highly toxic agents. DMMP and DIFP are the most common simulants employed to mimic soman and sarin respectively, however it is crucial to make sure that they accurately capture the adsorption behavior of the real molecules and this issue has been only rarely discussed so far in the literature. In this concern, Agrawal et al. [55] showed that dimethyl p-nitrophenyl phosphate (DMNP) is a suitable simulant to mimic the adsorption of Soman while DMMP, DIFP and diethyl chlorophosphite are more appropriate to reproduce the behavior of Sarin. To address this question in the case of MOFs, we considered the comparison of the adsorption behaviours of DIFP, DMMP, soman and sarin in two representative MOFs, namely the MOF-808-OH-H₂O and the MIP-177-OH-H₂O. Table 2 shows the simulated adsorption uptakes and adsorption enthalpies for all four molecules. It can be clearly stated that while DMMP and DIFP

accurately reproduce the behavior of sarin in terms of uptake and energetics this is far to be the case for soman. Therefore, we searched for an alternative simulant that can mimic more accurately soman. Indeed, the PMP molecule showing similar backbone than the real molecule (see Fig. 2) was thus considered. Table 2 indicates that this simulant reproduces much better the adsorption behavior of soman (in terms of both uptake and energetics), Fig. S31 showing that it occupies a preferential sitting in the pores similar to the real molecule. This observation suggests that this simulant of low toxicity should be considered as an alternative to the standard DMMP and DIFP molecules to explore the performances of MOFs regarding soman.

4. Conclusions

In summary, our GCMC simulations evidenced that a series of water stable Zr and Ti MOFs show outstanding adsorption uptakes for soman, sarin and their simulants combined with high adsorption enthalpies. This level of performance makes these materials potentially attractive as CWA filters with great promises in large payload and limitation of release under operating conditions. Although the CWA adsorption enthalpies reached for some MOFs values higher than -100 kJ.mol⁻¹, complementary DFT analysis precluded the existence of charge transfer between the CWA and the host framework consistent with a physisorption-based process involving mostly van der Waals interactions. Structure-CWA adsorption performances relationship was established with the definition of a geometric descriptor based on the free pore volume of the MOF and the molecular dimension of the CWAs. Finally, we evidenced that a special attention needs to be paid when one selects the simulants to mimic the adsorption of real CWAs in MOFs. While the standard DMMP and DIFP simulants reproduce well the behavior of sarin, this is not anymore true for soman and we established that an alternative simulant, namely the PMP molecule, needs to be considered. A further step will be to consider the competitive adsorption of CWAs with water and hydrocarbons to confirm the viability of these promising MOFs as CWA filters. Furthermore, such a computational approach can be applied in order to explore the adsorption performances of other materials with respect to different families of CWAs and toxic industrial compounds (TICs).

Conflicts of interest

There are no conflicts to declare.

Acknowledgements

The research leading to these results has received funding from a

bilateral project COFECUB-CAPEs France-Brazil 778-13. G.M. thanks the Institut Universitaire de France for its support.

Appendix A. Supplementary data

Supplementary data to this article can be found online at <https://doi.org/10.1016/j.micromeso.2019.01.046>.

References

- [1] Chemical Attack of 7 April 2018 (Douma, Eastern Ghouta, Syria) Syria's Clandestine Chemical Weapons Programme, (2018), pp. 1–7 2018.
- [2] B.M. Smith, Catalytic methods for the destruction of chemical warfare agents under ambient conditions, *Chem. Soc. Rev.* 37 (2008) 470–478, <https://doi.org/10.1039/b705025a>.
- [3] J.B. Decoste, G.W. Peterson, Metal – Organic Frameworks for Air Puri Fi Cation of Toxic Chemicals, (2014).
- [4] J.V. Romero, J.W.H. Smith, B.M. Sullivan, M.G. Mallay, L.M. Croll, J.A. Reynolds, C. Andres, M. Simon, J.R. Dahn, Gas adsorption properties of the ternary ZnO/CuO/CuCl₂ impregnated activated carbon system for multigas respirator applications assessed through combinatorial methods and dynamic adsorption studies, *ACS Comb. Sci.* 13 (2011) 639–645, <https://doi.org/10.1021/co200121c>.
- [5] J.W.H. Smith, J.V. Romero, T.R. Dahn, K. Dunphy, L.M. Croll, J.R. Dahn, The effect of co-impregnated acids on the performance of Zn-based broad spectrum respirator carbons, *J. Hazard Mater.* 235–236 (2012) 279–285, <https://doi.org/10.1016/j.jhazmat.2012.07.061>.
- [6] A. Saxena, A.K. Srivastava, B. Singh, A. Goyal, Removal of sulphur mustard, sarin and simulants on impregnated silica nanoparticles, *J. Hazard Mater.* 211–212 (2012) 226–232, <https://doi.org/10.1016/j.jhazmat.2011.07.117>.
- [7] A.K. Verma, A.K. Srivastava, B. Singh, D. Shah, S. Shrivastava, C. Kant, P. Shinde, Chemosphere Alumina-supported oxime for the degradation of sarin and diethylchlorophosphate, *Chemosphere* 90 (2013) 2254–2260, <https://doi.org/10.1016/j.chemosphere.2012.10.011>.
- [8] D.A. Panayotov, J.R. Morris, Uptake of a Chemical Warfare Agent Simulant (DMMP) on TiO₂: Reactive Adsorption and Active Site Poisoning, (2009), pp. 3652–3658.
- [9] G. Férey, Hybrid porous solids: past, present, future, *Chem. Soc. Rev.* 37 (2008) 191–214, <https://doi.org/10.1039/B618320B>.
- [10] B.F. Hoskins, R. Robson, Infinite polymeric frameworks consisting of three dimensionally linked rod-like segments, *J. Am. Chem. Soc.* 111 (1989) 5962–5964, <https://doi.org/10.1021/ja00197a079>.
- [11] O.M. Yaghi, H. Li, Hydrothermal synthesis of a metal-organic framework containing large rectangular channels, *J. Am. Chem. Soc.* 117 (1995) 10401–10402, <https://doi.org/10.1021/ja00146a033>.
- [12] K. Mitsuru, Y. Tomomichi, M. Hiroyuki, K. Susumu, S. Kenji, Three-dimensional framework with channeling cavities for small molecules: {[M₂(4, 4'-bpy)₃(NO₃)₄]xH₂O}_n (M Co, Ni, Zn), *Angew Chem. Int. Ed. Engl.* 36 (2003) 1725–1727, <https://doi.org/10.1002/anie.199717251>.
- [13] G. Maurin, C. Serre, A. Cooper, G. Férey, The new age of MOFs and of their porous-related solids, *Chem. Soc. Rev.* 46 (2017) 3104–3107, <https://doi.org/10.1039/c7cs90049j>.
- [14] N.S. Bobbitt, M.L. Mendonca, A.J. Howarth, T. Islamoglu, J.T. Hupp, O.K. Farha, R.Q. Snurr, Metal-organic frameworks for the removal of toxic industrial chemicals and chemical warfare agents, *Chem. Soc. Rev.* 46 (2017) 3357–3385, <https://doi.org/10.1039/C7CS00108H>.
- [15] A. Roy, A.K. Srivastava, B. Singh, D. Shah, T.H. Mahato, P.K. Gutch, A.K. Halve, Degradation of sarin, DECP and DECNP over Cu-BTC metal organic framework, *J. Porous Mater.* 20 (2013) 1103–1109, <https://doi.org/10.1007/s10934-013-9692-4>.
- [16] Z. Ni, J.P. Jerrell, K.R. Cadwallader, R.I. Masel, Metal-organic frameworks as adsorbents for trapping and preconcentration of organic phosphonates, *Anal. Chem.* 79 (2007) 1290–1293, <https://doi.org/10.1021/ac0613075>.
- [17] T. Islamoglu, M.A. Ortuño, E. Prousaloglou, A.J. Howarth, N.A. Vermeulen, A. Atilgan, A.M. Asiri, C.J. Cramer, O.K. Farha, Presence versus proximity: the role of pendant amines in the catalytic hydrolysis of a nerve agent simulant, *Angew Chem. Int. Ed.* 57 (2018) 1949–1953, <https://doi.org/10.1002/anie.201712645>.
- [18] M.J. Katz, S.-Y. Moon, J.E. Mondloch, M.H. Beyzavi, C.J. Stephenson, J.T. Hupp, O.K. Farha, Exploiting parameter space in MOFs: a 20-fold enhancement of phosphate-ester hydrolysis with UiO-66-NH₂, *Chem. Sci.* 6 (2015) 2286–2291, <https://doi.org/10.1039/C4SC03613A>.
- [19] M.R. Momeni, C.J. Cramer, Dual role of water in heterogeneous catalytic hydrolysis of sarin by zirconium-based metal-organic frameworks, *ACS Appl. Mater. Interfaces* 10 (2018) 18435–18439, <https://doi.org/10.1021/acsmi.8b03544>.
- [20] S.Y. Moon, G.W. Wagner, J.E. Mondloch, G.W. Peterson, J.B. DeCoste, J.T. Hupp, O.K. Farha, Effective, facile, and selective hydrolysis of the chemical warfare agent VX using Zr₆-based metal-organic frameworks, *Inorg. Chem.* 54 (2015) 10829–10833, <https://doi.org/10.1021/acs.inorgchem.5b01813>.
- [21] J.E. Mondloch, M.J. Katz, W.C. Isley III, P. Ghosh, P. Liao, W. Bury, G.W. Wagner, M.G. Hall, J.B. DeCoste, G.W. Peterson, R.Q. Snurr, C.J. Cramer, J.T. Hupp, O.K. Farha, Destruction of chemical warfare agents using metal-organic frameworks, *Nat. Mater.* 14 (2015) 512–516, <https://doi.org/10.1038/nmat4238>.
- [22] P. Li, R.C. Klet, S.-Y. Moon, T.C. Wang, P. Deria, A.W. Peters, B.M. Klahr, H.-J. Park, S.S. Al-Juaid, J.T. Hupp, O.K. Farha, Synthesis of nanocrystals of Zr-based metal-organic frameworks with csq-net: significant enhancement in the degradation of a nerve agent simulant, *Chem. Commun.* 51 (2015) 10925–10928, <https://doi.org/10.1039/C5CC03398E>.
- [23] F.J. Ma, S.X. Liu, C.Y. Sun, D.D. Liang, G.J. Ren, F. Wei, Y.G. Chen, Z.M. Su, A sodalite-type porous metal-organic framework with polyoxometalate templates: adsorption and decomposition of dimethyl methylphosphonate, *J. Am. Chem. Soc.* 133 (2011) 4178–4181, <https://doi.org/10.1021/ja109659k>.
- [24] C. Montoro, F. Linares, E. Quartapelle Procopio, I. Senkovska, S. Kaskel, S. Galli, N. Masciocchi, E. Barea, J.A.R. Navarro, Capture of nerve agents and mustard gas analogues by hydrophobic robust MOF-5 type metal-organic frameworks, *J. Am. Chem. Soc.* 133 (2011) 11888–11891, <https://doi.org/10.1021/ja2042113>.
- [25] L. Bromberg, Y. Klichko, E.P. Chang, S. Speakman, C.M. Straut, E. Wilusz, T.A. Hatten, Alkylaminopyridine-modified aluminum aminoterephthalate metal-organic frameworks as components of reactive self-detoxifying materials, *ACS Appl. Mater. Interfaces* 4 (2012) 4595–4602, <https://doi.org/10.1021/am3009696>.
- [26] I. Matito-Martos, P.Z. Moghadam, A. Li, V. Colombo, J.A.R. Navarro, S. Calero, D. Fairen-Jimenez, Discovery of an optimal porous crystalline material for the capture of chemical warfare agents, *Chem. Mater.* 30 (2018) 4571–4579, <https://doi.org/10.1021/acs.chemmater.8b00843>.
- [27] M. Dan-hardi, C. Serre, L. Rozes, G. Maurin, A new photoactive crystalline highly porous titanium (IV) dicarboxylate, *J. Am. Chem. Soc.* 131 (2009) 1–15, <https://doi.org/10.1021/ja903726m>.
- [28] V. Guillerme, F. Ragon, M. Dan-Hardi, T. Devic, M. Vishnuvarthan, B. Campo, A. Vimont, G. Clet, Q. Yang, G. Maurin, G. Férey, A. Vittadini, S. Gross, C. Serre, A series of isorecticular, highly stable, porous zirconium oxide based metal-organic frameworks, *Angew. Chem. Int. Ed.* 51 (2012) 9267–9271, <https://doi.org/10.1002/anie.201204806>.
- [29] C. Serre, A Private Communication, (2018).
- [30] S. Wang, T. Kitao, N. Guillou, M. Wahiduzzaman, C. Martineau-Corcors, F. Nouar, A. Tissot, L. Binet, N. Ramsahye, S. Devautour-Vinot, S. Kitagawa, S. Seki, Y. Tsutsui, V. Briois, N. Steunou, G. Maurin, T. Uemura, C. Serre, A phase transformable ultrastable titanium-carboxylate framework for photoconduction, *Nat. Commun.* 9 (2018) 1660, <https://doi.org/10.1038/s41467-018-04034-w>.
- [31] C.S. Sujing Wang, Ji Sun Lee, Mohammad Wahiduzzaman, Jaedeuk Park, Mégane Muschi, Charlotte Martineau-Corcors, Antoine Tissot, Kyung Ho Cho, Jérôme Marrot, William Shepard, Guillaume Maurin, Jong-San Chang, A robust energy-efficient metal-organic framework adsorbent for refrigeration, *Nat. Energy* 3 (2018) 985.
- [32] W. Liang, H. Chevreau, F. Ragon, P.D. Southon, V.K. Peterson, D.M. D'Alessandro, Electronic Supporting Information Tuning pore size in a zirconium-tricarboxylate metal-organic framework, *CrystEngComm* 16 (2014) 6530–6533, <https://doi.org/10.1039/c4ce01031k>.
- [33] J.E. Mondloch, W. Bury, D. Fairen-Jimenez, S. Kwon, E.J. Demarco, M.H. Weston, A.A. Sarjeant, S.T. Nguyen, P.C. Stair, R.Q. Snurr, O.K. Farha, J.T. Hupp, Vapor-phase metalation by atomic layer deposition in a metal-organic framework, *J. Am. Chem. Soc.* 135 (2013) 10294–10297, <https://doi.org/10.1021/ja4050828>.
- [34] J.H.H. Cavka, S. Jakobsen, U. Olsbye, N. Guillou, C. Lamberti, S. Bordiga, K.P.P. Lillerud, A new zirconium inorganic building brick forming metal organic frameworks with exceptional, *Stability* 130 (2008) 13850–13851, <https://doi.org/10.1021/ja8057953>.
- [35] Q. Yang, A.D. Wiersum, P.L. Llewellyn, V. Guillerme, C. Serre, G. Maurin, Functionalizing porous zirconium terephthalate UiO-66(Zr) for natural gas upgrading: a computational exploration, *Chem. Commun.* 47 (2011) 9603, <https://doi.org/10.1039/c1cc13543k>.
- [36] S.M.J. Rogge, J. Wieme, L. Vanduyffhuys, S. Vandenbrande, G. Maurin, T. Verstraelen, M. Waroquier, V. Van Speybroeck, Thermodynamic insight in the high-pressure behavior of UiO-66: effect of linker defects and linker expansion, *Chem. Mater.* 28 (2016) 5721–5732, <https://doi.org/10.1021/acs.chemmater.6b01956>.
- [37] A. Schaate, S. Dühnen, G. Platz, S. Lillenthal, A.M. Schneider, P. Behrens, A novel Zr-based porous coordination polymer containing azobenedicarboxylate as a linker, *Eur. J. Inorg. Chem.* (2012) 790–796, <https://doi.org/10.1002/ejic.201101151>.
- [38] J.P. Perdew, K. Burke, M. Ernzerhof, Generalized gradient approximation made simple, *Phys. Rev. Lett.* 77 (1996) 3865–3868, <https://doi.org/10.1103/PhysRevLett.77.3865>.
- [39] W.J. Hehre, K. Ditchfield, J.A. Pople, Self-consistent molecular orbital methods. XII. Further extensions of Gaussian-type basis sets for use in molecular orbital studies of organic molecules, *J. Chem. Phys.* 56 (1972) 2257–2261, <https://doi.org/10.1063/1.1677527>.
- [40] B. Delley, From molecules to solids with the DMol3 approach, *J. Chem. Phys.* 113 (2000) 7756–7764, <https://doi.org/10.1063/1.1316015>.
- [41] A.K. Rappé, C.J. Casewit, K.S. Colwell, W.A. Goddard, W.M. Skiff, UFF, a full periodic table force field for molecular mechanics and molecular dynamics simulations, *J. Am. Chem. Soc.* 114 (1992) 10024–10035, <https://doi.org/10.1021/ja00051a040>.
- [42] S.L. Mayo, B.D. Olafson, W.A. Goddard, DREIDING: a generic force field for molecular simulations, *J. Phys. Chem.* 94 (1990) 8897–8909, <https://doi.org/10.1021/j100389a010>.
- [43] N. Sokkalingam, G. Kamath, M. Coscione, J.J. Potoff, Extension of the transferable potentials for phase equilibria force field to dimethylmethyl phosphonate, sarin, and soman, *J. Phys. Chem. B* 113 (2009) 10292–10297, <https://doi.org/10.1021/jp903110e>.
- [44] A. Vishnyakov, G.Y. Gor, M.T. Lee, A.V. Neimark, Molecular modeling of organophosphorus agents and their aqueous solutions, *J. Phys. Chem. A* 115 (2011) 5201–5209, <https://doi.org/10.1021/jp200509u>.
- [45] T.J.H. Vlugt, E. García-Pérez, D. Dubeldam, S. Ban, S. Calero, Computing the heat of adsorption using molecular simulations: the effect of strong coulombic

- interactions, *J. Chem. Theor. Comput.* 4 (2008) 1107–1118, <https://doi.org/10.1021/ct700342k>.
- [46] G. Henkelman, A. Arnaldsson, H. Jónsson, A fast and robust algorithm for Bader decomposition of charge density, *Comput. Mater. Sci.* 36 (2006) 354–360, <https://doi.org/10.1016/j.commatsci.2005.04.010>.
- [47] P. Giannozzi, S. Baroni, N. Bonini, M. Calandra, R. Car, C. Cavazzoni, D. Ceresoli, G.L. Chiarotti, M. Cococcioni, I. Dabo, A. Dal Corso, S. De Gironcoli, S. Fabris, G. Fratesi, R. Gebauer, U. Gerstmann, C. Gougoussis, A. Kokalj, M. Lazzeri, L. Martin-Samos, N. Marzari, F. Mauri, R. Mazzarello, S. Paolini, A. Pasquarello, L. Paulatto, C. Sbraccia, S. Scandolo, G. Sclauzero, A.P. Seitsonen, A. Smogunov, P. Umari, R.M. Wentzcovitch, QUANTUM ESPRESSO: a modular and open-source software project for quantum simulations of materials, *J. Phys. Condens. Matter* 21 (2009), <https://doi.org/10.1088/0953-8984/21/39/395502>.
- [48] P. K. Hohenberg, Inhomogeneous electron gas, *Phys. Rev. B* 136 (1964) B864–B871, <https://doi.org/10.1103/PhysRevB.7.1912>.
- [49] W. Kohn, L.J. Sham, Self-consistent equations including exchange and correlation effects, *Phys. Rev.* 140 (1965), <https://doi.org/10.1103/PhysRev.140.A1133>.
- [50] G. Makov, M.C. Payne, Periodic boundary conditions in ab initio calculations, *Phys. Rev. B* 51 (1995) 4014–4022, <https://doi.org/10.1103/PhysRevB.51.4014>.
- [51] J.P. Perdew, Y. Wang, Accurate and simple analytic representation of the electron-gas correlation energy, *Phys. Rev. B* 45 (1992) 13244–13249, <https://doi.org/10.1103/PhysRevB.45.13244>.
- [52] D. Vanderbilt, Soft self-consistent pseudopotentials in a generalized eigenvalue formalism, *Phys. Rev. B* 41 (1990) 7892–7895, <https://doi.org/10.1103/PhysRevB.41.7892>.
- [53] P. Kowalczyk, P.A. Gauden, A.P. Terzyk, A.V. Neimark, Screening of carbonaceous nanoporous materials for capture of nerve agents, *Phys. Chem. Chem. Phys.* 15 (2013) 291–298, <https://doi.org/10.1039/C2CP43366D>.
- [54] Office of Research and Development National Homeland Security Research, Adsorption and Desorption of Chemical Warfare Agents on Activated Carbon: Impact of Temperature and Relative Humidity Adsorption and Desorption of Chemical Warfare Agents on Activated Carbon: Impact of Temperature and Relative Humidity, (2014).
- [55] M. Agrawal, D.F. Sava Gallis, J.A. Greathouse, D.S. Sholl, How useful are common simulants of chemical warfare agents at predicting adsorption behavior? *J. Phys. Chem. C* 122 (2018) 26061–26069, <https://doi.org/10.1021/acs.jpcc.8b08856>.

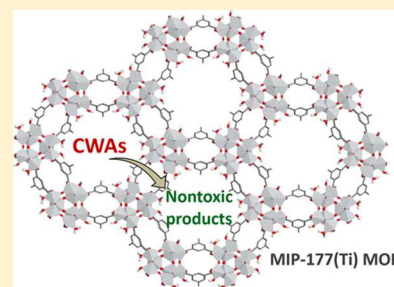
Computational Exploration of the Catalytic Degradation of Sarin and Its Simulants by a Titanium Metal–Organic Framework

C. Vieira Soares,^{†,‡} G. Maurin,^{*,†} and A. A. Leitão[‡]

[†]Institut Charles Gerhardt Montpellier, UMR-5253, Université de Montpellier, ENSCM, Place E. Bataillon, Montpellier cedex 05 34095, France

[‡]Departamento de Química, Universidade Federal de Juiz de Fora, Juiz de Fora, MG 36036-330, Brazil

ABSTRACT: The catalytic degradation of chemical warfare agents (CWAs) into nontoxic products by metal organic frameworks (MOFs) has been exclusively focused on Zr-based materials so far, although Ti-MOFs might be also of interest owing to the well-known capacity of Ti compounds to efficiently hydrolyze CWAs. Here, we report for the first time a computational exploration of several possible hydrolysis mechanisms on the activated Ti site of a recently discovered highly stable Ti-MOF, MIP-177(Ti), in the presence/absence of water, considering sarin and its simulants dimethyl methylphosphonate and diisopropyl phosphorofluoridate. Density functional theory calculations were performed at the periodic level to accurately assess the main states of the degradation reaction (reactants, transition states, and products) and the associated activation energy barriers for each degradation reaction that are further compared to the corresponding data previously reported for Zr-MOFs. MIP-177(Ti) was demonstrated to be a promising candidate for an efficient degradation of sarin and retention of the resulting products with a level of performance as attractive as that of the best Zr-MOFs reported so far. Furthermore, the simulations performed on the two simulants emphasized that diisopropyl phosphorofluoridate better mimics sarin in terms of the transition states and products obtained during the reaction as well as of the activation energy required to achieve their degradation.



1. INTRODUCTION

Chemical warfare agents (CWAs) containing phosphate ester bonds are highly toxic chemicals, since they are effective inhibitors of acetylcholinesterase, an enzyme that ensures the synaptic transmission in the nervous system.¹ Although the development, production, stockpiling, and use of these hazardous molecules have been prohibited during the chemical weapon convention of 1997, their threat is still a serious risk for humanity. Indeed, the development of materials and/or processes able to identify, capture, and even degrade CWAs remains an active field of research. In this context, the hybrid porous materials, namely, the metal organic frameworks (MOFs),^{2–6} have been recently envisaged as an alternative solution to the standard porous materials (carbons, zeolites, alumina, etc.) for the capture and the catalytic degradation of a broad range of G-type and vesicant agents owing to their unique degree of variability in terms of chemical features, e.g., nature of metal-active sites and organic linkers, as well as shape/size of porosity. Only few papers dealing with the physical adsorption of CWAs in MOFs have been published so far. We can cite the experimental work on the adsorption of blood agent arsine in Cu-BTC,⁷ cyanogen chloride in MOF-74,⁸ tabun and *O*-ethyl-*S*-2[2-(diethylamino)ethyl]-methylphosphonothiate in several IRMOFs,⁹ and dimethyl methylphosphonate (DMMP) in NENU-11,¹⁰ methylphosphonic acid in $Zn_2Ca(CO_2)_6(H_2O)_2$,¹¹ as well as diisopropyl fluorophosphate (DIFP) in lithium alkoxide doped UiO-66¹² and diethyl sulfide in $[Zn_4O(3,5\text{-dimethyl-4-carboxy-pyrazola-$

$to)_3]$.¹³ The most recent studies reported the use of molecular simulations as a predictive tool to anticipate the capture performance of a series of MOFs for diverse CWAs.^{14,15} We recently published a systematic computational evaluation of water-stable MOFs containing Zr or Ti as metal centers by means of grand canonical Monte Carlo simulations coupled with density functional theory (DFT) calculations to assess their adsorption uptakes, the energetics and the preferential adsorption sites for a series of nerve agents including sarin, soman, and their simulants DMMP and DIFP.¹⁶ Conversely, the majority of studies related to the MOF/CWA topic have been devoted to the catalytic degradation of these hazardous chemicals into nontoxic products from an experimental point of view. Several Zr-MOFs were shown to be promising catalysts for CWA hydrolysis owing to the presence of hydroxyl groups bridging two Zr atoms,^{12,17–41} which is reminiscent of the active sites Zn–OH–Zn present in enzymes that are known to allow an efficient degradation of phosphate ester.⁴² Typically, Mondloch et al. were among the first to demonstrate the efficiency of NU-1000 for the degradation of soman and the nerve agent simulant dimethyl 4-nitrophenyl phosphate (DMNP).⁴³ MOF-808 was further shown as a promising candidate for the hydrolysis of DMNP⁴⁴ with performances even better than those exhibited by other Zr-

Received: June 19, 2019

Revised: July 14, 2019

Published: July 15, 2019

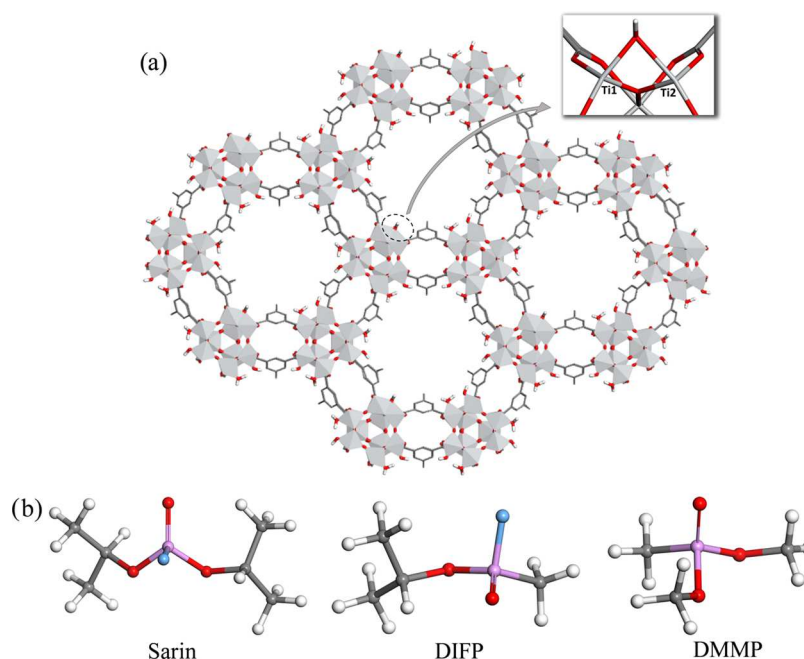


Figure 1. (a) Illustration of the crystal structure of MIP-177(Ti). The creation of the Ti open site through dehydration leads to a hydroxyl group coordinated in a bidentate manner to the Ti1 and Ti2. (b) Illustration of the CWAs molecules: (a) sarin, (b) DIFP, and (c) DMMP, respectively. Color scheme: Ti, gray polyhedron; C, gray; O, red; and H, white; P, pink and F, blue.

MOFs including UiO-66,³² UiO-66-NH₂,^{45,46} and NU-1000.^{43,47} Later, Plonka et al.²¹ and Sharp et al.³⁴ revealed that the catalytic conversion of DMMP is inhibited due to the strong bonds formed between the degraded products and the MOF frameworks.^{21,34} This observation motivated further investigations with the consideration of refined MOFs containing either functionalized linkers⁴⁸ or based on different metal centers (rare earth, Ce)^{49,50} for the degradation of various nerve agents including DMNP, soman, DIFP, and diethyl chlorophosphate. The literature is much less exhaustive in terms of computational studies related to the catalytic degradation of CWAs and their simulants using MOFs. Typically, Troya et al.⁵¹ carried out DFT calculations at the cluster level using localized basis sets to explore the hydrolysis degradation mechanism of sarin by UiO-66 and MOF-808. Wang et al.²¹ and Chen et al.⁵² followed the same computational strategy to investigate the decomposition of DMMP and DMNP by UiO-67 and NU-1000, respectively. Extended and truncated cluster models to represent the Zr-defective structure of $[\text{Zr}_{12}(\mu_3\text{-O})_8(\mu_3\text{-OH})_8(\mu_2\text{-OH})_6(\text{TPDC})_{18}]$ were further used by Momeni et al.²⁵ to model the hydrolysis of sarin in aqueous solution. Extended clusters were equally considered by Momeni et al.⁵³ to model the hydrolysis of sarin by Zr-based MOFs, MOF-808, NU-1000, and defective UiO-66. Recently, Harvey et al.⁵⁴ emphasized the importance of using periodic DFT calculations to more accurately capture the reactivity of organophosphorus compounds confined in the pores of MOFs. Typically, these authors mentioned that the consideration of a Zr formate cluster leads to an overestimation of the binding energy for DIFP and sarin compared to the scenario encountered with the use of a periodic system. This trend was explained by the lowering of the strength of interactions between the bulky isopropyl groups of the CWA and the active sites at the periodic level due to the steric hindrance induced by the MOF framework.

It is to be noted that these computational and experimental works have been almost exclusively focused on Zr-MOFs, although other highly valent stable MOFs, in particular Ti-MOFs, might be also of interest for the catalytic degradation of CWAs. Indeed, the use of titanium oxides as catalysts for the degradation of toxic industrial compounds is well documented.⁵⁵ Nanotubular titania were demonstrated to be attractive for the catalytic degradation of a series of CWAs including sarin, soman, sulfur mustard, and VX.^{26,56,57} Furthermore, recent works reported the incorporation of Ti compounds such as Ti(OH)₄, TiO₂, and TiCl₄ into MOFs to enhance the efficiency of the hydrolysis of CWA.^{26,56,58,59} All together, this experimental observation encouraged us to envisage for the first time a Ti-MOF as a potential candidate for the degradation of sarin and its simulants DMMP and DIFP. We selected the carboxylate Ti-MOF labeled as MIP-177(Ti) (Figure 1) in its low-temperature and formate free form (MIP stands for the Materials of the Institute of Porous Materials of Paris)⁶⁰ owing to its favorable 1D-type channel large enough (11 Å) to accommodate the CWA molecules; its attractive predicted performances in terms of adsorption uptakes and energetics¹⁶ for a series of CWAs including soman, sarin, DMMP, and DIFP; high chemical stability; and optimal chemical environment that incorporates free Ti-metal sites on its formate-free version able to act as active sites for catalysis.

Here, DFT calculations were performed at the periodic level to accurately assess the CWA catalytic degradation performances of this Ti-MOF. Compared to the cluster approach, the consideration of periodic boundary conditions presents several advantages including the absence of inductive effects created by the groups that saturate the terminal dangling bonds, an appropriate dielectric environment, no basis set superposition error, and Pule forces with the use of plane waves. Several possible hydrolysis mechanisms on the activated Ti site in the presence/absence of water were considered for sarin and its

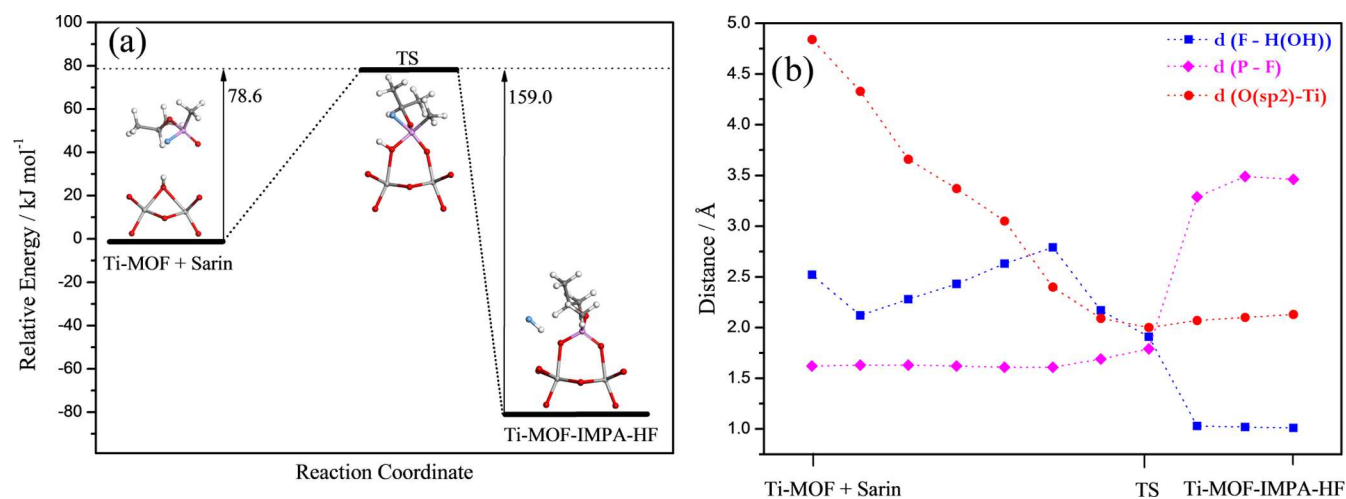


Figure 2. (a) Simulated minimum-energy path corresponding to the degradation mechanism of sarin on the activated Ti site. (b) Evolution of the main characteristic distances involving the atoms of sarin (F, P, and O(sp²)) and of Ti-MOF (Ti, H(OH)) along the reaction coordinate.

simulants DMMP and DIFP (see Figure 1b), with the aim to carefully characterize the main states of the degradation reaction (reactants, transition state (TS), and products), the minimum-energy reaction path, and the resulting activation energy barriers required to initiate the catalytic degradation and hence the most probable reaction pathway. These whole set of data are further compared with the corresponding data reported in the literature for the whole series of Zr-MOFs^{21,25,51–54} to assess the promises of MIP-177(Ti) as a CWA catalyst.

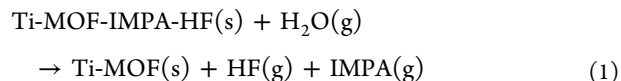
2. COMPUTATIONAL METHODS

The DFT calculations were performed using the Quantum-Espresso package^{61,62} with the consideration of pseudopotentials to describe the ion cores and plane wave basis sets,⁶³ as well as periodic boundary conditions. We adopted the generalized gradient approximation GGA-PBE for the exchange-correlation functional⁶⁴ and the Vanderbilt ultrasoft pseudopotentials⁶⁵ to describe the ion cores of Ti, P, C, O, H, and F atoms. The energy cutoff for the plane wave basis set was fixed at 50 Ry (400 eV), and the electron density was obtained at the Γ point in the first Brillouin zone.⁶⁶ The atomic positions and cell parameters of the low-temperature version of MIP-177(Ti) were taken from a previously reported study.⁶⁰ The structure was considered in its formate-free form, the corresponding linkers connecting two Ti sites being replaced by one terminal –OH and –H₂O, respectively. Among all the Ti pairs, we considered the creation of one activated Ti site by removing its bound –H₂O molecule, while the neighboring Ti keeps its –OH group. The corresponding structure model was fully DFT-geometry-optimized (both cell parameters and atomic positions relaxed) until all force components were smaller than 0.001 Ry Bohr⁻¹ and the convergence criterion of 10⁻⁴ Ry was reached for the total energy. The equilibrium nuclei positions of all structures were found by minimizing the total energy gradient. The DFT-geometry optimization of the empty MIP-177(Ti) converged toward a structure characterized by the formation of a bridging –OH group bounded to two neighbor Ti sites as illustrated in the inset of Figure 1.

Starting with this DFT-optimized empty MIP-177(Ti) structure, we introduced individually 1 molecule of sarin and its simulants in the hexagonal pore by means of Monte Carlo simulations performed in the canonical ensemble following the

same methodology (force-field parameters, charges, number of MC steps) detailed elsewhere.¹⁶ The resulting guest-loaded structures were further optimized at the DFT-level. Minimum energy paths (MEPs) for the different envisaged catalytic degradation mechanisms were further computed to identify the transition state and products, evaluate the corresponding reaction barrier, and characterize the main structural modifications along the reaction. The calculation of the MEPs connecting different minimum-energy geometries employed the climbing image nudged elastic band (CI-NEB) method.⁶⁷ The geometries of eleven images used to compute each MEP were optimized to establish the minimum-energy path on the potential surface of the system until the energy variation was below 0.05 eV Å⁻¹. The convergence criterion was satisfied when all components of the forces were smaller than 10⁻⁴ Ry Bohr⁻¹.

Finally, the energy involved in the process of desorption of isopropyl methyl phosphonic acid (IMPA) and hydrofluoric acid through the adsorption of one water molecule in MIP-177(Ti) was calculated according to the reaction as schematized by eq 1.



3. RESULTS AND DISCUSSION

3.1. Degradation of Sarin on the Activated Ti Site.

The first investigated mechanism corresponds to the nucleophilic addition of the –OH function, initially bridging two neighboring Ti sites, to the phosphorus atom of sarin. This activates the phosphate ester function and further leads to the formation of a phosphonate product and the release of hydrogen fluoride.⁵¹ The simulated MEP of the corresponding reaction is reported in Figure 2a with the identification of the initial reactant, the transition state (TS), and the resulting product.

Figure 3a illustrates the most stable DFT-optimized configuration of sarin initially adsorbed in the pore of the Ti-MOF corresponding to the reactant. Sarin adopts a preferential conformation in such a way than its fluorine atom interacts with the bridging –OH group of MIP-177 with a separating F–H(OH) distance of 2.52 Å. During the first

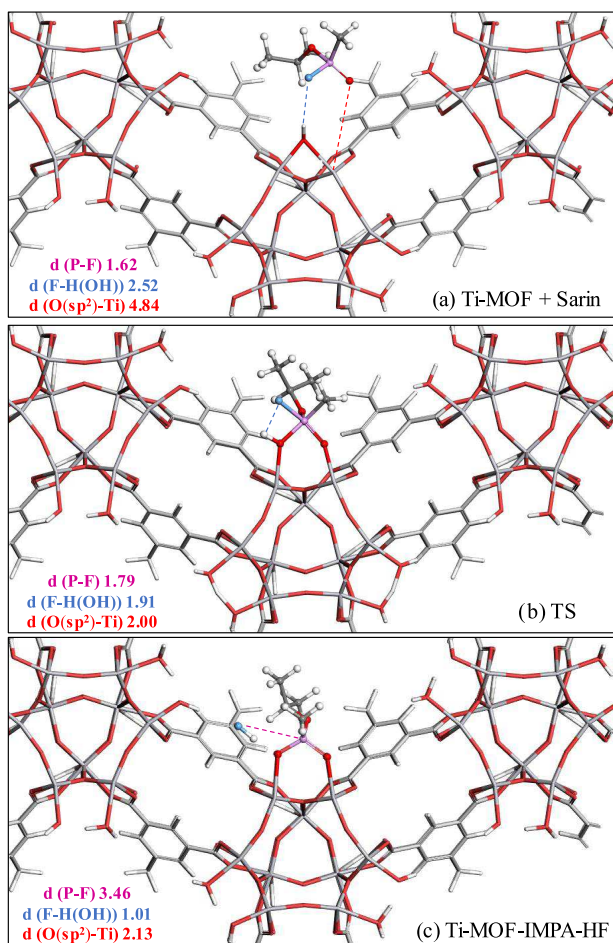


Figure 3. Illustration of the degradation mechanism of sarin on the activated Ti site of MIP-177(Ti). (a) Reactant (Ti-MOF + sarin), (b) transition state (TS), and (c) product (Ti-MOF-IMP-A-HF). The main distances involved in the degradation process, P–F (pink), F–H(OH) (blue), and O(sp²)–Ti (red), are represented and expressed in Å.

step of the reaction, this bridging –OH group moves away from one titanium site, creating extra space for the toxic

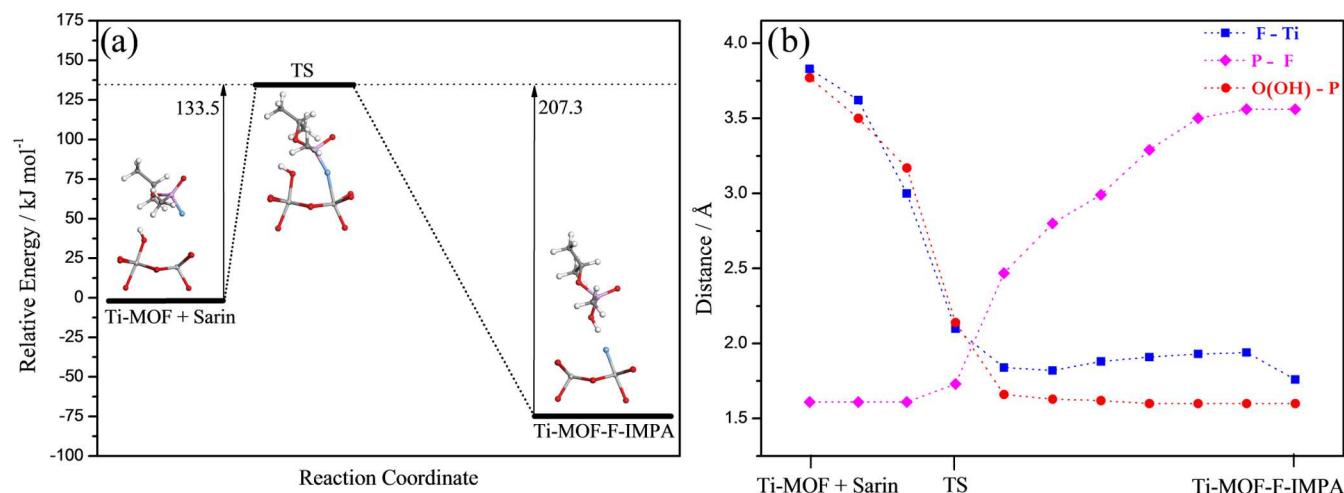


Figure 4. (a) Simulated minimum-energy path corresponding to the degradation mechanism where the activated Ti site binds to the fluorine atom of sarin. (b) Evolution of the main characteristic distances involving the atoms of sarin (F, P) and Ti-MOF (Ti, O(OH)) along the reaction coordinate.

molecule to access the activated Ti site; consequently, the distance between the O(sp²) atom of sarin (the oxygen atom bound to the phosphorus atom) and this titanium atom becomes shorter (see red line in Figure 2b). As the reaction proceeds through the transition state, there is a bond formation between the O(sp²) atom of sarin and the Ti site, and this leads to a 5-coordinated geometry of sarin as evidenced in Figure 3b. Beyond TS, we can observe a progressive increase of the distance separating the phosphorus and fluorine atoms of sarin (Figure 2b), which finally results in the breaking of the corresponding bond and consequently the formation of the HF bond. This gives rise to a stable configuration for the product where the organophosphorus fragment, namely, the isopropyl methyl phosphonic acid (IMP-A), is coordinated in a bidentate manner to the inorganic node of the Ti-MOF (Figure 3c).

The MEP reported in Figure 2a implies an activation energy barrier of 78.6 kJ mol⁻¹. This range of value is similar to the free energy previously reported⁵³ for the hydrolysis of sarin in diverse Zr-MOFs including MOF-808 (79.1 kJ mol⁻¹), NU-1000 (75.3 kJ mol⁻¹), and UiO-66 (71.5 kJ mol⁻¹). This observation suggests that this Ti-MOF is expected to perform as good as the best Zr-MOFs explored so far for the catalytic degradation of sarin. We can also note that the product represents the most stable configuration along the whole reaction path (–80.5 kJ mol⁻¹). This indicates that the coordination of IMP-A to the inorganic node of the MIP-177(Ti) leads to the formation of a stable complex. Finally, the desorption energy of IMP-A and HF from the product calculated by using eq 1 is predicted to be relatively high, i.e., 131.6 kJ mol⁻¹. This observation emphasizes that MIP-177(Ti) not only allows the degradation of sarin but also a strong retention of the resulting IMP-A product into their pores.

We further examined a second degradation mechanism corresponding to a scenario where the activated Ti site binds to the fluorine atom of sarin, leading to the formation of deactivated IMP-A molecule (Figure 4a). To do so, the molecule was initially slightly tilted from its most stable configuration reported in Figure 3a in such a way to favor an interaction between its F atom and the inorganic node of MIP-

177(Ti). A further DFT geometry optimization led to a local minimum energy where the OH group does not anymore bridge the two Ti neighbors, allowing the F atom of sarin to face the activated Ti site (Figure 5a). The reaction path leads

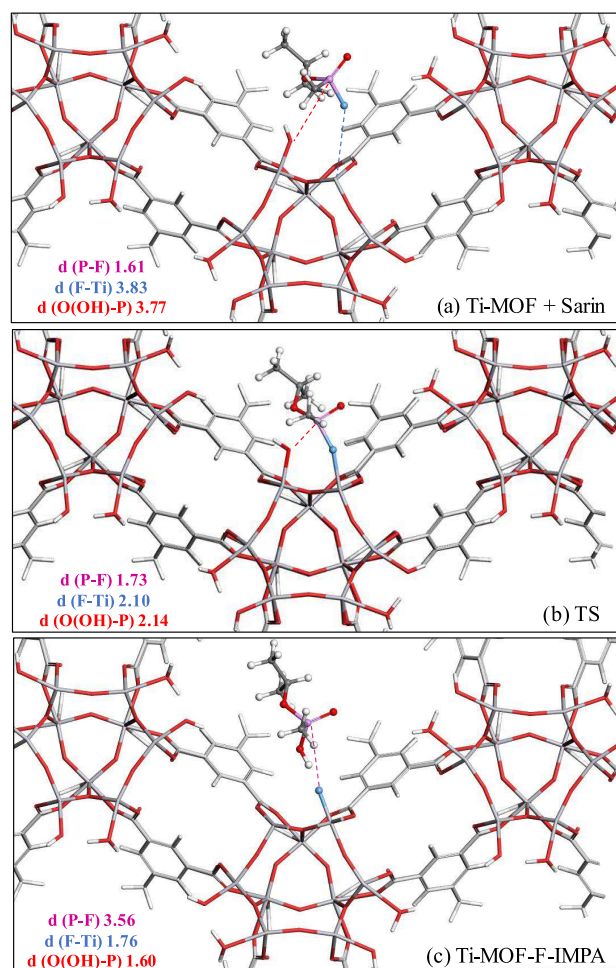


Figure 5. Illustration of the degradation mechanism of sarin on the activated Ti site of MIP-177(Ti), where the activated Ti site binds to the fluorine atom of sarin. (a) Reactant (Ti-MOF + sarin), (b) transition state (TS), and (c) product (Ti-MOF-F-IMPA). The main distances involved in the degradation process, P–F (pink), F–Ti (blue), and O(OH)–P (red), are represented and expressed in Å.

to a transition state involving the coordination of the –F atom toward the activated Ti site, while the phosphorous atom of sarin interacts with the oxygen atom of the –OH group (Figures 4b and 5b). Finally, the product (Ti-MOF-F-IMPA) implies the formation of a bond between the F atom and the activated Ti site, while the OH group of the Ti-MOF is transferred to the molecule via the formation of a P–OH bond (Figures 4b and 5c).

The MEP reported in Figure 4a implies an activation energy barrier of 133.5 kJ mol⁻¹, which is much higher compared to the value obtained for the first mechanism (Figure 2a; 78.6 kJ mol⁻¹). This clearly reveals that the degradation of sarin through the coordination of F atom toward the activated Ti site is much less probable, consistent with the previous findings reported in the case of Zr-MOFs.^{51,54,68}

3.2. Degradation of the Simulants of Sarin on the Activated Ti Site. We further explored the degradation mechanism of DMMP and DIFP involving the formation of

CH₃OH and HF, respectively, since it was shown to be the most probable mechanism in the case of sarin (Figures 2 and 3). Indeed, the two molecules were first individually loaded in MIP-177(Ti) using preliminary Monte Carlo simulations,¹⁶ and the resulting geometries were further optimized at the DFT level.

The corresponding minimum-energy paths for the catalytic degradation mechanism of DIFP and DMMP are plotted in Figure 6a,b, respectively. Regarding DIFP, the TS and products formed during the reaction are very similar than that evidenced for sarin, which, in this case, is the formation of the deactivated diisopropyl hydrogen phosphate (DHFP) molecule (Figure 7). This observation is consistent with an energy barrier associated with the degradation mechanism of DIFP (67.2 kJ mol⁻¹) (Figure 6a), which is relatively similar to the value calculated for sarin (78.6 kJ mol⁻¹) (Figure 4a).

When one switches to DMMP, Figure 8a first evidences that the initial configuration implies an interaction between its –OCH₃ function and the bridging –OH group of MIP-177(Ti) at a longer distance compared to the scenario implying the interactions between the F atom of both sarin and DIFP with the same group of the MOF. The transition state shows that the P–OCH₃ bond becomes collinear to the P–OH bond, and the nucleophilic addition of the bridging –OH group to the DMMP molecule results in the cleavage of the P–OCH₃ bond, leading to the formation of methanol and the deactivated dimethyl hydrogen phosphate (DMHP) molecule, as can be illustrated in Figure 8b,c.

The resulting activation energy barrier for the degradation of DMMP (115.2 kJ mol⁻¹) (Figure 6b) is significantly higher than the value calculated for sarin (78.6 kJ mol⁻¹). This trend that can be associated to the subsequent elimination of methanol instead of HF is consistent with what has been reported previously for UiO-67 by Troya et al.⁵¹ and Wang et al.²¹ for the degradation of sarin and DMMP, respectively. Interestingly, this calculation performed on the two simulants emphasizes that DIFP better mimics sarin in terms of the TS and products obtained during the reaction as well as of the activation energy required to achieve their degradation.

3.3. Degradation of Sarin on the Activated Ti Site in the Presence of Water. Since the catalyst is expected to operate under atmospheric condition, e.g., potentially under a given relative humidity, we also investigated the degradation mechanism of sarin in the presence of water confined in the pore of MIP-177(Ti). Starting with the configuration reported in Figure 2a corresponding to the most stable arrangement of sarin in MIP-177(Ti), the incorporation of 1 extra water molecule was considered by testing different initial positions. These resulting water-loaded configurations were further DFT-geometry-optimized and the two most stable ones reported in Figures 9a and 10a were subsequently selected for further exploration of the degradation mechanism.

Figure 9 illustrates the degradation mechanism of sarin starting with the first optimized configuration, where sarin forms a strong hydrogen bond with the –OH group of the MOF H(OH)–O(sp²) (1.75 Å, black dashed line). The degradation mechanism, similar to that already reported by Troya et al.⁵¹ for Zr-MOFs, then proceeds via a nucleophilic attack of water molecule on the P atom of sarin, resulting in a penta-coordination geometry where fluorine forms a hydrogen bond with the H atom of water (see transition state in Figure 9b). Water further dissociates and its proton migrates to the F-

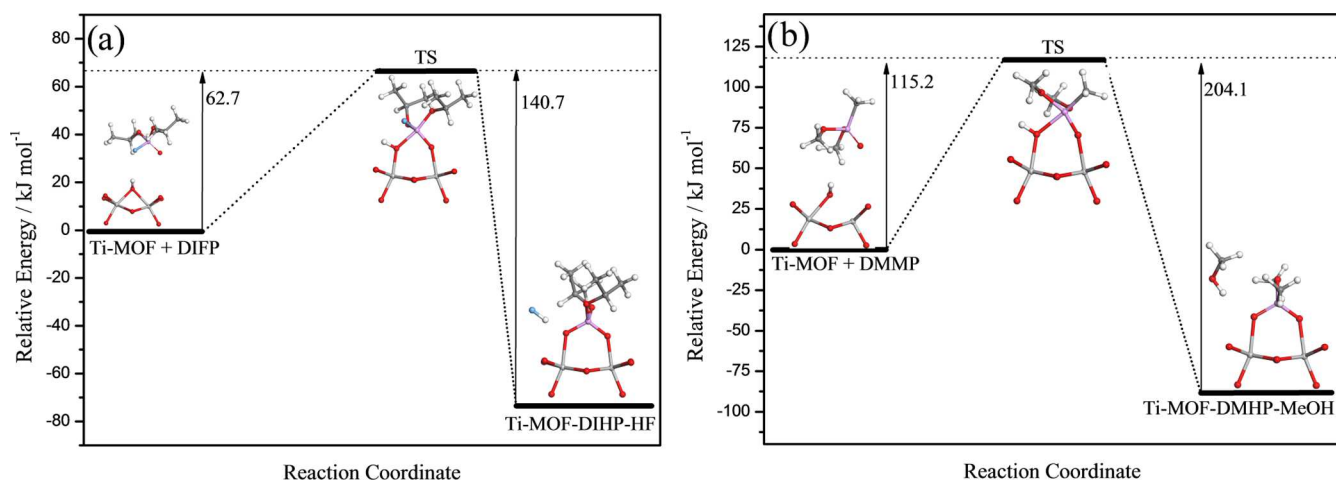


Figure 6. Simulated minimum-energy paths corresponding to the degradation mechanism of (a) DIFP and (b) DMMP on the activated Ti site.

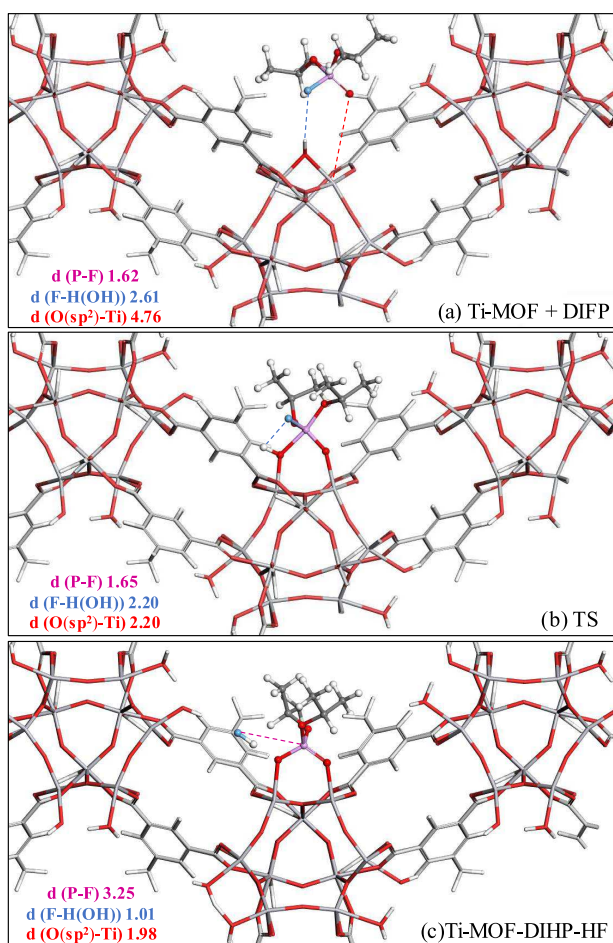


Figure 7. Illustration of the degradation mechanism of DIFP on the activated Ti site of MIP-177(Ti). (a) Reactant (Ti-MOF + DIFP), (b) transition state (TS), and (c) product (Ti-MOF-DIHP-HF). The main distances involved in the degradation process, P–F (pink), F–H(OH) (blue), and O(sp²)–Ti (red), are represented and expressed in Å.

atom, leading to the formation of HF and IMPA, as reported in Figure 9c.

In the second case, the water molecule interacts with both sarin and the –OH group of the MOF to form relatively strong H(H₂O)–O(sp²) (1.73 Å, black dashed line) and H(H₂O)–

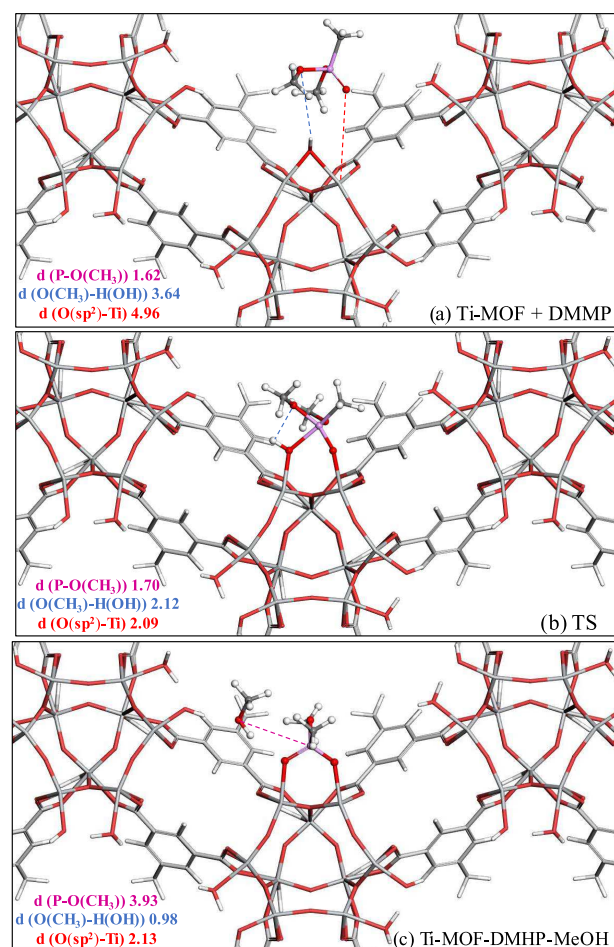


Figure 8. Illustration of the degradation mechanism of DMMP on the activated Ti site of MIP-177(Ti). (a) Reactant (Ti-MOF + DMMP), (b) transition state (TS), and (c) product (Ti-MOF-DMHP-MeOH). The main distances involved in the degradation process, P–O(CH₃) (pink), O(CH₃)–H(OH) (blue), and O(sp²)–Ti (red), are represented and expressed in Å.

O(OH) (1.69 Å, black dashed line) hydrogen bonds (see Figure 10a). Such an interaction makes the –OH group bonded to only 1 Ti site. The degradation mechanism involves the dissociation of water with one proton transferred to the O(sp²) atom of sarin, the resulting OH[–] anion remaining in

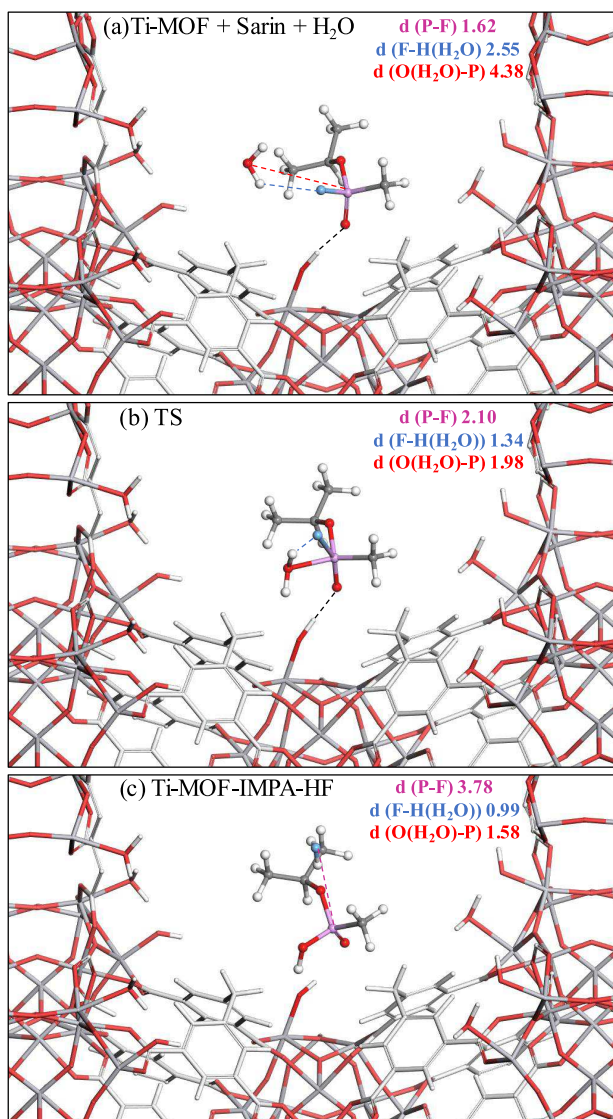


Figure 9. Illustration of the degradation mechanism of sarin on the activated Ti site of MIP-177(Ti) in the presence of water where sarin interacts predominantly with the MOF framework. (a) Reactant (Ti-MOF + sarin + H₂O), (b) transition state (TS), and (c) product (Ti-MOF-IMPA-HF). The main distances involved in the degradation process, P–F (pink), F–H(H₂O) (blue), and O(H₂O)–P (red) are represented and expressed in Å. The black dashed lines indicate the interaction between the molecules (water and IMPA) and the framework.

strong hydrogen bond interactions with the –OH group of MIP-177(Ti) (1.71 Å, black dashed line) and with the P–OH group (1.44 Å, black dashed line), as it can be observed in the transition state reported in Figure 10b. Finally, the oxygen atom of the OH[−] anion coordinates with the P atom of sarin, while its proton participates concertedly to the degradation of the toxic molecule into IMPA and the subsequent release of HF as reported in Figure 10c.

Figure 11 reports the corresponding minimum-energy paths for the reaction in the presence of water started with the two different arrangements of water described in Figures 9a and 10a. The associated energy barriers of 169.6 and 146.5 kJ mol^{−1}, respectively, are significantly higher than the value obtained in the absence of water (see Figure 3a). This observation emphasizes that the degradation performance of

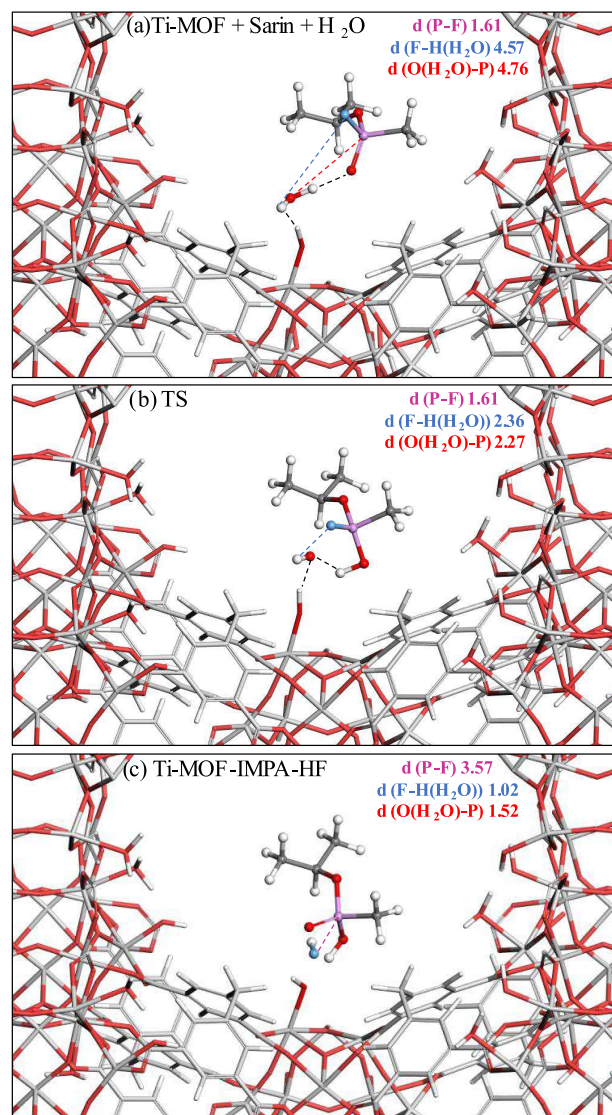


Figure 10. Illustration of the degradation mechanism of sarin on the activated Ti site of MIP-177(Ti) in the presence of water, where water interacts with both sarin and MOF framework. (a) Reactant (Ti-MOF + sarin + H₂O), (b) transition state (TS), and (c) product (Ti-MOF-IMPA-HF). The main distances involved in the degradation process, P–F (pink), F–H(H₂O) (blue), and O(H₂O)–P (red) are represented and expressed in Å. The black dashed lines indicate the interaction between the molecules (water and IMPA) and the framework.

MIP-177(Ti) is expected to be less attractive under humid conditions.

4. CONCLUSIONS

Our periodic DFT calculations explored for the first time the ability of a Ti-MOF, namely, the MIP-177(Ti) for the catalytic degradation of sarin. These simulations demonstrated the attractiveness of MIP-177(Ti) in terms of the level of performance similar than that of the best Zr-MOFs explored so far. The degradation mechanism proceeds with a coordination of sarin toward the activated Ti site via its oxygen atom, leading to the formation of isopropyl methyl phosphonic acid (IMPA) coordinated in a bidentate manner to the inorganic node of the Ti-MOF and the release of HF. The resulting product was shown to be highly stable and associated

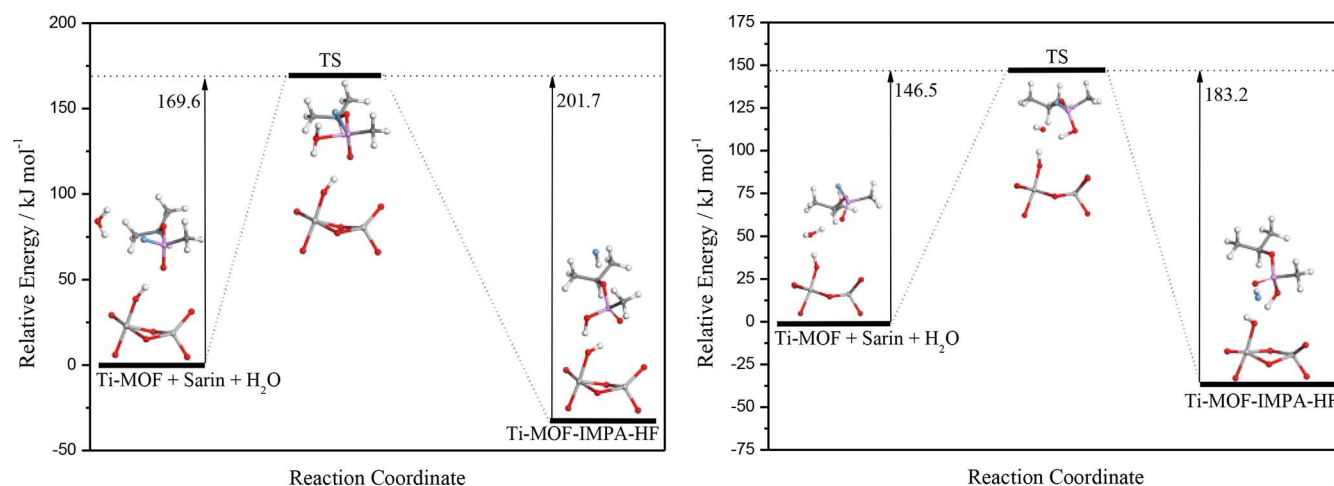


Figure 11. Simulated minimum-energy paths corresponding to the degradation mechanism of sarin on the activated Ti site in the presence of water for the two scenarios (Figure 9, sarin interacting predominantly with only MOF framework (left); and Figure 10, water interacting with both sarin and MOF framework (right)).

with the high energy required to desorb the so-formed IMPAA. This observation emphasizes that MIP-177(Ti) is able to strongly retain the IMPAA molecule once fixed to the Ti site. Finally, the exploration of the same degradation mechanism for two standard simulants of sarin revealed that DIFP reproduces a much better catalytic behavior of sarin than DMMP in terms of not only degradation mechanisms but also activation energy required to proceed to the corresponding reaction. This conclusion is of importance for the future experimental exploration that should proceed with the most reliable simulants to further extrapolate the behavior of the real toxic molecules.

AUTHOR INFORMATION

Corresponding Author

*E-mail: guillaume.maurin1@umontpellier.fr.

ORCID

G. Maurin: 0000-0002-2096-0450

Author Contributions

The manuscript was written through the contribution of all the three authors.

Notes

The authors declare no competing financial interest.

ACKNOWLEDGMENTS

The research leading to these results has received funding from a bilateral project COFECUB-CAPES 778-13.

REFERENCES

- Schwenk, M. Chemical Warfare Agents. Classes and Targets. *Toxicol. Lett.* **2018**, *293*, 253–263.
- Maurin, G.; Serre, C.; Cooper, A.; Férey, G. The New Age of MOFs and of Their Porous-Related Solids. *Chem. Soc. Rev.* **2017**, *46*, 3104–3107.
- Mitsuru, K.; Tomomichi, Y.; Hiroyuki, M.; Susumu, K.; Kenji, S. Three-Dimensional Framework with Channeling Cavities for Small Molecules: $\{[M_2(4, 4'-Bpy)_3(NO_3)_4] \cdot xH_2O\}_n$ ($M = Co, Ni, Zn$). *Angew. Chem., Int. Ed.* **2003**, *36*, 1725–1727.
- Yaghi, O. M.; Li, H. Hydrothermal Synthesis of a Metal-Organic Framework Containing Large Rectangular Channels. *J. Am. Chem. Soc.* **1995**, *117*, 10401–10402.
- Hoskins, B. F.; Robson, R. Infinite Polymeric Frameworks Consisting of Three Dimensionally Linked Rod-like Segments. *J. Am. Chem. Soc.* **1989**, *111*, 5962–5964.
- Férey, G. Hybrid Porous Solids: Past, Present, Future. *Chem. Soc. Rev.* **2008**, *37*, 191–214.
- Peterson, G. W.; Britt, D. K.; Sun, D. T.; Mahle, J. J.; Browe, M.; Demasky, T.; Smith, S.; Jenkins, A.; Rossin, J. A. Multifunctional Purification and Sensing of Toxic Hydride Gases by CuBTC Metal-Organic Framework. *Ind. Eng. Chem. Res.* **2015**, *54*, 3626–3633.
- Grant Glover, T.; Peterson, G. W.; Schindler, B. J.; Britt, D.; Yaghi, O. MOF-74 Building Unit Has a Direct Impact on Toxic Gas Adsorption. *Chem. Eng. Sci.* **2011**, *66*, 163–170.
- Lee, J.-H.; Houk, R. T. J.; Robinson, A.; Greathouse, J. A.; Thornberg, S. M.; Allendorf, M. D.; Hesketh, P. J. Investigation of Microcantilever Array with Ordered Nanoporous Coatings for Selective Chemical Detection. *Proc. SPIE, Micro Nanotechnol. Sens. Syst. Appl. II* **2010**, *7679*, No. 767927.
- Ni, Z.; Jerrell, J. P.; Cadwallader, K. R.; Masel, R. I. Metal-Organic Frameworks as Adsorbents for Trapping and Preconcentration of Organic Phosohonates. *Anal. Chem.* **2007**, *79*, 1290–1293.
- Zou, R.; Zhong, R.; Han, S.; Xu, H.; Burrell, A. K.; Henson, N.; Cape, J. L.; Hickmott, D. D.; Timofeeva, T. V.; Larson, T. E.; et al. A Porous Metal-Organic Replica of α -PbO₂ for Capture of Nerve Agent Surrogate. *J. Am. Chem. Soc.* **2010**, *132*, 17996–17999.
- López-Maya, E.; Montoro, C.; Rodríguez-Albelo, L. M.; Aznar Cervantes, S. D.; Lozano-Pérez, A. A.; Cenís, J. L.; Barea, E.; Navarro, J. A. R. Textile/Metal-Organic-Framework Composites as Self-Detoxifying Filters for Chemical-Warfare Agents. *Angew. Chem., Int. Ed.* **2015**, *54*, 6790–6794.
- Montoro, C.; Linares, F.; Quartapelle Procopio, E.; Senkovska, I.; Kaskel, S.; Galli, S.; Masciocchi, N.; Barea, E.; Navarro, J. A. R. Capture of Nerve Agents and Mustard Gas Analogues by Hydrophobic Robust MOF-5 Type Metal-Organic Frameworks. *J. Am. Chem. Soc.* **2011**, *133*, 11888–11891.
- Agrawal, M.; Sava Gallis, D. F.; Greathouse, J. A.; Sholl, D. S. How Useful Are Common Simulants of Chemical Warfare Agents at Predicting Adsorption Behavior? *J. Phys. Chem. C* **2018**, *122*, 26061–26069.
- Matito-Martos, I.; Moghadam, P. Z.; Li, A.; Colombo, V.; Navarro, J. A. R.; Calero, S.; Fairen-Jimenez, D. Discovery of an Optimal Porous Crystalline Material for the Capture of Chemical Warfare Agents. *Chem. Mater.* **2018**, *30*, 4571–4579.
- Soares, C. V.; Leitão, A. A.; Maurin, G. Computational Evaluation of the Chemical Warfare Agents Capture Performances of Robust MOFs. *Microporous Mesoporous Mater.* **2019**, *280*, 97–104.

- (17) Nath, I.; Chakraborty, J.; Verpoort, F. Metal Organic Frameworks Mimicking Natural Enzymes: A Structural and Functional Analogy. *Chem. Soc. Rev.* **2016**, *45*, 4127–4170.
- (18) Peterson, G. W.; Lu, A. X.; Epps, T. H. Tuning the Morphology and Activity of Electrospun Polystyrene/Uio-66-NH₂ Metal-Organic Framework Composites to Enhance Chemical Warfare Agent Removal. *ACS Appl. Mater. Interfaces* **2017**, *9*, 32248–32254.
- (19) Asha, P.; Sinha, M.; Mandal, S.; Thomas, F.; Derory, A.; Bernhardt, P.; Legaré, P.; Pourroy, G.; Al-Juaid, S. S.; Hupp, J. T.; et al. Effective Removal of Chemical Warfare Agent Simulants Using Water Stable Metal–organic Frameworks: Mechanistic Study and Structure–property Correlation. *RSC Adv.* **2017**, *7*, 6691–6696.
- (20) Bobbitt, N. S.; Mendonca, M. L.; Howarth, A. J.; Islamoglu, T.; Hupp, J. T.; Farha, O. K.; Snurr, R. Q. Metal–organic Frameworks for the Removal of Toxic Industrial Chemicals and Chemical Warfare Agents. *Chem. Soc. Rev.* **2017**, *46*, 3357–3385.
- (21) Wang, G.; Sharp, C.; Plonka, A. M.; Wang, Q.; Frenkel, A. I.; Guo, W.; Hill, C.; Smith, C.; Kollar, J.; Troya, D.; et al. Mechanism and Kinetics for Reaction of the Chemical Warfare Agent Simulant, DMMP(g), with Zirconium(IV) MOFs: An Ultrahigh-Vacuum and DFT Study. *J. Phys. Chem. C* **2017**, *121*, 11261–11272.
- (22) Nunes, P.; Gomes, A. C.; Pillinger, M.; Gonçalves, I. S.; Abrantes, M. Promotion of Phosphoester Hydrolysis by the Zr^{IV}-Based Metal-Organic Framework UiO-67. *Microporous Mesoporous Mater.* **2015**, *208*, 21–29.
- (23) Ploskonka, A. M.; Decoste, J. B. Tailoring the Adsorption and Reaction Chemistry of the Metal-Organic Frameworks UiO-66, UiO-66-NH₂, and HKUST-1 via the Incorporation of Molecular Guests. *ACS Appl. Mater. Interfaces* **2017**, *9*, 21579–21585.
- (24) Moon, S.; Proussaloglou, E.; Peterson, G. W.; Decoste, J. B.; Hall, M. G.; Howarth, A. J.; Hupp, J. T.; Farha, O. K. Detoxification of Chemical Warfare Agents Using a Zr₆-Based Metal – Organic Framework/Polymer Mixture. *Chem. - Eur. J.* **2016**, *14864*–14868.
- (25) Momeni, M. R.; Cramer, C. J. Structural Characterization of Pristine and Defective [Zr₁₂(μ₃-O)₈(μ₃-OH)₈(μ₂-OH)₆]¹⁸⁺ Double-Node Metal–Organic Framework and Predicted Applications for Single-Site Catalytic Hydrolysis of Sarin. *Chem. Mater.* **2018**, *30*, 4432–4439.
- (26) McCarthy, D. L.; Liu, J.; Dwyer, D. B.; Troiano, J. L.; Boyer, S. M.; DeCoste, J. B.; Bernier, W. E.; Jones, W. E., Jr. Electrospun Metal-Organic Framework Polymer Composites for the Catalytic Degradation of Methyl Paraoxon. *New J. Chem.* **2017**, *41*, 8748–8753.
- (27) Lee, D. T.; Zhao, J.; Peterson, G. W.; Parsons, G. N. Catalytic “MOF-Cloth” Formed via Directed Supramolecular Assembly of UiO-66-NH₂ Crystals on Atomic Layer Deposition-Coated Textiles for Rapid Degradation of Chemical Warfare Agent Simulants. *Chem. Mater.* **2017**, *29*, 4894–4903.
- (28) Li, P.; Moon, S. Y.; Guelta, M. A.; Lin, L.; Gómez-Gualdrón, D. A.; Snurr, R. Q.; Harvey, S. P.; Hupp, J. T.; Farha, O. K. Nanosizing a Metal-Organic Framework Enzyme Carrier for Accelerating Nerve Agent Hydrolysis. *ACS Nano* **2016**, *10*, 9174–9182.
- (29) Jang, Y. J.; Kim, K.; Tsay, O. G.; Atwood, D. A.; Churchill, D. G. Destruction and Detection of Chemical Warfare Agents. *Chem. Rev.* **2015**, *115*, 5345–5403.
- (30) Palomba, J. M.; Credille, C. V.; Kalaj, M.; DeCoste, J. B.; Peterson, G. W.; Tovar, T. M.; Cohen, S. M. High-Throughput Screening of Solid-State Catalysts for Nerve Agent Degradation. *Chem. Commun.* **2018**, 8–11.
- (31) Katz, M. J.; Klet, R. C.; Moon, S.-Y.; Mondloch, J. E.; Hupp, J. T.; Farha, O. K. One Step Backward Is Two Steps Forward: Enhancing the Hydrolysis Rate of UiO-66 by Decreasing [OH⁻]. *ACS Catal.* **2015**, *5*, 4637–4642.
- (32) Katz, M. J.; Mondloch, J. E.; Totten, R. K.; Park, J. K.; Nguyen, S. T.; Farha, O. K.; Hupp, J. T. Simple and Compelling Biomimetic Metal-Organic Framework Catalyst for the Degradation of Nerve Agent Simulants. *Angew. Chem., Int. Ed.* **2014**, *53*, 497–501.
- (33) Park, H. J.; Jang, J. K.; Kim, S. Y.; Ha, J. W.; Moon, D.; Kang, I. N.; Bae, Y. S.; Kim, S.; Hwang, D. H. Synthesis of a Zr-Based Metal-Organic Framework with Spirofluorenetetrazobenzoic Acid for the Effective Removal of Nerve Agent Simulants. *Inorg. Chem.* **2017**, *56*, 12098–12101.
- (34) Plonka, A. M.; Wang, Q.; Gordon, W. O.; Balboa, A.; Troya, D.; Guo, W.; Sharp, C. H.; Senanayake, S. D.; Morris, J. R.; Hill, C. L.; et al. In Situ Probes of Capture and Decomposition of Chemical Warfare Agent Simulants by Zr-Based Metal Organic Frameworks. *J. Am. Chem. Soc.* **2017**, *139*, 599–602.
- (35) De Koning, M. C.; Van Grol, M.; Breijjaert, T. Degradation of Paraoxon and the Chemical Warfare Agents VX, Tabun, and Soman by the Metal-Organic Frameworks UiO-66-NH₂, MOF-808, NU-1000, and PCN-777. *Inorg. Chem.* **2017**, *56*, 11804–11809.
- (36) Kalinovsky, Y.; Cooper, N. J.; Main, M. J.; Holder, S. J.; Blight, B. A. Microwave-Assisted Activation and Modulator Removal in Zirconium MOFs for Buffer-Free CWA Hydrolysis. *Dalton Trans.* **2017**, *46*, 15704–15709.
- (37) Liu, Y.; Howarth, A. J.; Vermeulen, N. A.; Moon, S.-Y.; Hupp, J. T.; Farha, O. K. Catalytic Degradation of Chemical Warfare Agents and Their Simulants by Metal-Organic Frameworks. *Coord. Chem. Rev.* **2017**, *346*, 101–111.
- (38) Gil-San-Millan, R.; López-Maya, E.; Hall, M.; Padial, N. M.; Peterson, G. W.; DeCoste, J. B.; Rodríguez-Albelo, L. M.; Oltra, J. E.; Barea, E.; Navarro, J. A. R. Chemical Warfare Agents Detoxification Properties of Zirconium Metal-Organic Frameworks by Synergistic Incorporation of Nucleophilic and Basic Sites. *ACS Appl. Mater. Interfaces* **2017**, *9*, 23967–23973.
- (39) Lu, A. X.; McEntee, M.; Browe, M. A.; Hall, M. G.; DeCoste, J. B.; Peterson, G. W. MOFfabric: Electrospun Nanofiber Mats from PVDF/UiO-66-NH₂ for Chemical Protection and Decontamination. *ACS Appl. Mater. Interfaces* **2017**, *9*, 13632–13636.
- (40) Dhummakupt, E. S.; Carmany, D. O.; Mach, P. M.; Tovar, T. M.; Ploskonka, A. M.; Demond, P. S.; DeCoste, J. B.; Glaros, T. Metal–Organic Framework Modified Glass Substrate for Analysis of Highly Volatile Chemical Warfare Agents by Paper Spray Mass Spectrometry. *ACS Appl. Mater. Interfaces* **2018**, *10*, 8359–8365.
- (41) Peterson, G. W.; Lu, A. X.; Hall, M. G.; Browe, M. A.; Tovar, T.; Epps, T. H. MOFwich: Sandwiched Metal-Organic Framework-Containing Mixed Matrix Composites for Chemical Warfare Agent Removal. *ACS Appl. Mater. Interfaces* **2018**, *10*, 6820–6824.
- (42) Bigley, A. N.; Raushel, F. M. Catalytic Mechanisms for Phosphotriesterases. *Biochim. Biophys. Acta, Proteins Proteomics* **2013**, *1834*, 443–453.
- (43) Mondloch, J. E.; Katz, M. J.; Isley, W. C., III; Ghosh, P.; Liao, P.; Bury, W.; Wagner, G. W.; Hall, M. G.; DeCoste, J. B.; Peterson, G. W.; et al. Destruction of Chemical Warfare Agents Using Metal–organic Frameworks. *Nat. Mater.* **2015**, *14*, 512–516.
- (44) Moon, S. Y.; Liu, Y.; Hupp, J. T.; Farha, O. K. Instantaneous Hydrolysis of Nerve-Agent Simulants with a Six-Connected Zirconium-Based Metal-Organic Framework. *Angew. Chem., Int. Ed.* **2015**, *66*, 6795–6799.
- (45) Katz, M. J.; Moon, S.-Y.; Mondloch, J. E.; Beyzavi, M. H.; Stephenson, C. J.; Hupp, J. T.; Farha, O. K. Exploiting Parameter Space in MOFs: A 20-Fold Enhancement of Phosphate-Ester Hydrolysis with UiO-66-NH₂. *Chem. Sci.* **2015**, *6*, 2286–2291.
- (46) Moon, S. Y.; Wagner, G. W.; Mondloch, J. E.; Peterson, G. W.; DeCoste, J. B.; Hupp, J. T.; Farha, O. K. Effective, Facile, and Selective Hydrolysis of the Chemical Warfare Agent VX Using Zr₆-Based Metal-Organic Frameworks. *Inorg. Chem.* **2015**, *54*, 10829–10833.
- (47) Li, P.; Klet, R. C.; Moon, S.-Y.; Wang, T. C.; Deria, P.; Peters, A. W.; Klahr, B. M.; Park, H.-J.; Al-Juaid, S. S.; Hupp, J. T.; et al. Synthesis of Nanocrystals of Zr-Based Metal–organic Frameworks with Csq-Net: Significant Enhancement in the Degradation of a Nerve Agent Simulant. *Chem. Commun.* **2015**, *51*, 10925–10928.
- (48) Kalaj, M.; Momeni, M. R.; Bentz, K. C.; Barcus, K. S.; Palomba, J. M.; Paesani, F.; Cohen, S. M. Halogen Bonding in UiO-66 Frameworks Promotes Superior Chemical Warfare Agent Simulant Degradation. *Chem. Commun.* **2019**, *55*, 3481–3484.
- (49) Islamoglu, T.; Atilgan, A.; Moon, S. Y.; Peterson, G. W.; Decoste, J. B.; Hall, M.; Hupp, J. T.; Farha, O. K. Cerium(IV) vs

Zirconium(IV) Based Metal-Organic Frameworks for Detoxification of a Nerve Agent. *Chem. Mater.* **2017**, *29*, 2672–2675.

(50) Sava Gallis, D. F.; Harvey, J. A.; Pearce, C. J.; Hall, M. G.; DeCoste, J. B.; Kinnan, M. K.; Greathouse, J. A. Efficient MOF-Based Degradation of Organophosphorus Compounds in Non-Aqueous Environments. *J. Mater. Chem. A* **2018**, *6*, 3038–3045.

(51) Troya, D. Reaction Mechanism of Nerve-Agent Decomposition with Zr-Based Metal Organic Frameworks. *J. Phys. Chem. C* **2016**, *120*, 29312–29323.

(52) Chen, H.; Liao, P.; Mendonca, M. L.; Snurr, R. Q. Insights into Catalytic Hydrolysis of Organophosphate Warfare Agents by Metal-Organic Framework NU-1000. *J. Phys. Chem. C* **2018**, *122*, 12362–12368.

(53) Momeni, M. R.; Cramer, C. J. Dual Role of Water in Heterogeneous Catalytic Hydrolysis of Sarin by Zirconium-Based Metal–Organic Frameworks. *ACS Appl. Mater. Interfaces* **2018**, *10*, 18435–18439.

(54) Harvey, J. A.; Greathouse, J. A.; Sava Gallis, D. F. Defect and Linker Effects on the Binding of Organophosphorous Compounds in UiO-66 and Rare-Earth MOFs. *J. Phys. Chem. C* **2018**, *122*, 26889–26896.

(55) Schneider, J.; Matsuoka, M.; Takeuchi, M.; Zhang, J.; Horiuchi, Y.; Anpo, M.; Bahnemann, D. W. Understanding TiO₂ Photocatalysis: Mechanisms and Materials. *Chem. Rev.* **2014**, *114*, 9919–9986.

(56) Lee, D. T.; Zhao, J.; Oldham, C. J.; Peterson, G. W.; Parsons, G. N. UiO-66-NH₂ Metal–Organic Framework (MOF) Nucleation on TiO₂, ZnO, and Al₂O₃ Atomic Layer Deposition-Treated Polymer Fibers: Role of Metal Oxide on MOF Growth and Catalytic Hydrolysis of Chemical Warfare Ag. *ACS Appl. Mater. Interfaces* **2017**, *9*, 44847–44855.

(57) Lemaire, P. C.; Lee, D. T.; Zhao, J.; Parsons, G. N. Reversible Low-Temperature Metal Node Distortion during Atomic Layer Deposition of Al₂O₃ and TiO₂ on UiO-66-NH₂ Metal-Organic Framework Crystal Surfaces. *ACS Appl. Mater. Interfaces* **2017**, *9*, 22042–22054.

(58) Zhao, J.; Lee, D. T.; Yaga, R. W.; Hall, M. G.; Barton, H. F.; Woodward, I. R.; Oldham, C. J.; Walls, H. J.; Peterson, G. W.; Parsons, G. N. Ultra-Fast Degradation of Chemical Warfare Agents Using MOF–Nanofiber Kebabs. *Angew. Chem., Int. Ed.* **2016**, *55*, 13224–13228.

(59) Vellingiri, K.; Philip, L.; Kim, K. H. Metal–organic Frameworks as Media for the Catalytic Degradation of Chemical Warfare Agents. *Coord. Chem. Rev.* **2017**, *353*, 159–179.

(60) Wang, S.; Kitao, T.; Guillou, N.; Wahiduzzaman, M.; Martineau-Corcos, C.; Nouar, F.; Tissot, A.; Binet, L.; Ramsahye, N.; Devautour-Vinot, S.; et al. A Phase Transformable Ultrastable Titanium-Carboxylate Framework for Photoconduction. *Nat. Commun.* **2018**, *9*, No. 1660.

(61) Giannozzi, P.; Baroni, S.; Bonini, N.; Calandra, M.; Car, R.; Cavazzoni, C.; Ceresoli, D.; Chiarotti, G. L.; Cococcioni, M.; Dabo, I.; et al. QUANTUM ESPRESSO: A Modular and Open-Source Software Project for Quantum Simulations of Materials. *J. Phys.: Condens. Matter* **2009**, *21*, No. 395502.

(62) Hohenberg, P.; Kohn, W. Inhomogeneous Electron Gas. *Phys. Rev. B* **1964**, *136*, B864–B871.

(63) Makov, G.; Payne, M. C. Periodic Boundary Conditions in Ab Initio Calculations. *Phys. Rev. B* **1995**, *51*, 4014–4022.

(64) Perdew, J. P.; Wang, Y. Accurate and Simple Analytic Representation of the Electron-Gas Correlation Energy. *Phys. Rev. B* **1992**, *45*, 13244–13249.

(65) Vanderbilt, D. Soft Self-Consistent Pseudopotentials in a Generalized Eigenvalue Formalism. *Phys. Rev. B* **1990**, *41*, A1133–A1138.

(66) Payne, M. C.; et al. Iterative Minimization Techniques for Ab Initio Total-Energy Molecular Dynamics and Conjugate Gradients Calculations: Molecular Dynamics and Conjugate Gradients. *Rev. Mod. Phys.* **1992**, *64*, 1045–1097.

(67) Henkelman, G.; Uberuaga, B. P.; Jónsson, H.; Henkelman, G. A Climbing Image Nudged Elastic Band Method for Finding Saddle

Points and Minimum Energy Paths A Climbing Image Nudged Elastic Band Method for Finding Saddle Points and Minimum Energy Paths. *J. Chem. Phys.* **2000**, 9901–9904.

(68) Bermudez, V. M. Quantum-Chemical Study of the Adsorption of DMMP and Sarin on γ -Al₂O₃. *J. Phys. Chem. C* **2007**, *111*, 3719–3728.